Characterisation and modelling of active fibre composites

Nelson, Luke J.

Award date:
2005

Awarding institution:
University of Bath

Characterisation and Modelling of Active Fibre Composites

Submitted by Luke J Nelson

for the degree of PhD

of the University of Bath

2005

ProQuest LLC
789 East Eisenhower Parkway
P.O. Box 1346
Ann Arbor, MI 48106-1346

ACKNOWLEDGEMENTS

This work was funded jointly by the University of Bath and the National Physical Laboratory (NPL), Teddington. I would like to acknowledge the financial support and laboratory facilities made available to me by both institutions.

I would also like to acknowledge my academic supervisors Dr. Chris Bowen and Prof. Ron Stevens for their support, guidance, ideas and helpful discussions during the course of this research. I would also like to thank Dr. Markys Cain and Dr. Mark Stewart of NPL, without whose help, advice and laboratory facilities much of the work presented in this thesis would not have been possible.

I am indebted to Dr. Andy Perry for his help and advice with the finite element software package ANSYS, and to Andrew Dent whose diligent efforts in his final year project were a great benefit to this thesis.

I would like to extend my thanks to all those within the Department of Engineering and Applied Science who I have known during my time spent undertaking this project. This includes technicians, members of academic and non-academic staff, and fellow research students whose help and friendship is very much appreciated.

Finally, I would like to express my thanks to my parents for all they have done for me, particularly the support they have given me throughout my education. Above all I would like to thank my wife Amanda-Jane, who has been a constant support and motivator throughout the time we have known each other, and especially during the writing of this thesis.

ABSTRACT

The objective of this study is to examine the major components of a newly developed active composite configuration, and to use the understanding gained to optimise its performance. The composite comprises active piezoelectric fibres in a passive polymer matrix, thus it falls into the research field termed 'smart structures and materials'. The composite, typically known as the Active Fibre Composite (AFC), is made 'active' by applying a voltage to the driving electrodes, which are positioned on the top and bottom faces of the composite ply. By developing techniques to measure the properties of piezoelectric fibres, a fundamental understanding into their characteristics will be obtained. It is expected that by combining this understanding with research into the influence of the interdigitated driving electrodes on the composite performance, the composite configuration can be optimised for inducing maximum strain.

Validation of an analytical model, using finite element analysis and experimental data, has enabled the low electrical field properties of active fibres to be calculated from measurements made on 1-3 geometry composites. Experimental validation revealed that large errors were encountered when calculating fibre properties from composites with volume fractions lower than approximately 0.2. With the limits of the analytical model well understood, standard characterisation techniques were used to measure d_{33}, d_{31}, coupling factor, dielectric constant and stiffness of a range of commercially available fibres, each manufactured using different production methods. The methods compared were extrusion, viscous suspension spinning process (VSSP), Alceru and viscous plastic processing (VPP). A large variation in properties between the fibre types was seen, with the VPP fibres exhibiting the largest d_{33} coefficient (425 PC N^{-1}). Interestingly, fibres produced using the same process (Alceru) but with different diameters displayed markedly different properties; d_{33} values were 340 and 295 pC N^{-1} for the 125 and 250 μm diameter fibres respectively. Reasons for these differences were examined in later work.

The analytical model used to extract low field material property data was then extended to allow the more important high field strain and polarisation characteristics to be measured. Finite element analysis was used to investigate the effects of deviation of the composite response from the iso-strain assumption. Further, the effects of non-linear material properties were investigated by varying material property parameters in the analytical equations. Errors associated with the fibres' polarisation response were found to be dominated by the non-linear nature of the piezoelectric d_{33} coefficients. The fibres' strain response was less influenced by

non-linear material properties, but rather strongly influenced by deviation from the iso-strain assumption. To reduce errors, and increase the accuracy of this technique, it was concluded that composites with fibre volume fractions greater than 0.6 are required.

The model was used to extract high field strain and polarisation responses from the same set of fibres that had had their low field properties characterised. As with the low field properties, the high field responses were found to differ markedly between the fibre types. Fibres manufactured using the VPP and VSSP techniques exhibited the greatest piezoelectric activity, generating strains in the region of 4000 ppm for an electric field cycle of ±2.0 kV mm^{-1}. The large variation in the fibre properties has been linked to the physical and chemical properties of the fibres including porosity, grain size and phase composition. In general, large grain sizes, high densities and compositions closer to the tetragonal side of the morphotropic phase boundary (MPB) contributed to a large piezoelectric activity.

Finite element analysis was used to gain an understanding into the effect of the interdigitated electrode (IDE) design on the performance of the AFC device. The electrode width, substrate thickness, and electrode finger separation were varied, and the resultant strain measured. It was found that the optimum electrode finger width was equal to half the substrate thickness. It was also shown that to maintain at least 80% of the ideal d_{33} response the electrode separation must be at least four times greater than the substrate thickness. The underlying reasons for these results were investigated by examining the electric field strength and direction within the substrate.

The optimised IDE design was successfully manufactured via a lithographic process. AFCs were manufactured using these electrodes, together with fibres manufactured using the VPP technique. A robust method of manufacture was developed, the process of which is given in detail, and used to successfully manufacture ten AFC devices. Characterisation of these devices showed that early samples, which were cured under a lower pressure compared to later devices, exhibited poor strain performance. The best performing devices exhibited d_{33} coefficients in the region of 100 pC N^{-1}, which is lower than predicted. Reduced strain performance in the devices was associated with a large fibre-electrode separation, measured indirectly by the device capacitance. It is therefore concluded that an increased pressure during the cure cycle of device manufacture will increase the actuation performance. It is expected that this simple correction will result in AFC devices with optimised strain performance.

CONTENTS PAGE

APPENDICES

NOMENCLATURE

Symbols	Definition	Units
A	Area	m^2
C	Capacitance	$C\ V^{-1}$
c^E	Stiffness under constant field	$N\ m^{-2}$
d	Induced strain piezoelectric coefficient	$m\ V^{-1}$ or $C\ N^{-1}$
$\overline{d}$	1-3 composite induced strain piezoelectric coefficient	$m\ V^{-1}$ or $C\ N^{-1}$
D	Electrical displacement	$C\ m^{-2}$
D_A	Area equivalent *or* ferret diameter	m
D_{max}	Maximum calliper length	m
D_{min}	Minimum calliper length	m
e	Induced stress piezoelectric constant	$C\ m^{-1}$
E	Electric field	$V\ m^{-1}$
E_c	Coercive field	$V\ m^{-1}$
f_a	Anti-resonant frequency	Hz
f_r	Resonant frequency	Hz
F	Force	N
F_e	Elongation form factor	—
g_{mli}	Mean linear intercept distance	m
I	Current	$C\ s^{-1}$
$I_{R(200)}$	Intensity of the (200) reflection of the rhombohedral phase	—
$I_{T(002)}$	Intensity of the (002) reflection of the tetragonal phase	—

$I_{T(200)}$	Intensity of the (200) reflection of the tetragonal phase	—
k_{33}	Longitudinal coupling factor	—
$\bar{k}_{33}$	1-3 composite longitudinal coupling factor	—
l	Length	m
l_t	Total line length	m
l_p	Total line length crossing large pores	m
m	Mass	g
m_c	Calibrated magnification	—
M	Figure of merit	$\times 10^{-6}$ m^3 kJ^{-1}
n	Number of fibres	—
N_i	Number of grain boundary intersections	—
p	Electrode finger spacing	m
P	Polarisation	C m^{-2}
$\overline{P}$	1-3 composite polarisation	C m^{-2}
P_{rem}	Remnant polarisation	C m^{-2}
P_{sat}	Saturation polarisation	C m^{-2}
P_R	Proportion of rhombohedral phase	—
Q	Charge	C
r	Radius	m
s	Compliance	m^2 N^{-1}
$\bar{s}$	Effective 1-3 composite compliance	m^2 N^{-1}
s^D	Compliances under constant displacement (open circuit)	m^2 N^{-1}

s^E	Compliances under constant field (short circuit)	$m^2 N^{-1}$
S	Strain	—
$\overline{S}$	1-3 composite strain	—
S_{rem}	Remnant strain	—
S_{sat}	Saturation strain	—
t	Thickness	m
T	Stress	$N m^{-2}$
T_c	Curie Temperarure	°C
T_g	Glass transition temperature	°C
U	Mechanical displacement (ANSYS terminology)	m
V	Voltage	V
v_f	Fibre volume fraction	—
v	Poisson's ratio	—
w	Electrode finger width	m
w_a	Width of the active area in an AFC	m
Y	Young's modulus	$N m^{-2}$
ε^S	Permittivity at constant strain (mechanically clamped)	$F m^{-1}$
ε^T	Permittivity at constant stress (mechanically free)	$F m^{-1}$
$\overline{\varepsilon}^T$	1-3 composite permittivity at constant stress	$F m^{-1}$
ε_0	Permittivity of free space	$F m^{-1}$
ρ	Density	$g m^{-3}$
ρ_a	Apparent density	$g m^{-3}$

Commonly used abbreviations

AFC	Active Fibre Composite
AR	Aspect ratio
DMTA	Dynamic mechanical thermal analysis
FE	Finite element
IDE	Interdigitated electrode
MPB	Morphotropic phase boundary
PZT	Lead zirconate titanate
RVE	Representative volume element
SEM	Scanning electron microscopy
VPP	Viscous plastic processing
VSSP	Viscous suspension spinning process
XRD	X-ray diffraction

CHAPTER 1

INTRODUCTION

1.1 Motivation

Over recent years the drive towards imparting a higher degree of functionality into materials and structures has created a new research discipline referred to as 'smart structures and materials'. The desire to develop 'intelligent structures' has created a wealth of research over the past 10 to 20 years covering a range of 'active' materials. Piezoelectric materials, unique because they can be used as both sensors and actuators in smart structures, offer attractive characteristics to the smart structure engineer. A recently developed smart structure, incorporating piezoelectric fibre elements, is the active fibre composite (AFC), which is expected to have applications ranging from structural vibration and noise control[1] to structural health monitoring.[2] Novel uses, such as peristaltic pumps, have also been suggested. Now, 10 years after the initial patent application for the AFC,[3] these devices are now commercially available.[4,5] However, the underlying science of the active piezoelectric elements, and the structural design governing the performance of the AFC, is still not fully understood. Gaining a fundamental understanding of these aspects forms the motivation of this PhD.

1.2 Literature Review

1.2.1 Introduction

Piezoelectric materials develop electrical charges when strained, and develop strains when subjected to an electric field. For these reasons they are commonly used as sensors and actuators. The most common piezoelectric ceramic is lead zirconate titanate, $Pb(Zr,Ti)O_3$ (PZT). Since its development in the 1950s compositional improvement has failed to significantly increase the piezoelectric activity, with the exception of the very recent progress being made in the field of piezoelectric single crystals.[6] Hence improvements have emanated from the development of novel component configurations, which aim to optimise actuation and sensing capabilities for a given application. A newly developed configuration is the active fibre composite (AFC). This class of composites has numerous benefits over other sensing and actuating devices.

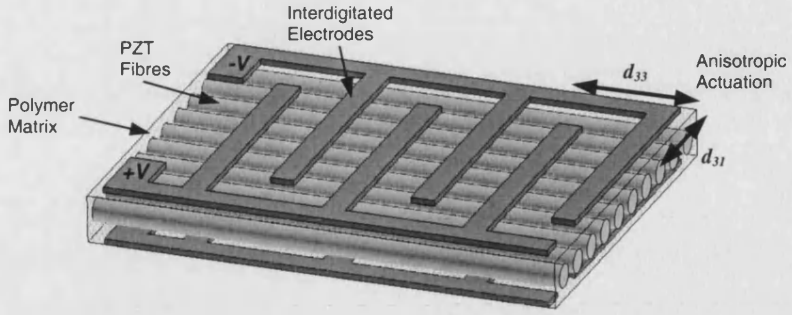

Figure 1.1: Illustration of the active fibre composite construction and mode of operation.

As shown in Figure 1.1, AFCs typically comprise a monolayer of uniaxially aligned piezoelectric fibres embedded in a polymer matrix between two interdigitated surface electrodes through which the driving voltage is supplied. This combination of interdigitated electrodes and composite technology aims to overcome many poor attributes associated with monolithic in-plane structural actuators.

The first AFCs were developed in the Active Materials and Structures Laboratory (AMSL) at the Massachusetts Institute of Technology (MIT), and patented in 1994.[3] Since their initial development significant advancement has been made in many areas, including fibre manufacture, matrix materials, electrode design, manufacturing techniques, and composite modelling. The aim of this review is to provide a critical overview of the major aspects of the Active Fibre Composite, highlighting areas in which research will be required to enable these composites to become established materials.

Following an introduction to the field of 'smart materials and structures', in which the AFCs are emerging as an important enabling technology, the development of the AFC is charted and its configuration and benefits are described. The major components of these composites (fibres, electrodes and matrix), together with composite manufacture, characterisation and modelling are critically assessed. Finally, the applications envisaged are reviewed. Areas in which future research and development is required to enable AFCs to become established materials are highlighted.

1.2.2 Smart materials and structures

Active fibre composites, which have the potential to be used as actuators and sensors for structural control, can be classed as 'smart materials and structures'. However, there is no universally accepted definition of the terminology in this field. Only recently have terms *adaptive*, *active*, *controlled*, *smart* and *intelligent* been used in conjunction with words such as *material*, *device*, *system* and *structure*. Ambiguity still exists concerning their use and meaning; all have been used, many times interchangeably, leading to confusion.[7] In light of this, a classification of these terms will be given, with the emphasis on structural control systems. Smart materials available for actuation and sensing are then introduced, highlighting the piezoelectric ceramics as key materials suitable for structural control.

Definitions

An *active material* is a material in which a response (output) is obtained on application of a stimulus (input). The stimulus could be, for example, a change in magnetic field or electric field, with the material's response being a change in viscosity or strain. Active materials can be broadly divided into two groups, those which respond to stimuli with a change in shape, and those which respond to stimuli with a change in a key material property, such as electrical conductivity or viscosity.[8] Materials from the first group, the 'classical' active materials, are commonly used for actuators in smart systems, and can also be used as sensors in which a strain experienced by the material is transformed into a useful signal allowing determination of strain levels. These concepts are illustrated in Figure 1.2.

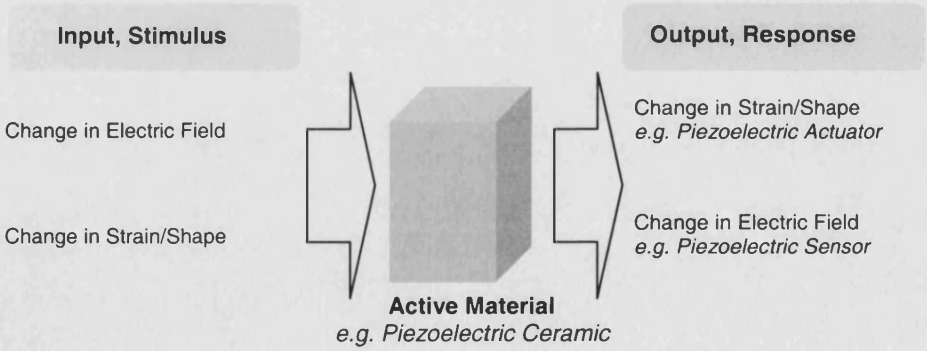

Figure 1.2: The concept of an 'active material' illustrating that piezoelectrics can be used as sensors or actuators depending on the stimulus-response direction. Adapted from intellimat.com.[8]

To respond effectively to change in its environment a *smart system* must fulfil three basic functions:

(i) Receive information: 'sensing'.

(ii) Process information: 'analysis and decision'.

(iii) Act on the decision: 'actuation'.

Structures that contain sensors are described as *sensory*, whereas structures having actuators distributed throughout are defined as *adaptive*, or *actuated*. Structures containing both sensors and actuators may be defined as *controlled* when sensing and actuation is linked by closed loop control. Other terms such as *active* and *intelligent* are typically used to denote a higher level of structural functionality and integration of the smart systems, and an increased sophistication and degree of integration of the control and power electronics.[9,10] This hierarchy is depicted in Figure 1.3.

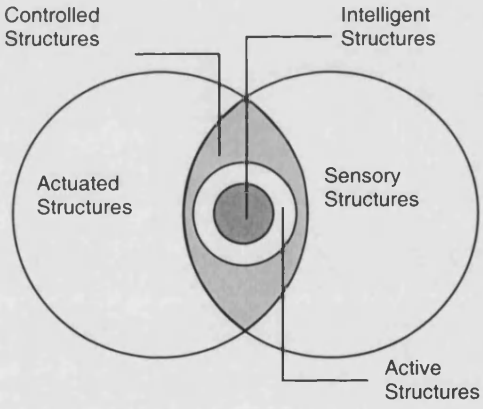

Figure 1.3: Representation of smart structures.[9,10]

It is important to understand that the field of smart materials and structures is truly multidisciplinary and that much of the technology, which includes composites, molecular electronics, micro-optics, polymer physics and chemistry, is still in its infancy. Thus the realisation of true intelligent structures is still yet to be achieved.

It is also important to classify the often carelessly used terms *material*, *device*, *system* and *structure*. In general the distinction may be made in terms of system complexity,[8] which increases from the active materials, to devices made from the materials, to systems constructed from devices, to structures comprising those systems.

From the above, it is apparent that the materials themselves are neither smart nor intelligent. The term 'smart material' simply implies that the material displays a level of *activity* enabling its use as an active element in a smart device.

Solid state actuator materials

The main active materials available for structural control are electrostrictives, magnetostrictives, shape memory alloys (SMA) and piezoelectric ceramics. Of these, the piezoelectrics receive most interest for high frequency structural control and vibration damping applications due to their high frequency response, linear response at low fields, high bandwidth and high stiffness (which imparts actuation authority; the ability to apply large forces). Moreover, piezoelectrics can be used as both an actuator and sensor. Although the alternative materials offer certain advantages, there are key disadvantages preventing their use for certain structural control applications. Electrostrictives have poor temperature stability, magnetostrictives offer similar properties to the piezoelectrics but are more inefficient when the magnetic field equipment is accounted for, and SMAs, although being researched for active composite sheets,[11] are capable only of a low frequency response. The piezoelectric ceramics are not without their disadvantages; they have high densities, produce relatively small strains, are brittle, and lack conformability. The development of the AFC attempts to overcome these disadvantageous material properties, and to extend the potential uses of piezoelectrics for structural control.

1.2.3 The piezoelectric effect

The piezoelectric effect, shown schematically in Figure 1.4, is the generation of a potential difference across the opposite faces of a piezoelectric crystal when a mechanical stress is applied between these faces. This is the 'direct' piezoelectric effect, and the potential difference developed is known as polarisation.

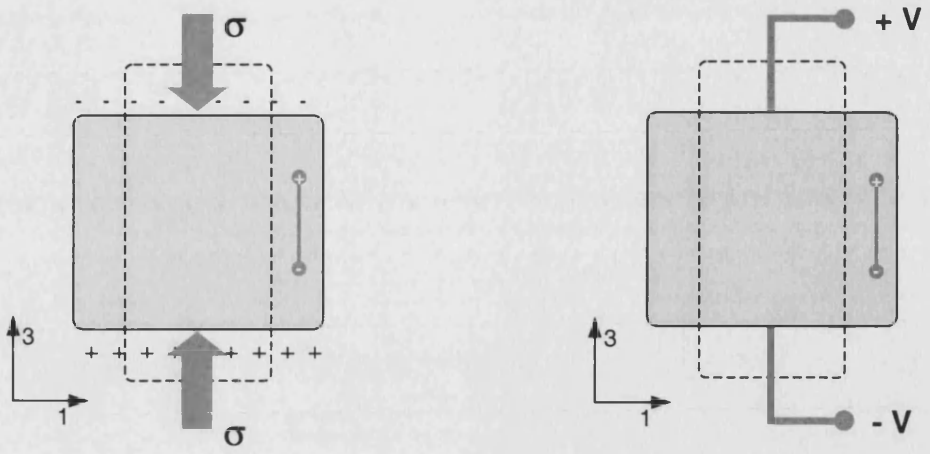

(a) (b)

Figure 1.4: Schematic 2-D representation of a) the direct and b) the converse piezoelectric effect. Broken outline represents the shape prior to the stimulus application. 2-direction is into page, poling is in the 3-direction.

The 'converse' piezoelectric effect is the change in strain for a free crystal (or stress for a clamped system) that accompanies a change in applied electric field. The direct and converse effects, shown in Figure 1.4(a) and Figure 1.4(b) respectively, are reversible and correspond to sensing and actuating modes of operation respectively.

Lead Zirconate Titanate (PZT)

Lead zirconate titanate, typically referred to as PZT, dominates the piezoelectric ceramic materials due to its high electro-mechanical coupling and the ability to tailor the piezoelectric properties by additions of dopant atoms. PZT is a solid solution formed between $PbTiO_3$ and $PbZrO_3$ and has the chemical formula $Pb(Zr_xTi_{1-x})O_3$. A phase diagram for this ceramic is presented in Figure 1.5.

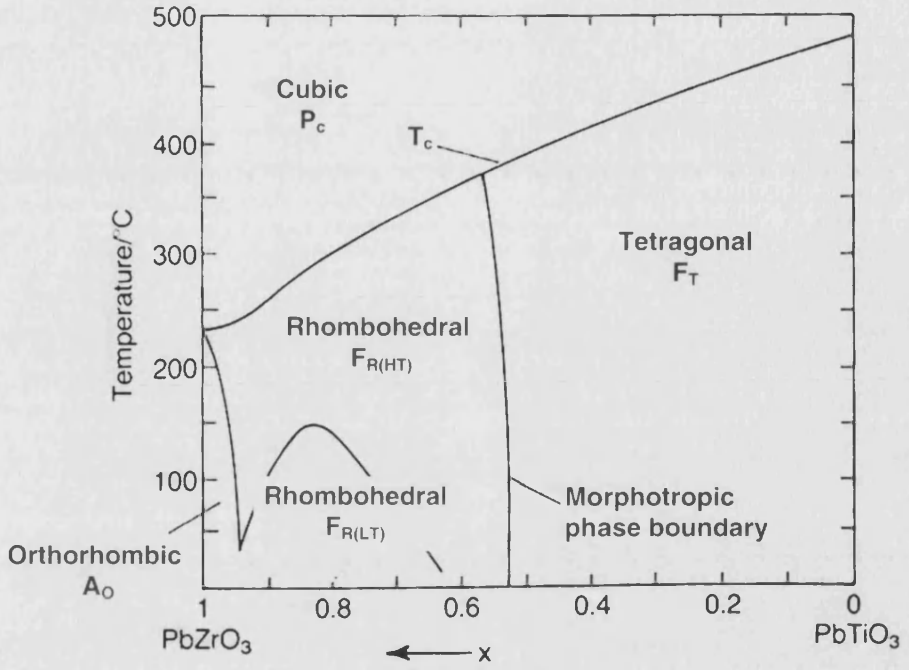

Figure 1.5: Phase diagram of the $Pb(Zr,Ti)O_3$ system.

At high temperatures, above the Curie point (T_c), the unit cell is cubic (P_c) and exhibits no piezoelectricity. On cooling below the Curie point the structure undergoes a phase transformation to either high temperature ferroelectric rhombohedral ($F_{R(HT)}$) or ferroelectric tetragonal (F_T) depending on the composition. A morphotropic phase boundary (MPB) exists between these two phases, and occurs at the Zr:Ti ratio of 52:48. At this composition rhombohedral and tetragonal phases are present in equal proportions and the strongest piezoelectric activity is observed. Other phases present in the PZT system are a low temperature rhombohedral phase ($F_{R(LT)}$) and an antiferroelectric orthorhombic phase (A_O).

PZT adopts an ABO_3 perovskite crystal structure as illustrated in Figure 1.6. The Zr^{4+} and Ti^{4+} ions occupy the body centre (B site) at random, Pb^{2+} ions occupy the corners (A sites), and O^{2-} ions occupy the centres of each face. Associated with the rhombohedral and tetragonal phases is a spontaneous polarisation, a result of a small relative shift of the B site cations. In the tetragonal phase the polarisation is towards one of the six faces of the unit cell (<100> directions) while in the rhombohedral phase it is toward one of the eight corners of the unit cell (<111> directions). Two of the possible six polarisation directions in the tetragonal unit cell are also illustrated in Figure 1.6. The lack of a centre of symmetry in the unit cells of these phases is the origin of the piezoelectric behaviour in PZT.

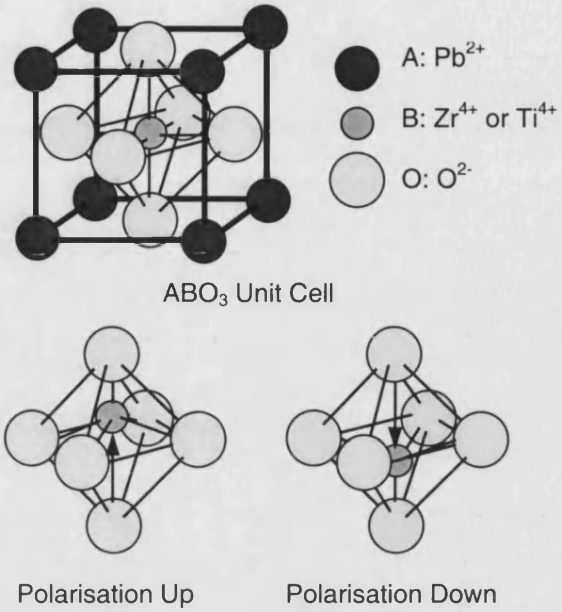

Figure 1.6: Perovskite ABO_3 unit cell for PZT, illustrating 180° polarisation reversal for two of the six possible polarisation states produced by the displacement of the central cation in the tetragonal phase. After Heartling, 1999.[12]

Domains

In a piezoelectric composition, when the crystal is cooled below T_c, the unit cells become spontaneously polarised as already discussed. Usually the crystal develops a twin structure, consisting of regions which have spontaneous polarisations with positive and negative polarity. Such a structure is shown schematically in Figure 1.7.

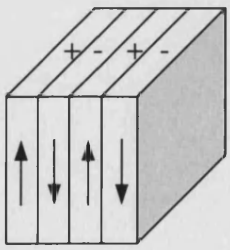

Figure 1.7: The simplest domain structure. Arrows indicate the direction of spontaneous polarisation.

Such a twin structure is known as the domain structure of the crystal. The twin component is called a domain, while the boundary between them is referred to as a domain wall. The domain walls in Figure 1.7 are termed 180-degree domain walls since the polarisations of the domains are orientated 180° to their neighbour.

In a tetragonal PZT crystal the domain structure presented in Figure 1.7 could consist, for example, of regions of the 'polarisation up' and 'polarisation down' unit cells shown in Figure 1.6. In other regions of the crystal the direction of spontaneous polarisation may be in another direction allowed by the unit cell symmetry, such as the formation of 90-degree domain walls in tetragonal PZT. In rhombohedral compositions, in addition to the 180-degree domains, 71-degee and 109-degree orientations are possible, representing adjacent cell diagonals.

Poling

For single crystal and polycrystalline materials to exhibit piezoelectricity the initial randomly orientated electrical dipoles must be aligned in a common direction in a process called 'poling'. Poling can be defined as the application of an electric field, usually at elevated temperatures, to orientate the polar axis of the domains to those directions allowed by symmetry, which are nearest to that of the applied electric field. The strong piezoelectric activity occurring at the morphotropic phase boundary in PZT is thought to be associated with the larger number of polarisation directions available.

Piezoelectric coefficients and notation

The piezoelectric coefficients *d*, *g*, *e* and *h* are essentially proportionality constants for the electrical-mechanical coupling of piezoelectric materials.[13] Of these, one of the most relevant for structural actuation and sensing is the piezoelectric *d*-coefficient. In actuator mode the *d*-coefficient is the strain (*S*) developed per unit applied field (*E*) and has units of metres per unit voltage (m V^{-1}). In sensor mode the *d*-coefficient is the electrical displacement (*D*) generated per unit applied stress (*T*) and has units of charge per unit force (C N^{-1}). These are defined in Equation (1.1), where the subscripts denote the parameter held constant.

$$d = \left(\frac{S}{E}\right)_T = \left(\frac{D}{T}\right)_E \tag{1.1}$$

The magnitude of the piezoelectric coefficients vary with direction of electrical and mechanical measurement. A general piezoelectric coefficient X is reported with a nomenclature of the form X_{ij} in which the subscripts i and j denote the direction of electrical and mechanical fields respectively. The 3 direction is defined as the direction of poling while 1 and 2 are perpendicular directions. Thus the d_{31} coefficient relates the strain developed in the 1 direction to the electrical field applied along the direction of poling (the secondary or transverse effect). The d_{33} coefficient relates to the strain developed in the direction of poling to the electrical field applied in the poling direction (the primary or longitudinal effect).

Bulk PZT properties

If we now consider piezoelectric fibres embedded in a structure, in actuation mode an imposed electric field causes the fibres to develop a strain, which is transferred to the host structure to induce deformation. In sensing, the piezoelectric fibres respond to strains in the host structure with the production of an electric field and an associated voltage, the magnitude of which is related to the imposed strain. For actuation, which is where the majority of research and development of AFCs is focused, the active fibres are driven at high fields (1 – 2 kV mm^{-1}) to obtain maximum actuation strains. It is therefore important that not only the commonly measured low field (< 1 V mm^{-1}) piezoelectric properties are characterised, but that the high field properties are characterised, and the underlying science is well understood.

To understand the response of a piezoelectric material under high electrical field conditions, examination of a polarisation-field (hysteresis) curve is useful. Such a curve is shown in Figure 1.8.

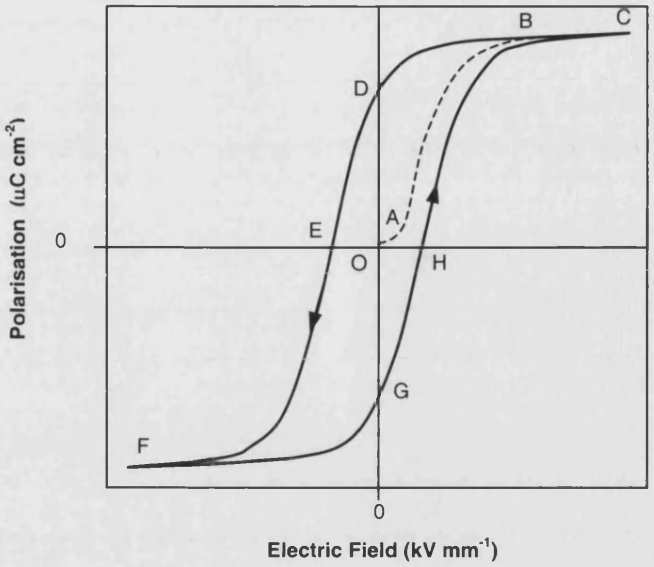

Figure 1.8: Schematic polarisation-field (hysteresis) curve for a piezoelectric material.

The shape of the hysteresis curve can be explained by considering the domain structure of the material. Initially the large number of domains are randomly orientated, which means that the overall polarisation of the crystal is zero. If a small field is applied to the sample a linear relationship between polarisation and field is seen (O→A) because the crystal is behaving as a linear dielectric. As the field strength is increased, domains align with the applied field. Associated with this domain switching is a large increase in the polarisation (A→B). At some field level all the domains are aligned in the field direction; this is the state of saturation (B→C). On decreasing the field strength the polarisation will generally not return to zero, but follow the path C→D. At zero field some of the domains that have been aligned by the applied field remain aligned so the crystal exhibits a remnant polarisation, P_{rem} (O→D). In order to remove the remnant polarisation induced by the applied field, the field direction must be reversed. The value of field required to reduce the polarisation to zero (O→E) is known as the coercive field, E_c. Further increase in the field in the negative direction will cause complete alignment of the dipoles in this direction (E→F). The cycle can be completed by reversing the field direction once again (F→G→H→C).

In addition to generating a characteristic polarisation-field curve, a piezoelectric material also generates a characteristic strain-field curve. An example of such a curve is shown in Figure 1.9.

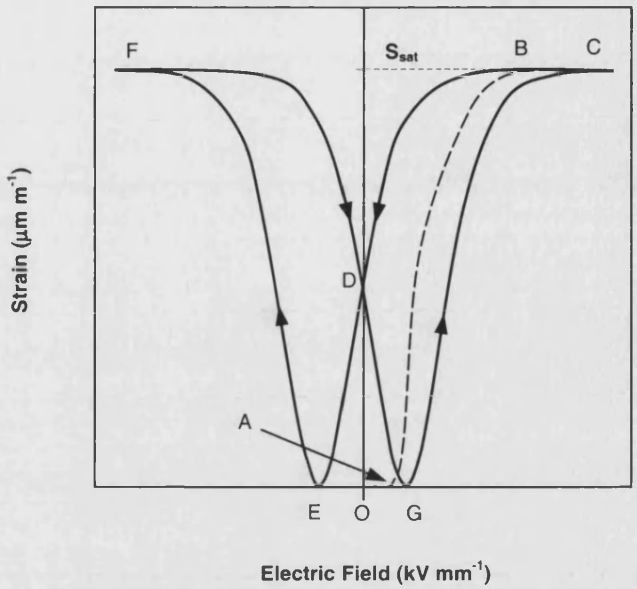

Figure 1.9: Schematic strain-field (butterfly) curve for a piezoelectric material.

Initially the domains are randomly orientated and the crystal is in its lowest strain state. On applying a small field to the sample the strain does not initially increase because the domains are randomly aligned (O→A). At some field level (A) the domains begin to change their polarisation direction to align with the direction of applied field. Associated with the change in polarisation direction is a dimensional change of the unit cell, and as the field is increased further, more domains switch their polarisation direction and the strain continues to increases with the applied field (A→B). A point is reached at which all the domains have been aligned with the field, and an increase in field leads to no further increase in strain (B→C). The crystal is said to have reached its saturation strain, S_{sat}. On removal of the field the strain will generally not return to zero, but follow the path C→D. At zero field some of the domains that have been aligned by the applied field remain aligned so the crystal exhibits a remnant strain, S_{rem} (O→D). In order to remove the remnant strain, the field direction must be reversed. The value of field required to reduce the strain to zero (O→E) is the coercive field, E_c, and is analogous to the coercive field measured in the polarisation-field loop (Figure 1.8). Further increase in the field in the negative direction will cause complete alignment of the dipoles in this direction, with an associated increase in strain (E→F). The cycle can be completed by reversing the field direction once again (F→D→G→C). Due to its characteristic shape, the strain-field curve of a piezoelectric material being driven at high fields is sometimes referred to as a 'butterfly loop'.

Since numerous compositions of PZT are available it is important to compare their merits for use as the active elements in AFCs. Table 1.1 presents both low field and high field properties for four grades of PZT, ranging from 'soft' to 'hard'. It can be seen that at low fields:

(i) d_{33} coefficients are generally higher for the softer piezoceramics i.e. soft materials are more active.

(ii) Dielectric constants increase with the degree of 'softness'.

(iii) Depolarisation stress and Young's modulus are higher for hard piezoceramics.

And that at high fields:

(i) The representative cycle strain, energy density and saturation strain are at a maximum for PZT-5A.

(ii) Hysteresis loss increases with degree of 'softness'.

(iii) The remnant polarisation and coercive field are at a maximum for PZT-5A.

Table 1.1: Property comparison of four Morgan ElectroCeramics PZT grades. High field properties relate to a cyclic field of ± 2×E_c for 5H and 5A and ± 48kVcm^{-1} for 4S and 8M. Representative Cycle (Rep. Cycle) data relates to a field of –75% E_c against the direction of poling, to +200% E_c (or 48kVcm^{-1} for 4S and 8M).[50]

		SOFT → HARD			
	PROPERTIES	**PZT 5H**	**PZT 5A**	**PZT 4S**	**PZT 8M**
LOW FIELD	Relative Dielectric constant, ε_{33}^T	3350	1770	1500	800
	Induced Strain, d_{33} (pm V^{-1})	555	392	360	215
	Coupling Coefficient, k_{33}	0.790	0.774	0.861	0.767
	Young's Modulus, Y (GPa)	48	53	60	77
	Depole Stress (MPa)	44	72	>150	>150
HIGH FIELD	Coercive Field, E_c (kV cm^{-1})	7.2	11.2	8	8.4
	Remnant Polarisation (mC m^{-2})	300	375	110	80
	Saturation Strain (ppm)	3200	4100	2100	1400
	Rep. Cycle Strain (ppm)	2350	2800	1875	1070
	Rep. Cycle Hysteresis (%)	24	24	7	4
	Rep. Cycle Energy Density (J kg^{-1})	17.7	27.7	14.1	5.9

In summary, PZT-5A displays attractive properties for the role of a high field actuator. However, hard piezoceramics are more suited to high applied stress applications where reducing the risk of mechanical and electrical depolarisation is important, but this is at the expense of poorer high field strains.

1.2.4 Development of the Active Fibre Composite

The failure to achieve significant improvement in the level of piezoelectric performance of PZT through compositional control led to the development of novel component configurations, such as the AFC. For high strain actuation it is desirable to make use of the larger longitudinal d_{33} piezoelectric effect, such as in piezoelectric stack actuators. Until recently, in-plane structural actuation and sensing has been unable to make use of longitudinal d_{33} actuation, simply because the electric field must be applied perpendicular to the actuation direction of interest. Instead, the transverse d_{31} piezoelectric effect, which is approximately half the longitudinal effect in magnitude ($d_{31} \approx -0.5 \times d_{33}$), has been employed. Two examples of using the transverse effect for actuation are the traditional monolithic piezoelectric actuator, and the more recent piezoelectric fibre composite (PFC) actuator[14] in which the piezoelectric is in fibre form and surrounded by a polymer matrix. Both of these designs have uniformly deposited electrodes causing the field direction to be in a direction perpendicular to the desired actuation direction. Illustrations of these two actuators, the electric field vectors, and the piezoelectric responses, are shown in Figure 1.10(a) and Figure 1.10(b) respectively.

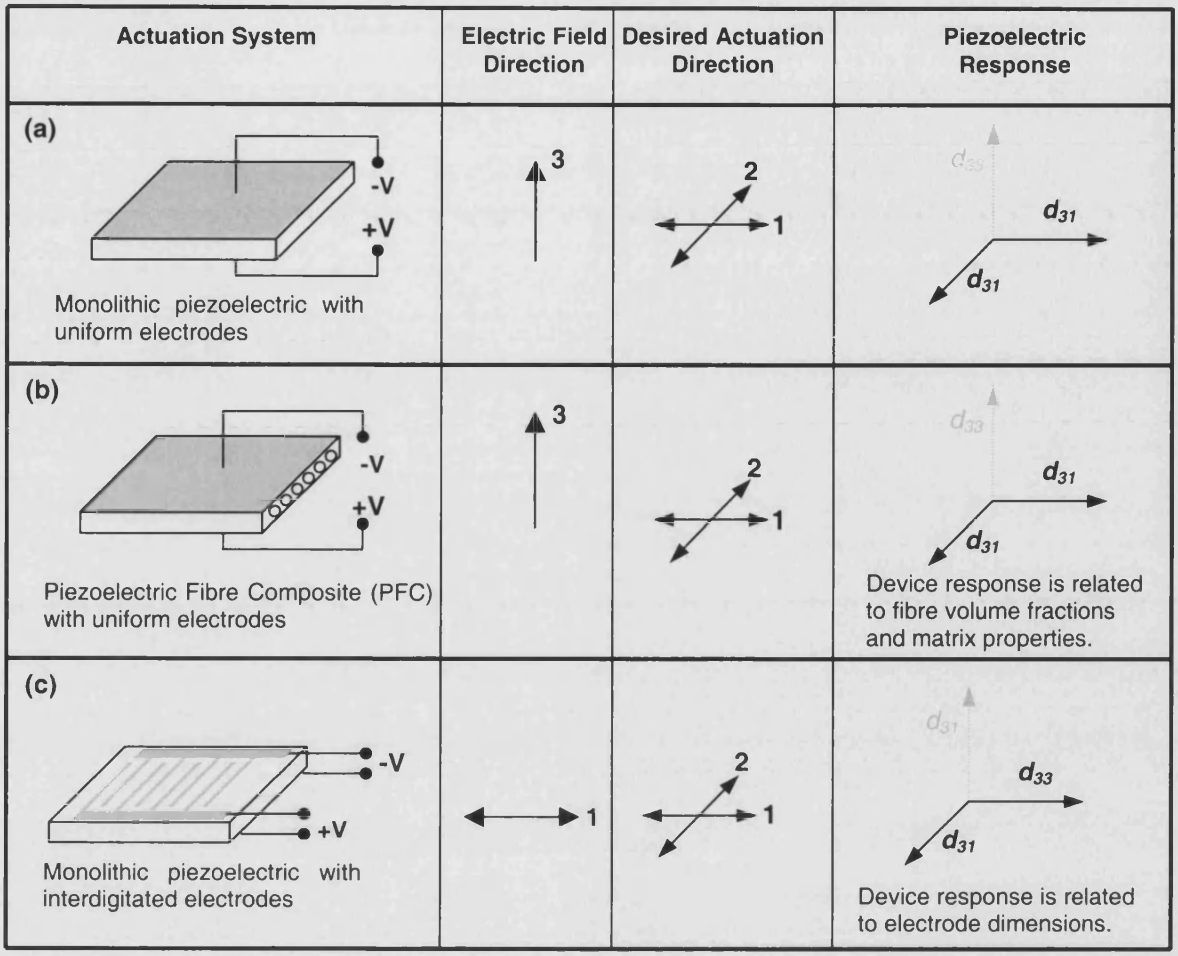

Figure 1.10: Overview of some piezoceramic actuator technologies.

The poor attributes of the monolithic piezoceramic actuators (e.g. low fracture strength, high stiffness, difficulty in producing complex shapes and high densities) are largely solved by the PFC configuration. Furthermore, the in-plane actuation of the PFC is anisotropic,[14,15] a useful feature which allows multi-ply composites to induce bending and torsional moments without having to rely on the host structure anisotropy. However, it can be seen from Figure 1.10 that in both the monolithic and PFC configurations the electric field direction (3) is normal to the desired actuation direction (1), and thus the in-plane actuator properties are dependant on the smaller d_{31} coefficient.

A novel electrode pattern, the interdigitated electrode (IDE), has been applied to monolithic actuators to direct the electric field into in-plane directions in an effort to exploit longitudinal in-plane actuation.[16] The IDE devices, such as shown in Figure 1.10(c), have been successful for low field applications, but when large fields are applied during poling or in operation, internal cracks and electrical shorts are occasionally observed. Internal cracks can develop as a result of non-uniform internal strains caused by the non-uniform electrical field in the material near the edges of the electrodes,[17] and at the electrode line connecting the IDE fingers. Electrical short circuits occur as a result of having alternating high and low voltage electrode fingers on a common side of the device. Furthermore, the manufacturing and property disadvantages associated with monolithic actuators still apply.

The Active Fibre Composite

The combination of the IDE with the PFC offers significant improvement to the actuators described above. This was realised by the Active Materials and Structures Laboratory at MIT where the interdigitated electrode piezoelectric fibre composite (IDEPFC), now known as the AFC, was developed. The concept was first patented in 1994[3] and since then significant advances have been made. Two major efforts concerned with research and development of AFCs are the German ADAPTRONIC program[18] and the US Active Fibre Composite Consortium (AFCC).

An AFC (Figure 1.1) typically comprise a monolayer of uniaxially aligned piezoelectric fibres embedded in a polymer matrix between two interdigitated surface electrodes through which the driving voltage is supplied. Performance is increased as result of the IDE configuration by allowing the longitudinal d_{33} piezoelectric effect, directed along the length of the active fibres, to be utilised. Moreover, the d_{31} effect is exhibited in the orthogonal in-plane direction giving rise to in-plane anisotropy, as indicated in Figure 1.10(c). The unidirectional nature of the fibres creates further in-plane actuation anisotropy, allowing torsional actuation and sensing.

As a result of the composite construction, AFCs offer increased robustness when compared to monolithic piezoceramics. The combination of fine scale, flexible ceramic fibres, in a low stiffness, tough polymer matrix provides load transfer mechanisms characteristic of fibre reinforced composites. The AFC configuration also offers increased conformability and can be applied to more irregular and curved surfaces, which is critical for large scale coverage. Large scale actuation and sensing with monolithic actuators would require an impracticably large number of leads and attachments, whereas a single actuation ply of an AFC can be an integral part of the existing structure. The ability to tailor the properties at material, lamina, and

laminate level (fibres, matrix, fibre volume fractions and ply angles) could allow integration into host structures without adversely affecting the host structure performance. The possibility of introducing a reinforcement phase, such as glass fibres, could see existing passive structures replaced with a truly active structure having built-in sensing and actuating functions. The advantages offered by AFCs are expected to be exploited in applications including contour control, vibration suppression, acoustic control and structural health monitoring.

1.2.5 Manufacture and characterisation of PZT fibres

The PZT fibres form the active elements of the AFC. Their properties are therefore crucial to device performance. PZT-5H was chosen for early research at MIT because of its large low field piezoelectric activity, ease of polarisation (soft piezoceramics, having higher domain mobility, are generally easier to pole) and commercial availability in fibre form. It is clear from Table 1.1 that PZT-5A has better high field properties, and as a result is commonly manufactured in fibre form and exploited in more recent AFC research. A benefit of using the harder piezoceramics is that their lower dielectric constants reduce the fibre-matrix dielectric mismatch, hence increase the percentage of field reaching the fibre.[19]

Manufacturing Methods

Early fabrication of fine scale PZT fibres was motivated by the potential to improve the performance of 1-3 connectivity composites[20] (uniaxially aligned piezoelectric fibres in a passive polymer matrix) for ultrasonic transducers and hydrophones.[21] Reducing the spatial scale of such composites by using fine fibres would increase the achievable resolution, for example in medical applications.[22] However, typical methods used to produce PZT fibres for these applications e.g. dicing, lost mould, and injection moulding, are limited in both the lengths (typically < 1 cm) and side dimensions (typically > 100 μm) that can be produced.

For AFCs, production of semi-continuous fibres of smaller diameter become essential. The small diameters are important for maintaining structural conformity with host structures such as glass fibre and carbon fibre composites.[23] Small diameter fibres also offer new possibilities for fibre arrangements within composites. However, the effect of fibre diameter on piezoelectric properties is uncertain;[24] It is possible that small fibre diameters and large surface areas will limit achievable properties. Lead oxide, a major component of PZT, has a high vapour pressure above its melting point of 880°C and is thus prone to volatilisation at a typical sintering temperature of 1250°C. One of the main technical challenges to the production of high quality

PZT fibres is maintaining compositional stoichiometry during sintering, which in turn strongly influences the electromechanical properties. Lead loss in small diameter fibres is a particular problem due to their high surface area/volume ratio. Additives can be employed as sintering aids, and smaller, more reactive powders used to reduce sintering temperatures. It is common practice to sinter such components in lead rich atmospheres to prevent excessive lead loss.

There are numerous methods of producing PZT fibres suitable for use in AFCs. They can be broadly classified into three categories:

(i) dry powder processing: this includes conventional extrusion and the related viscous plastic processing (VPP) technique,

(ii) wet powder processing: this includes the traditional viscous suspension spinning process (VSSP) and the more recent Lyocell or Alceru method,

(iii) chemical processing: primarily sol-gel spinning.

Additional methods of fibre fabrication, such as using a replication processes,[25, 26] and PZT coated inactive fibres,[27] have received little attention as fibre production methods. This is principally due to the poor piezoelectric properties achieved.

Extrusion

Research on AFCs at MIT has used circular cross section PZT 5A fibres produced using a proprietary extrusion and firing method, developed by CeraNova Corporation.[24] The process starts with mixing the powders and polymer binders. Composition, rheology, homogeneity and cleanliness of the mix have all been identified as key to successful fibre manufacture. The mix is then extruded; an important stage in which die design, temperature, pressure and draw down force are critical parameters. The 'green' fibres are then handled as single fibres or, more recently, using a mandrel capable of handling many hundreds of fibres. Binder burnout and sintering, or firing, then follows. During this stage the temperature, time and air flow must all be optimised. Finally, the fibres undergo quality control. This conventional ceramic processing technology produces straight, contamination free fibres, 80 to 250 μm in diameter with a grain size of ~2 μm, at low cost, and is capable of producing a range of cross sectional geometries. 'Ribbon' geometry fibres, essentially a rectangular fibre with rounded edges, have recently been used as active elements in AFCs.[28] These AFCs have both higher free strains and maximum

achievable fibre volume fractions, which combine to give a predicted increase in actuation compared with traditional circular fibre AFCs.

Viscous plastic processing (VPP)

The viscous plastic processing (VPP) technique was first applied to forming ceramics in work conducted at ICI during the 1980's.[29] This technique has recently been used to successfully produce PZT ceramic bodies of various forms, with enhanced structural and electrical properties.[30] The principle of the process is to achieve a de-agglomerated dough of ceramic and polymer, with far higher viscosity than conventional extrusion pastes. Both aqueous PVA and solvent PVB binder systems may be employed to form the stock material, loaded with a minimum of 50 volume percent PZT. The high viscosity of the dough improves sintered microstructure through two key mechanisms. Firstly, the dough has a gel like viscosity, allowing high levels of shear to be transferred to the ceramic particles, typically using twin roll milling. During mixing, transfer of shear forces causes agglomerates to break down, improving homogeneity. Secondly, mechanical forces from the thick polymer solution prevent re-agglomeration. This is in contrast to conventional colloidal mixtures, in which comparatively weak electrostatic interactions are the primary force.

To homogenise the material and remove entrapped air, the material is consolidated into a feedstock rod. Ceramic stock material prepared by VPP exhibits good formability and is compatible with commonly used plastic forming techniques.[31] PZT fibres may therefore be formed using an extrusion process as previously discussed, with suitable adaptations to accommodate the increased viscosity. The highly homogeneous, de-agglomerated mix allows production of fibres with diameters down to 40 μm,[32] compared to the 80 μm limit with traditional extrusion.

Viscous Suspension Spinning Process (VSSP)

The concept of developing ceramic fibres using the VSSP method first originated in 1987 when Advanced Cerametrics Inc. (ACI) attempted to make super-conducting ceramic wire.[33] The process has now been refined such that high quality ceramic fibres of almost any chemistry can be manufactured.[34] In the VSSP technique (Figure 1.11) a cellulose solution, obtained using the viscose process, acts as a carrier for the ceramic powder. In the viscose process, cellulose is treated with sodium hydroxide, causing the cellulose to swell. With the addition of carbon disulphide the cellulose is converted into cellulose xanthogenate which, when mixed with dilute sodium hydroxide, forms the spinning mix to which is added the ceramic powder. This is

pressure filtered to remove large agglomerates, and de-aired under vacuum. The spin mix is metered through a spinnerette immersed in a bath containing aqueous acid and salts. The acid coagulates the spin mix and regenerates cellulose by releasing xanthate groups, while the salt dehydrates the fibres, reducing fibre diameter by 60%. The fibres are stretched to increase green strength, washed, and sized before being wound onto a take-up reel. A unique feature of this fibre is that, prior to carrier burnout and sintering, PZT fibres can be woven into two- and three-dimensional shapes using conventional textile and composite forming processes.

This process can produce continuous PZT fibres having diameters as small as 10 μm,[34] although these are contained in 750 μm diameter tows containing upwards of 500 individual fibres. This form is inappropriate for AFCs where fibre diameters <200 μm are desirable. Research has thus focused on 1-3 composites typically used for ultrasonic transducer applications[35,36] and only recently have single VSSP fibres been used for AFC technologies.[5]

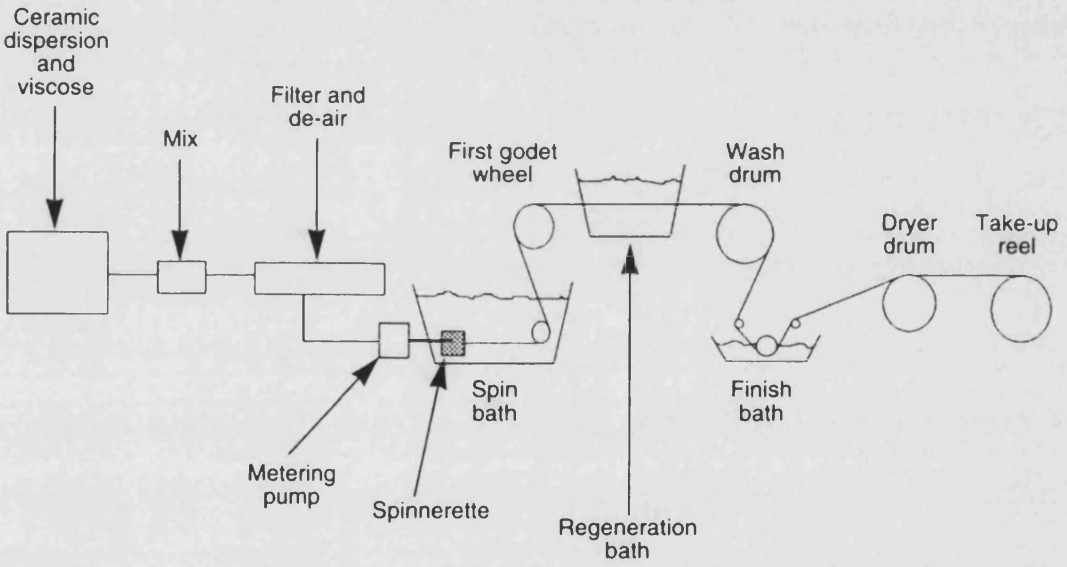

Figure 1.11: Schematic of VSSP continuous ceramic fibre production process.[34]

Lyocell or Alceru method

A key stage in the VSSP technique is the formation of a cellulose carrier solution. The viscose process employed requires the use of harmful chemicals, which prompted the development of a new, environmentally friendly method. Unlike the viscose process, in the Lyocell or Alceru process the cellulose is dissolved in the non-toxic aqueous solvent N-methylmorpholine-N-oxide, NMMO.[37] During fibre processing the NMMO solvent used to create the spinning solution is removed and almost completely recovered, making this an environmentally friendly and less wasteful process when compared to VSSP.

Sol-Gel Spinning

Sol-gel spinning differs from the previous processes because it is a chemical process, rather than a traditional powder process. Sol-gel routes are attractive because they offer compositional control, low temperature firing, continuous fibre production, and overall simplicity. PZT substituted with lanthanum,[21,38] niobium,[38,39,40] $CdBO_3$[39] and PMN,[41] have all been successful, demonstrating the flexibility of this technique, which is capable of producing fibres with diameters as small as 10 μm.[38]

The sol-gel process for PZT fibre production consists of preparing a non-aqueous precursor solution, usually alkoxides (typically zirconium butoxide and titanium isopropoxide) with metal cations (lead acetate trihydrate or lead acetylacetonate) in the desired stoichiometry.[42] This precursor solution is then partially hydrolysed, by the addition of acetic or nitric acid, to form a 'sol' (a colloidal suspension of solid particles or clusters in a liquid). This is subsequently dried to form a gel of the required viscosity, and formed into fibres by drawing using a glass rod[43] or extruding through a spinneret containing several small diameter holes.[38] In the extrusion technique, the spun fibres are collected on a variable speed rotary take-up drum. Factors identified as affecting green fibre diameters are the viscosity of the sol, spinneret diameter, and speed of the take-up drum. The green fibres are subsequently dried and fired.

Fibres may develop the required crystalline perovskite structure at temperatures as low as 700°C, thus preventing lead loss, but the grain size remains small, typically sub-micrometer.[38,43] Increasing the sintering temperature to 1250°C promotes grain growth producing a maximum grain size of 5-8 μm.[40,39] It has been shown that grain size may greatly influence the level of piezoelectric activity in PZT fibres, with a large grain size giving rise to superior piezoelectric properties,[44] in which case higher temperature sintering, together with control of the lead content, is desirable using present production techniques.

Fibre Characterisation

Of particular interest is the measurement of the electrical and piezoelectric properties of the individual fibres, such as dielectric constant, piezoelectric *d*-coefficients, and the strain response under high electric fields. Since fine scale fibres are fragile and give small signal responses, fibre properties are commonly deduced from measurements of 1-3 connectivity composites[44,45,46] for which analytical models have been developed.[47-49] However, the manufacture of 1-3 composites can be labour intensive and only provides an indication of the averaged fibre properties. Techniques are available for poling, measuring capacitance and polarisation,[40] and electric field-strain responses[50] of single fibres. However, the small diameter of the fibres, and the associated low signals obtained, make these measurements difficult.

For fracture mechanics and evaluating structural conformity, the mechanical properties are of interest. Impedance analysis of 1-3 composites can be used to evaluate the elastic properties of piezoelectric fibres,[51] and simple methods exist for testing single fibre tensile[52] and bend strengths,[53] but these have not been employed for characterisation of PZT fibres. Other characterisation techniques include scanning electron microscopy, energy dispersive spectroscopy and x-ray diffraction.

Current research shows that porosity and small grain size can greatly reduce the piezoelectric activity[44,54,55] and that PZT fibre piezoelectric properties, although following similar trends to bulk PZTs, are generally substantially lower.[50,56]

1.2.6 Interdigitated electrodes

In addition to the fibre geometry and properties, the electrode is an important component of the AFC. Interdigitated electrode (IDE) technology was introduced to increase the effective in-plane actuation properties of the piezoelectric fibre composite (PFC). The IDE pattern is shown in Figure 1.1 and a representative section can be seen in Figure 1.12. The IDE consists of a series of opposing polarity electrodes that generate components of electric field in the plane of the composite. The pattern is mirrored on the reverse side to maintain symmetry. The result is longitudinal in-plane actuation perpendicular to, and transverse actuation parallel to, the electrode finger direction.

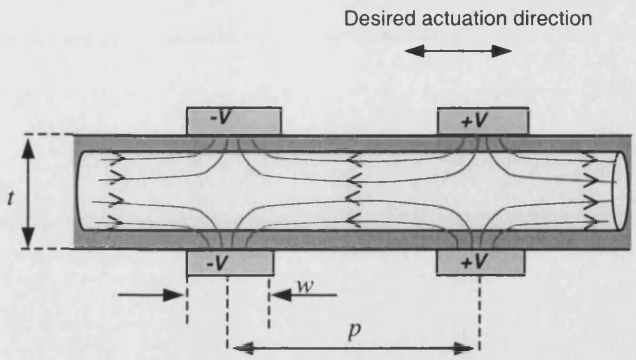

Figure 1.12: Schematic 2-D representation of an Interdigitated Electrode (IDE) pattern showing conventional dimensions and a representation of the electric field direction within the PZT fibre.

This geometry not only increases maximum possible induced stresses and strains, but also increases anisotropy in the plane of the composite. The IDEs, which are typically applied as a separate interlaminar layer, allow the fibres to remain functional in the presence of fibre damage.

IDE geometry and effect on AFC properties

It has been shown that a 'dead zone' exists directly under the electrode fingers where the field is small and normal to the desired actuation direction, producing little strain (Figure 1.12). Two approaches to reduce the detrimental dead zone effects are reducing the electrode width, w, and increasing the electrode spacing, p. Models show that reducing the electrode width increases the overall actuation strain by reducing the amount of material under the electrode in the dead zone.[16,57] Similarly, increasing the electrode spacing will result in a greater proportion of the field being distributed uniformly along the length of the fibre and a reduction in the number of dead zones per unit length. However, reducing the electrode width reduces the current carrying capabilities due to increased resistive heating. Increasing the electrode spacing results in larger driving and poling voltages, increasing the risk of electrical breakdown. The choice of electrode geometry must be a compromise between these factors. It has been shown that at least 80% of the monolithic values of piezoelectric activity are obtained for p/t ratios of 6 with $w = t$, while still maintaining the ability to pole and actuate with reasonable voltages. Typical electrode geometries are a spacing of 1.0 mm with a width of 0.2 mm. When the level of the applied voltage is an important factor it may be beneficial to reduce the electrode spacing to lower the driving voltage, at the expense of lower induced stresses and strains.

IDE materials and manufacturing

The materials used for the electrodes must have minimal electrical resistance in order to generate a uniform potential difference throughout the electrode. Copper has been the material of choice, but aluminium and silver paints have been used.[15] More recently electrically conductive adhesives have been investigated.[58]

There are typically three processing routes to obtain the IDE pattern:

(i) Manufacturing the AFC and lightly abrading its surfaces to increase electrode adhesion. The electrode pattern can then be applied to the cured composite surfaces by thermal vapour deposition or the application of conductive paints, using a mask to obtain the desired geometry.

(ii) Using screen-printing or photolithography to produce the desired IDE geometry on a supporting substrate (typically a thin polyimide film). These electroded films are subsequently positioned on both sides of the uncured composite, followed by curing as a complete unit. In this configuration, when the AFC is embedded into a passive structure the IDE substrates provide electrical insulation from surrounding passive layers.

(iii) Applying a conductive adhesive, via screen printing or inkjet printing, to a thin polymer substrate. The fibres are directly fixed into the electrode adhesive, which is allowed to cure.[59] This is followed by addition of the polymer matrix and positioning of the top polymer substrate followed by curing. This method has the advantage of fixing the fibres in position during manufacture and the proportion of field reaching the active fibres is maximised since fibre and electrode are in direct electrical contact.

1.2.7 Polymer matrix

The final component of the AFC is the matrix, typically an epoxy resin, which provides load sharing among the brittle fibres and load transfer around fibre breaks when damage occurs. A low viscosity matrix is advantageous for successful manufacture, giving better compaction, increased wetting, and reduced void content. The matrix also influences the transfer of electric field to the active fibres. Desirable electrical properties are a high dielectric constant (reducing the mismatch with the high dielectric fibres), low dissipation factor (dielectric loss), and a high

dielectric strength to avoid electrical breakdown. Optimising the transfer of electric field from the electrodes, through the matrix, and to the active fibres has been the focus of much research, which is now reviewed.

Fibre-Matrix Dielectric Mismatch

Even a thin layer of epoxy between the electrode and fibre seriously reduces the electric field sensed by the fibre material.[19,57] The low dielectric constant polymer essentially acts as a capacitor in series with the fibre, forming a voltage divider. In this situation a voltage applied to the electrode will be divided between the drop across the epoxy capacitor and the useful voltage applied to the piezoceramic element itself. Hence the efficiency of current AFCs is much lower than is potentially achievable, and the need for high poling and drive voltages to induce sufficient fields in the fibres increases risk of dielectric breakdown. Breakdown, which is also strongly dependent on the presence of manufacturing defects such as voids and electrode misalignment, has been shown to be a major limiting factor of high-field actuation performance and reliability.[50] It appears desirable to reduce the thickness of the insulating polymer layer; however, large electric field concentrations develop at the electrode edges, and when electrodes are too close to the brittle piezoelectric fibres the stress concentration induced in the fibres by the piezoelectric effect can lead to brittle fracture.[57]

Attempts have been made to reduce fibre/matrix mismatch by doping with fine piezoelectric or conductive carbon black powders to increase the apparent dielectric constant.[50] Neither dopant improved the system sufficiently. Dielectric fillers typically increase the thickness of the composite, thus increasing the size of the insulating layer between fibre and electrode, which tends to counteract the expected benefits. Carbon black doping leads to catastrophic electrical breakdowns at undesirably low voltage levels as a result of conductive networks formed between electrodes of opposing polarity. Both dopants increase the matrix viscosity, complicating the manufacturing process and increasing the risk of trapped voids.

Applying the fibres directly onto a conductive adhesive electrode ensures direct electrical contact, but increases the risk of brittle fracture. Potential exists to use intrinsically high dielectric polymers to reduce the mismatch with the fibres. One such polymer is polyvinylidene fluoride (PVDF), a piezoelectric thermoplastic polymer with a dielectric constant 3-4 times higher than typical thermosetting epoxies. No research on the use of PVDF, or any thermoplastic polymers, for manufacturing has been found in the literature.

Improved performance has been achieved with magnetic particle doping,[60] in which the matrix is uniformly doped with ferromagnetic electrically conducting nickel powder (Figure 1.13).

Before curing the matrix, a magnetic field is applied to align the powder in a pattern corresponding to the IDEs, creating an electrically conductive path between the electrodes and fibres.

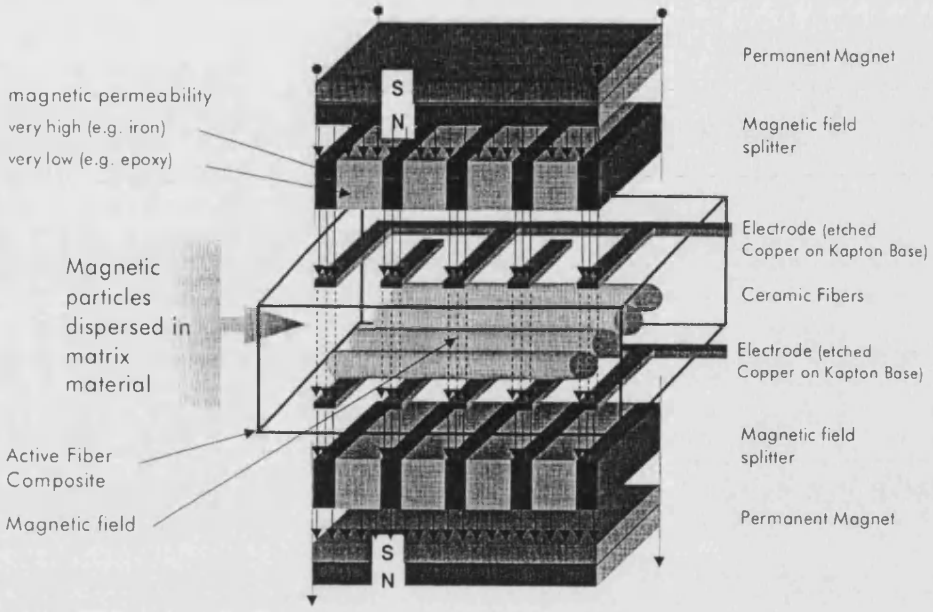

Figure 1.13: Set-up for magnetic particle (mp) AFC manufacture.[60]

This process effectively bridges the insulating polymer gap between the fibre and electrode, and allows thicker composites to be manufactured without degrading the free strain (Table 1.2).

Table 1.2: Actuation comparison of standard and magnetic particle (mp) AFCs.[60]

	mpAFC	Standard AFC
Vol% Nickel	1%	0%
Composite Thickness	0.71 mm	0.22 mm
Free Strain (Rep. Cycle)	**600 ppm**	**600 ppm**

The ability to manufacture thicker composite plies opens up the ability to tailor the composites for specific needs. Adding passive reinforcements such as glass fibres, which have been shown to improve robustness[61] and which are expected to improve residual actuation properties under mechanical loads without sacrificing performance,[62] is now becoming possible.

1.2.8 Manufacture, characterisation, and modelling of AFCs

Manufacture

Until recently, manufacture of AFCs has involved a laborious and inconsistent hand lay-up procedure, producing single composites for mechanical and electrical characterisation.[19] Techniques are now being developed that will allow bulk manufacture. Extruded fibre pre-forms are currently being developed,[24] analogous to structural composite prepregs, allowing fibre lay-up to be carried out as a unit placement operation. Sol-gel derived fibres, 50 μm in diameter, have been successfully positioned onto screen printed electrodes by means of micro assembly processing.[59] Both these methods remove the tedious fibre handling stage, reduce variability, and provide a means to precisely control fibre angles and volume fractions. A recent prototype, the Langley Research Centre Macro-Fiber Composite (LaRC-MFC),[63] utilises square fibres diced from piezoceramic wafers, making composite manufacture simple and more cost effective. A thin sheet of PZT is placed on a polymer carrier film and machined, using a computer controlled dicing saw, to leave rectangular fibres. This unit is placed on the bottom electrode, which has been prepared with epoxy adhesive. The fibre sheet and electrode assembly is cured and the carrier film removed. The top electrode is then positioned and the assembly cured. The polymer carrier film allows fibres to be transported and placed in a unit operation. Precise manufacturing tolerances and alignment are also readily achieved and the process is suitable for automation, although fibre side lengths are limited by cutting technology.

Characterisation

It is important to be able to characterise and predict the properties and performance of AFC devices by measuring parameters useful to the intended applications. For actuation applications there is a need to characterise the induced strain and stress capabilities. Hysteresis characteristics are required for determining power consumption and dissipated energy, which can lead to heating.[64] This is particularly important as the polymer phase lowers the effective thermal conductivity of the material. For sensing functions it is important to have knowledge of the sensitivity and resolution. It is also important to have knowledge of passive properties such as strength and stiffness. Accurate knowledge of properties is key for assessing performance to aid in designing smart structures, and for making comparisons with mathematical and finite element models.

Strain measurements under low electric fields can be used to determine the piezoelectric *d* coefficients while high electrical fields can be used to determine the peak actuation performance. Figure 1.14 shows the typical strain performance of an AFC driven at high fields.

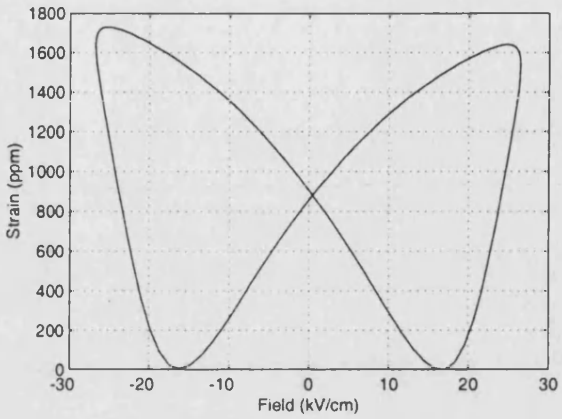

Figure 1.14: Typical high field strain performance of an AFC.[50]

Typically AFCs are capable of strains in the region of 1400 ppm, albeit for a high drive voltage cycle (-0.9 to 2.1 kV). Embedding an AFC into a laminate of known stiffness and measuring actuation strain allows the induced stress capabilities to be assessed.[19]

For sensor applications, measurements suggest a sensitivity of 0.8 pC per μm deflection.[65] The performance of these materials will no doubt improve with the progress being made in fibre, matrix and electrode technology.

Taking advantage of the longitudinal mode of actuation necessitates the alignment of the loading and poling axis, making the AFC vulnerable to stress depolarisation. It is well known that the piezoelectric response of soft PZT can be degraded by compressive stresses acting along the poling direction[66,67] and high electrical loading.[68] Since AFCs are typically operated under conditions of high electric fields, and are likely to be embedded into structures which are subjected to loads, degradation of performance via these mechanisms may be possible. Current research suggests that AFCs are much more resistant to compressive stress depolarisation than bulk material properties would suggest.[69] Under tensile loading, damage has been shown to occur in the form of active fibre fracture,[62,70] which reduces the residual actuation performance under load. Introducing reinforcing elements into the active ply has been shown to increase resistance to active fibre damage,[61] thus extending their operational stress range. However, passive reinforcements (typically glass fibres) tend to complicate the manufacturing process leading to poor quality composites; thus research on reinforced composites is limited. Much

more work is required in this area to allow designers of smart structures to exploit the best performance of these composites.

Modelling

Both analytical and finite element (FE) modelling have been applied to active structures. In terms of analytical modelling, the linear response of AFCs has been predicted successfully using a generalisation of the rule of mixtures model, which uses parallel and series (Voigt and Reuss) additions to model *effective* properties of two-phase materials. The main assumptions made are that the electrical and mechanical fields are uniform within each phase; the result is the uniform fields model.[19] Excellent agreement is seen with FE analysis. It has been shown that increasing the fibre volume fraction increases the free strain constant d_{33}, while the transverse strain constant d_{31} decreases. Fibre volume fractions can be increased simply by reducing the fibre spacing or by using non-circular cross section fibres that allow denser packing. The model also predicts the expected performance increase from a reduced thickness of low dielectric matrix between fibres and electrodes.

To model the laminated response of active composites, classical laminated plate theory, which is able to accurately predict the anisotropic actuation of laminated structures operating in the low-field regime, has been used.[15]

Effective composite properties have been used as input data for macroscopic FE analysis.[71] Noise suppression, an impact sensor, and a peristaltic pump have all been modelled using FE techniques.[1,71]

The main limitation of current analytical and FE models is an inability to predict high field characteristics such as coercive fields, remnant polarisation, and high field strain responses, since in this regime non-linear piezoelectric behaviour[72] and localised distortions of the electric field near the electrodes dominate the response. Since AFCs are typically operated in high field regimes to gain maximum performance, the ability to model high field responses is of great importance. The FE approach is more suited to modelling this non-linear material response and can also take into account the complex geometries and dynamic responses that will inevitably arise from real applications.

1.2.9 Applications

Successful applications must take advantage of the benefits AFCs offer, e.g. the ability to conform to curved surfaces, the capability of large area coverage and anisotropic actuation and sensing, since it is in these applications where increased performance will be best realised. The AFC can be surface mounted or embedded, as with conventional piezoceramic actuator systems.[73,74] Little has been published on the integration of AFCs into structures, but recent research regarding the *in-situ* strength of AFCs in laminates shows that host structure is detrimentally affected.[1] Technologies that have been investigated, or are under investigation by researchers working with AFCs are highlighted below.

Actuators

When used simply as actuators, AFCs are suitable for contour deformation and stabilisation. Typical applications for these functions are in adaptable mirrors and lenses. However, more research is focusing on employing the actuation capabilities dynamically for vibration and noise suppression.

One of the earliest suggested applications was for vibration control in rotor blades. Helicopter rotor blades experience significant vibration and emit high noise levels as a result of variations in aerodynamic loads. A prototype active twist rotor blade was built, in which the AFCs are integrated directly into the fibreglass and graphite/epoxy spar lay-up, formed around a foam core.[50] The active fibres orientated 45° with respect to the blades spanwise direction and are actuated to induce twist to the blade along its length. Current AFCs do not possess the actuation performance necessary to replace the blade tilt/rotate mechanism but are capable of reducing vibrations. The expected benefits of this technology include increased life of the structure, increased passenger comfort and an improved flight performance through better fuel efficiency, higher payloads and increased cruising speed.

The control of buffeting loads in high performance twin-tail aircraft using AFCs is a related area that is under investigation.[63,75] The AFC actuators are embedded beneath the fibreglass shell and are operated to counteract the bending and torsional stresses induced by buffeting loads.

Use of AFCs for vibration control in very large, lightweight deployable spacecraft structures has also been proposed.[63] The large structures will be constructed using inflatable, rigidisable composite struts containing AFCs that act to damp vibrations.

A specific project in the field of acoustic control is that of reducing torpedo radiated noise. In certain frequency regions the hull radiates noise due to power-plant, propulsor and flow sources,

which dominate the radiated noise signature of torpedoes. The AFCs reduce the noise signature by actively controlling hull vibrations.[1] Similar approaches can be applied to reducing noise in helicopter and aircraft fuselages and to decrease noise in submarine cabins.

Contour control of various surfaces, for example in adaptive optical systems, represents another possible application. In the example in Figure 1.15 the high anisotropy (high stiffness and piezoelectric strain coefficient parallel to, and low stiffness and low piezoelectric coefficient perpendicular to the fibre axis) results in the bending around the x_2 direction becoming nearly completely decoupled from the bending around x_1. This offers interesting possibilities for surface contour control.

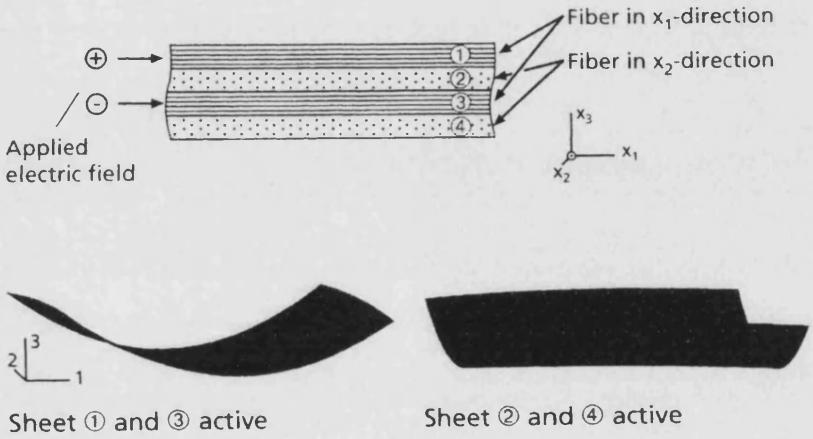

Figure 1.15: Composite with four active sheets in (0,90) plies with dimensions of 10×10×0.4 mm. Displacements magnified by a factor of 100.[71]

Based on this bending actuator, a peristaltic pump has been designed. The pump (Figure 1.16) consists of two plates, each containing a number of segments, each segment being an independently controlled bending actuator. The segments are electrically driven such that a cavity is formed between the two plates and is forced to move in one direction.

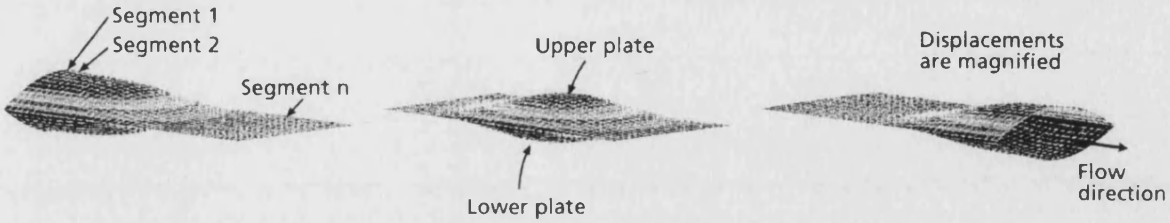

Figure 1.16: Simulation model of a peristaltic pump with dimensions of 10×5×1 mm. Displacements magnified.[71]

Sensors

The sensory potential of the composites has been simply demonstrated by dropping weights on a GFRP plate embedded with an AFC and monitoring the charge generated on the electrodes[65] (Figure 1.17).

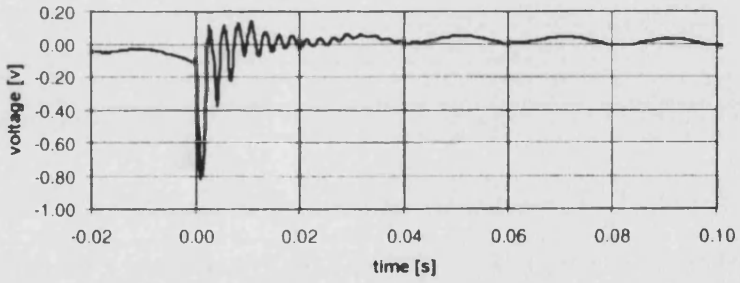

Figure 1.17: The signal of a non-destructive impact load (falling steel sphere of 14 grams from 150 mm) on a GFRP sheet with an embedded AFC.[65]

This response could be harnessed for impact and damage detection. Acoustic emission techniques, which detect crack propagation in metals and damage growth in composites, can be used to monitor structures during operation. It is thought that AFCs can be developed as an 'acoustic tape' for bonding onto the inner surface of the structures along rivet lines, or embedding within lap joints.[2] This sensor can be applied to large areas, is self powered and can be used to detect damage in complex areas where conventional non-destructive techniques may be difficult or impossible to use. The AFC tapes could also be used for active sensing (excitation and sensing) to interrogate structures not in operation.

1.2.10 Summary

Active fibre composites offer conformability and robustness, high actuation energy densities, anisotropic actuation, and tailorable mechanical properties. These are all distinct advantages over monolithic piezoceramic actuators and sensors, creating new possibilities in the fields of structural actuation and control, and sensing.

Piezoceramic fibres are produced by numerous methods; extrusion, viscous plastic processing (VPP), viscous suspension spinning (VSSP), Lyocell or Alceru methods and sol-gel techniques. Extruded fibre diameters are limited to > 100 μm while current sol-gel and viscous suspension spinning methods offer fibres with diameters in the range 10-70 μm. Fibre diameter is a critical factor for structural conformity, and the integration of PZT fibres with small diameters is still a new development on which little research has been published. Porosity and grain size have been identified as key parameters affecting fibre properties, and producing fibres with piezoelectric properties comparable to bulk materials is still yet to be achieved. More recently rectangular cross-section and ribbon fibres have been investigated, with preliminary results showing AFCs incorporating these fibres have an improved strain performance.

The fibre/matrix dielectric mismatch reduces the electric field delivered to the active fibres and limits the AFC performance. Use of conductive adhesive electrodes, which are in direct contact with the fibres, could solve this problem. Uniform matrix doping with high dielectric fillers has proved unsuccessful but recent research in using magnetic particles, which results in preferential doping profiles, appears promising.

Applications for AFCs are typically in the fields of structural actuation for contour control, vibration suppression, and acoustic control, while their sensory nature can be used as a method of structural health monitoring. As AFCs are a relatively new technology, it is inevitable that new and innovative applications will be developed.

Fibre technology is a key area for further research. Increasing the activity of the fibres, which currently suffer from reduced piezoelectric properties compared to bulk materials, is an essential part of improving the performance of the composites. Reducing the fibre diameter, while maintaining the piezoelectric activity is of great importance for improving integration into host structures and is perhaps the main challenge. The development of single crystal or preferred orientation fibres, which should increase the strain output for actuator functions and sensitivity of sensor functions, represents an area in which published research is limited. Closely linked to developing the fibres is the ability to measure the piezoelectric, electrical and mechanical properties of fibres accurately and reliably. This is especially true of properties under high electrical driving fields, for which there is little published research on characterisation methods.

Understanding the effects of incorporating these composites into structures, and the effects of stresses and temperature is also key to successful realisation of applications. However, problems of integration could be avoided altogether if incorporation of a structural fibre, such as glass, into the composite becomes successful. This will create a structural active material capable of replacing structures, representing an exciting advancement.

In the future a considerable increase in the performance of AFCs is to be expected by optimising the properties of the PZT fibres and the matrix, improving structural design and integration technology, and finally improving the 'intelligence' of the control system.

1.3 Thesis Structure

The literature review has highlighted that there are numerous methods for the production of PZT fibres. However, there is no comparative study on their piezoelectric, mechanical, physical and chemical properties. If AFCs are to be optimised this is an important task. Chapter 2 through Chapter 6 cover this requirement.

Chapter 2 introduces the methodology used to measure the low field piezoelectric and mechanical properties of a range of PZT fibres. The method involves extracting fibre property data from measurements made on 1-3 composite. Analytical equations used to perform this task are presented, and are confirmed by finite element modelling.

Chapter 3 describes the techniques used to manufacture 1-3 composites, and introduces the experimental techniques used in their characterisation. The measured 1-3 composite properties are then used with the equations presented in Chapter 2 to extract fibre properties. This enables the low field properties of a range of commercially available fibres to be compared.

Chapter 4 and Chapter 5 deal with the high field properties of the fibres, which, like the low field properties, are extracted from the responses of 1-3 composites. Chapter 4 covers the modelling of the high field response, and proposes a methodology to assess the strain and polarisation of the fibres under high electrical fields.

In Chapter 5 the high field testing of the 1-3 composites is described. Results of this testing are used with the models developed in Chapter 4 to extract the high field responses of the fibres. This enables the high field properties of a range of commercially available fibres to be compared.

Chapter 6 covers the characterisation of the chemical and physical properties of the range of fibres. The results of this analysis are used to draw structure-property relationships, to help identify properties beneficial for high performance fibres. The low and high field properties,

together with the aspects important for successful AFC manufacture, are used to select an appropriate fibre type for the manufacture of an optimised AFC device.

Optimisation and manufacture of the interdigitated electrode is the focus of Chapter 7. Finite element modelling is used to gain an understanding of the electrode parameters that affect the AFC performance. The result is an optimised electrode design, the manufacturing of which is then discussed.

Chapter 8 combines the work of the previous chapters. Manufacture of optimised AFCs, incorporating the optimum fibre and optimised electrode design, is described. The testing used to characterise the devices is presented and the results discussed.

Finally, Chapter 9 summarises the work presented in this thesis, and comments on future work.

CHAPTER 2

LOW FIELD FIBRE PROPERTIES – MODELLING

2.1 Introduction

Fine scale piezoelectric fibres, typically less that 250 μm in diameter, have recently become commercially available. The driving force to bring such a form of piezoelectric material to the marketplace is predominantly from a demand for high resolution ultrasonic transducers, where small diameter fibres are essential. However, the fibres are also finding uses in novel devices, such as the AFC. One would expect, because of the short time they have been available, other novel uses for the functional fibres will emerge.

Understanding the properties of these fibres is important for a number of reasons. With knowledge of the material properties it is possible to optimise the fibre production process to produce high quality fibres. It also becomes possible to compare fibre production methods. This allows selection of the most appropriate fibre type for incorporation into a new product, such as an AFC. Further, it allows existing products to be improved by selection of a fibre having the most appropriate material properties. Material properties are also vital to perform accurate finite element modelling, which is useful for understanding, developing and optimising products. Even with such a demand for fibre properties, commercial producers and scientific researchers have failed to supply the relevant fibre property data. This is due in part to the limited time these fibres have been commercially available, but an overriding reason is the difficulty of obtaining such measurements; commonly used measurement techniques are simply not capable of testing small scale piezoelectric elements.

To avoid difficulties associated with single fibre testing, fibre properties are to be extracted from measurements made on composites. By incorporating a large number of fibres into a composite, measurements become increasingly accurate with a higher signal/noise ratio. A composite can also be made significantly larger and more robust than a single fibre, enabling the use of common piezoelectric characterisation techniques to measure the material properties. Many types of piezoelectric composite geometry can be constructed,[20] but the most useful geometry for the purpose of measuring fibre properties comprises piezoelectric fibres aligned in a parallel orientation surrounded by a polymer matrix. A composite of this geometry, termed a 1-3 composite, is depicted in Figure 2.1.

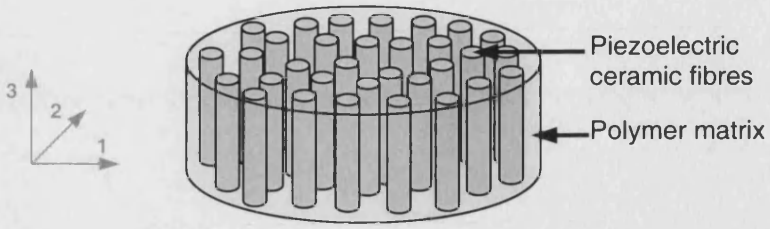

Figure 2.1: Schematic of a 1-3 piezocomposite comprising active piezoelectric ceramic fibres and a passive polymer matrix. Electrodes are applied to the top and bottom faces and poling is in the 3-direction.

In this arrangement analytical and finite element modelling becomes relatively simple, enabling fibre properties to be easily calculated from measurements performed on the composites.

This chapter begins by introducing an existing analytical model that will be used to extract fibre data from measurements made on 1-3 composites. Finite element (FE) models, developed to confirm the response of the composites, are then described. Results from the FE models are compared to the analytical model results, thereby confirming the validity of the simpler analytical approach.

2.2 Analytical Modelling of 1-3 Composites

2.2.1 Overview of models and their relevance

Composites with 1-3 connectivity were initially developed in an attempt to improve the performance of transducers and hydrophones, which traditionally rely on bulk PZT for the active element. There are two regimes in which 1-3 composites are used, and they can be divided into the following categories:

(i) *High frequency*. For example, thin plate transducers operating near the thickness resonance mode for medical ultrasonic imaging.

(ii) *Low frequency*. For example, underwater hydrophones operating in the hydrostatic mode.

Analytical models are available for both the high frequency[47,48] and low frequency regimes[76] and were developed to predict how the composite response would be influenced by fibre and matrix properties, and their volume fractions. In this work the models will be used, in reverse, to extract properties of fibres from a measured composite response. The models for the two frequency regimes differ in the assumptions made about the composite response, thus it is important that the correct model is selected.

A key distinguishing feature between the two models concerns lateral clamping. In the high frequency model the composite is assumed to be thin disk operating at its thickness-extensional mode resonance (Figure 2.2a). Because these oscillations occur at a higher frequency than the radial mode resonance, shown Figure 2.2b, the composite as a whole is assumed to be laterally clamped.

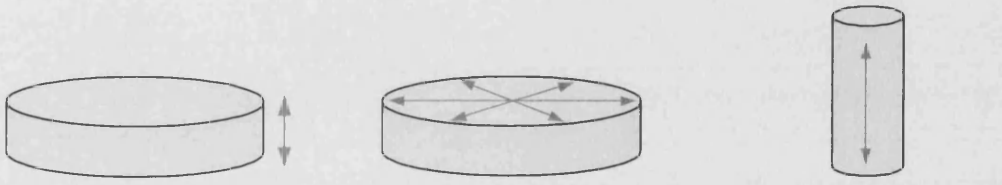

Thickness-extensional mode **Radial mode** **Longitudinal-length mode**

(a) (b) (c)

Figure 2.2: Illustrations of sample dimensions appropriate for exciting either the lateral mode or longitudinal-length mode.

In the low frequency model the composite is assumed to be operating at such low frequencies that the sound wavelength is much larger than the composite's lateral dimension (hydrostatic conditions). Thus, the model for this situation assumes the composite is not laterally clamped. To select the appropriate model for this research, in which fibre properties are to be predicted from 1-3 composite measurements, testing frequencies and modes of vibration must be considered.

Composites manufactured for this research have dimensions appropriate for excitation of the longitudinal-length resonance mode as shown in Figure 2.2c. The highest frequency experienced by samples during experimental testing occurs in the impedance analysis technique, in which the samples are driven at their longitudinal-length resonance frequency. Because the longitudinal-length is the lowest frequency resonance mode able to be excited, the composite is still free to strain laterally. It is therefore appropriate to use the low frequency analytical model, which assumes no lateral clamping. A brief overview of the low frequency hydrostatic model is now given.

2.2.2 The hydrostatic model

Smith[76] has made a number of assumptions and simplifications concerning the response of the 1-3 composite presented in Figure 2.1. By assuming that the composite substructure is sufficiently fine such that the fibre and matrix develop equal strains in the 3-direction and equal stresses in the 1-direction it is possible to define a new set of *effective* material properties, which are related to the fibre and matrix properties and their volume fractions. Equations derived from this model, which predict a 1-3 composite response, are given in Equations (2.1) to (2.6). For detailed mathematical derivations of these equations the reader is guided to reference [76].

The equations show how the fibre properties (namely the piezoelectric induced strain coefficients d_{33} and d_{31}, the short circuit and open circuit compliances s_{33}^{E} and s_{33}^{D}, the constant stress permitivity ε_{33}^{T} and the longitudinal coupling factor k_{33}), and the polymer properties (namely the compliances s_{11} and s_{12}, and the permitivity ε_{11}), together with the fibre volume fraction v_f, determine the effective composite properties (denoted by a bar, e.g. $\bar{d}_{33}$).

$$\bar{d}_{33} = d_{33}\frac{v_f s_{11}}{v_f s_{11} + (1-v_f)s_{33}^{E}} \tag{2.1}$$

$$\bar{d}_{31} = v_f\left[d_{31} + d_{33}\frac{(1-v_f)(s_{12}-s_{13}^{E})}{v_f s_{11} + (1-v_f)s_{33}^{E}}\right] \tag{2.2}$$

$$\bar{s}_{33}^{E} = \frac{s_{33}^{E} s_{11}}{v_f s_{11} + (1-v_f)s_{33}^{E}} \tag{2.3}$$

$$\bar{s}_{33}^{D} = \frac{s_{33}^{D} s_{11}}{v_f s_{11} + (1-v_f)s_{33}^{D}} \tag{2.4}$$

$$\bar{k}_{33} = \left(1 - \frac{\bar{s}_{33}^{D}}{\bar{s}_{33}^{E}}\right)^{1/2} \tag{2.5}$$

$$\bar{\varepsilon}_{33}^{T} = v_f\left[\varepsilon_{33}^{T} - d_{33}^{2}\frac{(1-v_f)}{v_f s_{11} + (1-v_f)s_{33}^{E}}\right] + (1-v_f)\varepsilon_{11} \tag{2.6}$$

Knowing the relevant matrix and composite properties, the equations can be used to calculate the fibre properties. However, certain assumptions have been made during the derivation of these equations, which include:

(i) strains in the 3-direction are equal in fibre and matrix,

(ii) stresses in the 1-direction are equal in fibre and matrix,

(iii) fringing fields do not exist.

Therefore, before these equations are used to extract fibre data from 1-3 composite measurements it is necessary to validate the accuracy of the analytical model. This will be performed by comparing the analytical model results with results obtained from finite element analysis. The finite element methodology is now introduced.

2.3 Finite Element Modelling

2.3.1 The finite element technique

Finite element modelling is an analysis technique used to calculate the effect of loads (structural, thermal, magnetic or electric) on the response of a body (solid, liquid or gas). The finite element method is able to predict the response of complex geometrical shapes under complex loading conditions by dividing the body into a number of smaller 'elements'. The effect of the loads on each element are calculated using the material properties of the body, which are often supplied by the user. The results of each element are then combined to determine the overall response of the body.

The finite element analysis conducted in this thesis used the finite element software package ANSYS (versions 5.4 through 5.7.1). A detailed 'user guide' to modelling piezoelectric materials using ANSYS has been written, and is included in Appendix A1.

ANSYS uses the following form of the piezoelectric constitutive equation, which describes the coupling between stress (T), electrical displacement (D), strain (S), and electric field (E), to solve piezoelectric problems:

$$\begin{Bmatrix} T \\ D \end{Bmatrix} = \begin{bmatrix} c^E & -e_t \\ e & \varepsilon^S \end{bmatrix} \begin{Bmatrix} S \\ E \end{Bmatrix} \tag{2.7}$$

The subscript t denotes a matrix transpose.

ANSYS requires the user to input the stiffness under constant field (c^E), induced stress piezoelectric constant (e), and constant strain dielectric constant (ε^S) for a model to be solved successfully. Since the finite element method is computationally intensive the process of modelling is performed using a computer. The following paragraph introduces the methodology for the modelling work of this chapter, which is equally relevant for the modelling work performed in other chapters of this thesis (Chapter 4 and Chapter 7).

1) *Identify problem dimensionality*: In this work this is either 2D (for plane strain and axi-symmetric models) or 3D.

2) *Identify the 'representative volume element' (RVE)*: This is the smallest portion of the geometry that is representative of the entire geometry through translation, reflection or rotation. It can be thought of as the 'unit cell' of the structure being modelled.

3) *Construct the model geometry*: This stage requires the shape and dimensions of the RVE to be specified. This stage was performed using the ANSYS software, but models can be imported from CAD packages.

4) *Specification of material properties*: The material properties required for the modelling are supplied to the ANSYS software by the user. For modelling piezoelectric materials relevant material properties are the mechanical [c] matrix, the piezoelectric [e] matrix and the electrical [ε] matrix.

5) *Specification of element type*: Three element types are available for modelling piezoelectric materials. Although all the elements respond according to Equation (2.7), the piezoelectric constitutive equation, the correct choice of the element will depend on the model geometry and the problem dimensionality (2D, 3D etc).

6) *Mesh Generation*: Discretisation of the solid model into a number of smaller elements is performed by the software to the users requirements.

7) *Application of loads and boundary conditions*: Structural and electrical loads are applied to the model to represent the loads experienced by the body being modelled.

8) *Solution*: The stage of solving the model is performed by the finite element software package.

9) *Post Processing*: Once solved, the model may be interrogated in various ways to display the results of the solved model. These results may include for example displacements, electric fields, stresses etc. in the RVE.

2.3.2 Finite element modelling of 1-3 composites

The piezoelectric, dielectric and mechanical behaviour of 1-3 composites was modelled to confirm the analytical model predictions. Because of the symmetry present in a 1-3 composite structure it is possible to model a $^1/_8$th section of the composites unit cell. This 'representative volume element' or RVE is shown in 2D in Figure 2.3(a). The 3D model geometry and a typical FE mesh are shown in Figure 2.3(b) for a fibre volume fraction of 0.5. Figure 2.3(c) numbers the model faces to allow references to be made when describing applied boundary conditions. Faces opposite 1, 2, and 3 are referred to as 1a, 2a and 3a respectively.

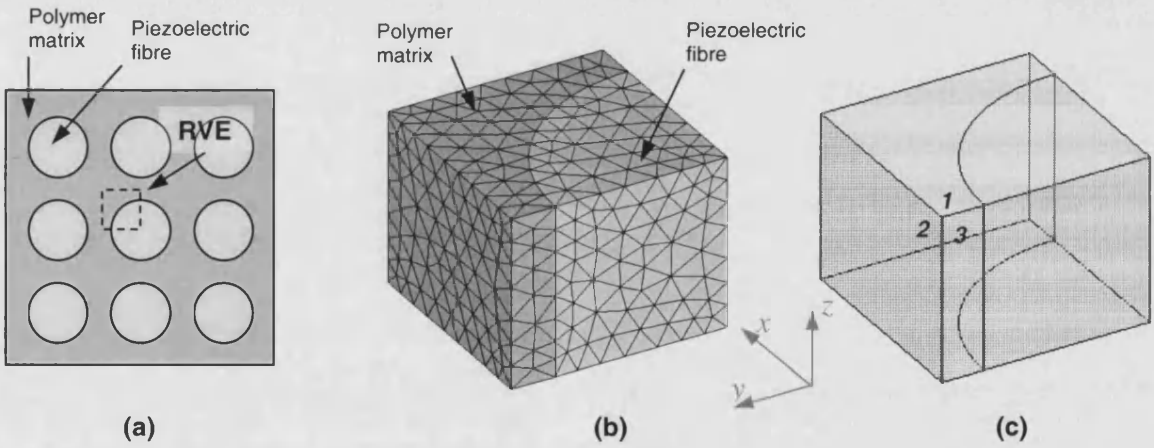

Figure 2.3: (a) 2D view showing the 1-3 composite representative volume element. The 3D meshed model of the RVE is shown in (b). The numbered faces in (c) are to facilitate boundary condition references in the text.

The fibre was modelled as a cylindrical PZT fibre with a diameter of 100 μm, typical of the fibre dimensions that will be tested. A coupled-field 10 node tetrahedral element (SOLID98), with a single voltage and three displacement degrees of freedom, was used to mesh the piezoelectric fibre and polymer matrix. The fibre was given the material properties of PZT-5A fully poled in the z-direction, the values of which are located in Appendix A2. The polymer matrix was modelled as an isotropic solid with a Poisson's ratio of 0.38, a relative dielectric constant of 5.0 and Young's modulus of either 1.0 or 3.0 GPa, allowing the effect of matrix stiffness on composite response to be investigated. Fibre volume fractions up to 0.78 were

modelled, this upper limit being set by the theoretical maximum packing of cylinders in a simple cubic arrangement.

For the volume element presented in Figure 2.3(b) to be representative of the entire 1-3 composite structure, symmetry boundary conditions were applied to the 1a, 2a and 3 faces. The nodes on the top and bottom faces (1 and 1a respectively) had their voltage degree of freedom coupled such that they responded as two separate equipotential surfaces, simulating the electrodes that are applied to 1-3 composites. Appropriate electrical and mechanical loads were then applied to the model to simulate conditions experienced by the composites during material property measurement tests, which are discussed in the proceeding paragraphs. The model was then solved to determine how $\bar{d}_{33}$, $\bar{d}_{31}$, $\bar{s}^E_{33}$, $\bar{s}^D_{33}$, $\bar{k}_{33}$ and $\bar{\varepsilon}^T_{33}$ vary as a function of fibre volume fraction and polymer modulus.

The following sections present the appropriate electrical and mechanical load cases required for a valid solution for each material property measured by briefly describing the experimental characterisation methods. A more detailed description of these test methods is given in Section 3.3 in Chapter 3.

Load cases for $\bar{d}_{33}$ and $\bar{d}_{31}$

The piezoelectric d coefficients (both d_{33} and d_{31}) of the 1-3 composites were experimentally determined in a Take Control Piezometer. To measure $\bar{d}_{33}$ the Piezometer applies a 0.1 N, 97 Hz sinusoidal force to the electroded end faces of the composites using metallic studs, and measures the charge generated on these faces. This is the 'dielectric displacement per unit applied stress' definition of the d coefficient (Equation (1.1) in Chapter 1).

The contact area of metallic studs on the composite surface is much larger than the composite spatial scale (fibres are typically 0.1 to 0.25 mm diameter). This is illustrated in Figure 2.4.

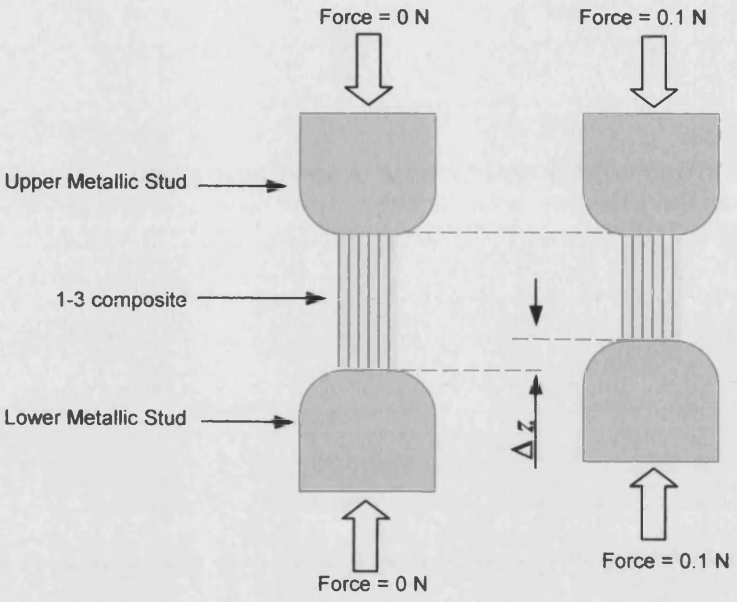

Figure 2.4: Schematic illustration of the mode of operation of the Take Control Piezometer showing uniform displacement of the entire 1-3 composite.

To represent this situation in the FE model, the displacement of the nodes on electroded face 1 are coupled such that they all displace with the same magnitude in the z-direction (representative of the hard metallic surface pressing onto the surface of the composite). The nodes on faces 2 and 3a have their y and x-direction displacements coupled respectively, forcing them to displace by the same magnitude in these directions. This represents a freedom for the composite to expand laterally. The nodes on the electroded faces are both grounded (short circuit/set to $V = 0$) to enforce the constant electric field boundary condition. A static force of 0.1 N is applied to the 1 face of the model representing the quasi-static load applied to the composite by the Piezometer. The charge generated on the electroded sufaces is evaluated and used to calculate $\bar{d}_{33}$.

For the detrmination of $\bar{d}_{31}$ the Piezometer applies a 0.1 N 97 Hz sinusoidal force to the composites in the 1-direction (x or y in the model), and measures the charge generated on the electrode surface. Since the force is applied via small non-conducting studs that do not extend to the edges of the composites, only the central portion is under test and edge effects can be ignored. To model this situation, the nodes on the electroded face 1 have their displacement in the z-direction coupled. The nodes on 2 and 3a faces have their y and x-direction displacements coupled respectively. A force of 0.1 N is then applied on face 2 of the model (since the composite is transversely isotropic about the 3-axis this is identical to applying the force to the

1a face) representing the quasi static load applied to the composite by the Piezometer. The charge generated on the grounded electroded sufaces is evaluated and used to determine $\bar{d}_{31}$.

The static 0.1 N force applied in the FE models is reprentative of the quasi-static (97 Hz) mechanical loads applied to the actual composite during measurement because this frequency is well below the sample resonant frequency, which is typically in the range 200 – 300 kHz.

Load Cases for $\bar{s}_{33}^{E}$ and $\bar{s}_{33}^{D}$ and $\bar{k}_{33}$

The compliances and the coupling factor of 1-3 composites will be measured experimentally using impedance analysis techniques, requiring the composites to be operating in the region of their longitudinal-length resonant frequency. However, for simplicity of the modelling, a static load case is used.

Compliance is defined as the strain developed per unit applied stress. For a piezoelectric material it is possible to define two compliance terms; the compliance under constant electric field, s^{E}, and the compliance under constant dielectric displacement, s^{D}. To determine these parameters using finite element analysis it is important to apply the appropriate electrical boundary conditions. The constant dielectric displacement condition can be achieved by setting the electrodes to open circuit conditions (voltage coupled and floating), while the constant electric field condition can be achieved by setting the electrodes to short circuit conditions (voltage coupled and equal to zero).

The mechanical boundary conditions were identical for both compliance terms and are now described. The nodes on faces 1, 2 and 3a have their displacements in the *z*, *y* and *x*-directions coupled respectively. A force of 1.0 N is applied to electroded face 1. The two compliance terms, $\bar{s}_{33}^{E}$ and $\bar{s}_{33}^{D}$, are obtained by the appropriate choice of electrical boundary conditions applied to the nodes on the electroded faces (1 and 1a). The resulting displacement of this face is used to calculate strain, and the compliance calculated from the strain per unit stress.

The finite element predicted response of $\bar{k}_{33}$ is obtained by using results from the analysis of $\bar{s}_{33}^{E}$ and $\bar{s}_{33}^{D}$ with Equation (2.5).

Load Case for $\bar{\varepsilon}_{33}^{T}$

The dielectric constant of the composites is to be experimentally determined from capacitance measurements made under constant stress conditions using an LCR meter. The LCR meter applies a 1 volt sinusoidal voltage at a frequency of 1 kHz to the sample's top electrode, while holding the base electrode at ground. To represent this situation in the FE model the nodes on faces 1, 2 and 3a have their displacements in the z, y and x-directions coupled respectively. The nodes on faces 2 and 3a are mechanically free representing a freedom for the composite to displace laterally. The nodes on electroded face 1 in the model are also set to be mechanically free, fulfilling the constant stress conditions experienced by the composites during measurement in the LCR meter. One volt is applied to electroded face 1 while the opposite electroded surface (1a) is held at ground ($V = 0$).

The solved model was used to measure the charge (Q) developed on the electroded sufaces. This was used to calculate the sample's dielectric constant (ε), which is related to the electroded surface area (A), the sample thickness (t) and the applied voltage (V) through Equation (2.8).

$$\varepsilon = \frac{Qt}{AV} \tag{2.8}$$

The one volt static voltage applied in the FE models is representative of the quasi-static (1 kHz) electrical load applied to the actual composite during measurement because this frequency is well below the sample's resonant frequency.

2.4 Analytical Model Validation

The trends of the key composite material properties ($\bar{d}_{33}$, $\bar{d}_{31}$, $\bar{s}_{33}^{E}$, $\bar{s}_{33}^{D}$, $\bar{k}_{33}$ and $\bar{\varepsilon}_{33}^{T}$) as a function of volume fraction and matrix stiffness, as predicted by the FE and analytical models, are presented in the following sections. In all graphs the composite property is normalised by the fibre value, so that the value of the composite property at $v_f = 1$ (i.e. 100% fibres) is 1.0, the fibre value. It is hoped that results obtained from the FE method will match the analytical model predictions, thus validating the analytical model.

2.4.1 $\bar{d}_{33}$ and $\bar{d}_{31}$ versus fibre volume fraction

Figure 2.5(a) and Figure 2.5(b) plot the FE and analytical results obtained for the piezoelectric d-coefficients of the composite as a function of fibre volume fraction. In both figures the FE results are represented by open squares and triangles, while the analytical model prediction is shown as a continuous line. Figure 2.5(a), which plots $\bar{d}_{33}$ versus fibre volume fraction for two polymer stiffnesses, shows that the composite still retains a high percentage of the fibres' piezoelectricity, even at relatively low fibre volume fractions. At $v_f = 0.2$ the composite $\bar{d}_{33}$ is over 80% of the fibre d_{33}. This can be attributed to the large stiffness difference between the fibre and the matrix. As the volume fraction is reduced an increasing proportion of load is taken by the stiffer fibres. Since the fibres produce charge in proportion to load, the piezoelectric activity of the composite remains high as the volume fraction is reduced. Figure 2.5(a) shows clearly that reducing the polymer stiffness increases the level of piezoelectricity retained in the composite. This is simply due to an increased proportion of load being taken by the fibres due to the reduced polymer stiffness.

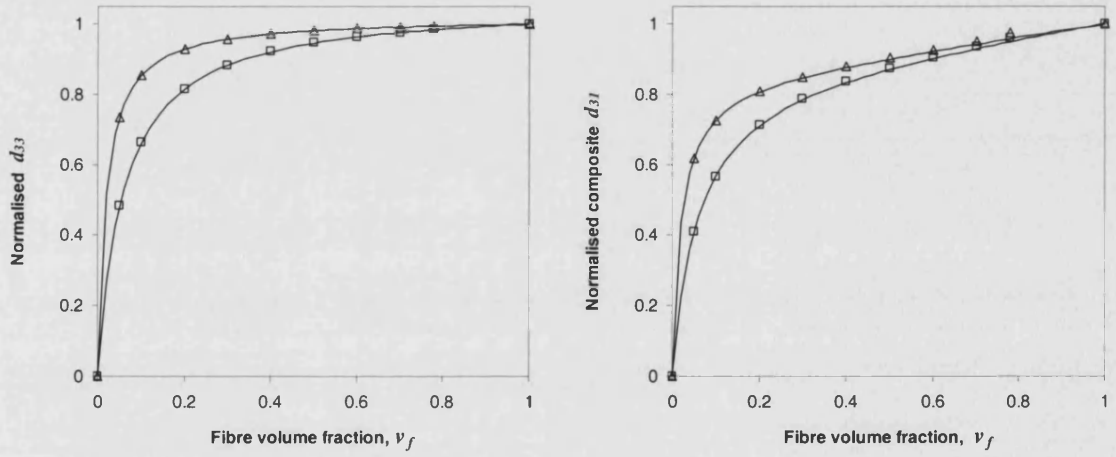

Figure 2.5: Analytical (solid lines) and finite element (□ and △) results of (a) composite d_{33} and (b) composite d_{31} versus fibre volume fraction. Results are normalised and shown for a matrix with a Young's modulus of 3.0 GPa (□) and of 1.0 GPa (△).

Figure 2.5(b), which plots $\bar{d}_{31}$ versus fibre volume fraction for two matrix stiffnesses, reveals that the analytical model accurately predicts the composite response. As with the composites $\bar{d}_{33}$, the $\bar{d}_{31}$ remains high at low volume fractions. However, the retained activity is not as high

as the $\bar{d}_{33}$ case. It is possible to understand the trend in $\bar{d}_{31}$ by rewriting the $\bar{d}_{31}$ analytical equation (Equation (2.2)) in the following manner:

$$\bar{d}_{31} = \underbrace{v_f d_{31}}_{d_{31}\text{ component}} + \underbrace{(1-v_f)\frac{s_{12}-s_{13}^E}{s_{11}}\bar{d}_{33}}_{d_{33}\text{ component}} \tag{2.9}$$

In this form it can be seen that there are two components contributing to the composite response. The first contribution arises from the d_{31} response of the fibres. The model assumes that the stress in the lateral direction is equal in both phases, thus the charge developed from the fibres' d_{31} is simply proportional to their volume fraction in the composite. The second contribution arises as a result of a Poisson's ratio effect. The stress in the lateral plane causes the polymer (being more compliant) to deform more than the fibres. The polymer not only compresses in the lateral direction, but extends in the vertical direction due to its Poisson's ratio. This transfers an extensional force into the ceramic fibres, enhancing the charge developed. A graph showing the level of these two contributions as a function of volume fraction is shown in Figure 2.6.

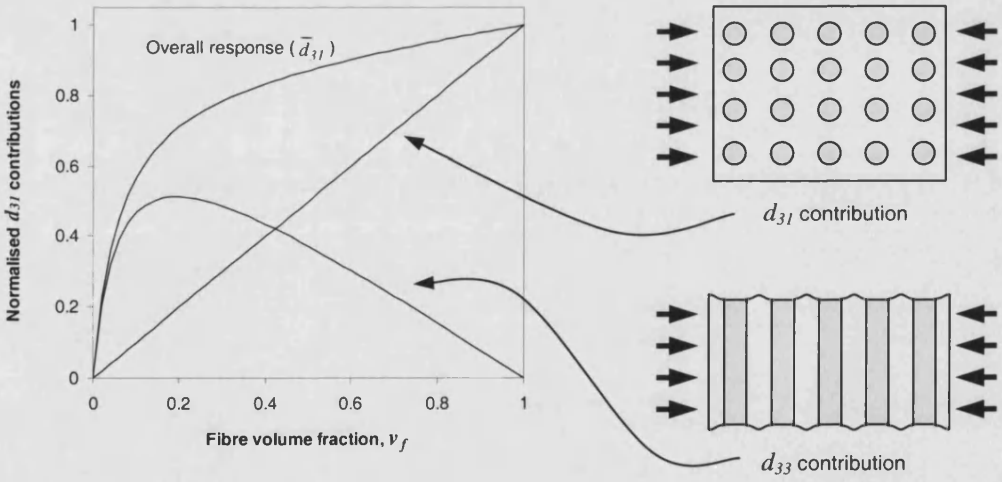

Figure 2.6: Analysis of the analytical equation showing the d_{31} and d_{33} components that sum to form the overall composite $\bar{d}_{31}$ response.

Figure 2.6 shows that for determination of $\bar{d}_{31}$ high volume fraction composites are desirable. In such composites the fibres' d_{31} component forms a significant proportion of the measured composite response. In contrast, at low fibre volume fractions the d_{31} response may be masked by the relatively large contribution from the fibres' d_{33}.

Figure 2.5(a) and (b) show that the analytical model is able to accurately predict the composite $\bar{d}_{33}$ and $\bar{d}_{31}$ responses as a function of both volume fraction and matrix stiffness.

2.4.2 $\bar{s}_{33}^{E}$, $\bar{s}_{33}^{D}$ and $\bar{k}_{33}$ versus fibre volume fraction

The variation of $\bar{s}_{33}^{E}$ and $\bar{s}_{33}^{D}$ with volume fraction and matrix stiffness, predicted by the analytical and finite element models, is shown in Figure 2.7(a) and (b) respectively. The responses of both $\bar{s}_{33}^{E}$ and $\bar{s}_{33}^{D}$ are in agreement with the analytical model and show the same trend: the composite value is identical to the matrix value at $v_f = 0$, and tends towards the fibre value (a normalised value of 1.0) as the volume fraction is increased. The rapid decrease in compliance with increasing fibre volume fraction at low volume fractions arises from the large stiffness difference between the fibre and the matrix; addition of only a small percentage of the stiffer fibres has a considerable stiffening effect on the composite.

Figure 2.7 shows that reducing the matrix stiffness only has an appreciable effect on the properties of low volume fraction composites ($v_f < 0.2$), where the polymer dominates the composite response. As the volume fraction is increased above 0.2 the response becomes dominated by the fibres, hence the difference between the two different matrices becomes undetectable. Therefore, by testing high volume fraction composites errors from the matrix become minimised.

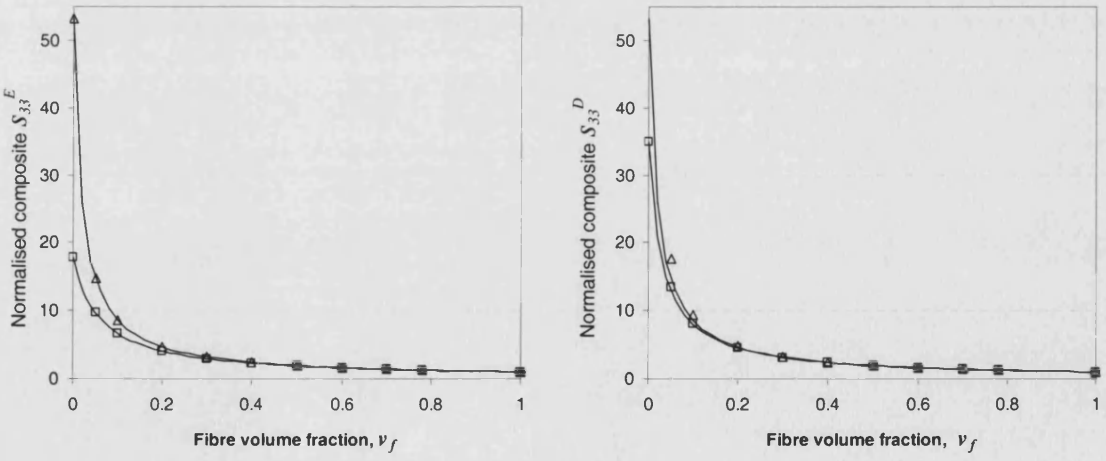

Figure 2.7: Analytical (solid lines) and finite element (□ and △) results of (a) composite s_{33}^{E} and (b) composite s_{33}^{D} versus fibre volume fraction. Results are normalised and shown for a matrix with a Young's modulus of 3.0 GPa (□) and of 1.0 GPa (△).

The composite longitudinal coupling factor, $\bar{k}_{33}$, is a measure of the electrical to mechanical conversion efficiency, which for bulk PZT-5A is 0.7. The fibre value was evaluated using the results from the analysis of $\bar{s}_{33}^{E}$ and $\bar{s}_{33}^{D}$ with Equation (2.5). The coupling factor as a function of volume fraction for the two matrix stiffnesses is plotted in Figure 2.8. The $\bar{k}_{33}$ of the composite retains a high percentage of the fibre value at low volume fractions. In fact, at volume fractions as low as 0.1, composites exhibit a coupling factor of over 85% of the fibre value. Once again, the analytical model accurately predicts the composite response as a function of both volume fraction and matrix stiffness.

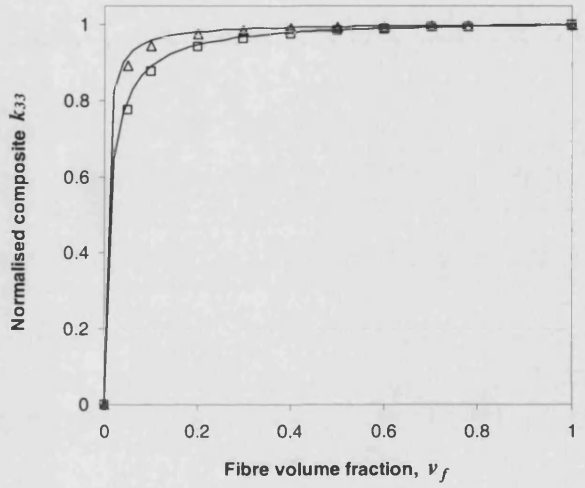

Figure 2.8: Analytical (solid lines) and finite element (□ and △) results of composite k_{33} versus fibre volume fraction. Results are normalised and shown for a matrix with a Young's modulus of 3.0 GPa (□) and of 1.0 GPa (△).

2.4.3 $\bar{\varepsilon}_{33}^{T}$ versus fibre volume fraction

Figure 2.9(a) plots the finite element and analytical results for $\bar{\varepsilon}_{33}^{T}$ as a function of volume fraction for only one value of matrix Young's modulus (Y = 3.0 GPa). Almost identical behaviour is observed when the matrix stiffness is varied, as would be expected. The slight difference observed can be attributed to a clamping effect, the nature of which is now described.

The dielectric response of the composite is dominated by the electrical charge developed as a direct result of the dielectric properties and volume fractions of the constituent materials. This gives rise to the linear trend with volume fraction. However, the application of an electric field also causes the piezoelectric fibres to strain. The fibre strain is partially clamped by the non-

piezoelectric matrix. This clamping induces charges, via the fibres' d_{33} effect, which counteracts the dielectric charge developed, thus reducing the composites dielectric constant. Figure 2.9(b), which quantifies the contribution to $\bar{\varepsilon}_{33}^{T}$ associated with clamping effects, shows this reduction is small (< 2%).

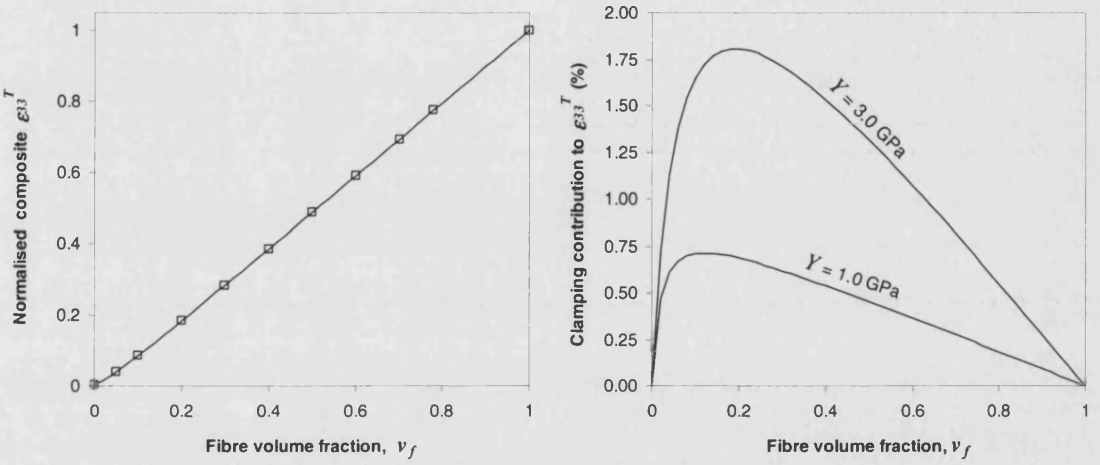

(a) (b)

Figure 2.9: (a) Analytical (solid lines) and finite element (□) results of composite ε_{33}^{T} versus fibre volume fraction. Results are normalised and shown for a matrix with a Young's modulus of 3.0 GPa. (b) The contribution to the composite dielectric constant arising from active fibre clamping predicted by the analytical model.

Figure 2.9(b) shows the clamping effect contribution reaches a maximum of approximately 1.8% at a volume fraction of v_f = 0.2 for the stiffer polymer. The figure also shows the clamping effect can be reduced, and the maximum shifted to lower volume fractions, by using a more compliant matrix material.

2.5 Chapter Summary

The aim of this chapter was to use an appropriate analytical model to predict the response of 1-3 composites as a function of fibre and matrix properties, and their volume fractions. An existing analytical model was introduced and compared to finite element models, developed to simulate testing conditions to be experienced during experimental composite characterisation. Finite element results confirm that the analytical model is able to accurately predict the composite response over the full fibre volume fraction range. This suggests the analytical model simplifications, such as neglecting fringing fields, introduce negligible errors. In addition, this

also provides evidence that the finite element models are acting correctly and that the mesh is sufficiently fine.

It is still necessary for the model to be experimentally verified before it can be used with confidence to extract fibre properties from composite measurements. This is covered in Chapter 3.

CHAPTER 3

LOW FIELD FIBRE PROPERTIES - EXPERIMENTAL

3.1 Introduction

Chapter 2 has introduced, and verified by finite element techniques, an analytical model capable of extracting fibre properties from measurements made on 1-3 composites. It was shown that as the fibre volume fraction is reduced the composite response becomes dominated by the matrix properties. It is possible that this, combined with the weaker signals developed as fibre volume fraction is reduced, will place a lower limit on the fibre volume fraction of composites from which reliable, and accurate material properties can be measured. This can only be investigated by using experimental data obtained from 1-3 composites. Data available from current research does not span a wide enough fibre volume fraction range to investigate the volume fraction limits of the analytical model. This is partly due to the difficulty of manufacturing high quality composites with low volume fractions.

At low volume fractions, fibres tend to collect in one area so that the composite does not possess a random fibre distribution, making material properties location sensitive. An additional problem is maintaining the vertical alignment of the fibres, which can lead to errors being introduced into the expected composite response. Some methods of composite construction also place an upper limit on the fibre volume fraction they are capable of producing. An example is a manufacturing method in which matrix material is ejected from the uncured composite by application of pressure to the mould. Attaining high fibre volume fractions requires high pressures, resulting in fibre fracture, and poor results.[45] This chapter is divided into five main sections: composite manufacture; composite characterisation; matrix characterisation; analytical model validation; fibre property comparison. These are detailed below.

The first section of this chapter describes the techniques developed to manufacture composites with randomly distributed and vertically aligned fibres over a wide volume fraction range. The second section introduces the test methods employed to characterise the piezoelectric, dielectric and mechanical properties of the manufactured composites. Before it is possible to compare measured composite responses with analytical model predictions it is necessary to have knowledge of the relevant matrix material properties. Thus, characterisation of the matrix properties forms the third section. In the fourth section, results obtained from the 1-3 composites are used in conjunction with the matrix properties to plot the composite trends.

Analysis of the results allows identification of the most valid volume fraction regimes in which the analytical model can be utilised.

With the range of validity of the analytical model examined, and the matrix material properties characterised, it is then possible to determine the fibre properties from the composite responses with confidence. Thus, the final section reports the fibre properties of a range of fibres, each produced by a different fibre manufacturing technique. The aim of this is to establish the ability of the different manufacturing techniques to produce high quality fibres, ideally with material properties approaching those of bulk PZT. Manufacturing techniques can then be compared to help identify important stages required for optimised fibre manufacture. The fibre properties will also be useful for selecting the optimum fibre for incorporation into an AFC, and for finite element modelling inputs.

3.2 Manufacture of 1-3 Composites

The successful manufacture of 1-3 composites with a wide range of fibre volume fractions is greatly influenced by the fibre and matrix selection. The manufacturing methods are also critical and must be able to produce composites with a large volume fraction range for validation of analytical model predictions. These issues are discussed in this section.

3.2.1 Fibre and matrix choice

Piezoelectric fibres 250 μm in diameter with PZT-5A composition, manufactured using the Alceru method and supplied by Smart Materials Corp. were selected for composite manufacture. Fibres of this composition display appealing material properties for incorporation into AFC actuators, as highlighted in Table 1.1. Thus, in addition to validating the analytical model, the manufactured composites will allow the material properties of a useful fibre type to be extracted. The relatively large diameter of these fibres is also appealing, making individual fibre handling and composite construction easier.

A low viscosity 2-part epoxy resin, Struers Specifix-40, was chosen as the 1-3 composite matrix material. This choice was based on four important features exhibited by this epoxy system. Firstly, the low viscosity of the resin prior to curing allows good infiltration into the small spaces between fibres during manufacture of 1-3 composites. Secondly, any air that becomes trapped during mixing or infiltration is easily removed. Thirdly, the epoxy adheres well to the PZT fibres (although the level of adhesion has not been quantitatively determined). The final useful feature exhibited by this resin is optical transparency. This allows manufactured

composites to be assessed for fibre mis-orientations, fibre fracture, and trapped voids, all of which could affect the composite performance.

3.2.2 Manufacturing methods

To manufacture 1-3 composites the fibres were cut into 8 mm lengths and aligned in cylindrical moulds 2.0 mm in diameter and approximately 8 mm in length. The fibre filled mould was subsequently infiltrated with the low viscosity epoxy resin under vacuum to reduce void formation. It is important that the fibres remained vertically aligned in the mould otherwise deviation from the analytical predicted response would arise[49] making extraction of fibre properties a difficult task. It is also important to obtain a random distribution of fibres. If some portions of the composite have a high fibre volume fraction while others are depleted of fibres the measured response will become location sensitive. To achieve vertical alignment and random distributions, three different methods of fibre alignment were used. The method selected depended on the desired fibre volume fraction of the composite to be manufactured.

For high volume fraction composites ($v_f > 0.5$) the ceramic fibres were placed directly into the mould, and infiltrated with resin. The fibres close proximity held them vertically aligned during matrix curing. Medium volume fractions ($0.2< v_f >0.5$) were manufactured by pre-coating the fibres with epoxy and allowing it to cure prior to placing in the moulds. Mould filling with these coated fibres resulted in medium volume fraction composites comprising aligned and randomly distributed fibre arrangements. Low volume fraction composites ($v_f < 0.2$) were manufactured using a 'pick and place' technique. In this technique the fibres were partially inserted in a soft pliable modelling clay capable of holding the fibres vertically in the mould, which was subsequently filled with the resin.

After curing for 24 hours at 40 °C, the composites were cut to 5 mm lengths and polished on their end faces using a Beuhler Motopol 12 polishing machine using progressively finer diamond suspensions. The final stage used a 0.05 μm colloidal silica suspension. This developed a high optical contrast between fibre and matrix suitable for determination of fibre volume fraction using image analysis techniques. For this purpose the image analysis software OPTIMAS 6.1 was used. Images of samples displaying a range of volume fractions, typical of those used to determine fibre volume fractions, are shown in Figure 3.1.

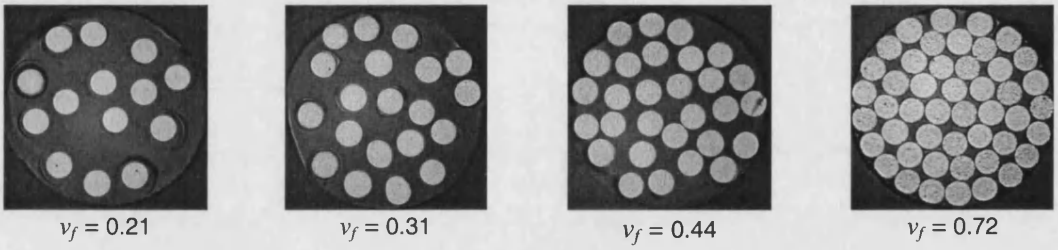

Figure 3.1: Images of a range of 1-3 composites manufactured showing the typical fibre distributions. The composites have a diameter of approximately 2 mm.

The composites show randomly distributed fibre arrangements, even at low volume fractions. Observation using a low powered binocular microscope revealed that fibres were aligned parallel to the composites length and were unbroken. No voids were found in the samples.

After image analysis a silver conductive paint (Electolube®) was applied to the composite end faces to form electrodes. The smooth end faces prepared for image analysis now ensure good electrical contact between the silver paint and the fibres, enabling the composites to be easily poled.

3.2.3 Poling

Poling was performed using the apparatus shown schematically in Figure 3.2.

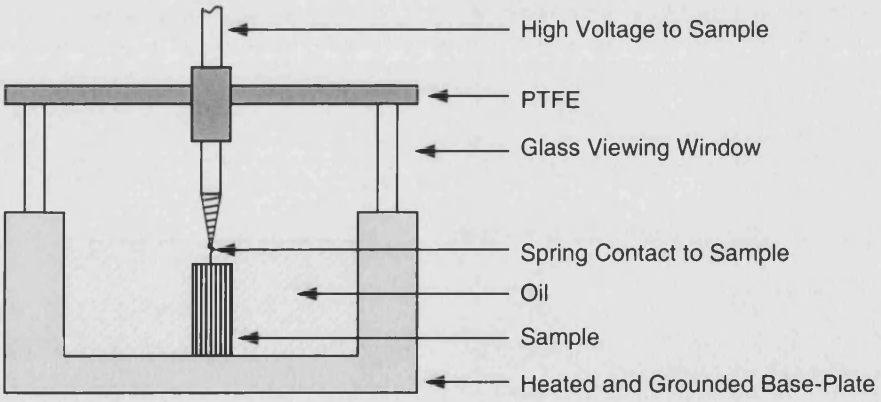

Figure 3.2: Schematic cross section of the poling apparatus for poling 1-3 geometry composites.

The sample was loaded into the oil bath of the poling apparatus, and the high voltage needle lowered onto the surface of the sample until the spring made contact. The heated base plate was set to 100 °C and left at temperature for 10 minutes to allow the oil and sample to achieve

thermal equilibrium. The voltage to the sample was increased to the appropriate level to achieve a field of 2.25 kV mm^{-1} across the sample. After 10 minutes with the field applied the heated base plate was switched off, and the poling apparatus was left to cool to below 40 °C before reducing the voltage to zero and removing the sample. The total poling time was approximately 1 hour, with the field being applied for the majority of this time. This poling regime was known to fully pole commercially obtained bulk PZT-5A samples and was thus considered suitable for the poling of the 1-3 composites. Once removed, the samples were cleaned in a solvent to remove oil residue from the surfaces. This was especially important for the electroded ends where oil residues could affect subsequent measurements.

After this whole process the composites were poled along the fibre long axis direction, designated the 3-direction, while the 1-direction is orthogonal and in the sample's radial plane as shown in Figure 2.1. The poling direction was marked by placing a small red mark on the surface that was held at a positive voltage during the poling process. This allowed for correct alignment in subsequent testing apparatus. Finally, the samples length, diameter and mass were measured. Once the composites were aged for 24 hours they were ready for experimental testing, using the methods described in the following section.

3.3 Characterisation of 1-3 Composites

The experimental techniques employed to measure the composite's piezoelectric ($\bar{d}_{33}$, $\bar{d}_{31}$, $\bar{k}_{33}$), dielectric ($\bar{\varepsilon}_{33}^{T}$) and mechanical properties ($\bar{s}_{33}^{E}, \bar{s}_{33}^{D}$), which have already been briefly introduced in the description of the FE load cases in Chapter 2, are described in detail in this section. The principles of each measurement method, and how they are applied to testing the 1-3 composites, are now introduced.

3.3.1 Berlincourt method for measurement of $\bar{d}_{33}$ and $\bar{d}_{31}$

A Take Control Piezometer was used to evaluate the $\bar{d}_{33}$ and $\bar{d}_{31}$ coefficients of the composites. The system uses the direct piezoelectric effect (charge generation via an applied load) to measure the piezoelectric coefficients. This is historically referred to as the Berlincourt method after D. Berlincourt who developed the technique. The system set-up is shown in Figure 3.3.

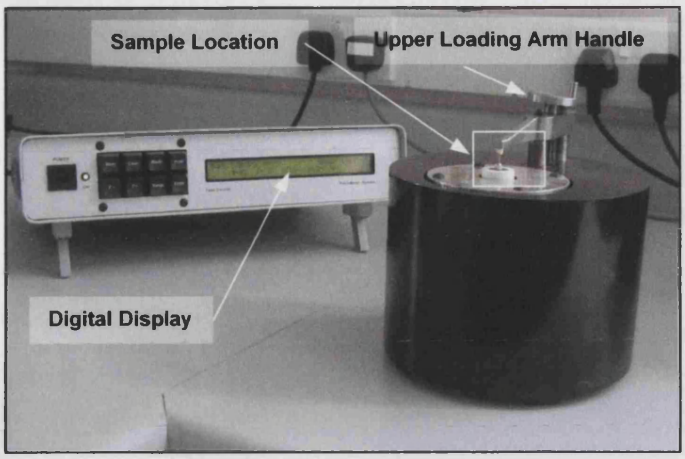

Figure 3.3: The Take Control Piezometer system (set-up shown for measuring d_{33})

The Piezometer consists of a digital display unit where the measurements are displayed, and an upper and lower loading arm for applying the load to, and measuring the charge generated from the sample. The upper loading arm can be moved vertically on the screw-threaded pillars by rotation of the loading arm handle. The lower loading arm is spring loaded and vibrates in the vertical plane at a frequency of 97 Hz, applying a sinusoidal force of approximately 0.1 N to the sample in mechanical contact. This oscillatory force is in addition to the static preload that is applied by rotation of the upper loading arm handle. Various studs can be screwed into the upper and lower loading arm in the 'sample location' section of Figure 3.3, which are dependent on the sample size and the measurement being made (d_{33} or d_{31}). An expanded and labelled view of this location set up for measuring d_{33} and d_{31} is shown in Figure 3.4(a) and Figure 3.4 (b) respectively.

For evaluation of $\bar{d}_{33}$, conducting metal studs are screwed into the upper and lower loading arms, and the sample positioned between the two studs with the 3-direction in the vertical plane, as shown in Figure 3.4(a). The upper loading arm handle is turned to bring the studs into mechanical and electrical contact with the sample's electroded end faces. The handle is then rotated one full turn to apply a 10 N preload to the sample via depression of the spring loaded lower loading arm. In this case the force is applied parallel to the poling direction and the charge generated by the sample is collected through the studs and used to calculate $\bar{d}_{33}$. In this case $\bar{d}_{33}$ is measured as the charge produced per unit applied force (C N^{-1}).

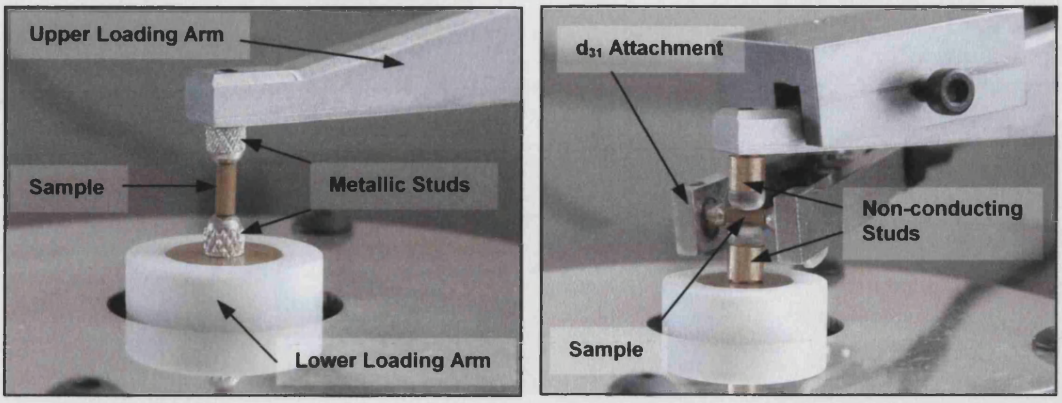

(a) (b)

Figure 3.4: The Piezometer 'sample test location' showing measurement of (a) d_{33} and (b) d_{31} for a 1-3 composite.

For evaluation of $\bar{d}_{31}$ the metallic studs are replaced with non-conducting polymer tipped studs. The sample is positioned between the studs with the 3-direction in the horizontal plane and the upper loading arm handle turned so that the studs make mechanical contact in the 1-direction. The handle is turned one full turn to apply a 10 N preload to the sample via the spring loaded lower loading arm. In this case the force is applied normal to the poling direction. The charge generated on the electroded ends of the sample is collected by a special d_{31} attachment, which is attached in position on the upper loading arm. This test set-up can be seen in Figure 3.4(b).

3.3.2 Impedance analysis for measurement of $\bar{s}_{33}^{E}$ and $\bar{s}_{33}^{D}$ and $\bar{k}_{33}$

The impedance analysis technique[77] was used to determine $\bar{s}_{33}^{E}$, $\bar{s}_{33}^{D}$ and $\bar{k}_{33}$ of the composites. A body will exhibit a number of modes of vibration, the lowest frequency mode being the fundamental mode associated with the largest dimension of the body. For a rod geometry, such as the 1-3 composites to be tested, the lowest frequency mode will be the fundamental mode associated with the rod's length, termed the longitudinal-length mode. Other higher frequency vibrational modes will be harmonics of this fundamental mode, and fundamentals of other modes and their harmonics. The nominal geometry of the 1-3 composites (*length* = 5.0 mm, *diameter* = 2.0 mm) satisfies the geometry constrains of BS EN 50324-2[77] allowing excitation of the longitudinal-length mode without interference from other modes.

Piezoelectric materials are unique in that mechanical resonance can be induced by applying an AC voltage across the sample. When the electrical drive frequency coincides with a mechanical resonance of the sample an impedance minimum occurs. Conversely, when the electrical drive frequency coincides with a mechanical anti-resonance of the sample an impedance maximum

occurs. The frequency of the resonance and anti-resonance modes is governed by the sample dimensions, density and various piezoelectric, dielectric and mechanical coefficients. Therefore, with knowledge of the impedance response of a sample, it is possible to calculate various piezoelectric and mechanical coefficients. Equations appropriate for the longitudinal-length mode are given in Equations (3.1) to (3.3)[77] in which l and ρ are the sample length and density and f_r and f_a are resonance and anti-resonance frequencies respectively.

$$s_{33}^{D} = \frac{1}{4\rho f_s^2 l^2} \tag{3.1}$$

$$s_{33}^{E} = \frac{s_{33}^{D}}{1 - k_{33}^2} \tag{3.2}$$

$$k_{33} = \left[\frac{\pi}{2} \frac{f_r}{f_a} \cot\left(\frac{\pi}{2} \frac{f_r}{f_a} \right) \right]^{1/2} \tag{3.3}$$

To evaluate the $\bar{s}_{33}^{D}$, $\bar{s}_{33}^{E}$ and $\bar{k}_{33}$ coefficients of the composites the impedance of the 1-3 composites was measured using an Agilent 4194A impedance analyser. The experimental set-up, which shows a typical impedance spectrum being generated on the analyser display, is shown in Figure 3.5. An expanded view of the sample test location is also shown.

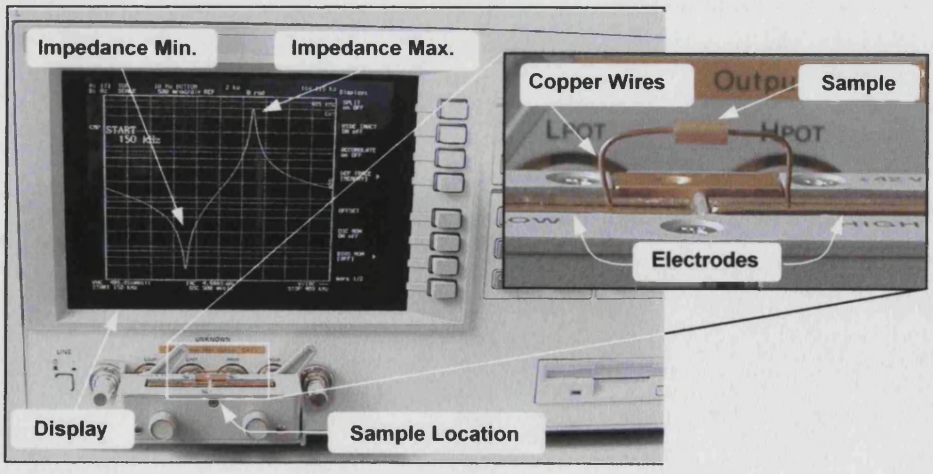

Figure 3.5: Test set-up for impedance spectroscopy of 1-3 geometry composites. The impedance versus frequency curve generated on the display is typical of high volume fraction composite response.

Two thin copper wires were attached to the low and high electrodes to allow connection to the sample. Since this test set-up is not a standard fixture, compensation was performed for both open-circuit and short-circuit conditions in accordance with the procedure in the Agilent 4194A instruction manual. Open-circuit conditions were enforced by ensuring no sample was loaded between the copper wires, while short-circuit conditions were enforced by loading a copper sample, with similar dimensions to the composites, into position between the wires. Once fixture compensation had been performed samples were positioned between the copper wires in preparation for testing. Care was taken not to allow the wires to clamp the samples too strongly, since this would force deviation from the 'mechanically free' boundary conditions required by the test method. Once loaded the impedance was measured over the frequency range 150 kHz to 500 kHz with an excitation voltage of 500 mV. This frequency range encompassed the fundamental resonance of the longitudinal-length mode associated with the sample's rod geometry. Maximum and minimum impedance values, and the corresponding frequencies at which they occurred, were recorded. These values were used in Equations (3.1) to (3.3) to calculate the relevant material properties.

3.3.3 LCR meter for measurement of $\bar{\varepsilon}_{33}^{T}$

The constant stress permittivity of the 1-3 composites ($\bar{\varepsilon}_{33}^{T}$) was evaluated from capacitance measurements performed using a HP16451B dielectric test fixture attached to a HP4263B LCR meter. A picture of the experimental set-up is given in Figure 3.6, which shows the digital display of the LCR meter and an expanded view of the sample location in the dielectric test fixture.

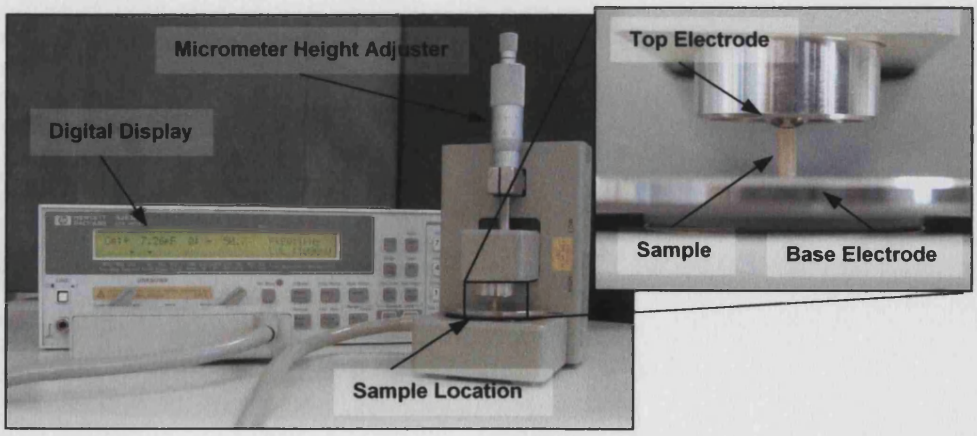

Figure 3.6: Experimental set-up for measurement of the dielectric constant.

To perform a measurement the sample was positioned on the base electrode, and the top electrode was lowered onto the upper surface of the sample using the micrometer height adjuster. The spring loaded ball-bearing which forms the top electrode allows electrical contact to be made to the sample without excessive clamping, thus ensuring constant stress (mechanically free) boundary conditions. A voltage of 1.0 V was applied to the top electrode at a frequency of 1 kHz. The capacitance measurement (C), displayed on the digital display of the LCR meter, was used to calculate the dielectric constant of the sample using Equation (3.4).

$$\bar{\varepsilon}_{33}^{T} = \frac{Ct}{A} \tag{3.4}$$

Where t = sample thickness

A = sample electroded area

This concludes the low field testing performed on the composites. In addition to the characterisation of the composites, the matrix material must also be characterised to allow extraction of fibre data. This is the focus of the following section.

3.4 Characterisation of the Polymer Matrix

To enable the material properties of the fibres to be calculated from 1-3 composite measurements it is necessary to evaluate both the mechanical properties (Young's modulus and Poisson's ratio) and electrical properties (dielectric constant) of the matrix. The methods used for this are described below.

3.4.1 Young's modulus: stress-strain

Polymer dumbbell samples suitable for mechanical characterisation were made by a casting method. A mould was fabricated by punching out dumbbell shapes (gauge length 25.0 mm) from a 2.0 mm thick plastic sheet. This mould was then placed on a flat glass plate coated with mould release. The two-part Specifix-40 epoxy resin system used in the manufacture of the 1-3 composites was mixed in accordance with the manufactures instructions and placed under vacuum to aid in the removal of trapped air from the mixing process. The resin was then poured into the mould assembly and placed in an oven at 40 °C for 24 hours to allow full curing. Once

cured, the dumbbell samples were removed from the mould. Their gauge length was sanded with fine grade grit paper to remove any surface irregularities.

The dumbbell samples were loaded into an Instron 1122 test machine. A calibrated clip-on extensometer was fixed to the gauge length to monitor strain, while a 500 kg capacity load cell monitored load. Five dumbbell samples were tested with a crosshead speed of 0.5 mm min^{-1}. The Young's modulus was evaluated from the resulting stress-strain curves in accordance with BS 2782: 1994[78] (Young's modulus is defined by the ratio of the stress difference T_2 minus T_1 to the corresponding strain difference $S_2 = 0.0025$ minus $S_1 = 0.0005$).

3.4.2 Young's modulus: dynamic mechanical thermal analysis (DMTA)

The mechanical properties of polymers are well known to be frequency dependant, with Young's modulus increasing with increasing frequency. Thus the Young's modulus evaluated by the low strain rate (low frequency) stress-strain technique described above may not be representative of the high frequency value. In the impedance analysis technique, used for the characterisation of the 1-3 composites, the frequency is between 150 and 500 kHz. The polymer matrix is clearly experiencing frequencies above those of the stress-strain test. Ideally one would like to evaluate the matrix Young's modulus at test frequencies. Mechanical testing at such high frequencies (150 kHz to 500 kHz) is not a simple task, thus an estimation of the Young's modulus at these frequencies must be made.

The high frequency Young's modulus can be estimated by making use of the time-temperature equivalence displayed by polymers. By testing at low temperatures it is possible to gain an insight into the mechanical properties at high frequencies. Therefore, dynamic mechanical thermal analysis (DMTA) was used to measure Young's modulus as a function of temperature.

Rectangular samples 3 mm in thickness were cast between two glass microscope slides coated in mould release and left to cure for 24 hours at 40 °C. Samples 10 mm × 20 mm were cut from the cured sheet using an ISOMET 2000 precision saw (Buehler) and loaded into a TRITEC 2000 Dynamic Mechanical Analyser (Tritron Technology) in single cantilever beam configuration. This set-up can be seen in Figure 3.7. The oven was then positioned over the sample in preparation for testing.

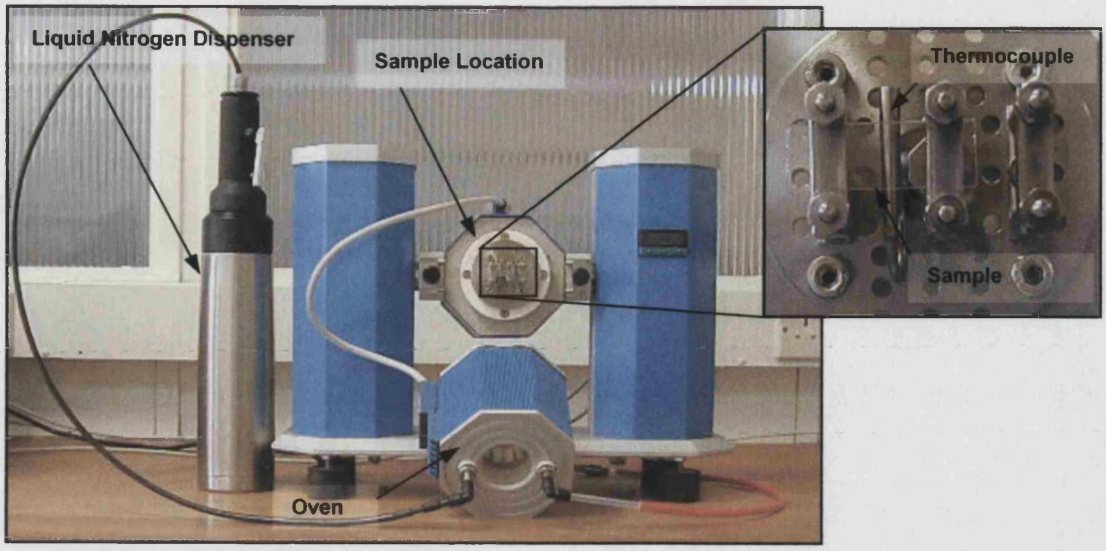

Figure 3.7: Experimental set-up for the measurement of Young's modulus versus temperature for the epoxy matrix. The oven has been removed for clarity.

A predetermined dynamic displacement of 50 μm is induced in the polymer sample by applying a force to the central clamp. The force required to induce this displacement is measured and used with beam bending equations to calculate Young's modulus. The controlling software then outputs Young's modulus versus temperature curves. This measurement was performed at 1 Hz over a temperature range from 0 °C to 100 °C with a ramp rate of 2 °C min^{-1}. Cooling below room temperature required use of liquid nitrogen, which was introduced into the oven from the liquid nitrogen dispenser.

3.4.3 Dielectric constant

For determination of the matrix dielectric constant thin disks of epoxy, 30 mm in diameter, and ranging from 0.8 to 2.0 mm in thickness, were cut from a solid epoxy cylinder using a precision saw. Silver paint was applied to the surfaces to form electrodes. Capacitance measurements were made using a HP16451B dielectric test fixture attached to a HP4263B LCR meter (Figure 3.6) at a frequency of 1 kHz and a voltage of 1.0 V. The capacitance value was used together with sample dimensions to calculate the dielectric constant ε_{11} of the polymer.

3.5 Analytical Model Validation

This section contains the results of the matrix characterisation and the composite analysis. They are used to (i) calculate fibre data, and (ii) compare experimentally determined composite responses with the analytical model predictions presented in Section 2.4 of Chapter 2. The model predictions and experimental responses are used to determine the fibre volume fraction range over which the analytical model is most valid.

3.5.1 Matrix property results

The matrix Young's modulus (Y_{11}) determined from stress-strain testing was measured to be 2.8 GPa. This value is readily converted into the s_{11} compliance term required by the analytical equations using Equation (3.5).

$$s_{11} = \left(\frac{1}{Y_{11}} \right) \tag{3.5}$$

The matrix Young's modulus as a function of temperature measured at a fixed frequency of 1 Hz, obtained from DMTA, is plotted in Figure 3.8.

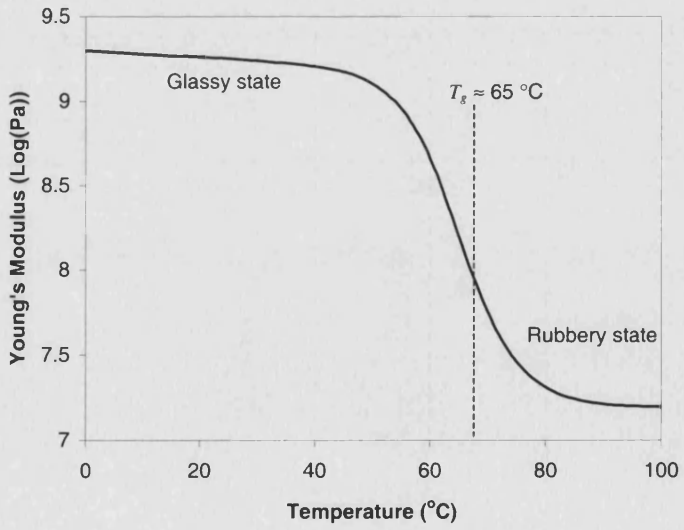

Figure 3.8: Matrix Young's modulus as a function of temperature evaluated using DMTA.

Figure 3.8, although not giving accurate modulus results because of clamping effects associated with the single cantilever beam configuration, does show that the matrix is in its glassy state at room temperature, exhibiting a glass transition temperature (T_g) of approximately 65°C. Because of the well-documented time-temperature equivalence displayed by polymers, to estimate the effect of increasing the test frequency, it is possible to examine the effect of lowering the test temperature. Since the matrix at room temperature is already below T_g (the primary transition associated with gross main chain movement) a rise in test frequency will only result in secondary transitions being encountered. Secondary transitions, associated for example with side group rotations, are accompanied by only a small rise in the modulus. This implies that the low frequency room temperature modulus of 2.8 GPa, determined from the stress-strain technique, is representative of the matrix modulus at high frequencies and will not introduce a significant error.

To determine the matrix s_{12} compliance it is necessary to have knowledge of the Poisson's ratio, v_{12}. Although not experimentally determined, it is possible to make a reasonable estimate for v_{12}. Glassy polymers typically display Poisson's ratios ranging from approximately 0.33 for short time (high frequency) behaviour, to 0.5 for long time (low frequency) behaviour.[79] Since typical testing will be short time (minimum test frequency is 97 Hz for the Piezometer) a value close to 0.33 is likely. Recent research has reported a Poisson's ratio value of 0.38 for an epoxy resin,[56] which agrees with the range introduced above. Using this value allows evaluation of the s_{12} compliance through Equation (3.6).

$$s_{12} = -v_{12}s_{11} \tag{3.6}$$

The matrix relative dielectric constant ($\varepsilon_{11}/\varepsilon_0$) was calculated to be 5.0 using capacitance measurements obtained from the LCR meter. This is in agreement with typical dielectric constant values for polymers.[80]

With the relevant matrix properties evaluated it is possible to extract fibre data from experimental 1-3 composite results.

3.5.2 Composite property results

Results from the characterisation of $\bar{d}_{33}$, $\bar{d}_{31}$, $\bar{s}^E_{33}$, $\bar{s}^D_{33}$, $\bar{k}_{33}$ and $\bar{\varepsilon}^T_{33}$ of the composites are shown in graphs presented in Figure 3.9 through Figure 3.14 respectively. Each figure presents the results of one material property in two graphs, (a) and (b). The first graph of each pair, (a), shows the composite property as it varies with fibre volume fraction. The second graph uses this composite data, together with the matrix properties and the analytical model equations (Equations (2.1) to (2.6)), to extract the property of the fibres. Ideally, properties of the fibre should not be a function of the volume fraction. Thus, when the fibre property is plotted against volume fraction (the second graph in each pair) a straight horizontal line should be formed, the average value of which represents the fibre value. This value can then be used in the analytical equations, together with the measured matrix properties, to construct the analytical trend line for the composite. This trend line is plotted in the first graph of each pair.

$\bar{d}_{33}$ and $\bar{d}_{31}$ versus fibre volume fraction

Figure 3.9(a) shows the experimental values of the composites' d_{33} as a function of volume fraction. Figure 3.9(b) shows that the fibre values extracted from each composite fall on a horizontal line, as would be expected. The fibre d_{33} is taken as the average of the results presented in Figure 3.9(b) and used to construct the trend line in Figure 3.9(a). The experimental results and model prediction are in good agreement.

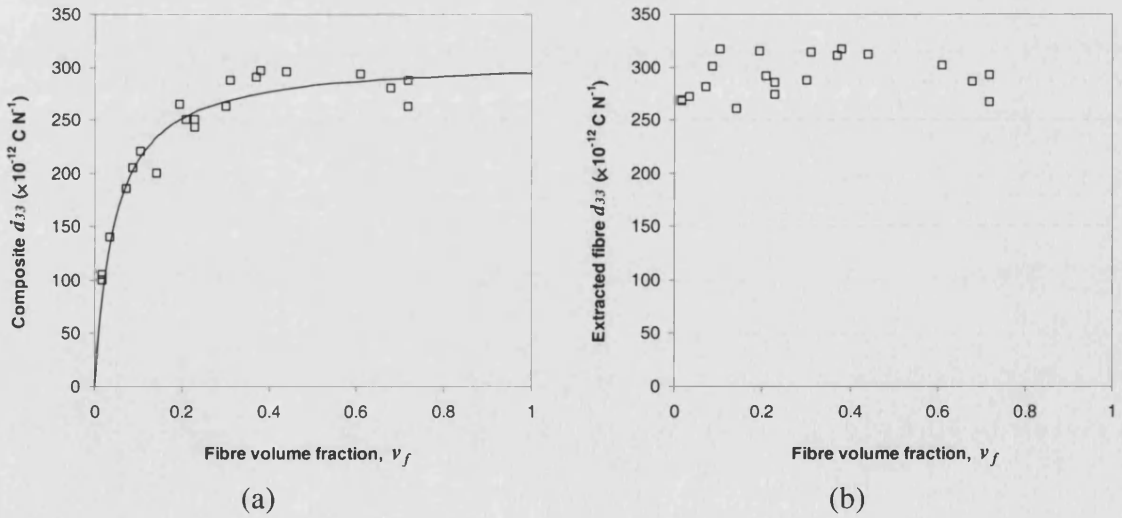

Figure 3.9: Graphs showing (a) experimental results (□) and the analytical trend line (——) for $\bar{d}_{33}$ versus volume fraction and (b) the fibre d_{33} value extracted from composite measurements.

Figure 3.10(a) plots the experimental results of the composites' d_{31} versus volume fraction. Figure 3.10(b), which plots the fibre d_{31} values versus fibre volume fraction, reveals a large variation in the extracted fibre value. It was shown from the graph presented in Figure 2.6 in Chapter 2 that the contribution to the composite response associated with the fibres' d_{31} coefficient increases with increasing fibre volume fraction. Thus fibre properties extracted from the higher volume fraction composites are likely to yield results more representative of the true fibre d_{31} value. Due to the large deviation at low volume fractions, the fibre value is calculated by averaging the results from composites with $v_f > 0.35$. This fibre d_{31} value, together with the previously determined fibre d_{33} value, has been used with the analytical model equation to construct the trend line in Figure 3.10(a).

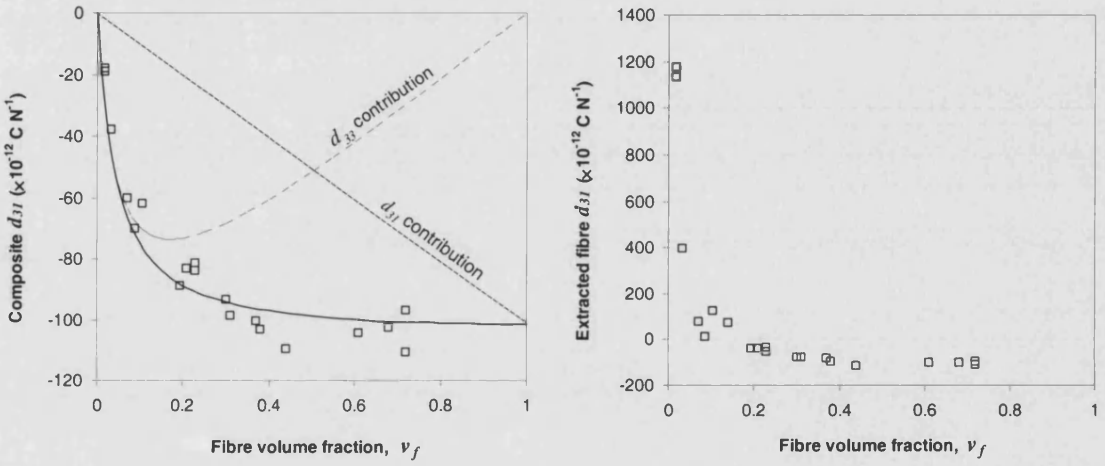

Figure 3.10: Graphs showing (a) the experimental results (□) and the analytical trend line (——) for $\bar{d}_{31}$ versus volume fraction and (b) the fibre d_{31} value extracted from composite measurements. The fibres' d_{33} and d_{31} contribution is plotted in (a) as a broken line (------).

Figure 3.10(a) shows that, despite the large variation in the extracted fibre response, the composite results appear to follow the analytical model trend line well. We recall from Section 2.4.1 in Chapter 2 that the composite $\bar{d}_{31}$ response is the sum of the fibres' d_{31} effect and a contribution from the fibres' d_{33} effect, associated with load transfer from the matrix. The contribution of both of these effects to the overall composite response, calculated using Equation (2.9), are plotted in Figure 3.10(a) as a broken line. At high volume fractions, $v_f > 0.5$, the fibres' d_{31} contribution exceed that associated with the fibre d_{33} effect. However, at low volume fractions the fibre d_{33} effect becomes the dominant contributor to the overall composite response. Thus at low volume fractions, any errors in the contribution from the fibre d_{33} effect (resulting from inaccurate model assumptions or errors in any of the measurements), will have

serious implications on the value of the predicted fibre d_{31} coefficient; the value we wish to measure.

It is likely that the largest source of error in the low volume fraction composites is deviation from the iso-strain assumption of the analytical model. It is postulated that when pressure is applied to a 1-3 composite in the 1- or 2-direction, the corresponding Poisson's ratio extension in the 3-direction is not the same in the fibres and matrix phases, as assumed by the model. The polymer matrix will extend more than the fibres, essentially not transferring the predicted load to the fibres. The charge liberated from the fibre d_{33} effect will therefore be lower than predicted by the model, leading to errors in the calculated d_{31} response. The results presented in Figure 3.10(b) indicate that these errors increase as the volume fraction reduces. For composites with volume fractions below $v_f = 0.2$, the over-estimation of the contribution from the fibre d_{33} effect causes the extracted fibre d_{31} to become positive. This is clearly not possible since d_{31} must be opposite in sign to d_{33}.

Although the iso-strain assumption is thought to be primarily responsible for the errors observed in the calculated fibre d_{31} coefficient, there are other contributory factors. Low volume fraction composites only contain a small number of fibres creating the possibility of large variations between samples, arising from the intrinsic fibre variability. Additionally, errors in measurement of fibre volume fraction, which are more significant in low volume fraction composites, combined with their small signal responses, can introduce further error into the measurements.

Since large errors are associated with this measurement at low volume fractions, the fibre d_{31} is taken as the average of the results from composites with $v_f > 0.35$.

$\bar{s}_{33}^{E}$, $\bar{s}_{33}^{D}$ and $\bar{k}_{33}$ versus fibre volume fraction

Figure 3.11(a) shows the composites' $\bar{s}_{33}^{D}$ as a function of volume fraction. Figure 3.11(b), which plots the fibre $\bar{s}_{33}^{D}$ versus fibre volume fraction, shows that fibre values extracted from composites with low volume fractions show a large variation. Unlike the fibre d_{31} results, there appears to be no trend in the fibre s_{33}^{D} errors as the volume fraction is reduced. At volume fractions below approximately 0.2 there appears to be a general scatter of the experimental results, with some falling above, and others below, the high volume fraction estimates. It is thought that the origin of this scatter results from variability in the small number of fibres present in these low v_f composites. For this reason, only composites with $v_f > 0.2$ are used for the determination of the fibre value. This value is used to construct the analytical model trend

line, shown in Figure 3.11(a). The model prediction follows the experimental results with accuracy.

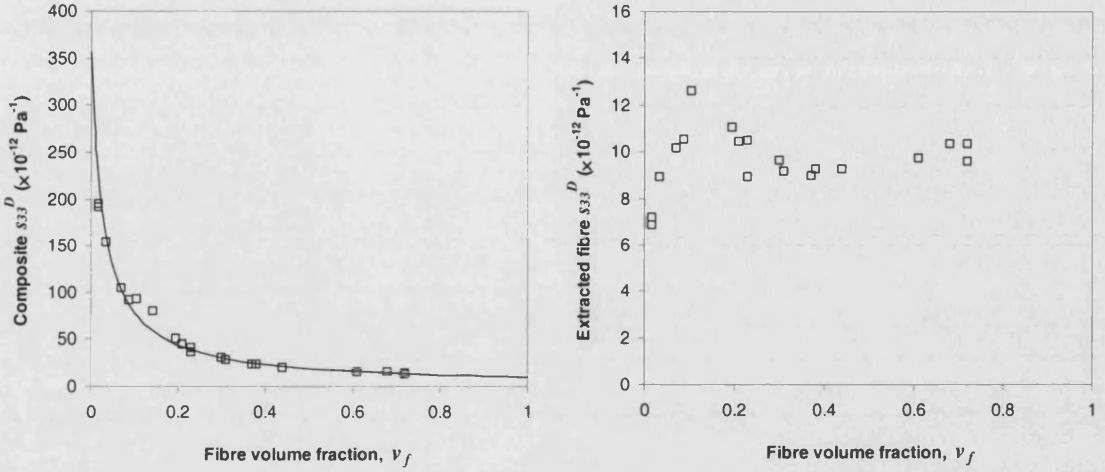

(a) (b)

Figure 3.11: Graphs showing (a) experimental results (□) and the analytical trend line (——) for $\bar{s}_{33}^D$ versus volume fraction, and (b) the fibre s_{33}^D value extracted from composite measurements.

The results of the extracted fibre s_{33}^E (Figure 3.12(b)) show a similar variation at low volume fractions as was seen in the s_{33}^D results, and is attributed to the same source. Therefore, as with the s_{33}^D fibre value, the s_{33}^E fibre value is determined by averaging the results from composites with $v_f > 0.2$. The trend line constructed from this value, and the composite data of $\bar{s}_{33}^E$, are shown in Figure 3.12(a). Again, measured data follows analytical model predictions well.

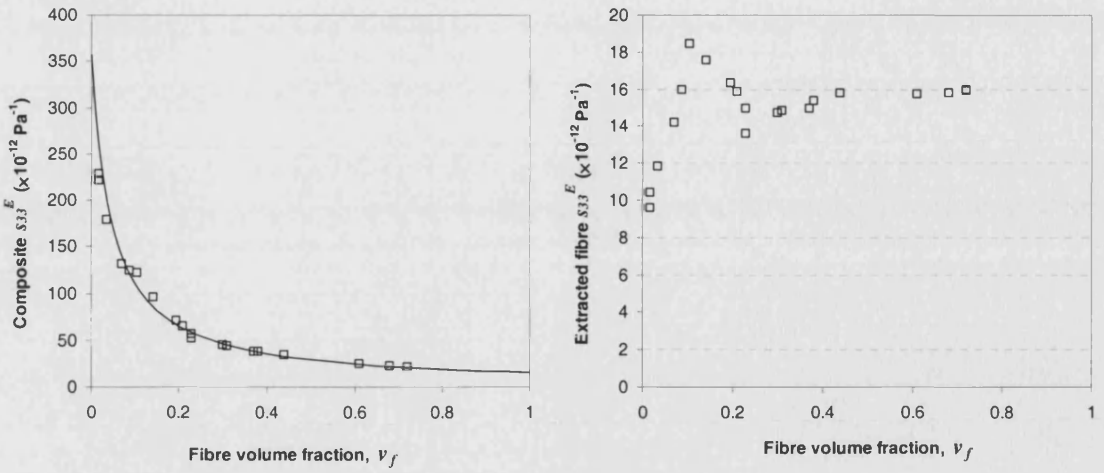

(a) (b)

Figure 3.12: Graphs showing (a) experimental results (□) and the analytical trend line (——) for $\bar{s}_{33}^E$ versus volume fraction, and (b) the fibre s_{33}^E value extracted from composite measurements.

Figure 3.13(a) shows the composites' coupling coefficient, $\bar{k}_{33}$, as a function of volume fraction. Figure 3.13(b) plots the extracted fibre value as a function of fibre volume fraction.

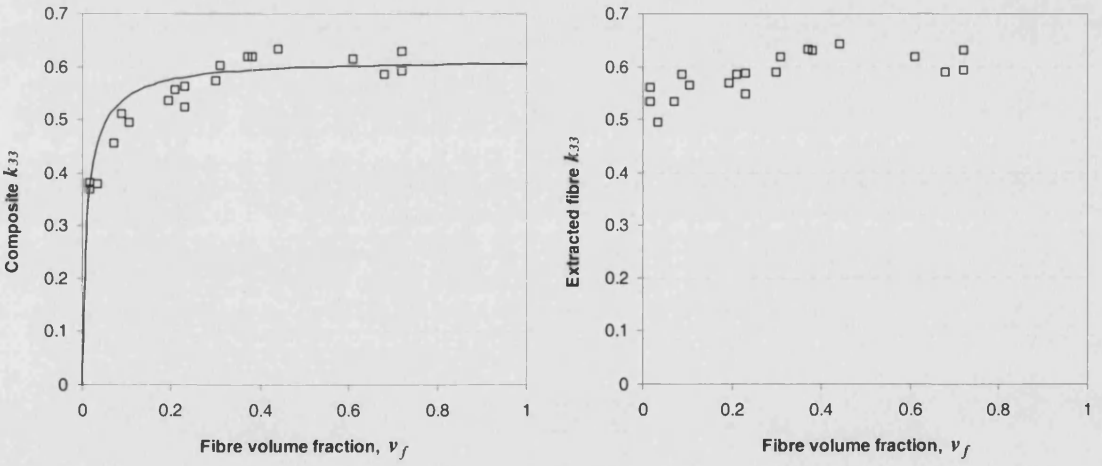

(a) (b)

Figure 3.13: Graphs showing (a) experimental results (□) and the analytical trend line (——) for $\bar{k}_{33}$ versus volume fraction, and (b) the fibre k_{33} value extracted from composite measurements.

The scatter in these results is lower than observed in the compliance results since the coupling factor is related to the ratio of the open and closed circuit compliance, as shown by Equation (3.2). Since a slight deviation in the extracted fibre value is seen in composites with fibre volume fraction lower than 0.2, the fibre value is calculated from composites with volume fractions exceeding this value. The calculated value has been used to construct the analytical trend line for the composite $\bar{k}_{33}$, which is presented in Figure 3.13(a).

$\bar{\varepsilon}_{33}^{T}$ *versus fibre volume fraction*

Figure 3.14(a) shows the composites' dielectric constant as a function of volume fraction. Figure 3.14(b), which plots the extracted fibre results, ε_{33}^{T}, shows that values from low volume fraction composites ($v_f < 0.2$) are greatly over estimated. Thus the fibre value is calculated from composites with volume fractions greater than 0.2, where errors are reduced. This fibre value is used to construct the analytical trend line in Figure 3.14(a).

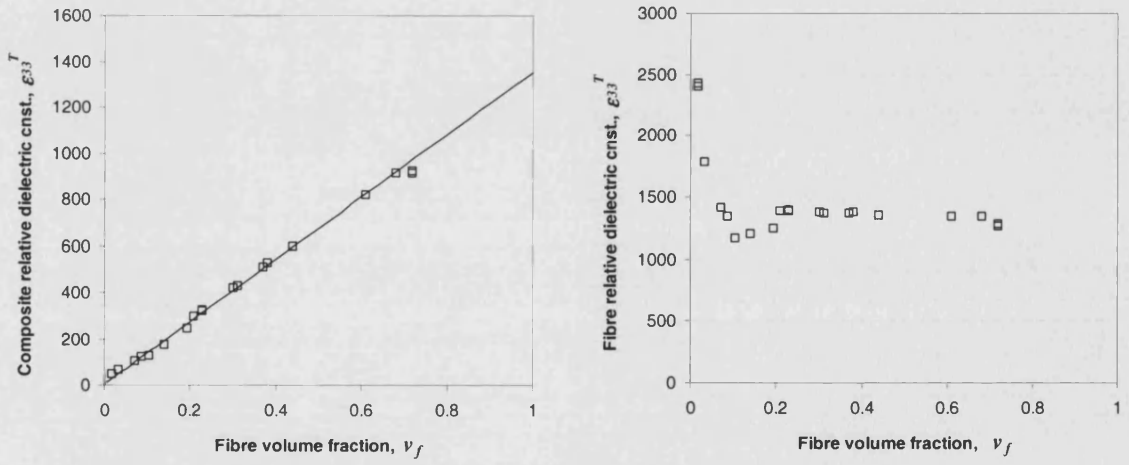

Figure 3.14: Graphs showing (a) experimental results (□) and the analytical trend line (——) for $\bar{\varepsilon}_{33}^{T}$ versus volume fraction, and (b) the fibre ε_{33}^{T} value extracted from composite measurements.

Even though there is large deviation in the calculated fibre value at low volume fractions, Figure 3.14(a) reveals that the experimental results of $\bar{\varepsilon}_{33}^{T}$ follow the model prediction. This is similar to the composite $\bar{d}_{31}$ results, and indeed the reasons for the large error in the calculated fibre results are similar. The over-estimation of the fibre ε_{33}^{T} at low volume fractions can be

attributed to the matrix clamping effect described in Section 2.4.3. At low v_f the composite $\bar{\varepsilon}_{33}^T$ is reduced by matrix clamping, which generates charges via the fibres' d_{33} effect. If this clamping contribution is weaker than predicted by the analytical model, the reduction in $\bar{\varepsilon}_{33}^T$ will be lower than expected, and the fibre ε_{33}^T will be over-estimated. This is precisely the trend seen in Figure 3.14(b). Additional sources of error affecting low volume fraction composites, including the small number of fibres and weak signals, further contribute to the variability in the results.

This section has shown that the analytical model is able to accurately predict the composite's response for all the material properties measured. However, for low volume fraction composites, invalid model assumptions, measurement errors, and individual fibre variability create uncertainty in the extracted fibre value. Results show that accurate fibre properties can only be obtained from composites with volume fractions over approximately 0.2. This value rises to 0.35 for the fibre d_{31} coefficient. In general, it is advisable to manufacture high volume fraction composites, in which errors have a smaller effect on the calculated fibre value. These findings are used in the following section, which reports the fibre properties for the full range of fibres tested.

3.6 Comparison of Fibre Properties

The previous section has shown that it is possible to determine fibre properties from 1-3 composite measurements, provided that the volume fraction is high enough to minimise errors. This section reports on the material properties of a range of commercially available fibres, measured using the techniques described in this chapter. Firstly, a justification of the fibre types selected for characterisation is given. This is followed by a discussion of the fibre properties extracted from 1-3 composites comprising these fibre types.

3.6.1 Fibre selection

There are a number of suppliers of piezoelectric fibres, each using a different manufacturing technique and offering a range of fibre diameters and compositions. Only fibres suitable for incorporation into AFCs were selected for characterisation.

It is important to keep the fibre diameter small to allow the AFC spatial scale to be reduced, enabling a more integrated, and greater structurally conformable active ply to be manufactured.

Based on this approach, fibres with diameters between 125 μm and 250 μm were selected. The lower limit represented the smallest diameter fibre commercially available at the time of this research. The upper limit was chosen since fibres with diameters larger than 250 μm become inflexible, removing one of the key features of AFCs: structural conformability.

Fibre composition determines many important material properties. As shown in Table 1.1 in Section 1.2.3, PZT-5A composition offers the most suitable range of properties for incorporation into AFCs. Most importantly this composition develops large strains at high electrical driving fields. Based on this, only fibres of PZT-5A composition were selected.

Information on the selected fibres, including the manufacturing route, diameter and supplier is located in Table 3.1.

Table 3.1: Summary of the PZT-5A fibres tested.

Fibre Production Method	Diameter (μm)	Supplier
Extrusion[24]	130	CeraNova
Alceru Method	125 & 250	Smart Material Corp.
Viscous Plastic Processing (VPP)[29]	250	IRC in Materials, Birmingham, UK
Viscous Suspension Spinning Process (VSSP)[34]	235	Advanced Cerametrics

Fibres produced by the sol-gel method,[43,38] as used by the German Adaptronic programme, are not available commercially, thus have not been examined. The details of each fibre production method have already been described in the literature review presented in Chapter 1.

The fibres in Table 3.1 were incorporated into 1-3 composites using the manufacturing methods described in Section 3.2. Fibre volume fractions were kept high, typically >0.65, to reduce the errors introduced into the extracted fibre values. Composites were characterised using the techniques described in Section 3.3, and fibre properties calculated from the measured composite properties using the analytical model equations (Chapter 2), and the matrix material properties (Section 3.5.1). The fibre properties are compared and analysed in the following section.

3.6.2 Fibre properties

The piezoelectric properties of the extruded, Alceru, VSSP and VPP derived fibres, as predicted from measurements made on the 1-3 composites comprising these fibres, are shown graphically in Figure 3.15. This figure plots the piezoelectric material properties for each fibre type. The value of the fibre property has been normalised by the literature quoted values of bulk PZT-5A, located in Appendix A2. The numerical value of the each fibre property is shown above the bar relating to that particular fibre.

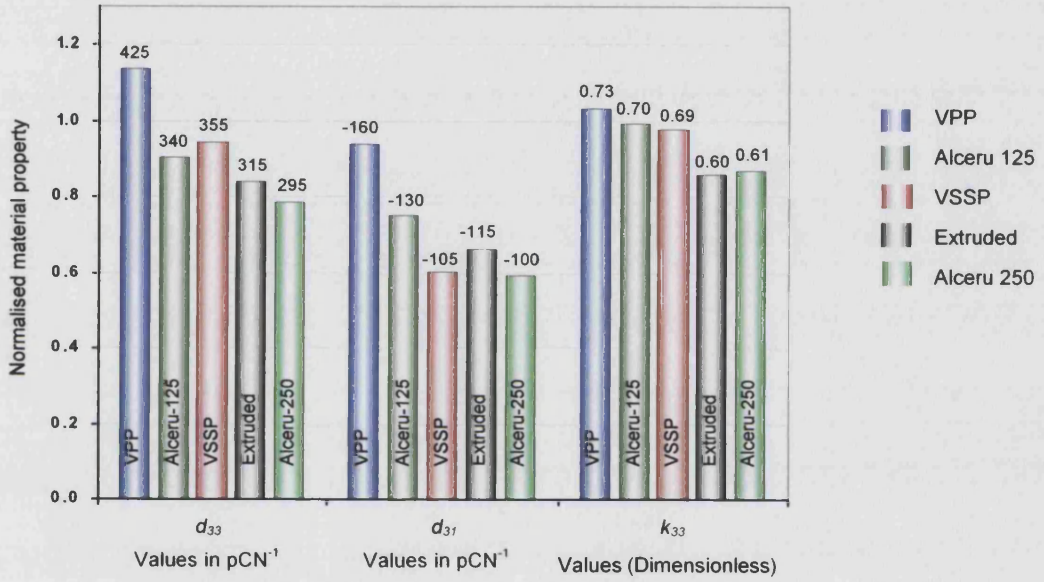

Figure 3.15: Bar chart showing the piezoelectric properties of the five fibre types, normalised by bulk PZT-5A properties. The value for each property is shown above its bar.

It is apparent from this figure that the VPP processed fibres exhibit the highest d_{33} coefficient, which is actually larger than the d_{33} coefficient quoted for bulk PZT-5A. The other fibres' d_{33} coefficients are approximately 20% lower than the VPP fibre value. VPP fibres also exhibit the highest d_{31} coefficient, with a value close to the bulk material value. Other fibre types show a d_{31} ranging from 60% to 75% of the bulk value. For the piezoelectric coupling factor, k_{33}, it is the VPP fibre that again shows the highest value. As with the d_{33}, this value exceeds bulk material values. From the figure it is apparent that the two Alceru derived fibres, 125 and 250 μm in diameter, do not posses the same piezoelectric activity. In all cases the smaller diameter fibre out performs the larger one.

The large piezoelectric activity in the VPP processed fibres may be a result of the manufacturing process, which uses a highly loaded green mix which, prior to extrusion, is mixed using high shear forces to de-agglomerate the PZT powder. This process could lead to higher density PZT fibres than the normal extrusion process, in which the solids loading and shear mixing forces are not as high. However, other factors such as chemical composition and microstructure, which are well known to influence the piezoelectric activity, could be responsible. These factors, which are unknown at this stage, could also be the reason for the differences observed between the two Alceru fibres.

The mechanical and dielectric properties of the fibres are shown graphically in Figure 3.16. The results are presented normalised by bulk PZT-5A values.

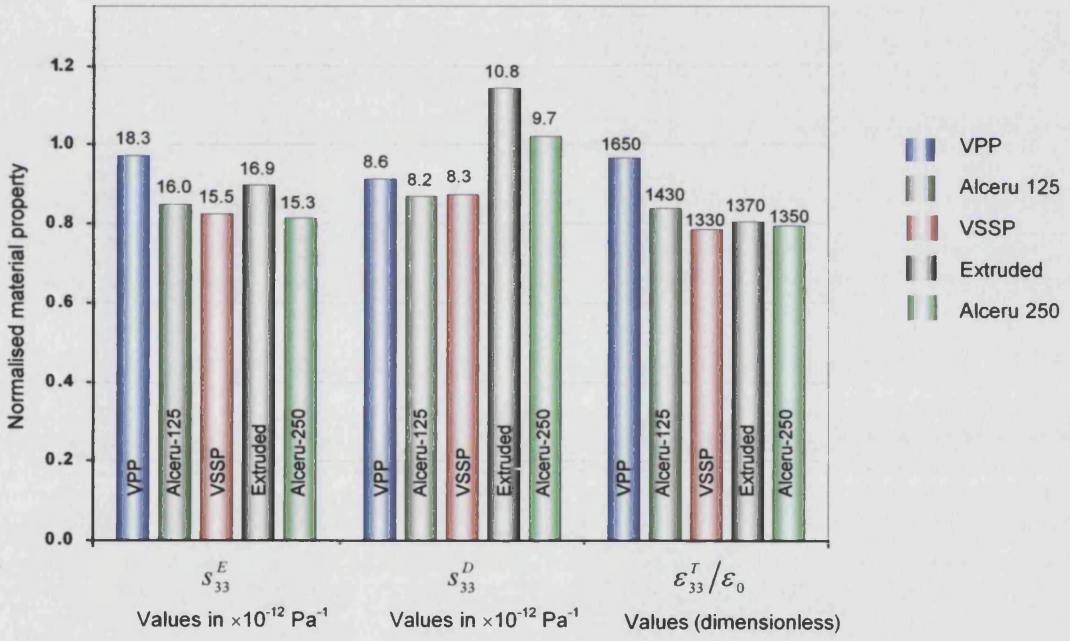

Figure 3.16: Bar chart showing the mechanical and dielectric properties of the five fibre types, normalised by bulk PZT-5A properties. The value for each property is shown above it bar.

The VPP fibres show the highest compliance under short-circuit conditions ($\bar{s}_{33}^E$), close to the bulk value. The other fibre types have a value that is between 80% and 90% of the bulk material value. Under open-circuit conditions ($\bar{s}_{33}^D$), the extruded and Alceru-250 fibres are the most compliant, both exceeding bulk material values. The remaining fibres (VPP, VSSP and

Alceru-125) exhibit values approximately 85% to 90% of the bulk material values. The reason these fibres are stiffer under open-circuit conditions can be attributed to their larger d_{33} coefficients. Loading these fibre under open-circuit conditions causes a larger amount of charge to be developed compared to the extruded and Alceru-250 fibres, which suffer from a lower d_{33} coefficient. Since the generated electrical field is the mechanism that acts to stiffen the fibres, those possessing a higher d_{33} behave more stiffly. The dielectric constant is highest for the VPP fibres, close to the bulk material value. Other fibre types display values approximately 80% of the bulk value. The difference in these values could be attributed to microstructure and/or composition, both of which will be examined in Chapter 6.

Both Figure 3.15 and Figure 3.16 show a clear difference exists between the properties of the two Alceru fibres. The larger diameter fibre has a significantly lower piezoelectric activity, making it a more compliant fibre under open-circuit conditions. Electro–mechanical coupling in the larger diameter fibre is approximately 12% lower than the smaller diameter fibre. The dielectric constant is also lower for the larger diameter fibre. Reasons for this difference will be examined in Chapter 6.

In comparing the fibres it is clear that the VPP fibre exhibits the highest level of piezoelectric activity, suggesting it is the most suitable fibre for incorporation into AFCs. However, other factors, such as the fibre properties under high electric fields (E = 2.0 kV mm^{-1}), must be considered before a final choice can be made.

3.7 Chapter Summary

This chapter has presented methods for manufacturing 1-3 composites with a large range of volume fractions. Composites manufactured using the larger diameter Alceru fibres, which spanned the volume fraction range $0.02 < v_f < 0.72$, were characterised using conventional techniques to measure key material properties. The matrix material's Young's modulus, glass transition temperature and dielectric constant were also evaluated using conventional techniques. Measurements of the effective composite properties, together with knowledge of the matrix properties, enabled comparison of experimental results with analytically predicted trends. Generally, the experimental results were shown to fit well. However, when extracting fibre properties from low volume fraction composites (typically $v_f < 0.2$) large deviations from expected results were seen. This was attributed to experimental and measurement error (the small number of fibres and low signals obtained) and analytical model failure (deviation from the iso-strain assumption), which were more pronounced in these low volume fraction regimes.

With the limits of the analytical model verified it was then possible to calculate fibre properties with confidence, using high v_f composites to minimise errors.

A range of commercially available fibres were selected for characterisation, all of which would be suitable for incorporation into AFC devices. Manufacturing only high v_f 1-3 composites ensured accurate fibre results could be obtained. The piezoelectric, dielectric and mechanical properties of fibres, extracted from measurements made the composites, revealed important information about the different fibres. The extruded and Alceru 250 μm fibres showed the lowest piezoelectric activity. A large difference was observed between the properties of the two Alceru fibres, with the smaller diameter fibre exhibiting superior properties. The reason for this difference is not known, but is thought to be attributed to microstructure and compositional differences. The VPP fibres exhibited the highest piezoelectric activity, exceeding that of bulk PZT, suggesting that fibres produced by this method are the most suitable for incorporation into AFCs. However, the fibre properties under high driving fields are perhaps more important in an AFC device. This will form the focus of the following two chapters.

CHAPTER 4

HIGH FIELD FIBRE PROPERTIES – MODELLING

4.1 Introduction

The dielectric, elastic and piezoelectric coefficients of piezoelectric ceramics are known to be non-linear,[72] being influenced by the applied electric field strength and applied stress. Since AFC actuators will operate in the high field regime to generate maximum strains, it is important to have an understanding of the active fibre properties under these conditions. Typically two responses are measured for piezoelectric materials operating as actuators, these are:

(i) strain-field responses, and

(ii) polarisation-field responses.

Both of these responses were introduced and discussed in Chapter 1, Figure 1.8 and Figure 1.9.

Analysis of the strain-field response gives an indication of the level of actuation the material is able to achieve. Due to material non-linearities, one cannot rely on the low field *d*-coefficient (strain per unit applied field) to predict the strain response of a piezoelectric under high fields. For a soft composition PZT, like 5A or 5H, the strain developed under an increasing electric field is highly non-linear, even at moderate electric fields (0.1 kV mm^{-1}). In fact, even though PZT-5A has a lower d_{33} coefficient than PZT-5H, it develops higher strains under high field conditions. This was the basis for selecting a PZT-5A composition fibre for the role of the AFC actuator material.

Analysis of the polarisation-field response allows predictions of the material's power consumption, which can aid in the design of power and control electronics. Knowledge of power consumption can also be used to calculate heat dissipation rates, which may be a critical factor if the composite is to be incorporated into a laminate structure as an active ply. Consideration must be given to thermal dissipation rates to minimise thermal stresses and reduce the risk of interfacial deterioration, which may lead to delamination.

The importance of characterising the strain and polarisation response of the fibres under high fields is now clearly apparent. However, as for the low field properties, the small diameters and

fragile nature of fibres makes measurements on single fibres difficult. Hence this chapter focuses on developing methods for extracting the high field response of the fibres from measured 1-3 composite responses.

This chapter begins by deriving equations that predict the strain-field and polarisation-field response of 1-3 composites in terms of the fibre and matrix properties, and their volume fractions. Two possible factors could cause the composite's responses to deviate from the model predictions, resulting in incorrect calculations of the fibre properties. These are:

(i) non-linear material properties, and

(ii) deviation from the iso-strain assumption of the model.

The effects of non-linear material properties are considered within the analysis of the derived analytical model equations. The effect of deviation from the iso-strain assumption is considered in a separate section, in which finite element modelling is used to predict errors introduced into strain and polarisation measurements.

4.2 Analytical Modelling

By developing analytical models for 1-3 composites suitable for the high field regime, it becomes possible to extract the high field fibre responses from measurements made on the composites. Fibre properties of particular interest are the strain-field response in the 3-direction, and the polarisation-field response in the 3-direction. Since it is uncommon to use 1-3 composites in the high field regime, models describing their high field behaviour do not exist. To enable equations for these two responses to be derived the 2D models presented in Figure 4.1 will be used.

Figure 4.1 illustrates two possible strain responses of a 1-3 composite subjected to an electric field in the 3-direction. Figure 4.1(a) depicts the response for a composite in which the fibres are unconstrained by the matrix, while Figure 4.1(b) depicts the response for a composite in which the fibres are well bonded to the matrix.

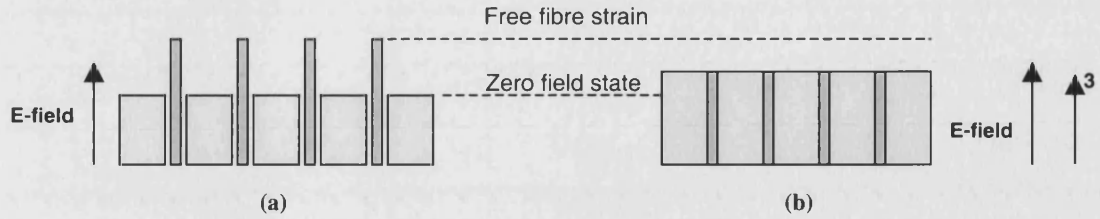

Figure 4.1: The model representation of a 1-3 composite subjected to an electric field where (a) the fibres are unconstrained and develop the full free fibre strain. This is in contrast to (b) in which the fibre and matrix are well bonded and the strains are identical, but lower than the free fibre strain.

In the un-bonded model the fibres develop the full free fibre strain. In the bonded model the fibre and matrix strain is identical (the iso-strain assumption), but the passive matrix restrains the active fibres, reducing their strain compared to the free fibre strain. In the following sections equations are derived for the strain and polarisation responses, making reference to Figure 4.1. The influence of deviation from the iso-strain assumption will be discussed later in Section 4.3.

4.2.1 Strain response

Analytical equation derivation

Consider the model in Figure 4.1(a) in which the fibre and matrix are not bonded, and are independent of each other. When subjected to an electric field in the 3-direction the fibre strain is purely piezoelectric. It is this piezoelectric strain, $S_3^{f\,piezo}$, which needs to be determined if we wish to calculate fibre properties from composite strain measurements. The matrix piezoelectric strain is zero since it is a passive polymer that exhibits no piezoelectric behaviour.

Now we consider the case when these two phases are perfectly bonded and combined into a 1-3 composite, as shown in Figure 4.1(b). It is assumed that the strain of the fibre and the matrix, S_3^f and S_3^m respectively, are identical and equal the composite strain, $\overline{S}_3$ (the iso-strain assumption). This is represented by:

$$S_3^f = S_3^m = \overline{S}_3 \tag{4.1}$$

The fibre strain in the composite (S_3^f) is a combination of the piezoelectric strain of the free fibre (S_3^{fpiezo}) and the restraining mechanical strain (S_3^{fmech}), imposed by the passive matrix, acting on the fibre. This can be expressed as:

$$S_3^f = S_3^{fpiezo} + S_3^{fmech} \tag{4.2}$$

This shows that to calculate the piezoelectric strain of the fibres both the mechanical strain and the composite strain must be known (since $S_3^f = \bar{S}_3$). The composite strain will be determined by experimentation, while the restraining mechanical strain can be determined in the following manner.

It is necessary to firstly calculate the force introduced into the matrix (F_3^m) by the fibres extending under an applied field. This can be defined as the stress in the matrix (T_3^m) multiplied by the area of the matrix (A^m) and can be expressed as:

$$F_3^m = A^m T_3^m = \frac{A^m \bar{S}_3}{s_{11}} \tag{4.3}$$

where s_{11} is the matrix compliance. The force on the fibres (F_3^f) is equal and opposite to the force in the matrix:

$$F_3^f = -F_3^m = -\frac{A^m \bar{S}_3}{s_{11}} \tag{4.4}$$

which induces a mechanical strain in the fibres of:

$$S_3^{fmech} = \frac{F_3^f s_{33}^E}{A^f} \tag{4.5}$$

In which A^f and s_{33}^E are the fibre area and short circuit compliance respectively. Substituting Equation (4.4) for F_3^f gives the mechanical strain in the fibres as:

$$S_3^{fmech} = -\frac{A^m \bar{S}_3 s_{33}^E}{A^f s_{11}} \tag{4.6}$$

Since the ratio of the matrix area to the fibre area is identical to the ratio of their volume fractions, Equation (4.6) can be written as:

$$S_3^{fmech} = -\bar{S}_3 \frac{(1-v_f)s_{33}^E}{v_f s_{11}} \tag{4.7}$$

Substituting this into Equation (4.2) allows the fibre piezoelectric strain to be expressed as:

$$S_3^{fpiezo} = \bar{S}_3 \left[1 + \frac{(1-v_f)s_{33}^E}{v_f s_{11}}\right] \tag{4.8}$$

Equation (4.8) allows the fibre piezoelectric strain to be evaluated by measuring the composite strain, provided the compliance and volume fraction of each phase are known. By rearranging this equation it is possible to express the composite strain as a function of the fibres' free strain (S_3^{fpiezo}) and a clamping reduction due to the matrix (Equation (4.9)).

$$\bar{S}_3 = \underbrace{S_3^{fpiezo}}_{\text{Free Fibre Strain}} \underbrace{\left[\frac{v_f s_{11}}{v_f s_{11} + (1-v_f)s_{33}^E}\right]}_{\text{Clamping Factor}} \tag{4.9}$$

Equation (4.9) can be obtained by multiplying the analytical expression for 1-3 composites d_{33} (strain per unit applied field), developed by Smith,[76] by the electric field.

Predicted trends

The percentage of the fibres' piezoelectric strain that is clamped by the matrix, predicted by Equation (4.8), is presented in Figure 4.2(a) as a function of fibre volume fraction.

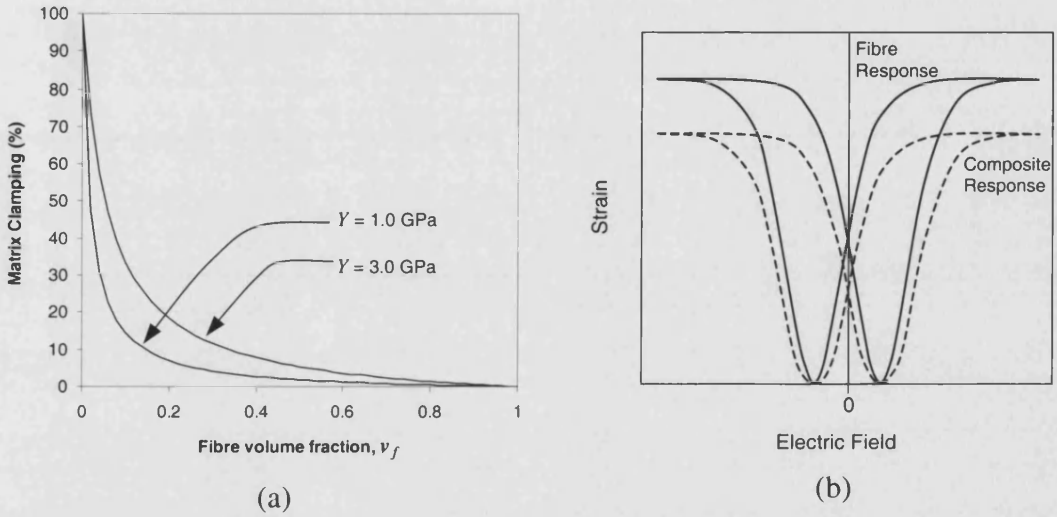

Figure 4.2: (a) The strain developed in a 1-3 composite subjected to an applied field normalised by the free fibre strain. Results are presented for two matrix stiffnesses as a function of fibre volume fraction. (b) A schematic high field response of a fibre, and the response of a composite with v_f = 0.2 and Y = 3 GPa (composite strain is approximately 80% of fibre strain).

Figure 4.2(a) shows that as v_f tends to zero there is full clamping of the fibre strain by the passive matrix. As the fibre volume fraction increases the degree of clamping is reduced until at $v_f = 1$ there is no clamping, and the composite strain equals the fibre strain. The effect of matrix Young's modulus reveals that the strain of the fibres is more heavily clamped when the matrix is a stiffer polymer. Since the fibres are much stiffer than the matrix the degree of clamping is relatively small, and the fibre strain reduces approximately by only 7% or 18% for a matrix stiffness of 1.0 GPa and 3.0 GPa respectively at $v_f = 0.2$.

Figure 4.2(b) presents a schematic high field strain response of a 1-3 composite with a fibre volume fraction of 0.2 and a matrix with a stiffness of 3.0 GPa (dashed line). It has already been predicted that such a composite exhibits an 18% reduction from the free fibre strain.

Using Equation (4.8) the free fibre strain response can be obtained simply by multiplying the strain at each electric field value by the factor:

$$\left[1+\frac{(1-v_f)s_{33}^E}{v_f s_{11}}\right] \tag{4.10}$$

This 'free fibre' response is shown in Figure 4.2(b) as a solid line.

This methodology allows us to measure the strain-field characteristics of a composite and determine the strain-field response of the fibres. However, it is possible that non-linear material properties of the fibres, and deviation from the models iso-strain assumption, may introduce inaccuracies into the predicted fibre responses. The influences of non-linear material properties are now discussed.

Effect of material non-linearities

The only parameter in Equation (4.8) that is non-linear, and could therefore lead to inaccuracies in the calculated fibre strain response, is the short circuit stiffness of the fibres, s_{33}^E. Figure 4.3 depicts qualitatively what happens in a PZT ceramic under a compressive load applied parallel to the poling direction. At small loads, the compressive strain depends linearly on stress (A-B). With increasing stress, domain switching occurs; domains with their polarisation directions aligned with the applied stress switch by 90°. This causes additional strain (B-C) until all domains have switched, after which linear behaviour occurs again (C-D). The point of inflection is defined as the coercive stress, T_{coer}.

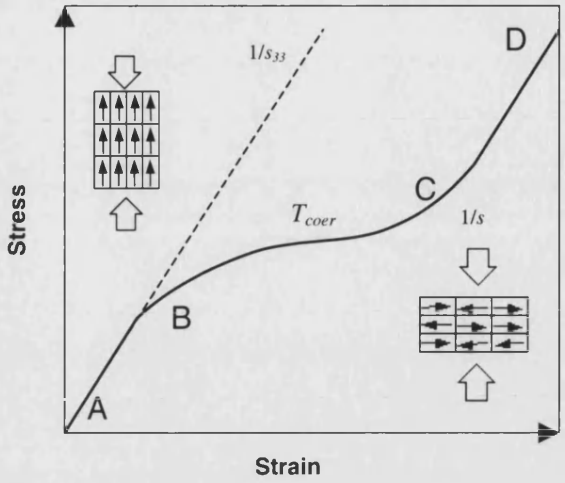

Figure 4.3: Schematic strain response under uni-axial stress parallel to the poling direction (A-B, linear behaviour before domain switching; B-C, domain switching; C-D, linear behaviour after domain switching. After Schäufele and Härdtl. [81]

It has been reported that soft PZT compositions display linear stress-strain behaviour up to approximately 20 MPa, and have a coercive stress of approximately 50 MPa.[81] Application of an electric field helps to maintain the original domain alignment, and raises the coercive stress (coercive stress value rises linearly from 50 MPa at zero applied field to approximately 125 MPa under an applied electric field of 2.0 kV mm^{-1} in the poling direction).[81] To determine if the compliance of the fibres in 1-3 composites will enter the non-linear regime it is necessary to determine the level of compressive stress, exerted from restraining force of the polymer matrix, they experience. Figure 4.4 shows this stress level, which has been calculated using Equation (4.7), for composite strains of 500, 1000 and 2000 ppm. These are typical strain levels developed in composites subjected to electric fields reaching 2.0 kV mm^{-1}.

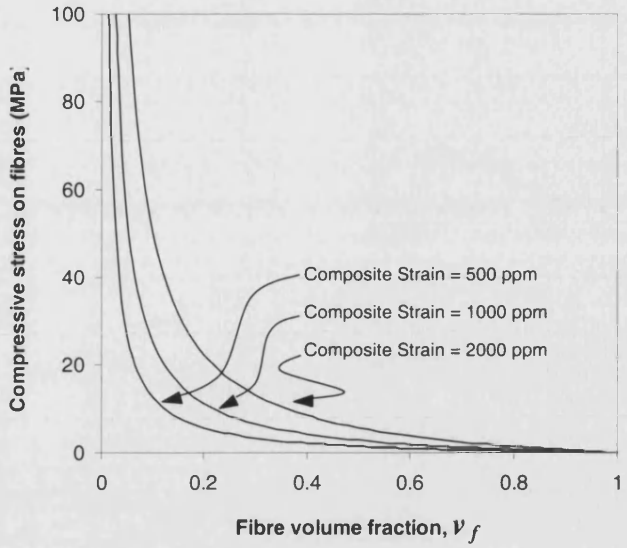

Figure 4.4: Compressive stress in the fibres of a 1-3 composite as a function of fibre volume fraction, for composite strains of 500, 1000, and 2000 ppm.

Figure 4.4 shows that the level of stress experienced by the fibres increases as the volume fraction is reduced. This is because at low volume fractions a larger restraining force is exerted by the passive matrix. The figure also shows that stress levels in the fibres rise as the composite strain is increased, as would be expected. It has already been stated that to enter the non-linear regime the fibres must be under a compressive stress of 20 MPa at zero applied field, increasing 2.5 times to approximately 50 MPa under an applied electric field of 2.0 kV mm^{-1} in the poling direction. Examination of Figure 4.4 shows that the mechanical restraining force will only exceed this stress level at the lowest volume fractions ($v_f < 0.10$).

From this analysis it can be concluded that non-linear effects will introduce negligible errors into the extracted fibre strain response if the fibre volume fraction is kept above 0.1. This result is supported by a non-linear FE study into depolarisation of fibres during poling of 1-3 composites.[82]

4.2.2 Polarisation response

Analytical equation derivation

The application of an electric field to a material causes a shift in the electron cloud and, in polar materials, dipoles are caused to align. This volume polarisation is offset by charges that collect on the surface. Polarisation is described as the surface charge that exactly cancels the volume charge, and has units of coulombs per square meter (C m^{-2}). For a 1-3 composite, in which two materials are present, each material contributes to the total polarisation in an amount proportional to their dielectric constants, and volume fractions. If it is assumed that the electric field in the 3-direction is the same in both phases, and the fibres are unconstrained by the matrix (Figure 4.1(a)) it is possible to express the composites polarisation in the 3-direction ($\overline{P}_3$) as:

$$\overline{P}_3 = v_f P_3^f + (1 - v_f) P_3^m \tag{4.11}$$

in which P_3^f and P_3^m are the polarisation of the ceramic fibre and polymer matrix in the 3-direction, and v_f is the fibre volume fraction. If this model is extended to encompass the situation in which the fibre and matrix are perfectly bonded, and strains in the 3-direction are identical (Figure 4.1(b)), an additional charge is developed from the ceramic fibres via their d_{33} effect. This clamping charge (Q^{clamp}) contributes to the overall polarisation and Equation (4.11) becomes:

$$\overline{P}_3 = v_f P_3^f + (1 - v_f) P_3^m + Q_3^{clamp} \tag{4.12}$$

Equation (4.11) shows that to calculate the fibre polarisation the fibre volume fraction, composite polarisation, matrix polarisation, and the charge generated via active fibre clamping must all be known. The composite polarisation ($\overline{P}_3$) and fibre volume fraction (v_f) will be determined by experimentation. The matrix polarisation (P_3^m) can be calculated from linear dielectrics as the product of the dielectric constant (ε_{11}) and electric field in the 3-direction (E_3):

$$P_3^m = \varepsilon_{11} E_3 \tag{4.13}$$

The charge generated from active fibre clamping can be calculated as follows.

It has previously been shown (Equation (4.4)) that the force acting on the fibres due to clamping by the passive matrix is:

$$F_3^f = -\frac{(1-v_f)\bar{S}_3}{s_{11}} \tag{4.14}$$

Substituting this force into the following definition of the fibres' d_{33} coefficient:

$$d_{33} = \left(\frac{D_3}{T_3^f}\right)_E = \left(\frac{Q_3}{F_3^f}\right)_E \tag{4.15}$$

allows the charge developed to be expressed as:

$$Q_3^{clamp} = -d_{33}\frac{(1-v_f)\bar{S}_3}{s_{11}} \tag{4.16}$$

Equation (4.16) shows that to calculate the clamping charge it is necessary to have knowledge of the composite strain response. If the strain response of the composite is known then substituting Equations (4.13) and (4.16) into (4.12) gives the composite polarisation to be:

$$\bar{P}_3 = \underbrace{[v_f P_3^f]}_{\text{Fibre contribution}} + \underbrace{[(1-v_f)\varepsilon_{11}E_3]}_{\text{Matrix contribution}} - \underbrace{\left[d_{33}\frac{(1-v_f)\bar{S}_3}{s_{11}}\right]}_{\text{Clamping contribution}} \tag{4.17}$$

If the strain response of the composite ($\bar{S}_3$) is unknown it can be calculated using Equation (4.9), where:

$$S_3^{f_{piezo}} = d_{33}E_3 \tag{4.18}$$

This gives:

$$\overline{S}_3 = d_{33}E_3\left[\frac{v_f s_{11}}{v_f s_{11} + (1-v_f)s_{33}^E}\right] \tag{4.19}$$

Substituting Equation (4.19) into Equation (4.17) the polarisation response then becomes:

$$\overline{P}_3 = \underbrace{[v_f P_3^f]}_{\text{Fibre contribution}} + \underbrace{[(1-v_f)\varepsilon_{11}E_3]}_{\text{Matrix contribution}} - \underbrace{\left[\frac{v_f(1-v_f)(d_{33})^2 E_3}{v_f s_{11} + (1-v_f)s_{33}^E}\right]}_{\text{Clamping contribution}} \tag{4.20}$$

Equation (4.20) can be obtained by multiplying the analytical expression for 1-3 composite permitivity, developed by Smith,[76] by the electric field. Rearranging Equation (4.20) to make the fibres' polarisation response (P_3^f) the subject gives:

$$P_3^f = \frac{1}{v_f}\left[\overline{P}_3 - \underbrace{[(1-v_f)\varepsilon_{11}E_3]}_{\text{Matrix contribution}} + \underbrace{\left[\frac{v_f(1-v_f)(d_{33})^2 E_3}{v_f s_{11} + (1-v_f)s_{33}^E}\right]}_{\text{Clamping contribution}}\right] \tag{4.21}$$

Equation (4.21) allows the fibre polarisation response to be evaluated from the 1-3 composite response, provided the volume fraction and stiffness of each phase, the matrix permitivity, and the fibre d_{33} are known.

Predicted trends

Equation (4.21) clearly shows that to calculate the fibre polarisation level at a given electric field level the contributions from the matrix and the active fibre clamping must be subtracted from the measured composite response. This value must then be divided by the fibre volume fraction. A typical high field polarisation response of a 1-3 composite is represented by the broken line presented in Figure 4.5. The composite comprises 20% fibres with PZT-5A properties, in a matrix with a Young's modulus of 3.0 GPa. Using these material properties together with Equation (4.21) it is possible to calculate the response of the fibres (P_3^f). This is shown in Figure 4.5 as a solid line.

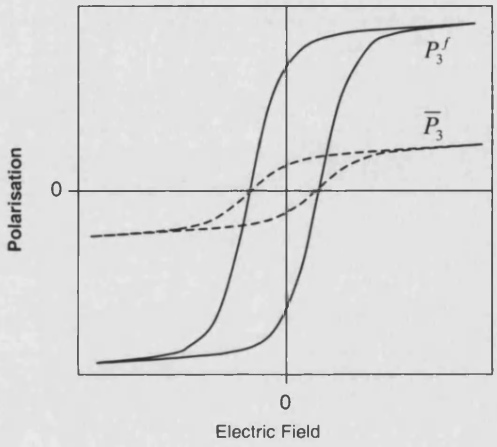

Figure 4.5: A schematic high field polarisation response of a composite with v_f = 0.2 (broken line) and the response of the fibre (solid line) extracted using Equation (4.21). The composite polarisation is approximately 20% of fibre polarisation.

Since the composite has a fibre volume fraction of 0.2 it exhibits approximately 20% of the free fibre polarisation, as predicted by Equation (4.21). However, it is possible that non-linear material properties of the fibres and deviation from the models iso-strain assumption may introduce inaccuracies into the calculated fibre response. The influences of non-linear material properties are now discussed.

Effect of material non-linearities

Equation (4.21) shows that to calculate the fibre polarisation, the matrix contribution and clamping contribution must be accounted for. The dielectric constant of the polymer matrix is assumed to remain constant with electric field, hence this contribution can be calculated accurately. The clamping contribution, resulting from the active fibres being clamped by the

polymer matrix, is influenced by two material properties that are known to be non-linear; d_{33} is non-linear with applied field, and we have already seen that s_{33}^{E} is non-linear with applied stress. Therefore, the 'clamping contribution' term of Equation (4.21) could introduce significant errors into the predicted fibre response.

The s_{33}^{E} coefficient is likely to exhibit linear elastic behaviour over the field levels to be encountered for all but the lowest volume fractions ($v_f < 0.1$), as has already been discussed in Section 4.2.1, and will therefore introduce negligible errors. This is not the case for the non-linear d_{33} coefficient.

The d_{33} coefficient in soft piezoelectrics is well known to be dependant upon the electric field and applied stress,[72] hence the charge developed by clamping will be a function of these parameters. It has been shown that the d_{33} coefficient of soft PZT increases linearly by approximately 25% under an applied stress of 7 MPa[83], and at relatively high electric fields it is not uncommon for the d_{33} coefficient of a soft PZT to increase by 300% of its quoted low field value (600 pC N^{-1} at zero field raising to 2000 pC N^{-1} at fields of 0.5 kV mm^{-1}).[72] Using the low field value of d_{33} in Equations (4.17) or (4.20) to calculate the charge developed may therefore introduce significant errors into the predicted polarisation response at high fields. Figure 4.6 quantifies the error by plotting the contribution to the composite polarisation ($\overline{P}$) arising from fibre clamping (P^{clamp}), as a function of fibre volume fraction for increasing values of fibre d_{33}.

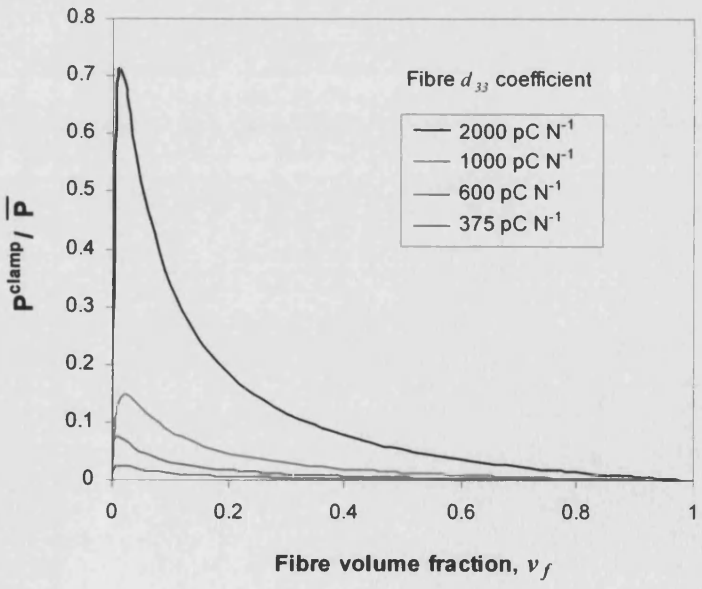

Figure 4.6: Contribution to the total polarisation of a 1-3 composite from fibre clamping (for four different d_{33} coefficients) as a function of fibre volume fraction.

Figure 4.6 shows that at high fibre volume fractions, in which the matrix exerts very little restraining force on the fibres, the contribution to the total polarisation from clamping is small. As the fibre volume fraction is reduced the matrix begins to exert a stronger clamping effect, and the contribution is seen to increase. A maximum contribution is achieved in composites comprising approximately 2% fibres. On reducing the volume fraction below 2% the fibre clamping continues to increase, but the area of fibre from which the charge is generated decreases such that the overall contribution from the clamping effect diminishes.

The effect of the fibre d_{33} coefficient is also shown in Figure 4.6 to highlight the effect of high fields and mechanical stress, which can easily cause the d_{33} to reach 2000 pC N^{-1}. Increasing the fibre d_{33} significantly increases the level of charge generated from fibre clamping. This is especially noticeable at low volume fractions, where fibre clamping is high. If it is assumed the fibre d_{33} remains at its low field value of 375 pC N^{-1} then significant errors could be introduced into the predicted response (polarisations predicted using Equation (4.21) would be under-estimated). The degree of under-estimation will increase as the fibre d_{33} increases, and as fibre volume fractions are reduced. Where the polarisation is strongly affected by the fibre d_{33}, such as at low volume fractions, knowledge of d_{33} as a function of electric field and stress is required for accurate determination of the fibre polarisation response. For samples with high volume fractions the polarisation developed from fibre clamping is small, and less affected by the fibre d_{33}. For high volume fraction composites (v_f = 0.75) estimating the fibre polarisation response using the low field value of d_{33} in Equation (4.21) will introduce minimal errors (a maximum of 5% at field levels where d_{33} is maximum).

In summary, to maximise accuracy in predicted fibre responses it is advisable to test composites with as high a fibre volume fraction as is possible. In such composites the contribution to the total polarisation is dominated by the fibre polarisation; the contribution from fibre clamping, and associated errors, are minimised.

To summarise the findings of the strain and polarisation analysis, it has been shown that the fibre strain-field response is unlikely to be affected by material non-linearities since the fibre s_{33}^{E} coefficient will remain linear in composites with all but the lowest fibre volume fractions. However, the fibre polarisation-field response is strongly influenced by non-linear properties, particularly the non-linear nature of the fibres' d_{33}.

An additional consideration is the validity of the iso-strain assumption on which the analytical model equations are based. If the composite response deviates from this assumption, further errors will be introduced into the calculated fibre response. Analysis of this assumption, and its effect on the strain and polarisation of 1-3 composites, forms the focus of the following section.

4.3 Validity of the Iso-Strain Assumption

In the derivation of both the strain and the polarisation equations it is assumed that the composite behaves as a homogeneous medium, with the strain in the fibre and matrix being identical in the 3-direction (Figure 4.1). In reality, it is likely that the composites will respond as shown in Figure 4.7, which depicts a composite extending and contracting under an applied field. The figure also shows the analytical model predicted iso-strain response as a broken line.

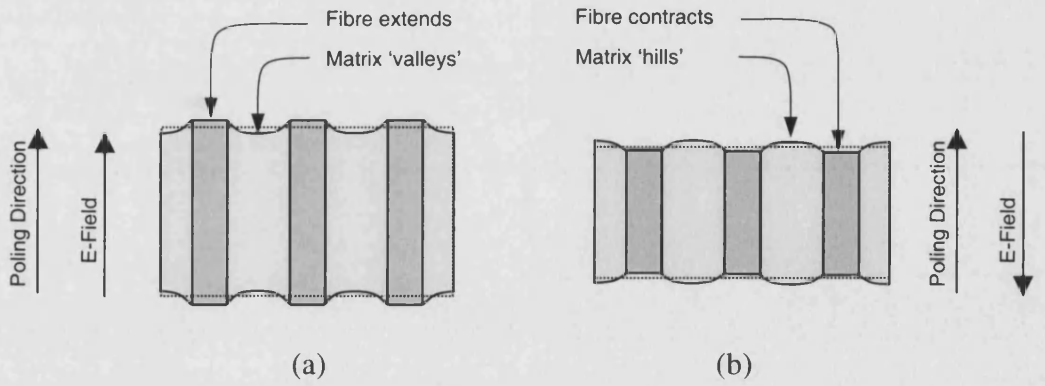

Figure 4.7: Schematic 2D representation of a 1-3 composite surface profile not conforming to the iso-strain assumption. When a voltage is applied the fibres either (a) extend or (b) contract depending on field direction. The broken lines represent the analytical model iso-strain predictions.

If the iso-strain assumption is not satisfied, fibre strains and polarisations extracted from measurements made on composites will differ from the true fibre response. The percentage error will depend on the extent to which the iso-strain assumption has been violated.

Figure 4.7(a) shows that when the composite extends under the influence of an applied field, the active fibres extend from the passive matrix. In this case, composite strains measured using surface contact techniques, as used in this thesis, will exceed the level predicted by the analytical model. In the second situation, Figure 4.7(b), in which a field is applied causing the composite to contract, the fibres contract to a greater degree than the matrix, leaving the matrix sitting proud. In this case, composite strains measured using surface contact techniques will be lower than model predictions.

The composite's polarisation will also be affected by deviation from the iso-strain assumption; incomplete stress transfer from the matrix to the fibres, at both positive and negative fields, will reduce the charge generated via the fibres' d_{33} effect. The 'clamping contribution' (Equation (4.21)) will be lower than analytical model predictions, leading to over-estimated fibre polarisations at both positive and negative fields.

The amount of deviation from the iso-strain model response will depend upon three main factors. In general the composite will approach the iso-strain assumption as:

(i) matrix stiffness increases,

(ii) fibre aspect ratio decreases (towards long thin fibres),

(iii) fibre volume fraction increases.

To perform a detailed experimental analysis of the interaction of these factors would be a difficult and time-consuming task. Finite element methods allow errors associated with these effects to be predicted in a more efficient manner. However, before relying on finite element results it is necessary to experimentally determine if the FE technique is capable of predicting composite surface profiles as a function of the above parameters. A simple confirmation test, which can be easily modelled and measured, is the surface displacement profile of a single fibre in a matrix, subjected to a static electric field. The FE technique can be validated by comparing the modelled surface profile to the profile measured experimentally using surface profilometry. The FE technique can then be used with confidence to predict the errors associated with the actual 1-3 composites being tested. Experimental validation of the finite element method forms the next section.

4.3.1 Validation of the finite element method

A simple experimental composite was compared to FE prediction to determine the ability of FE analysis to predict surface profiles of 1-3 composites. This section comprises both the experimental and FE modelling work, together with a comparison of the results obtained from both methods.

Experimental

Prior to casting into the polymer matrix material, a single PZT-5A rod, manufactured using the Viscous Plastic Process (VPP) technique,[29] was poled at 2.25 kV mm^{-1} at 100 °C. The poled rod, 0.7 mm in diameter and 10 mm in length, was positioned in soft pliable modelling clay such that the majority of the fibre was free from the clay, and extended vertically. The rod was surrounded by a cylindrical mould, which was infiltrated with a low viscosity epoxy resin (Struers Specifix-40) until the fibre was fully covered. This stage was performed under vacuum to reduce trapped voids. After curing for 12 hours at 40 °C the composite was removed from

the mould. Both ends of the composite were cut in a plane perpendicular to the long axis of the rod, such that the sample had the appearance of that presented in Figure 4.8. To enable accurate surface profile measurements to be made, one end of the composite was polished using a MOTOPOL 12 automated polishing machine (BUEHLER UK Ltd., Coventry, England). The sample surface was polished with progressively finer diamond suspensions, with the final stage using a 0.05 μm grade alumina polishing suspension. A thin gold electrode was sputter coated onto the polished face, while air dried silver paint was used to electrode the base.

Composite surface profiles were measured on the polished face using a non-contact surface profilomiter with a resolution of 0.01 μm in the *y*-direction (Proscan 2000, Scantron Industrial Products Ltd., Somerset, England). The surface profilometer consists of an *x*-*y* scanning stage onto which the sample is positioned, and a displacement measuring probe fixed in the *z*-direction. White light is passed down the probe and split into its constituent wavelengths over a 300 μm range. A sample placed within this 300 μm measuring range will reflect light back into the probe, the wavelength of which is determined by the sample position in the 300 μm range. A spectrometer analyses the wavelength of reflected light and calculates a relative distance from the probe. By rastering the *x*-*y* stage it is then possible to build up a 3-D surface profile of the sample surface. To measure the surface profiles of the single rod sample under the influence of an applied field, the sample was positioned on a support ring so the active central portion was free from any surface contact. The support ring and sample assembly were then positioned on a levelling stage, allowing the surface of the composite to be brought perpendicular to the measurement probe, reducing measurement errors. An initial surface profile scan was made with a 2.0 μm step size in the *x*-direction with no field applied. The scan was repeated with a field of 2.0 kV mm^{-1} applied to the sample. Applying the high voltage to the sample's base ensured that the risk of arcing to the displacement probe was minimised. Subtraction of the initial scan from the final scan yielded the field induced surface profile. The experimental set-up is shown schematically in Figure 4.8.

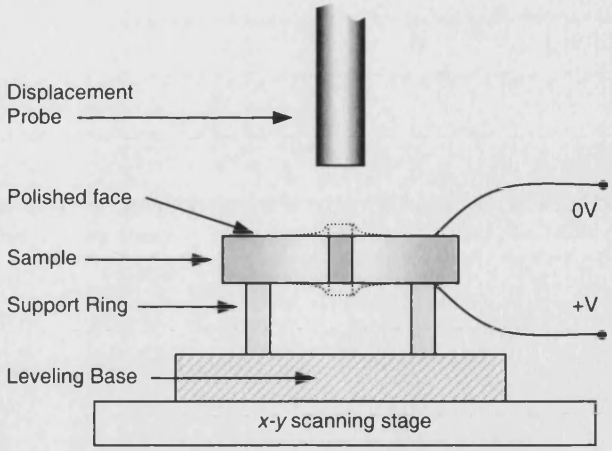

Figure 4.8: Schematic set-up for measurement of the surface profile of a single piezoelectric fibre embedded in a polymer matrix subjected to a static voltage.

The fibre aspect ratio (AR), defined by diameter/length, was incrementally increased from 0.125 to 1.0 by using a polishing wheel to remove the required amount of material from the sample's base. For each aspect ratio the base electrode was re-applied, and the scanning process repeated. The sample was left for 24 hours between measurements to reduce errors associated with aging. The surface profile results of this analysis were compared to profiles predicted by finite element analysis, the procedure for which is now introduced.

Finite element modelling

FE analysis was used to model the effect of fibre aspect ratio on the surface displacement profile for a single piezoelectric fibre surrounded by a passive polymer matrix. Since the structure has geometric symmetry about a centre axis (the fibre long axis) it can be modelled as an axisymmetric structure in equivalent 2-D form. The full 3-D model is shown in Figure 4.9(a) with the 2-D axisymmetric representation in Figure 4.9(b). The modelled representative volume element (RVE), depicted in Figure 4.9(b), is shown in Figure 4.9(c) with appropriate dimensions.

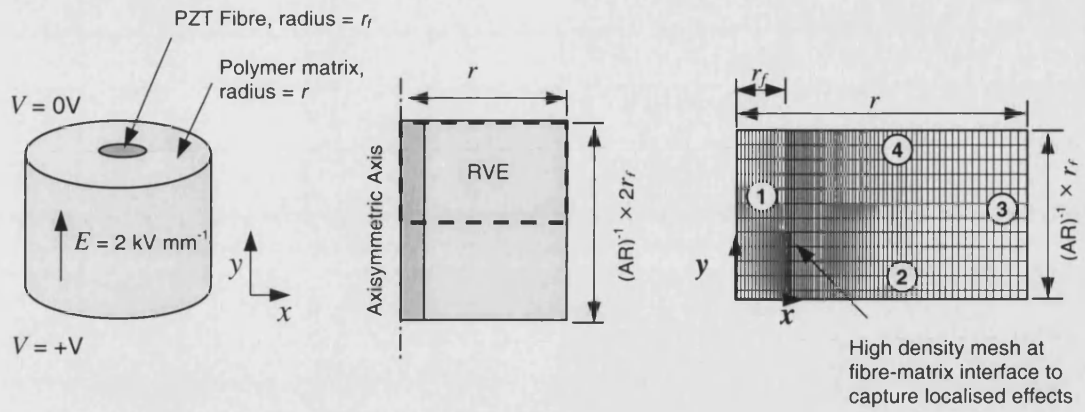

(a) (b) (c)

Figure 4.9: (a) 3-D representation of a fibre embedded in a matrix and (b) the axisymmetric 2-D representation with appropriate dimensions and showing the representative volume element and (c) the RVE with a typical finite element mesh and appropriate dimensions. Boundaries are numbered for defining boundary conditions.

The structure was modelled with the fibre long axis aligned with the *y*-axis (the centre of symmetry). The model was meshed with 2-D coupled-field axisymmetric elements with piezoelectric capability (PLANE 13 4-node quadilateral). The mesh was constructed as shown in Figure 4.9(c) with a fine mesh at the fibre-matrix interface to capture localised effects. The fibre was modelled as PZT-5A poled in the +*y* direction (material properties located in Appendix A2) and the matrix as an isotropic solid with a Young's modulus of 2.8 GPa, a Poisson's ratio of 0.38, and a relative dielectric constant of 5.0. The interface between the fibre and matrix was assumed to be perfect. Appropriate mechanical and electrical boundary conditions are shown in Table 4.1.

Table 4.1: Boundary conditions of displacement (U), electrical potential (*V*) and electrical displacement (D) applied to the RVE.

Surface Number	Mechanical Conditions	Electrical Conditions
1	Axisymmetric symmetry axis $U_x = 0$	$D_x = 0$
2	Symmetry ($U_y = 0$)	V = +V/2
3	Free	$D_y = 0$
4	Free	V = 0 V

The potential difference was set such that the field in the fibre was constant at 2.0 kV mm^{-1}. The model was then solved and the resultant surface displacement was recorded. The fibre aspect ratio was varied from 1 to 0.05 by varying the thickness of the modelled composite.

Results and discussion

Results of the finite element analysis are presented in Figure 4.10, which shows the surface displacement profiles for a single rod surrounded by an epoxy matrix versus the radial distance, r, from the fibre centre (where r_f is the fibre radius). Profiles are shown for fibre aspect ratios ranging from 1.0 to 0.05. The strain in this figure has been normalised by the free fibre strain.

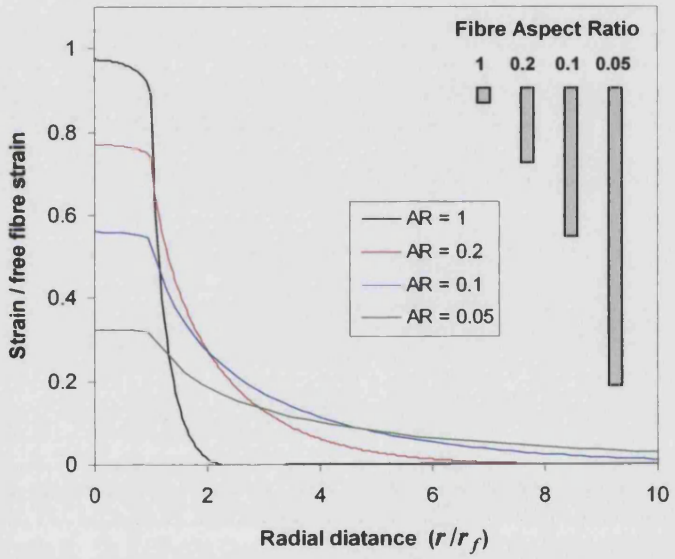

Figure 4.10: Finite element results of the surface profile of a single fibre embedded in an epoxy matrix as a function of fibre aspect ratio (electric field is 2.0 kV mm^{-1})

At high aspect ratios (short fibres), for example AR = 1.0, the fibre constraint by the matrix is minimal and the fibre achieves over 95% of the free fibre strain. The matrix strain diminishes sharply with increasing distance from the fibre (r), and reaches zero strain at a distance of just over one fibre radius from the fibre-matrix interface. This displacement profile is highly non-uniform. In contrast, at low fibre aspect ratios (long fibres), for example AR = 0.05, the matrix has a more significant constraining effect on the fibre. For this composite the fibre only achieves approximately 32% of the free fibre strain. In contrast with high AR composites, the matrix strain decrease to zero is attained over a much larger distance (> $10 \times r_f$). In this test we are not concerned with developing the greatest strain, but in observing the nature of the surface

profile, which becomes increasingly uniform as AR reduces, towards long thin fibres. It is now necessary to compare these findings with the profiles measured experimentally.

Experimental surface profile plots obtained from a sample with a rod aspect ratio of 0.2 are presented in Figure 4.11. This figure contains two profiles; one from the sample under zero applied field (Figure 4.11(a)), and another from the sample under an applied field of 2.0 kV mm^{-1} (Figure 4.11(b)).

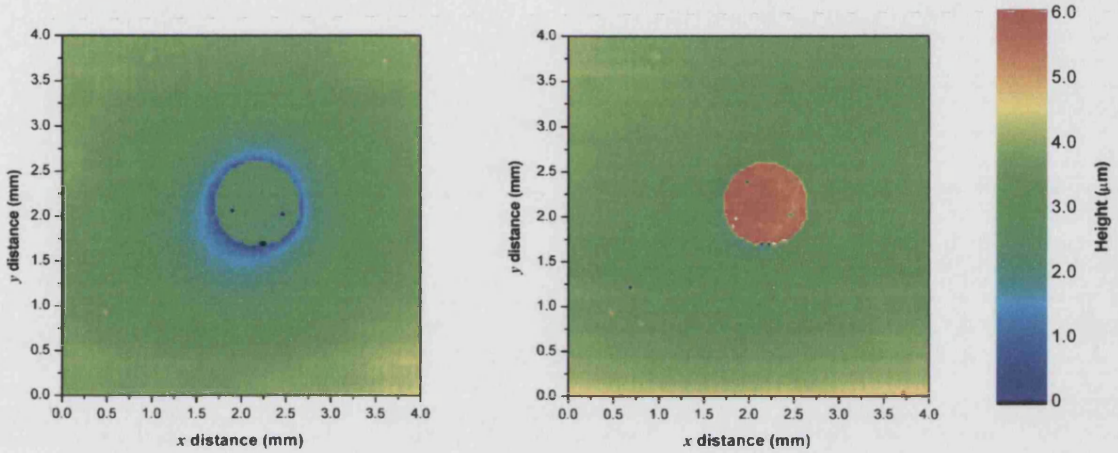

Figure 4.11: The surface profiles of a PZT rod surrounded by a polymer matrix subjected to (a) zero field and (b) 2.0 kV mm^{-1}. Rod aspect ratio is approximately 0.2.

Observation of the zero field profile reveals that the sample height at the fibre-matrix interface is approximately 3 μm lower than the bulk of the fibre and the matrix. This is thought to be associated with preferential polishing or de-bonding at the fibre–matrix interface resulting from the polishing process. Figure 4.11(b) shows very clearly the ceramic rod has extended in height compared to the zero field state, while the passive matrix remains at the same level. By subtracting the zero field profile from the applied field profile, the profile generated due to the applied field is obtained, and is shown in Figure 4.12.

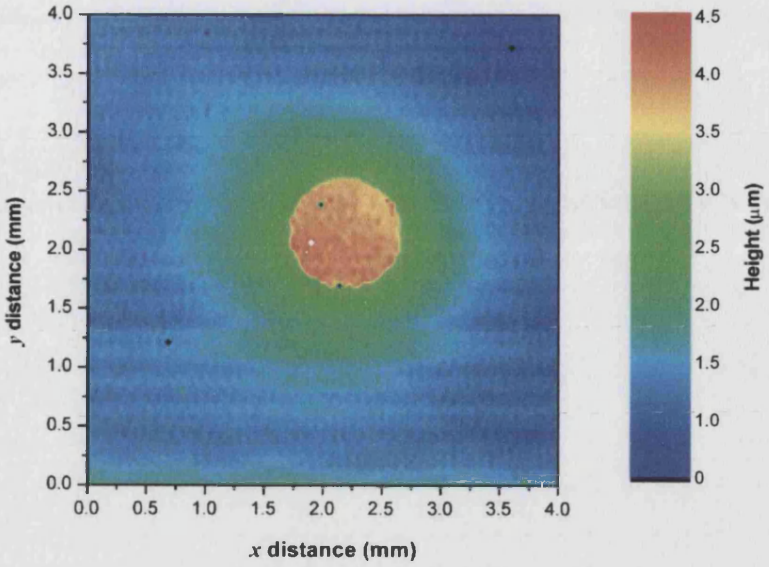

Figure 4.12: Profile scan remaining after the subtraction of the zero field profile from the 2.0 kV mm^{-1} profile (Figure 4.11(b) minus Figure 4.11(a)).

Figure 4.12 shows the field induced profile is axisymmetric, as would be expected, and the fibre extends approximately 4.5 μm from the matrix. This profile is shown in 3-D in Figure 4.13 to give an indication of the rate of decline of displacement from the fibre to matrix.

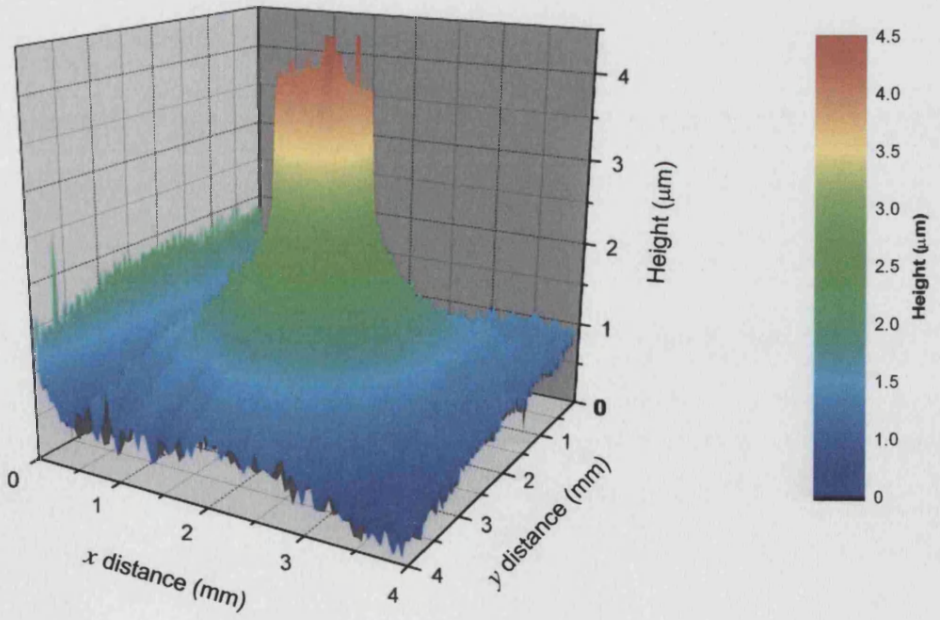

Figure 4.13: 3D representation of the profile scan presented in Figure 4.12.

With the proven axisymmetric behaviour it is now only necessary to perform a line profile scan. This allows the scan time to be reduced significantly, and direct comparison with the FE model results is possible.

Figure 4.14 contains the experimental results for the surface displacement profile for three fibre aspect ratios (1.0, 0.2 and 0.125) taken along a line extending from the fibre centre. Finite element results relating to these aspect ratios are overlaid for comparative purposes.

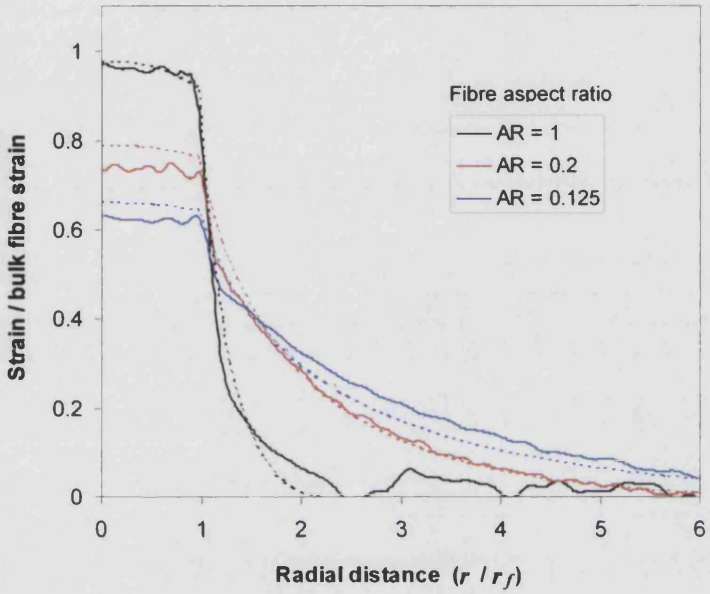

Figure 4.14: Experimental surface displacement profiles (solid lines) for a range of fibre aspect ratios under an applied field of 2.0 kV mm^{-1}. FEA predictions (broken lines) are shown for comparison to model predicted behaviour.

These results show that the FE analysis accurately predicts the experimentally measured response of a 1-3 composite, and the effect of fibre aspect ratio on the displacement profile is clearly distinguishable. Fibres with a high AR achieve a high strain, but exhibit a highly non-uniform displacement profile, while low AR fibres develop a more uniform surface profile.

Results from this section show that FE modelling accurately predicts the response of a simple 1-3 composite subjected to a static voltage. Confidence can now be placed in the 3-D modelling used to predict the influence of aspect ratio and fibre volume fraction on strain and polarisation responses. The FE modelling used to investigate these effects is now described.

4.3.2 Finite element modelling of 1-3 composite strain and polarisation

Model dimensions

Deviation from the iso-strain assumption increases as the fibre aspect ratio is increased (towards short fibres), the matrix becomes softer, and fibre volume fraction is reduced. Since all 1-3 composites are nominally the same length and are manufactured with the same matrix material, composites comprising the larger diameter fibres (250 μm) will exhibit the maximum deviation (since these fibres will possess the largest aspect ratio). To capture the 'worst case scenario' the finite element model was constructed with a fibre aspect ratio of 0.05, representing a composite 5.0 mm long comprising the larger 250 μm diameter fibres.

Finite element methodology

The FE model developed is similar to the model used in Chapter 2, and is shown below in Figure 4.15. The 'representative volume element' or RVE is shown in 2D in Figure 4.15(a). The 3D model geometry, and a typical FE mesh, is shown in Figure 4.15(b) for a fibre volume fraction of 0.5. The model extends 2.5 mm in the minus z-direction, and the faces are numbered to allow reference to be made when describing applied boundary conditions. Faces opposite 1, 2, and 3 are numbered 1a, 2a and 3a respectively.

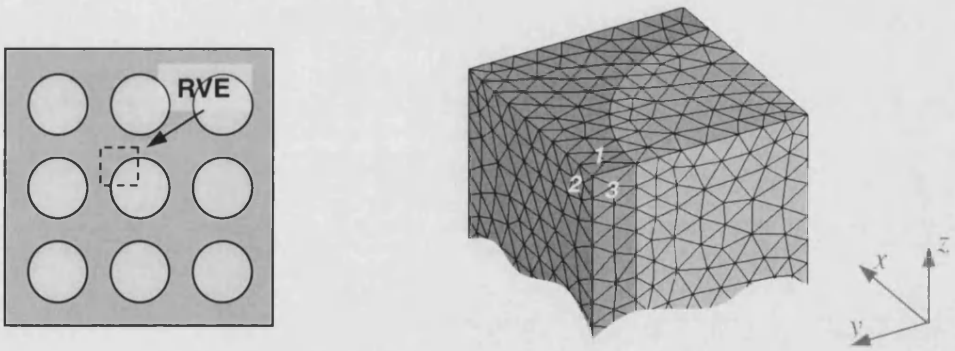

(a) (b)

Figure 4.15: (a) 2D view showing the 1-3 composite representative volume element. The 3D meshed model of the RVE is shown in (b) with numbered faces to facilitate boundary condition references.

Boundary conditions are applied to simulate experimental testing conditions. Faces 1(a), 2(a) and 3 have symmetry boundary conditions applied. The nodes on faces 1, 2 and 3(a) are mechanically free, representing a freedom to displace in any direction. The nodes on the top and bottom faces, 1 and 1(a) respectively, have their voltage degree of freedom coupled so they

respond as equi-potential electroded surfaces. The voltage of the base is grounded (V = 0), while a positive or negative voltage of 1000 V is applied to the top electrode to induce an electric field, and a corresponding extension or contraction of the composite, as required. This information is summarised in Table 4.2.

Table 4.2: Boundary conditions of displacement (U), electrical potential (V) and electrical displacement (D) applied to the RVE.

Surface Number	Mechanical Conditions	Electrical Conditions
1	Free	$V = 0$ V
1a	Symmetry ($U_z = 0$)	V = +1000 V (or -1000 V) (E = + or - 0.4 kVmm^{-1})
2	Free	$D_y = 0$
2a	Symmetry ($U_y = 0$)	$D_y = 0$
3	Symmetry ($U_x = 0$)	$D_x = 0$
3a	Free	$D_x = 0$

The matrix properties were those measured for Specifix-40, and the fibre properties were set to be PZT-5A poled in the 3 or z-direction. The fibre volume fraction of the model was varied, the model solved, and the polarisation and displacement response determined. The strain was calculated using the displacement data obtained from the top electroded surface. The polarisation (charge per unit area) was calculated by measuring the charge generated on the top electrode, and dividing by the electrode surface area. The results of this analysis are now presented.

Results and discussion

Strain deviation

Figure 4.16 shows three dimensional displacement profiles of the top surface of a solved model with a volume fraction of 0.4 and AR of 0.05. The model has been expanded from the ¼ model constructed (Figure 4.15) to show the entire fibre and surrounding matrix. Figure 4.16(a) shows that an electric field applied in the poling direction causes the active fibre to extend from the

matrix material. Figure 4.16(b) shows that fields applied against the poling direction cause the fibre to contract, leaving the matrix sitting proud, as would be expected from the schematic representation presented in Figure 4.7.

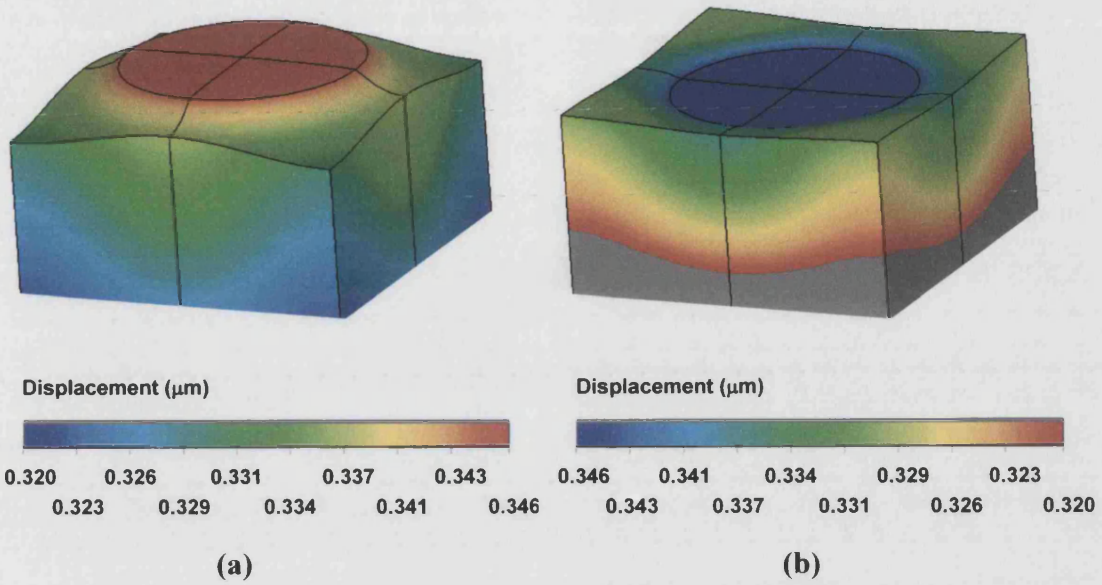

Figure 4.16: Displacement profiles of a 1-3 composite volume element subjected to (a) 0.4 kV mm^{-1} in the poling direction and (b) 0.4 kV mm^{-1} against the poling direction. Fibre volume fraction = 0.4. Aspect ratio = 0.05. Displacements magnified.

Quantification of the surface strain is critical, allowing errors introduced into strain measurements arising from the non-uniform surface profile to be evaluated. Figure 4.17 shows results from the solved models, presented as strain profiles at the composite surface. To aid visualisation, the results have been translated to create a profile that spans three fibres, and the fibres have been shaded. The profiles are plotted along a line drawn between opposite diagonals of the models presented in Figure 4.16. Figure 4.17(a) is the profile developed due to active fibre extension while Figure 4.17(b) is the profile resulting from active fibre contraction. The analytical model prediction is represented by the broken black line.

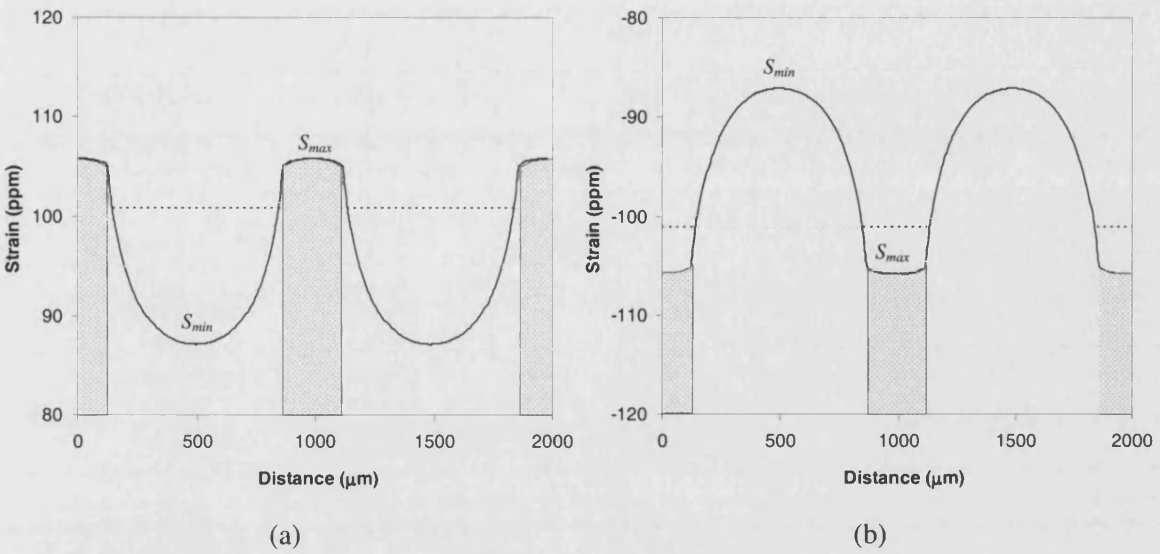

Figure 4.17: Surface strain profiles of a 1-3 composite with a fibre volume fraction of 0.1 subjected to (a) +0.4 kV mm^{-1} and (b) –0.4 kV mm^{-1}. The broken black line is the analytical model prediction.

In experimental 1-3 composite testing the strain will be measured using a surface contact technique. Since the spatial scale of the composite is small compared with the contact made on the composite surface (such as the case in Figure 2.4), the strain will always be measured from the portion of the composite surface exhibiting maximum extension (or minimum contraction if the field is reversed). Figure 4.17(a) shows that under active fibre extension the strain measured by surface contact techniques will be S_{max}. This is greater than the iso-strain prediction (the broken line) and is a result of active fibres protruding from the composite surface. However, Figure 4.17(b) shows that under active fibre contraction the strain as measured by surface contact techniques will be S_{min}. This is less than the analytical model prediction (the broken line) and is a result of the matrix sitting proud of the fibres, which are themselves drawn into the composite.

It is apparent from studying the graphs in Figure 4.17(a) and (b) that the profile developed during active fibre contraction is simply a mirror image of the profile developed under active fibre extension. The reflection line is the x-axis at zero strain. However, the reflection symmetry exhibited by the two profiles does not imply that the deviation from the analytical model is the same for contraction as it is for extension. For extension, the deviation in strain from analytical predictions can be defined as:

$$\%Deviation = \left(\frac{S_{max}}{\bar{S}_3} - 1 \right) \times 100\% \tag{4.22}$$

While for contraction the deviation is defined as:

$$\%Deviation = \left(\frac{S_{min}}{\bar{S}_3} - 1 \right) \times 100\% \tag{4.23}$$

For a cyclic electrical field with no DC offset the total deviation will be the sum of these two deviations, giving:

$$\%Total\ \ Deviation = \left(\frac{S_{max} + S_{min}}{\bar{S}_3} - 2 \right) \times 100\% \tag{4.24}$$

The results obtained from using these three equations with the finite element results are plotted in Figure 4.18 as a function of fibre volume fraction.

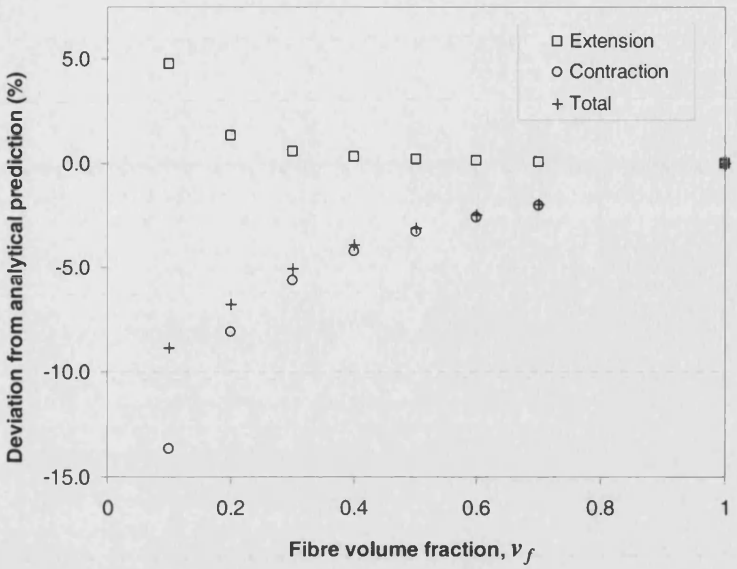

Figure 4.18: The deviation in composite strain from analytical model predications as predicted by finite element analysis. Fibre aspect ratio is 0.05.

The results presented in Figure 4.18 shows that deviations from the analytical model predictions increase as the fibre volume fraction is reduced. Under active fibre extension errors are small (less than 1.4% for composites with $v_f > 0.2$, and less than 0.2% for $v_f > 0.5$). Under active fibre contraction errors are larger, ranging from 8% at $v_f = 0.2$, to 2% at $v_f = 0.7$. The sum of the errors resulting from fibre extension and contraction produces a trend, shown in Figure 4.18 as 'Total', in which the overall strain level is lower than predicted by the analytical model. This is based on a cyclic field symmetrical about the zero field producing equal fibre extension and contraction. The deviation from the analytical model increases as the fibre volume fraction is reduced. For example, a composite with fibre volume fraction of 0.7 comprising fibres with an aspect ratio of 0.05 (250 μm in diameter and 5.0 mm in length) tested under a cyclic field will be measured as having a peak to peak strain approximately 2.0% lower than predicted by the analytical model. The peak-to-peak strain is approximately 9% lower than predicted if the composites volume fraction is reduced to 0.1. It is clear that high volume fractions composites are required to minimise these errors.

The effect of non-uniform surface profiles on a measured strain-field response is shown schematically in Figure 4.19.

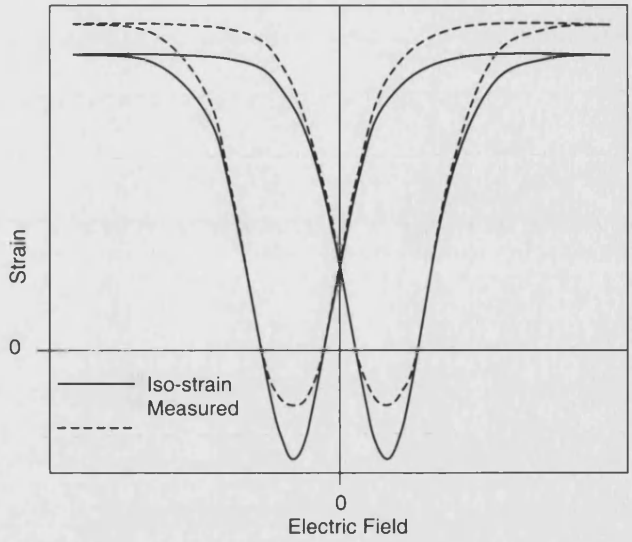

Figure 4.19: A schematic high field strain-field response of a 1-3 composite. Shown are the 'iso - strain' model prediction, and the 'measured' response of a composite not satisfying this assumption.

In this figure positive strains are measured greater than the iso-strain prediction while negative strains are measured less than the iso-strain prediction. The strain during composite contraction deviates more than the strain during composite extension. It has been shown that the composite strain response is unlikely to be affected by the non-linear nature of the fibres' s_{33}^{E} compliance term (Figure 4.4, Section 4.2.1). The errors in the strain response can therefore be considered as originating solely from the analytical model's iso-strain assumption, and can be minimised by testing high volume fraction composites.

The effect of the non-uniform strain profile on the polarisation response is now examined.

Polarisation deviation

The potential errors in calculating fibre polarisations from the analytical model arise from failing to predict the clamping contribution accurately. This can be due to non-linear material properties, such as we have seen with the d_{33} coefficient, or due to invalid model assumptions. It is the latter that is the focus of this section. The non-uniform displacement profiles developed as fibres extend and contract under an applied field is clearly a violation of the iso-strain assumption. The ability of the fibres to displace in this manner implies that they are not experiencing the full restraining force of the passive matrix. The contribution to the polarisation arising from the clamping contribution is now reduced and the composite generates a larger

polarisation than predicted by the analytical model. The analytical model now over-estimates the extracted fibre polarisation response.

Figure 4.20(a), (b) and (c) shows the stress distribution in three solved FE models with fibre volume fractions of 0.2, 0.4 and 0.7 respectively. The model has been subjected to an applied field of 0.4 kV mm^{-1}, causing the piezoelectric fibre to extend. The stress distribution arises from the inactive polymer matrix restraining the extension of the active fibres. The ¼ representation allows the internal stress distributions within the fibre and matrix to be seen.

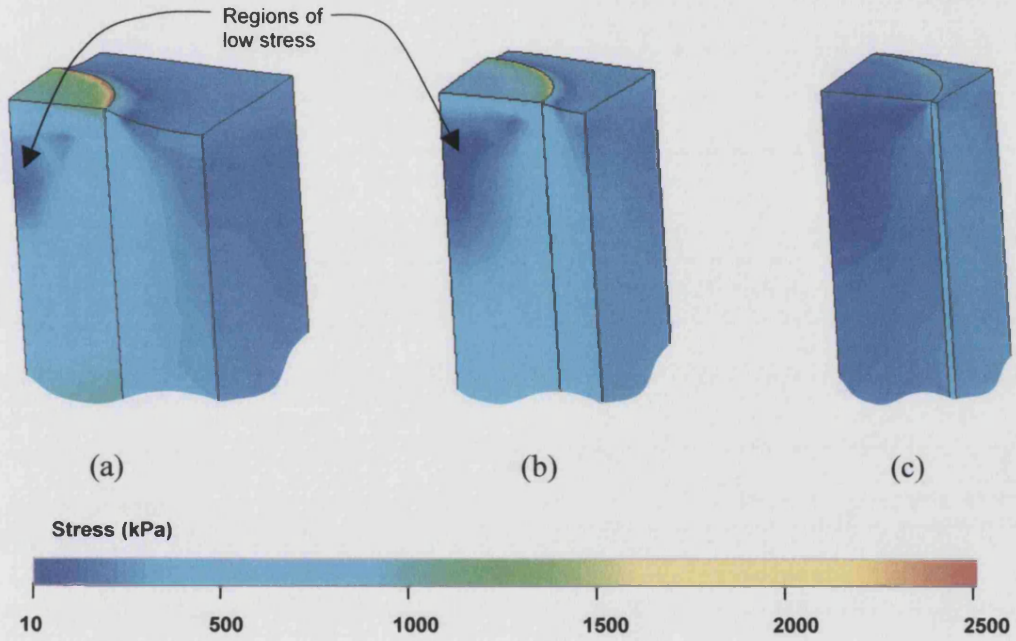

Figure 4.20: Von-Mises' stress distributions in a representative volume elements of 1-3 composites with volume fractions of (a) 0.2 (b) 0.4 and (c) 0.7, subjected to a field of 0.4 kV mm^{-1} in the poling direction. Displacements magnified.

Figure 4.20 reveals that as the fibre volume fraction is increased the stress in the fibre is reduced. This is because as the fibre volume fraction increases, the proportion of matrix acting to clamp the fibre reduces. It is also apparent from the figure that the stress distributions within the fibres is not uniform. Immediately below the fibre surface the stress level is lower than observed in the bulk fibre, as indicated in the figure. The charge developed from the fibre d_{33} is now lower than predicted. The figure also shows that at low fibre volume fractions the stress distribution becomes more inhomogeneous. Therefore, deviation from the predicted response is likely to be larger for low volume fraction composites.

Using the analytical model prediction of the composite polarisation $\overline{P_3}$ (Equation (4.20)), and the polarisation measured from the finite element analysis, P_3^{FEA}, the deviation in composite polarisation from analytical predictions can be defined as:

$$\%Deviation = \left(\frac{P_s^{FEA}}{\overline{P_3}} - 1 \right) \times 100\% \tag{4.25}$$

The graph in Figure 4.21 presents the results of this analysis.

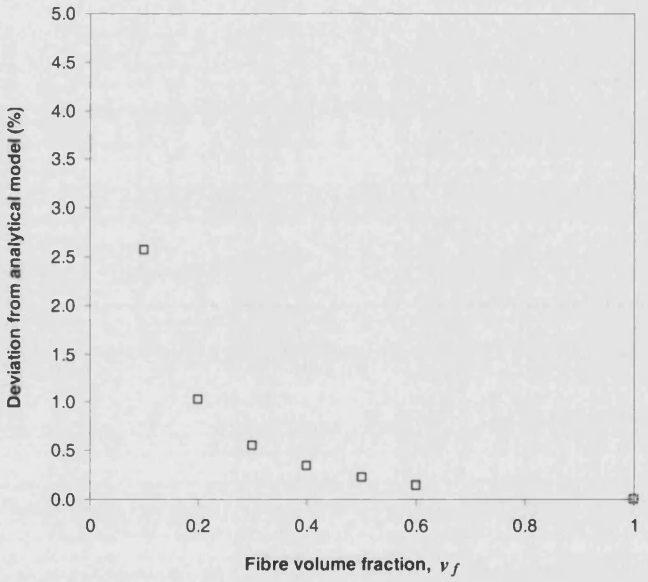

Figure 4.21: The deviation in composite polarisation from analytical model calculations as predicted by finite element analysis. Fibre aspect ratio is 0.05.

Figure 4.21 shows that, as predicted, the polarisation developed from 1-3 composites in the FE model is larger than the polarisation predicted by the analytical model. Unlike the strain, the magnitude of this effect is identical in fibre extension and contraction. Polarisation values determined from composites using the analytical model will be over-predicted if the composite does not conform to the iso-strain assumption. The percentage over-prediction will increase as the composite volume fraction reduces. However, the percentage deviations in the polarisation response are small, even at low volume fractions; at fibre volume fractions as low as 0.1 the composite develops only approximately 2.5% more polarisation than predicted by the analytical model. At fibre volume fractions greater than 30% this effect introduces errors of less than

0.5%. Thus errors from violation of the analytical models iso-strain assumption can be ignored for all but the very low volume fractions.

A schematic polarisation-field response is shown in Figure 4.22, showing the analytical models iso-strain prediction (solid line), and the 'true' measured response of a composite in which fibres extend from, and draw into, the polymer matrix, increasing the polarisation developed.

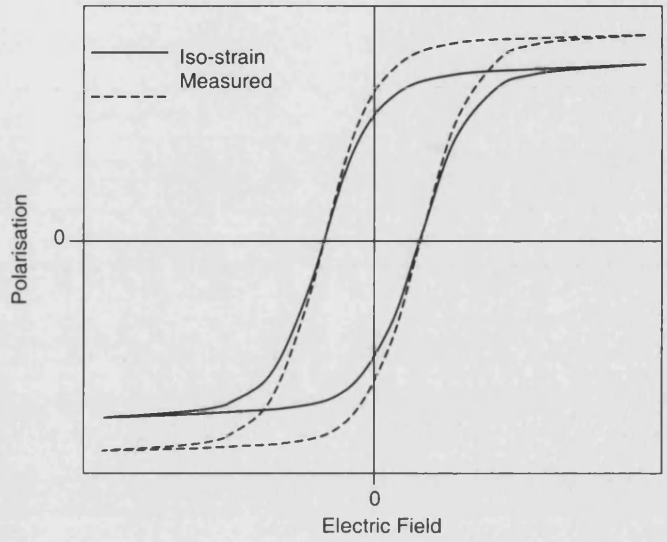

Figure 4.22: A schematic high field polarisation-field response of a 1-3 composite. Shown are the 'iso -strain' model prediction, and the 'measured' response of a composite not satisfying this assumption. The difference is exaggerated.

In this figure both positive and negative polarisations of the measured response are larger than the iso-strain prediction, although the figure exaggerates the magnitude to allow the effect to be visualised. Since the coercive field is a measurement at zero strain, at which there can be no contribution from fibre clamping, its value will remain unchanged.

Errors in the composite polarisation response associated with the iso-strain deviation are much smaller than those attributed to non-linear d_{33} effects. Because of this, the overall composite polarisation will be dominated by the non-linear d_{33} effect, resulting in composite polarisations that are lower than analytical model predictions. Thus fibre polarisation responses extracted from 1-3 composites are likely to be under-estimated.

4.4 Chapter Summary

This chapter has developed analytical models that can be used to extract the high field strain and polarisation response of fibres from measurements made on 1-3 composites. Deviation from the analytical model predictions of strain-field and polarisation-field responses were identified as resulting from non-linear material properties and deviation from the iso-strain condition. The effect of non-linear material properties was examined empirically by investigating the analytical model equations, while the effect of deviation from the iso-strain condition was examined using finite element analysis. The ability of the finite element technique to predict the response of 1-3 composites was validated by comparing experimentally measured surface profiles, developed from a single fibre embedded in a polymer matrix, to finite element predictions. The finite element method was then extended to investigate the effect of the iso-strain assumption on the strain-field and polarisation-field response of 1-3 composites with varying fibre volume fractions.

It was shown that the stress levels likely to be experienced by the fibres due to matrix clamping are insufficient to cause the s_{33}^{E} coefficient of the fibres to enter the non-linear regime. Using the low field value of stiffness in the analytical model equation will therefore introduce negligible errors into the predicted strain response of the fibres. Violation of the iso-strain assumption could however cause potentially significant errors to be introduced into the composite's strain response. Finite element results show active fibres protruding from, and drawing into the passive matrix during electrical cycling. This has the effect of reducing the composite strain compared to analytical model predictions. Fibre strains extracted from 1-3 composite responses are therefore under-estimated.

The polarisation of 1-3 composites was shown to be less affected by deviation from the iso-strain assumption, and more influenced by the non-linear nature of the fibres' d_{33} coefficient. Finite element analysis revealed that deviation from the iso-strain assumption causes 1-3 composites to develop a higher level of polarisation than predicted by the analytical models. This is because incomplete transfer of stress from the matrix to the fibres reduces the contribution to polarisation arising from active fibre clamping. The over-estimation of composite polarisation arising from this effect is small; less than 1% for composites comprising more than 20% fibres. In contrast to the strain response, the polarisation response was shown to be strongly influenced by non-linear material properties. The increase in d_{33} at high fields increases the charge developed by active fibre clamping, and fibre polarisations calculated using the analytical model will be under-estimated. At low volume factions, where fibre clamping is high, non-linearity has most effect.

The non-linear fibre d_{33} therefore dominates the polarisation errors, while errors in the strain response are dominated by deviation from the iso-strain assumption.

It was shown that as fibre volume fractions increase, composite responses tend towards the iso-strain assumption, and also become less influenced by the non-linear material properties. Therefore, fibre properties extracted from high volume fraction composites are more representative of the actual fibre response. These effects will be examined in the following chapter in which experimental results are compared to the analytical model predictions.

CHAPTER 5

HIGH FIELD FIBRE PROPERTIES – EXPERIMENTAL

5.1 Introduction

Chapter 4 developed analytical models to allow calculation of the high field strain and polarisation response of piezoelectric fibres from measurements made on 1-3 composites. This chapter aims to identify the accuracy of the models using experimental results, and to use them to compare the responses of fibres produced using four manufacturing methods. Through quantifying the strain and polarisation of the different fibre types, their suitability for incorporation into AFC devices is discussed. This chapter is divided into three main sections; measurement techniques, analytical model validation, and fibre comparison.

The first section of this chapter describes the measurement techniques employed to characterise the strain-field and polarisation-field response of 1-3 composites. The second section assesses the magnitude of errors in composite responses. It is possible that the influence of material non-linearity and the iso-strain assumption discussed in Chapter 4, which have a greater influence at low volume fractions, may place a lower limit on the fibre volume fraction of composites from which reliable and accurate fibre responses can be extracted. Having determined the range over which the analytical models are most valid it is possible to calculate fibre response from 1-3 composites with confidence. The final section in this chapter uses the models to calculate the high field response of a number of fibre types, each being produced by a different manufacturing technique. These high field properties complement the low field properties measured in Chapter 3, and allow comparisons to be made between the fibre types. The results also aid in the selection of the best fibre for incorporation into an AFC device, the manufacture of which is described in Chapter 8.

5.2 Strain and Polarisation Testing of 1-3 Composites

The ability to measure the strain and polarisation accurately is important for determining the actuation level and power consumption of the active fibres. This section describes the strain and polarisation testing performed on 1-3 composites, which was conducted using a system developed by the National Physical Laboratory.

5.2.1 Polarisation-strain-field (P-S-E) system

Composite strain-field (*S-E*) and polarisation-field (*P-E*) responses were measured simultaneously using a system designed at the National Physical Laboratory, Teddington, UK.[84] The sample holder rig of this system is shown in Figure 5.1.

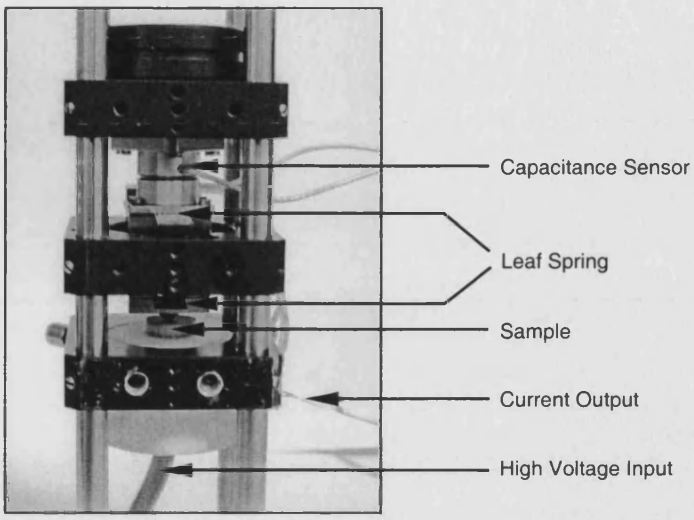

Figure 5.1: The NPL polarisation-strain-field measurement system (sample holder and capacitance sensor). The sample is approximately 10 mm diameter.

The software control and analysis for the system is achieved through a series of LabView routines. For the acquisition of *P-E* and *S-E* loops, a voltage is generated by a function generator under computer control, which is then passed through a high voltage amplifier. The amplified waveform output is sent to the sample while the monitor output is sent to a data acquisition card in the control computer to record the voltage applied to the sample. The sample strain is measured using a capacitance sensor which is mechanically linked to the sample surface via a leaf spring, as shown in Figure 5.1. The sensor's capacitance is inversely proportional to, and varies linearly with the separation of the plate. The output from this sensor is similarly sent to the data acquisition card on the control computer. The final measurement concerns the polarisation state of the material. The system measures and amplifies the current flowing through the sample, which is subsequently converted to a voltage and sent to the data acquisition card. The polarisation state of the sample is determined from the current data in the following manner:

The surface charge (Q) stored by the test sample at any time (t) is calculated by numeric integration of the current data (I).

$$Q(t) = \int_{t_1}^{t_2} I dt \tag{5.1}$$

The electrical displacement (D) is calculated as the surface charge density:

$$D(t) = \frac{Q(t)}{A} \tag{5.2}$$

where A is the specimen surface area.

The electrical displacement is related to the polarisation (P) through

$$D(t) = P(t) + \varepsilon_0 E(t) \tag{5.3}$$

and so

$$P(t) = D(t) - \varepsilon_0 E(t) \tag{5.4}$$

The three channels of data (voltage, current and strain) are analysed by the LabView software routines to produce polarisation-field and strain-field responses. A schematic representation of this set up is shown in Figure 5.2.

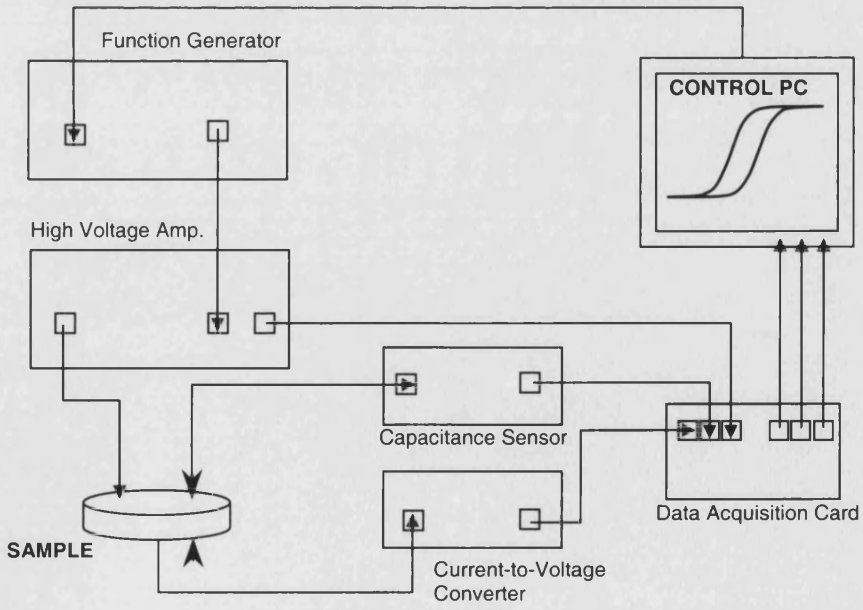

Figure 5.2: Schematic of the NPL P-S-E loop system

5.2.2 Test parameters

To perform a test the sample was positioned in the test rig shown in Figure 5.1, which was subsequently immersed in oil to prevent electrical breakdown at high field levels. Two electrical field cycles were applied to each sample, which can be described as:

(i) Saturation Cycle

(ii) Operational Cycle

The 'saturation cycle' involved applying a 1 Hz sinusoidal voltage of ±2 kV mm^{-1} to the samples. This field was strong enough to cause complete domain reorientation, and allowed measurement of the coercive field, saturation strain and saturation polarisation of the composites. However, piezoelectric actuators are not operated with fields strong enough to cause domain reversal because of the large amounts of power consumed in such a cycle, which can lead to excessive heating and deterioration of the piezoelectric elements.

For this reason the 'operational cycle' was defined, simulating typical fields the fibres will be exposed to in operational environments. Strain and polarisation results can be used to assess the level of strain and power consumption likely to be experienced in actuator operation. It has been shown that an operational cycle of $2\times E_c$ in the direction of poling to $0.75\times E_c$ against the poling direction induces maximum strains whilst minimising the hysteresis developed in the polarisation response.[85] Typical coercive fields for PZT-5A are in the region of 1 kV mm^{-1}; thus the operational cycle was set to be a 1 Hz sinusoidal voltage of +2.0 kV mm^{-1} to –0.75 kV mm^{-1}. Both the saturation cycle and operational cycle field waveforms are shown in Figure 5.3.

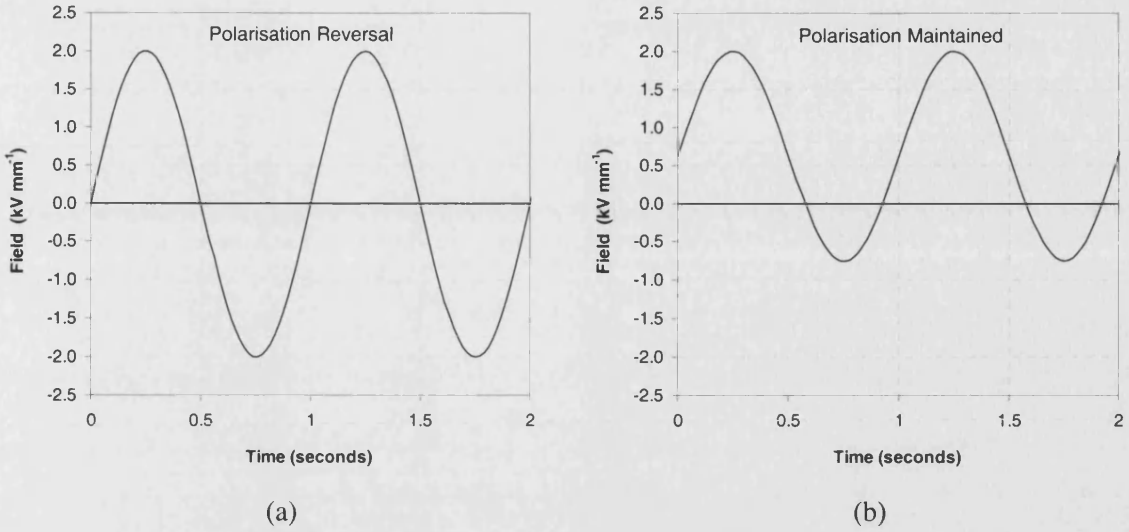

(a) (b)

Figure 5.3: Graphs showing field-time plots for (a) the saturation cycle and (b) the operational cycle

The results obtained from this analysis can now be used to assess the volume fraction range over which the analytical models, developed in Chapter 4, are most accurate.

5.3 Comparison of Experimental Data with the Analytical Model

Results from composites comprising the Alceru-250 fibres, which were manufactured for the low field analysis in Chapter 3, are used in this section to assess the high field analytical models. The fibre volume fraction of these composites ranges from 0.02 to 0.72, allowing examination over a large volume fraction range. Both the strain and the polarisation analytical equations are assessed for their accuracy by using the saturation cycle and the operational cycle composite responses. The results are presented in the following sections.

5.3.1 Strain response of 1-3 composites

Saturation strain response

Figure 5.4 plots the strain response of the Alceru-250 composites at three different fibre volume fractions subjected to the saturation cycle. The figure shows that all composites display the typical butterfly loop behaviour, characteristic of a piezoelectric being driven at fields greater than the coercive field with domain switching, as described in Section 1.2.3 of Chapter 1. It is also apparent that reducing the fibre volume fraction reduces the overall strain the composites can develop, due to increased fibre clamping by the passive matrix.

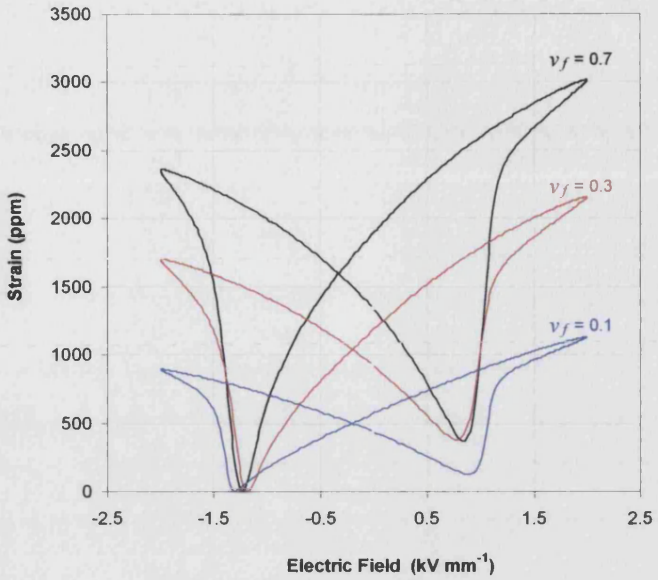

Figure 5.4: The saturation cycle strain response of 1-3 composites comprising Alceru-250 fibres in three different fibre volume fractions.

The analytical model equation (Equation (4.8)) shows that the fibre strain at any applied field level is simply equal to the composite strain multiplied by a factor that incorporates the clamping effect, which is related to the relative stiffness of the fibre and matrix, and their volume fractions. Equation (4.8) is compared to experimental data by measuring the composite strain at 2.0 kV mm^{-1} for each composite tested. The analytical model equation is used to determine the 'free fibre strain' (fibre strain free from the matrix clamping effects) for each composite. Relevant low field fibre and matrix material properties are taken from values measured in Chapter 3. To assess the accuracy of the model, these free fibre strain results are plotted against the fibre volume fraction of the composite from which they have been extracted. For an accurate model, free fibre strains should be constant since the fibre property is assumed to be independent of volume fraction, and a graph of free fibre strain versus fibre volume fraction should form a horizontal line. The average value of this line then represents the free fibre strain at 2.0 kV mm^{-1}. Such a graph, constructed using the Alceru-250 composite results, is presented in Figure 5.5(a).

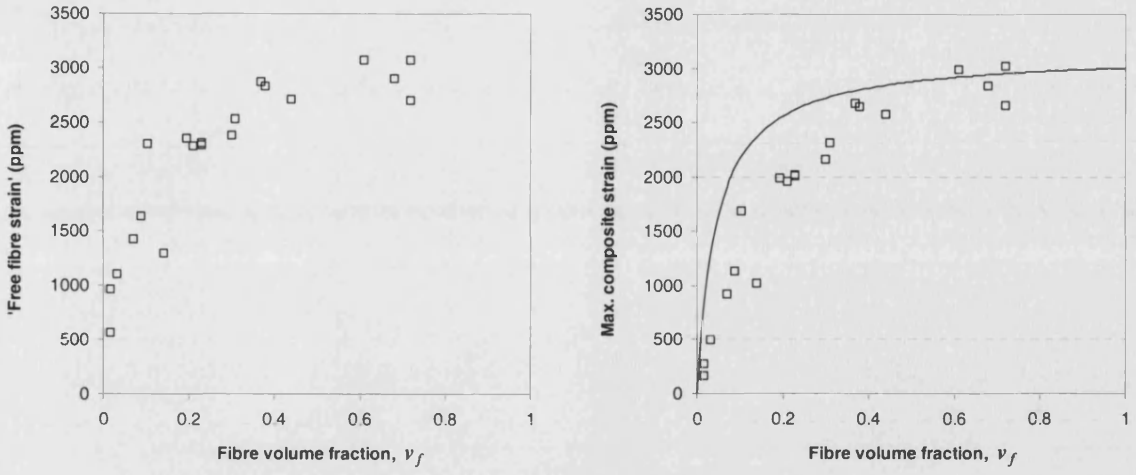

(a) (b)

Figure 5.5: (a) Free fibre strain at 2.0 kV mm^{-1} for the saturation cycle extracted from composite measurements using the analytical equation and (b) Composite strain at 2.0 kV mm^{-1} with the analytical model trend line.

From Figure 5.5(a) it can be seen that, unlike the predictions, the strain results do not form a horizontal line; the free fibre strain calculated from low volume fraction composites is lower than strains calculated from high volume fraction composites. It was concluded in Chapter 4 that high volume fraction composites are subject to less error than low volume fraction composites since they conform better to the iso-strain assumption. Thus fibre responses extracted from the high volume fraction composites are more representative of the true fibre response. To avoid errors associated with measurements performed on low fibre volume fraction composites, the fibre strain at 2.0 kV mm^{-1} was calculated by averaging the fibre results from composites with $v_f > 0.6$. This value of 3000 ppm was subsequently used to construct a trend line of composite strain at 2.0 kV mm^{-1} versus fibre volume fraction. The analytical trend line and the experimental results are presented in Figure 5.5(b). The graph confirms that the composite strain at low fibre volume fractions is lower than the analytical model trend. Deviation from the iso-strain assumption, which has been shown to reduce composite strains (Chapter 4), is considered to be responsible for this behaviour.

This method of assessing the analytical model accuracy performed with 1-3 composites tested under the operational cycle is described next.

Operational strain response

Figure 5.6 plots the strain response of the Alceru-250 composites at three different fibre volume fractions subjected to the operational cycle. The figure shows that reducing the fibre volume fraction reduces the strain the composites can develop, as seen in the saturation cycle.

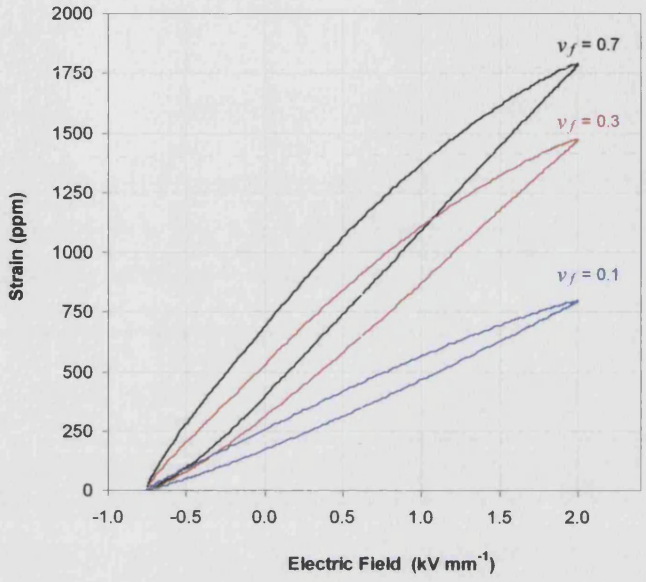

Figure 5.6: The operational cycle strain response of 1-3 composites comprising Alceru 250 fibres in three different fibre volume fractions

The analytical model's accuracy is assessed with the same procedure used for the saturation cycle results. The extracted 'free fibre strain' at 2.0 kV mm^{-1} as a function of fibre volume fraction is presented in Figure 5.7(a). As with the saturation cycle results, the free fibre strain results for the operational cycle do not form a horizontal line. The free fibre strain from low volume fraction composites is lower than for high volume fraction composites. The fibre strain is therefore calculated by averaging the results from composites comprising $v_f > 0.6$, since these high volume fraction composites are subject to less errors. The measured fibre value of 1850 ppm is used to construct the analytical model trend line, which is presented together with the composite results in Figure 5.7(b). This figure shows the extent of the deviation from the model trend line as the fibre volume fraction is reduced.

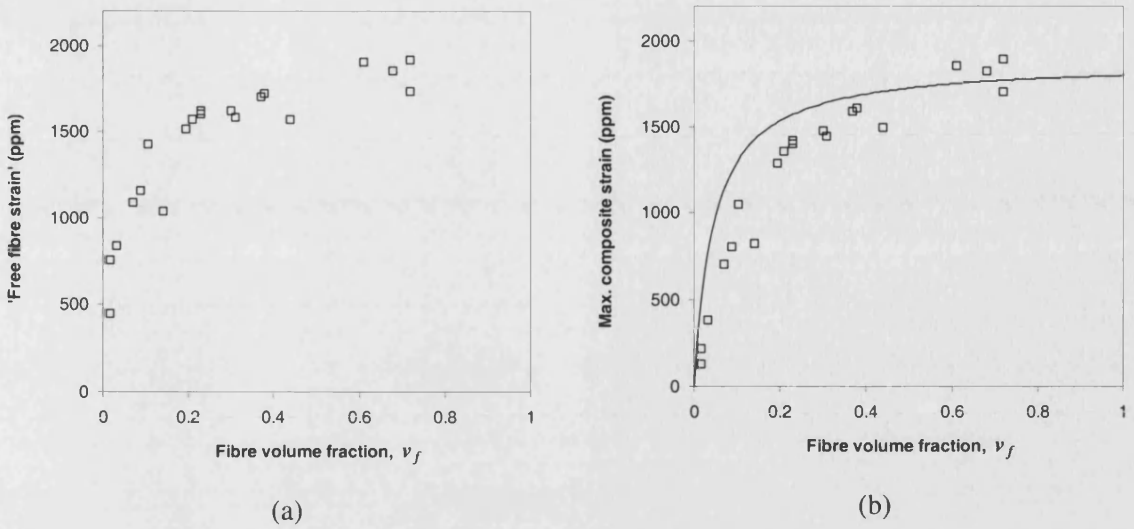

(a) (b)

Figure 5.7: a) Fibre strain at 2.0 kV mm^{-1} for the operational cycle extracted from composite measurements using the analytical equation and (b) Composite strain at 2.0 kV mm^{-1} with the analytical model trend line.

Analysis of both the saturation cycle and the operational cycle has shown that strains calculated from composites with fibre volume fractions less than 0.6 are significantly reduced compared to the high volume fraction composites, which are subjected to less errors. Deviation from the iso-strain assumption is thought to be responsible for this observed behaviour. In conclusion, the analytical model provides a method of measuring the high field piezoelectric strain responses of fine scale piezoelectric fibres, provided the volume fraction is kept greater than 0.6.

Having examined the volume fraction range for which the analytical model for the strain response is most accurate, it is now necessary to apply the same procedure to the polarisation model.

5.3.2 Polarisation response validation

Saturation polarisation response

Figure 5.8 plots the polarisation response of the Alceru-250 composites at three different fibre volume fractions subjected to the saturation cycle. The figure shows that all composites display the typical hysteresis loop behaviour, characteristic of a piezoelectric being driven at fields greater than the coercive field. It is also apparent that reducing the fibre volume fraction reduces the overall polarisation the composites can develop, due to the increasing contribution of the low dielectric polymer matrix.

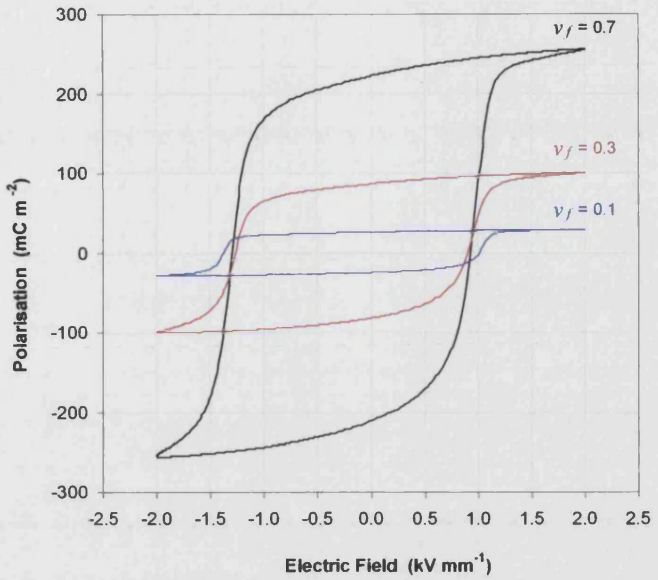

Figure 5.8: The saturation cycle polarisation response of 1-3 composites comprising Alceru-250 fibres in three different fibre volume fractions

The analytical model equation (Equation (4.20)) shows that the fibre polarisation at any applied field level is simply equal to the composite polarisation minus the contributions arising from the polymer matrix and active fibre clamping. The ability of Equation (4.20) to predict fibre responses is assessed by measuring the composite polarisation at 2.0 kV mm^{-1} for each composite tested. The analytical model equation is used to determine the 'free fibre polarisation' (fibre polarisation free from the matrix effects). Relevant low field fibre and matrix material properties are taken from values measured in Chapter 3. To assess the accuracy of the model, these free fibre polarisation results are plotted against the fibre volume fraction of the composite from which they have been calculated. For an accurate model, free fibre polarisations should be constant since the fibre property is assumed to be independent of volume fraction, and a graph of free fibre polarisation versus fibre volume fraction should form a horizontal line. The average value of this line then represents the free fibre polarisation at 2.0 kV mm^{-1}. Such a graph, constructed using the Alceru-250 composite results, is presented in Figure 5.9(a).

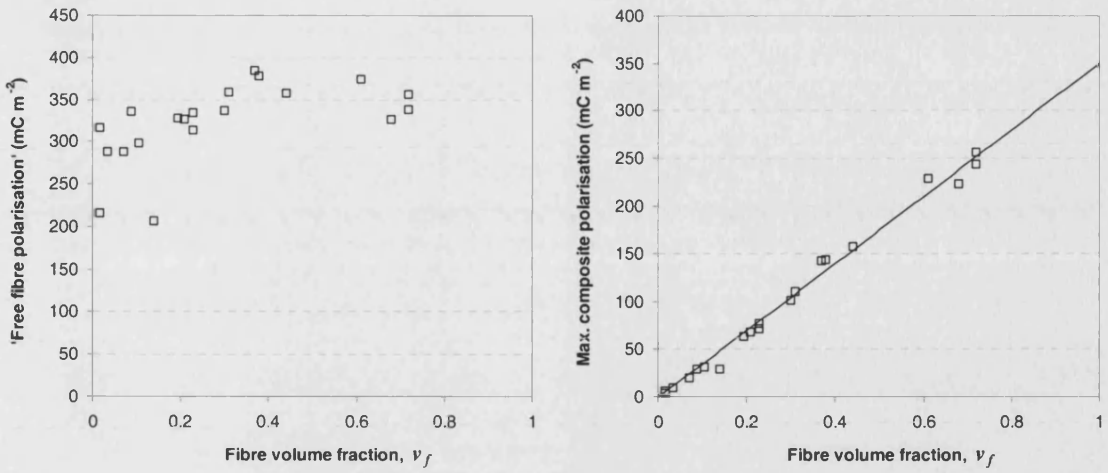

(a) (b)

Figure 5.9: (a) Fibre polarisation at 2.0 kV mm^{-1} for the saturation cycle extracted from composite measurements using the analytical equation and (b) Composite polarisation at 2.0 kV mm^{-1} with the analytical model trend line.

The free fibre polarisation results in Figure 5.9(a) reveal that the polarisation model is capable of predicting the fibre response over a wider volume fraction range than the strain model. However, it can be seen that the fibre polarisation does deviate from a horizontal line at volume fractions below approximately 0.4. This deviation is thought to arise from the non-linear fibre d_{33} coefficient. At low volume fractions the charge generated from the matrix clamping effect is strongly influenced by the fibres' d_{33} coefficient, as shown in Section 4.2.2 in Chapter 4, and as such errors in the extracted fibre response become more significant. To avoid this effect, the fibre polarisation at 2.0 kV mm^{-1} was calculated by averaging the fibre results from composites with $v_f > 0.4$. This value of 350 mC m^{-2} was used to construct a trend line of composite polarisation at 2.0 kV mm^{-1} versus fibre volume fraction, using Equation (4.20). The analytical trend and the experimental results are presented in Figure 5.9(b). This graph demonstrates that it is difficult to see the deviation in the polarisation response at low volume fractions.

This method of assessing the analytical model accuracy was then applied to 1-3 composites tested under the operational cycle.

Operational polarisation response

Figure 5.10 plots the polarisation response of the Alceru-250 composites at three different fibre volume fractions subjected to the operational cycle. The figure shows that reducing the fibre volume fraction reduces the polarisation the composites can develop, as observed in the saturation

cycle. In contrast with the saturation response, the level of polarisation and hysteresis displayed under the operational cycle is significantly lower.

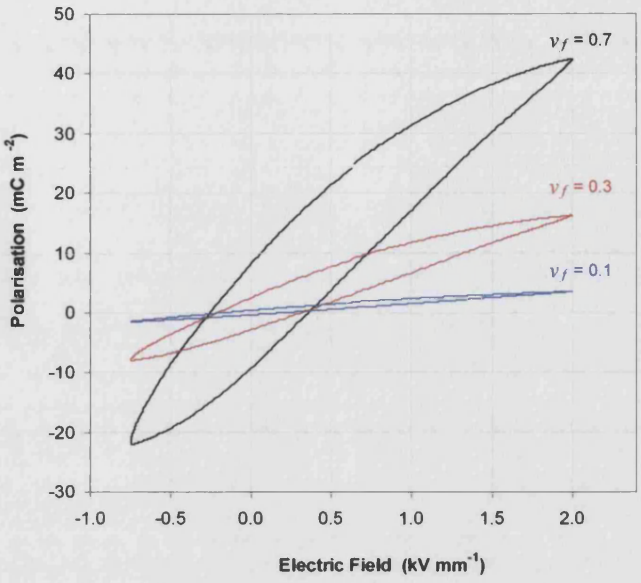

Figure 5.10: The operational cycle polarisation response of 1-3 composites comprising Alceru 250 fibres in three different fibre volume fractions

The analytical model's accuracy is assessed with the same procedure used for the saturation cycle results. The 'free fibre polarisation' at 2.0 kV mm^{-1} as a function of volume fraction is presented in Figure 5.11(a). The results deviate from a horizontal line at volume fractions below $v_f = 0.6$. As a consequence, the free fibre polarisation is calculated by averaging the free fibre polarisation results from composites with $v_f > 0.6$. The averaged free fibre value of 90 mC m^{-2} is used to construct the analytical model trend line, which is presented together with the composite results in Figure 5.11(b). The deviation in the composite response from the predicted trend of the model is clearer in this figure compared to Figure 5.9(b).

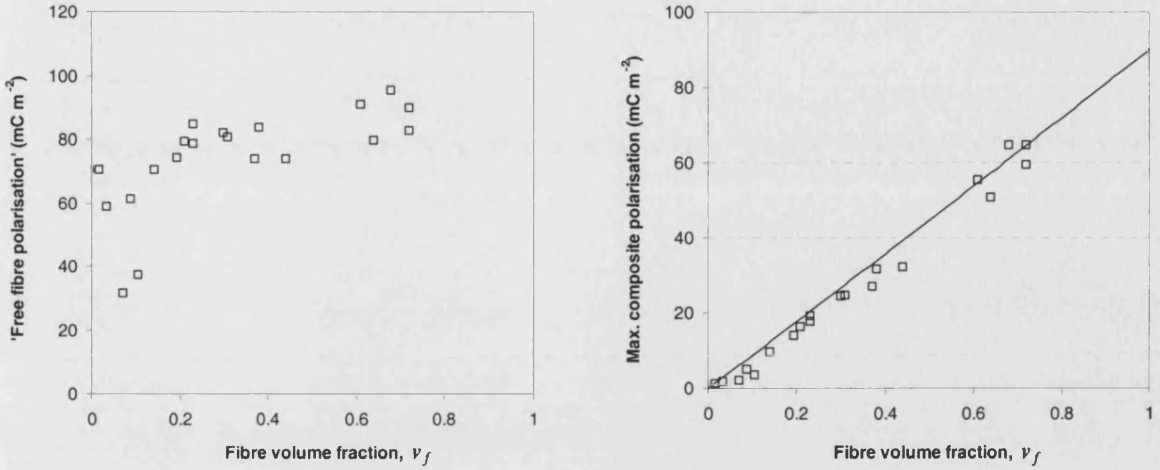

(a) (b)

Figure 5.11: (a) Fibre polarisation at 2.0 kV mm^{-1} for the operational cycle extracted from composite measurements using the analytical equation and (b) Composite polarisation at 2.0 kV mm^{-1} with the analytical model trend line.

This section has assessed the volume fraction range over which the strain and polarisation analytical models are most valid. For accurate predictions of the strain and polarisation responses under the saturation and operational cycle it is necessary to extract responses from composites with $v_f > 0.6$. Poor correlation is seen between experimental results and analytical model predicted trends for the strain responses for composites with $v_f < 0.6$. This has been attributed to deviation from the iso-strain assumption. Poor correlation with the analytical model predicted trends in polarisation for composites with $v_f < 0.6$ has been attributed to non-linear fibre d_{33} coefficients. This approach of evaluating fibre properties will now be used to compare a range of piezoelectric fibres, and to assess their suitability for incorporation into AFC devices.

5.4 Comparison of Fibre Responses

The previous section has shown that it is possible to extract high field fibre responses from 1-3 composite measurements, provided that the volume fraction is greater than 0.6 in order to minimise errors. This section compares the high field responses from the range of commercially available fibres characterised in Chapter 3. The fibre types are summarised in Table 5.1.

Table 5.1: Suppliers and diameters of the fibre types to be characterised for their high field response.

Fibre Production Method	Diameter (μm)	Supplier
Extrusion[24]	130	CeraNova
Alceru® Method	125 & 250	Smart Material Corp.
Viscous Plastic Processing (VPP) [29]	250	IRC in Materials, Birmingham, UK
Viscous Suspension Spinning Process (VSSP) [34]	235	Advanced Cerametrics

Strain and polarisation measurements were performed on the same 1-3 composites used in the low field property measurements of Chapter 3. To minimise errors, only composites with $v_f > 0.6$ were tested. The saturation cycle and the operational cycle responses for each fibre type are presented in the following sections. Key high field material parameters, such as the coercive field, hysteresis loss and saturation strain are compared to allow selection of the most appropriate fibre type for AFC manufacture.

5.4.1 Saturation fibre responses

Representative strain and polarisation response of the fibres subjected to the saturation cycle are presented in Figure 5.12. The response has been extracted from composites with high fibre volume fractions using Equations (4.8) and (4.21) respectively, and the material properties used in the equations are the low field properties described in Chapter 3. The scale of each graph is identical, allowing responses of the different fibre types to be compared easily. The responses of the two Alceru fibres are presented on the same graph, and have been labelled '125' and '250', relating to the fibres' diameter in microns.

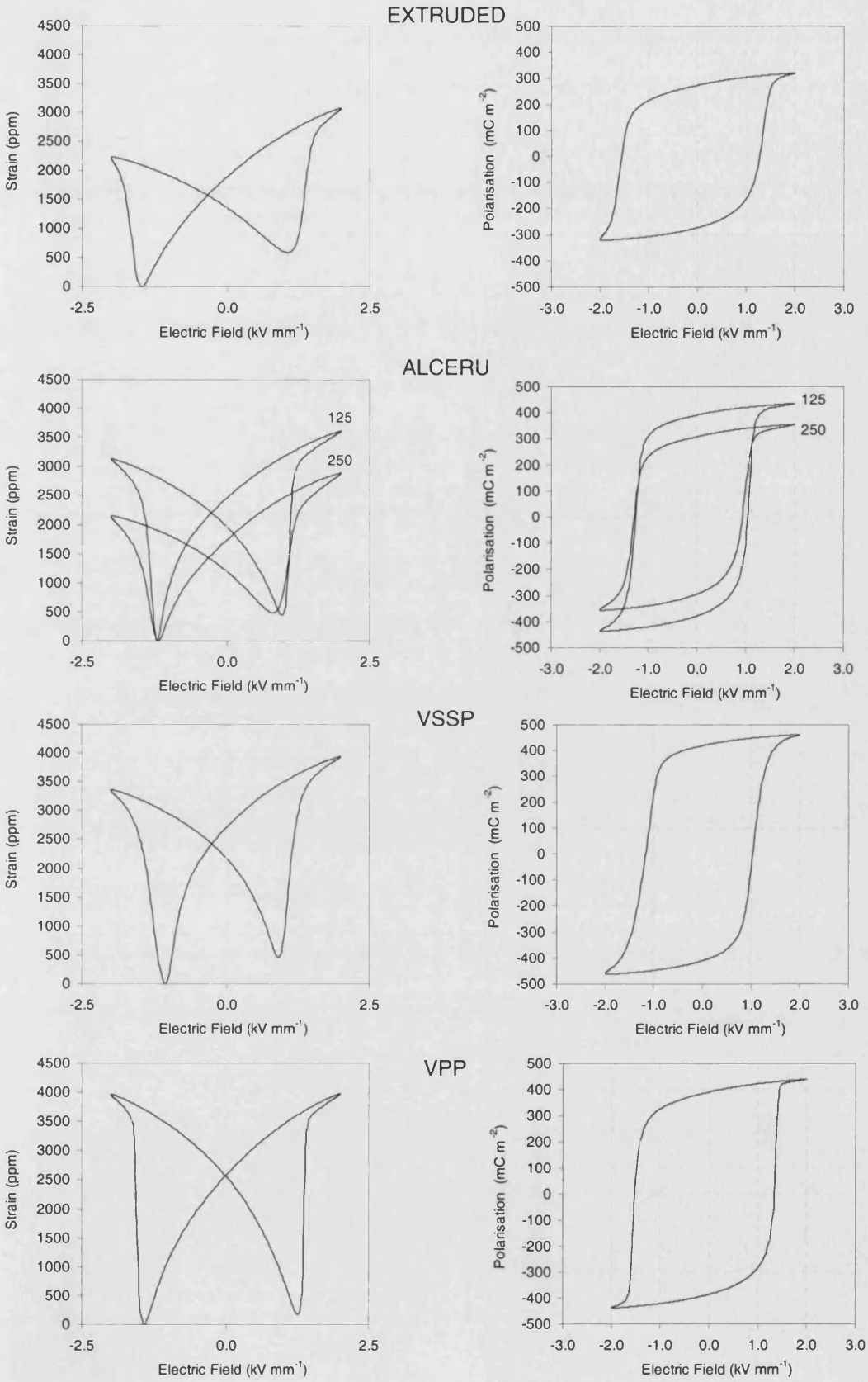

Figure 5.12: Saturation cycle strain and polarisation responses of fibres manufactured by different production methods. The fibre response is extracted from composites with $v_f > 0.6$.

Figure 5.12 shows clear differences exist between the four fibre types, and between the two Alceru fibres with different diameters. Important parameters relating to the efficiency of operation can be obtained from high field responses, allowing comparisons to be drawn between the fibre types. These include the saturation strain, hysteresis loss, and coercive field. The saturation strain is important for quantifying the maximum strain that can be developed by a material. Hysteresis loss, defined as the area enclosed by the hysteresis curve, is the energy dissipated during one cycle of the fibre. The dissipated energy leads to heating, which is known to degrade piezoelectric properties. This is particularly important to quantify in AFCs, since the fibres are surrounded by a low thermal conductivity polymer. Finally, the coercive field provides an indication of the domain mobility and sets the upper and lower operational voltage cycle. Figure 5.13 presents these three properties in bar chart form. In each case the fibre properties, obtained from saturation cycle testing and averaged from composites with $v_f > 0.6$, have been normalised by the highest performing fibre, which in all cases is the VPP fibre. The numerical value of each fibre property is shown above the bar relating to that fibre.

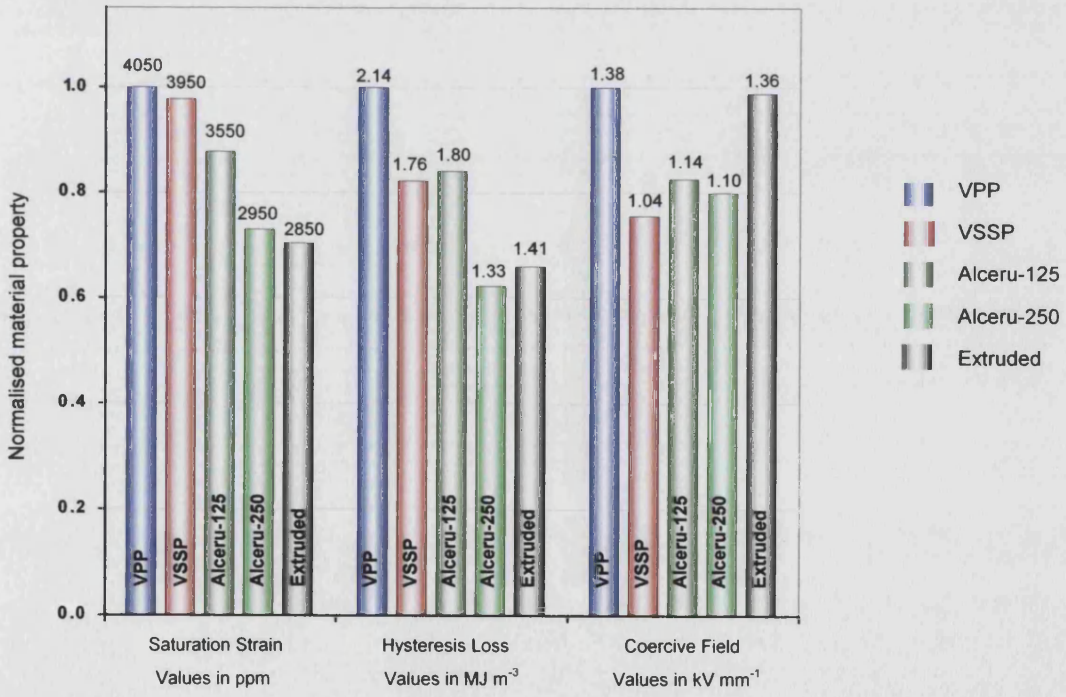

Figure 5.13: Comparison of the high field performance of the fibre types extracted from 1-3 composite data. The material properties are normalised by the highest value and presented as a bar chart, while the numerical values of the property are above each bar.

The saturation strain results show that the VPP and VSSP fibres develop the highest strain, in the region of 4000 ppm, while the Alceru-250 and Extruded fibres develop the lowest strain,

approximately 2900 ppm. It is interesting to note that the strain developed by the Alceru-125 fibres is approximately 20% higher than the larger diameter Alceru-250 fibres. This is in agreement with results from Chapter 3, which showed the low field d_{33} coefficient of Alceru-125 fibres to be significantly higher than the Alceru-250 fibre value.

The hysteresis results reveal that VPP fibres consume most energy in the saturation cycle. The VSSP and Alceru-125 fibres consume 20% less energy, while the extruded and Alceru-250 fibres consume approximately 35% less. Again, a clear distinction between the two differently sized fibres produced by the Alceru method is apparent.

The coercive field, which is a measure of the energy required to reverse the domain polarisation vector, and therefore a measure of domain stability, is highest for the VPP and extruded fibres. The VSSP fibres have the lowest coercive field of 1.04 kV mm^{-1} while the Alceru-125 and Alceru-250 fibres have similar coercive field values of 1.14 and 1.10 kV mm^{-1} respectively.

With the material parameters obtained from the saturation cycle discussed, it is now important to compare their ability to perform under the operational cycle. This will give an insight into the expected responses when fibres are incorporated into AFC devices.

5.4.2 Operational fibre responses

The strain and polarisation response of the fibres under the operational cycle have been extracted using Equations (4.8) and (4.21) respectively. The material properties used in the equations are the low field properties measured in Chapter 3. The responses, which have been extracted from the same composites as the saturation cycle results, are presented in Figure 5.14. The scale of each graph is identical, allowing responses of the different fibre types to be compared easily. The responses of the two Alceru fibres are presented on the same graph, and have been labelled '125' and '250', relating to the fibres' diameter in microns.

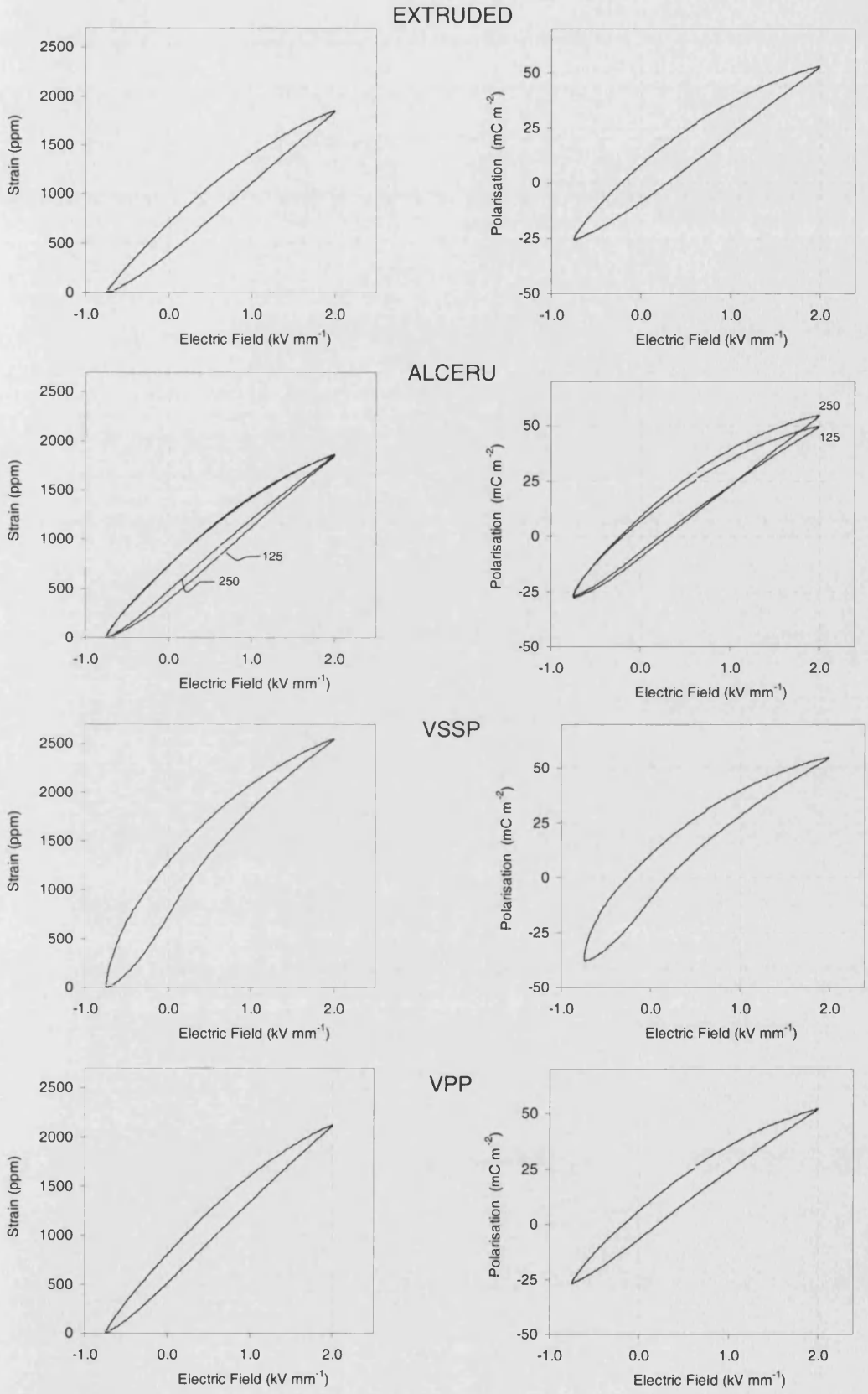

Figure 5.14: Operational cycle strain and polarisation responses of fibres manufactured by different production methods. The fibre response is extracted from composites with composites with $v_f > 0.6$.

Two important fibre properties obtained from the operational cycle responses relevant for AFC operation are the operational strain and operational hysteresis loss. These are presented in a bar chart form in Figure 5.15. In each case the fibre values, averaged from composites with $v_f > 0.6$, have been normalised by the highest performing fibre, which in both cases is the VSSP fibre. The numerical value of each fibre property is shown above the bar relating to that fibre.

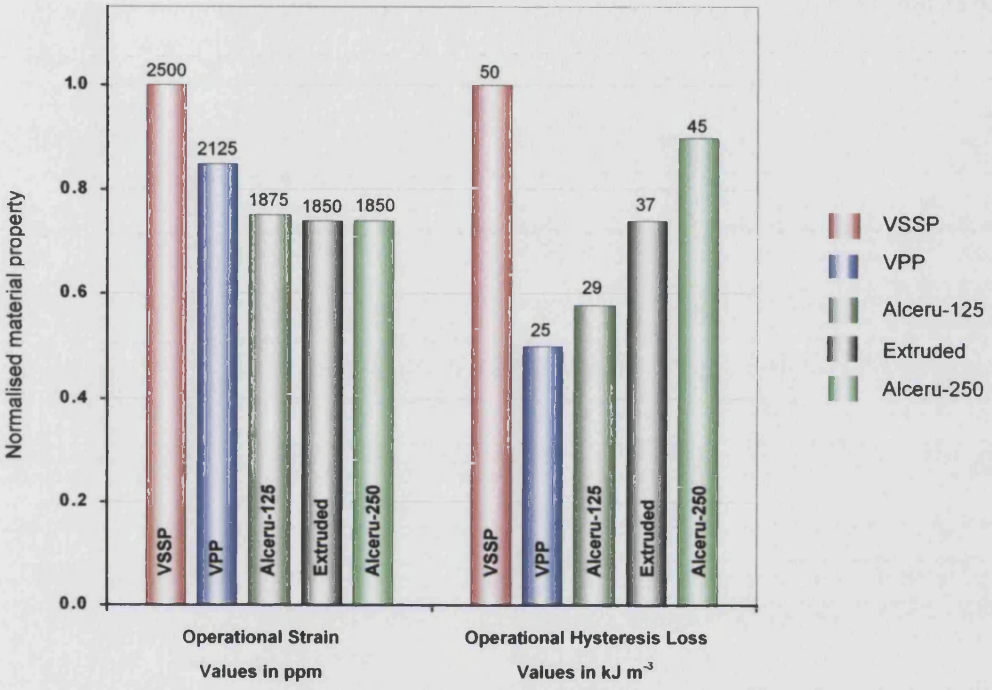

Figure 5.15: Comparison of the operational performance of the fibre types extracted from 1-3 composite data. The material properties are normalised by the highest value and presented as a bar chart, while the numerical values of the property are above each bar.

The figure shows that the VSSP fibres develop the largest strain, reaching 2500 ppm, while the VPP fibre develops a strain of 2125 ppm for the same cycle. Both Alceru fibres, and the extruded fibre, develop a strain in the region of 1850 ppm, which is only 75% of the strain developed by the VSSP fibre. However, hysteresis loss results reveal that the VSSP fibres, which develop the highest strain, also develop the highest hysteresis loss of 50 kJ m^{-3}. The VPP fibres, which developed the second largest strain, exhibit the lowest hysteresis loss, only 50% of the VPP fibre value. Again, a difference between the two Alceru fibres is observed, with the Alceru-125 fibres developing a loss approximately 35% lower than the Alceru-250 fibres.

Since a high strain and a low hysteresis loss is desired, a figure of merit for the operational cycle (M) useful for comparing the fibres can be defined as:

$$M = \frac{Strain\ developed\ (\ ppm\ )}{Hysteresis\ loss\ (\ kJ\ m^{-3}\ )} \tag{5.5}$$

Table 5.2 shows the figure of merit for the operational cycle for the fibre types tested.

Table 5.2: The strain per unit hysteresis figure of merit for the operational cycle.

Fibre Production Method	Diameter (μm)	Figure of Merit, *M* ($\times 10^{-6}$ m^3 kJ^{-1})
VPP	250	85
Alceru-125	125	65
Extrusion	130	50
VSSP	235	50
Alceru-250	250	41

From this table it is clear that the VPP fibres display superior performance characteristics for incorporation into an AFC. However, one must consider both the level of actuation required and the frequency of operation. The larger hysteresis loss associated with the VSSP fibres could be tolerated if a low frequency operation is required.

5.5 Chapter Summary

This chapter has introduced the test methods employed to measure the strain and polarisation response of 1-3 composites subjected to high electrical fields, up to 2.0 kV mm^{-1}, typical of fields experienced in AFC operation. The validity of the analytical equations from Chapter 4, which allow the strain-field and polarisation-field responses of fibres to be extracted from measurements made on composites, has been assessed using data obtained from 1-3 composites comprising Alceru-250 fibres. The equations were assessed using two electrical cycles, one termed the 'saturation cycle' and the other the 'operational cycle'. Results from this analysis showed that the strain response of the composites with low volume fractions was poorly predicted by the analytical equation for both electrical cycles. This was attributed to deviation from the iso-strain assumption

(the non-uniform surface profile developed under active fibre extension and contraction presented in Chapter 4). Similarly, hysteresis measurements from low volume fraction composites did not correlate well with predictions made using the analytical equation. This has been attributed to the non-linear d_{33} of the fibres at high electrical driving fields. As a result of this analysis, the analytical model was considered accurate only above fibre volume fractions of ~0.6.

The model was then used to compare the strain-field and polarisation-field responses from a range of commercially available fibres. The results have been presented as typical hysteresis and butterfly loops, and the numerical results presented in bar chart form to allow comparison between the fibre types. Clear differences were observed in the response of the fibres to both the saturation and operational cycles. A figure of merit was determined for the operational cycle allowing a fibre ranking to be made. Based on this, the VPP fibres exhibit superior properties for incorporation into AFCs, displaying a high strain and low hysteresis response. It is possible that microstructure and composition could be the key to understanding why differences exist between fibres manufactured by the different methods. The following chapter examines the passive properties of the fibres in an attempt to explain the performance differences observed at high electrical fields as seen in this chapter, and at low fields as seen in Chapter 3.

CHAPTER 6

PHYSICAL AND CHEMICAL FIBRE PROPERTIES

6.1 Introduction

In addition to the electro-mechanical properties of fibres at high and low electrical fields, which have been measured in the previous chapters, it is essential that the physical and chemical properties are characterised. The majority of publications characterising fibres for AFC applications focus on measuring the electromechanical properties, providing little information on factors that have contributed to the observed piezoelectric activity of the fibre. It is well known that the piezoelectric properties of PZT and other piezoelectric compositions are related to grain size,[86] porosity[87] and composition.[13] Quantifying these parameters for fibres manufactured via different production methods will enable manufacturers to optimise their fibre production methods, thereby producing fibres with high piezoelectric activity. For successful manufacture of AFC devices other factors, such as diameter distribution and general morphology of fibres, are also important. For the AFC configuration, irregular shaped fibres can complicate the manufacturing process. Irregular fibres will also produce a variable distance between the fibre layer and electrodes, resulting in uneven electric fields, reduced performance and even breakdown during poling.[88] For circular fibres, large variations in diameter can lead to the same problems.

The following parameters were identified for investigation in the study:

(i) **Grain morphology.** It has been reported that small grain sizes are detrimental to piezoelectric performance in bulk piezoelectrics because of the increased influence of grain boundary interfaces.[55, 89-91] Grain size strongly influences domain size,[86,92] whose characteristics are ultimately responsible for the magnitude of the observed piezoelectric activity.

(ii) **Fibre morphology.** The diameter and roundness of the fibres are required to be uniform for successful AFC manufacture, as described above. Variability in these parameters also implies inadequate control during manufacture.

(iii) **Porosity.** High levels of porosity reduce electro-mechanical coupling,[87,93] and are also detrimental to ultimate tensile strength of the fibres. This is undesirable both

during the manufacturing stages and in actuator applications where maximum durability is required. Porosity also limits the fibre bending radius; thus the ability to conform to curves surfaces is diminished.

(iv) **Phase composition.** Significant amounts of research have shown that optimum electro-mechanical coupling occurs at the rhombohedral/tetragonal phase boundary.[13] Stoichiometric control in small diameter fibres can be difficult due to the large surface are/volume ratio, which facilitates the loss of lead oxide during sintering. Phase analysis will allow quantification of this effect.

The first section of this chapter describes the experimental methods used to characterise the properties of the five fibre types presented in Table 5.1 (Chapter 5). In the second section the results of the testing are presented and analysed. Links are then drawn between the physical and chemical properties and the electro-mechanical properties measured in Chapter 3 and Chapter 5 in an attempt to explain the difference in piezoelectric activity between the fibre types. Finally, this chapter describes how the most appropriate fibre type for AFC manufacture was selected, based on a combination of the electro-mechanical, physical and chemical properties

Measurement and analysis of a large number of the results presented in this chapter was conducted by Andrew Dent during his Final Year Project.[94] More specifically his inputs include the grain size and fibre morphology analysis, and the porosity measurements.

6.2 Physical and Chemical Characterisation Methods

6.2.1 Fibre microstructure and grain size

Sample preparation

Three types of sample were prepared for assessing the fibres':

(i) interior microstructure

(ii) surface microstructure

(iii) grain size.

For assessing interior microstructure, fibres were fractured under a tensile load and mounted vertically on a metal dish such that the fractured end was uppermost. Surface microstructure was examined by laying several fibres onto a conductive carbon pad adhered to a metal dish for support. This allowed inspection of the surface grains along the lengths of the fibre. To assess the grain size, in excess of 100 fibres were incorporated into a 1-3 composite using the same technique described in Section 3.2. Following polishing of the composite face, an etching solution consisting of 12.5 ml HNO_3, 2.5 ml HF and 8.5 ml H_2O, was applied for 10 to 30 seconds. The etch solution was removed by rinsing the surface in industrial methylated spirits and flushing with distilled water. This etching process preferentially attacks the grain boundaries, providing contrast in the scanning electron microscope (SEM).

Microscopy and measurement

All samples were sputtered with gold and examined using a JEOL JSM-6310 scanning electron microscope in secondary electron imaging mode. Micrographs of the fibres' interior and surface microstructure were taken from the samples prepared for this purpose.

For grain size analysis, the polished and etched 1-3 composite samples were viewed typically at 2,000× magnification. For each fibre type five micrographs were taken from five different fibres in the 1-3 composite. The surfaces of several fibres for each fibre type were examined to ensure that the fibres selected for analysis were representative of the material batch.

Before analysis, digital images were enhanced with 'Paint Shop Pro', using the automatic contrast feature to improve the definition of grain boundaries. Numerous methods exist to quantify grain size, although the linear intercept method is commonly used due to the efficiency with which large areas can be surveyed.[95] The linear intercept method was followed as described in BS 623-3.[96] Analysis was conducted with 'UTHSCSA ImageTool'.

The linear intercept method requires at least five straight lines to be drawn on the micrograph. Each line length is measured, and the total line length, l_t, is calculated. The number of intersections of the line with grain boundaries, N_i, is counted. If the line intersects a junction of three grains, this is counted as 1.5 intersections. If the line crosses a large pore, this is counted as one intersection. The mean linear intercept distance, g_{mli}, in micrometers, is calculated using:

$$g_{mli} = \frac{l_t - l_p}{m_c N_i} \tag{6.1}$$

where: l_t = total line length

l_p = total line length crossing large pores

N_i = the number of intersections on each micrograph

m_c = calibrated magnification of the micrograph.

It is recognised that the numerical value obtained for the mean linear intercept size is somewhat smaller than the actual grain size because intercepts can cross grains at any position, and not necessarily along the largest axis. The relationship between the mean linear intercept size and true three-dimensional grain size is not simple, and depends on the grain shape and the average number of facets. For this reason the results obtained can only be used for comparative purposes, and not as a true measure of grain size.

6.2.2 Fibre morphology

Microscopy

Evaluation of morphological properties, such as diameter and shape factor, requires the fibre cross section to be characterised. This was achieved by examining the same 1-3 composite specimens prepared for the grain size analysis. For fibres with diameters of ~250 μm and ~125 μm, SEM images with magnifications of 80× and 160× respectively were taken, until the entire composite surface had been surveyed. In both cases a low magnification macro image (30×), with a field of view incorporating the entire sample was taken to keep account of which fibres had been measured. A typical pair of images (low and high magnification) can be seen in Figure 6.1(a) and (b) respectively. Images were stored digitally for subsequent processing and image analysis.

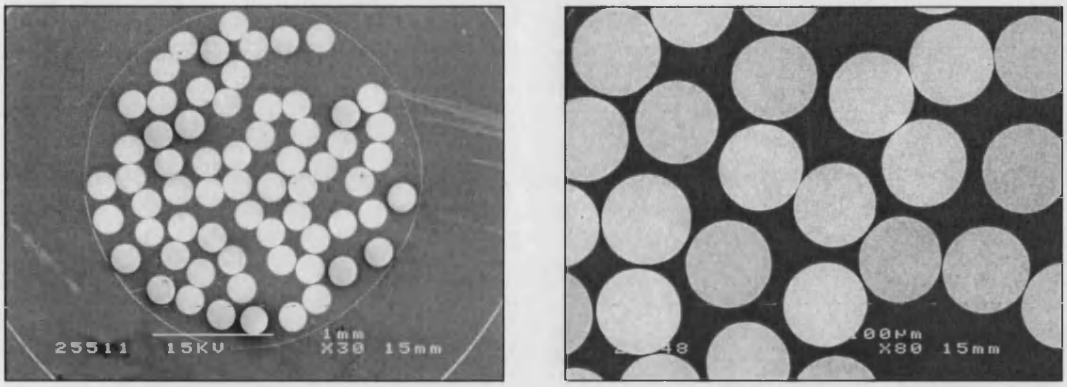

(a) (b)

Figure 6.1: Secondary electron images of PZT fibres. (a) Macro micrograph of entire sample used to record measurement of fibres. (b) Typical image of fibre cross-sections, without digital enhancement.

Image analysis

Prior to image analysis, micrographs were digitally enhanced with the commercial program 'Paint Shop Pro' (Version 7) for Windows. The purpose of enhancement was to improve contrast between the PZT fibres and polymer matrix and reduce topographic features such as voids without altering the fibre edge dimensions. After careful testing to ensure that the processing would not introduce artefacts, the following operations were applied:

(i) ***Contrast and brightness adjustment*** - Contrast and brightness were manually adjusted until fibre-matrix contrast was sufficient for later processing.

(ii) ***Noise reduction*** - An edge-preserving filter was applied to reduce noise.

(iii) ***Removal of pores and blemishes*** - Pores and blemishes were reduced by a 'Salt and Pepper' filter, which identifies specks of high or low tone relative to the surrounding area.

(iv) ***Thresholding*** – Thresholding levels were set manually to convert the greyscale image to binary (black and white) for image analysis.

The effect of these processes is shown in Figure 6.2.

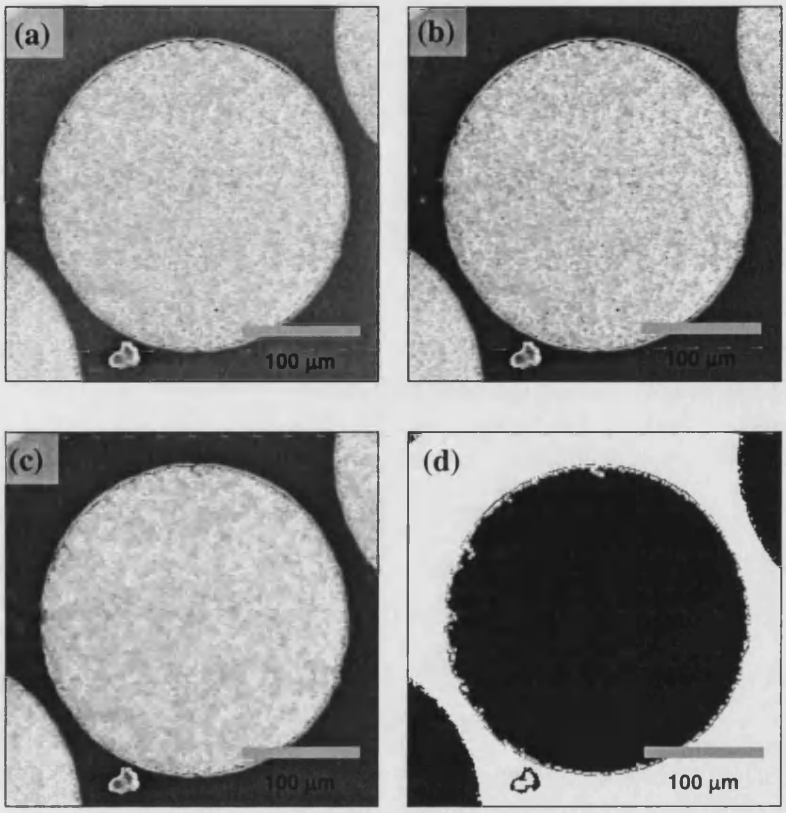

Figure 6.2: Image enhancement as used to improve the accuracy of analysis. (a) Original image from SEM. (b) Contrast and brightness adjusted followed by application of an edge-preserving filter to reduce noise. (c) 'Salt and Pepper' filter. (d) Thresholding (this tends to create a jagged edge, producing a highly convoluted perimeter).

Image analysis was performed with the public domain application 'UTHSCSA ImageTool' (Version 3) for Windows. Spatial calibrations were entered and the binary images were analysed to compute area and maximum and minimum calliper lengths. Two factors were measured from the image analysis performed on the fibres: elongation and diameter.

Elongation, a form factor describing the approximation to a circle, was selected as a comparative figure of merit. The elongation form factor, F_e, is defined as the ratio of the maximum to minimum calliper diameter, Equation (6.2).

$$F_e = \frac{D_{min}}{D_{max}} \tag{6.2}$$

Where D_{min} = minimum calliper length

D_{max} = maximum calliper length

An elongation factor of one corresponds to a circular cross section, with extended shapes such as ellipses possessing elongation factors less than unity. The geometrical data from image analysis was tabulated in a spreadsheet package, allowing the elongation shape factor to be calculated for 100 fibres of each type. The distribution of values was considered approximately symmetrical, so that mean and standard deviation are reasonable descriptive statistics for the data.

Accurate measurement of fibre diameter is important for computer modelling, for calculation of properties such as density, and for practical purposes such as AFC construction. Furthermore, the variation in diameter provides an indication of the control associated with individual manufacturing processes. An estimated diameter may be calculated by assuming the fibre is circular and calculating the area equivalent diameter, D_A, (also known as the feret diameter), given by Equation (6.3):

$$D_A = \sqrt{4A/\pi} \tag{6.3}$$

Where A = fibre cross-sectional area

This value of diameter provides an accurate method of determining the fibre volume, used in the density measurements.

6.2.3 Density/Porosity

Density is defined as the mass of a quantity of material divided by the volume of that same quantity. Two densities are typically defined; absolute density and apparent (*or bulk*) density. Absolute density excludes the pores in the material for volume measurements, and as such measures the density of the material forming the structure. We wish to know the density or the fibre itself, not the ceramic from which it is composed. Therefore, the apparent density is more appropriate, in which the pores are included in the measurement of volume. These concepts are illustrated in Figure 6.3.

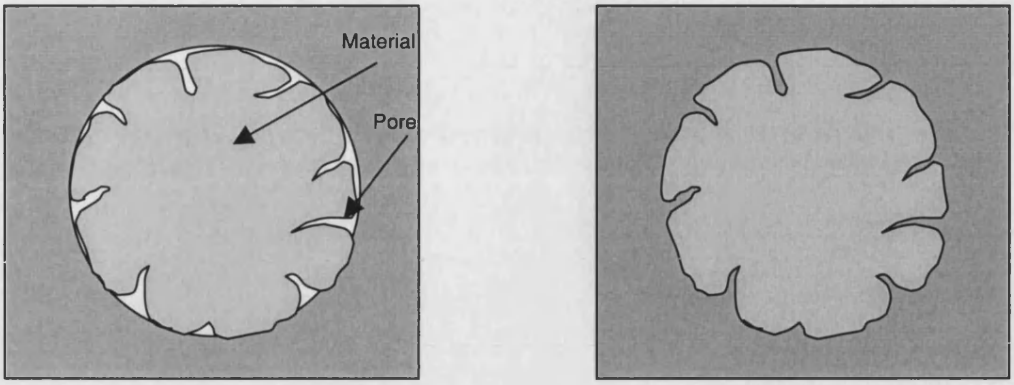

(a) Apparent (*or bulk*) density (b) Absolute density

Figure 6.3: Illustration of the concept of (a) apparent density and (b) absolute density for a fibre of circular cross section.

Apparent density, ρ_a, is calculated as the quotient of the measured mass and the measured volume of the material. For a fibre with a circular cross section it is defined by:

$$\rho_a = \frac{m}{\pi r^2 l} \tag{6.4}$$

Where: m = mass of fibre

r = fibre diameter

l = length of fibre

One hundred fibres were selected for each material type. Length measurements were made with digital callipers accurate to 0.05 mm and the mass measured using a Sartorius analytical balance, accurate to 0.05 mg. Since the diameter of each individual fibre was not measured, it was impossible to calculate a true density for each measured fibre. Therefore it was not possible to obtain a density distribution for each fibre type. However, it was possible to calculate a mean fibre density with Equation (6.4) using the summed length and masses of the 100 fibres tested, together with the mean fibre diameter presented in Section 6.2.2. Because of the symmetrical diameter distribution of all the fibre types, the calculated mean fibre density is an accurate and comparable measurement.

6.2.4 Phase analysis and composition

X-ray diffraction was used to assess two aspects of the fibre characteristics:

(i) identify the phases present

(ii) measure the relative proportion of these phases.

The phases present were identified to ensure no phases other than the rhombohedral and tetragonal phases associated with PZT were present. Particularly important is the presence of pyrochlore phase ($Pb_2(Zr,Ti)_2O_{6+x}$), a lead deficient cubic phase that exhibits no piezoelectric activity. The presence of this phase could explain the difference in piezoelectricity observed in previous chapters, since it would diminish the piezoelectric activity in the fibres.

Measuring the relative proportions of the rhombohedral and tetragonal phases could provide further insight into the difference observed in the piezoelectric activity. Ideally both rhombohedral and tetragonal phases should be present, indicating a composition close to the morphotropic phase boundary (MPB), with enhanced piezoelectric performance. It is difficult to specify an exact composition for optimum activity, but it has been shown[56] that the tetragonal to rhombohedral phase ratio strongly influences d_{33}, d_{31}, and ε_{33}^T of fibres, as in bulk PZT. Contrary to popular belief, maximum coupling has been shown to occur just outside the two-phase region, on the tetragonal side of the MPB.[98] Consequently, a composition with an excess of tetragonal phase would suggest stronger piezoelectric activity.

Experimental method

Un-poled fibres, as received from the manufactures, were ground to a fine powder using a pestle and mortar. X-ray diffraction was performed on the powders using a Phillips powder diffractometer fitted with a 4kW x-ray generator, copper target and a graphite monochromator. Control of the diffractometer was achieved using the diffraction software (PW1877 PC-APD Version 3.5b, Oct 1999).

To assess the phases present a wide-angle scan, in the range two-theta 20° to 60°, was performed. The location of the reflection peaks in the x-ray diffraction profile were compared to a reference spectrum for PZT,[97] which was used to assign crystallographic planes to the observed reflection peaks. Any unaccounted peaks could then be attributed to non-PZT phases, and investigated further.

To assess the relative proportions of the tetragonal and rhombohedral phases a high-resolution scan was performed in the two-theta range 43° to 46°. Rhombohedral and tetragonal phases are distinguishable on x-ray diffractograms since the {002} planes form a set of reflections in this two-theta range as a doublet and a singlet for the tetragonal and rhombohedral phases respectively.[98] Because of the close proximity of the three peaks, overlapping was observed. It was necessary to use the built in function of the diffractometer software to de-convolute the spectrum into the three distinct peaks. An example spectrum showing the raw data and the three de-convoluted peaks is presented in Figure 6.4. This figure has an insert in the top left showing the full PZT spectrum. The dotted rectangle in this insert indicates the location of the high resolution scan.

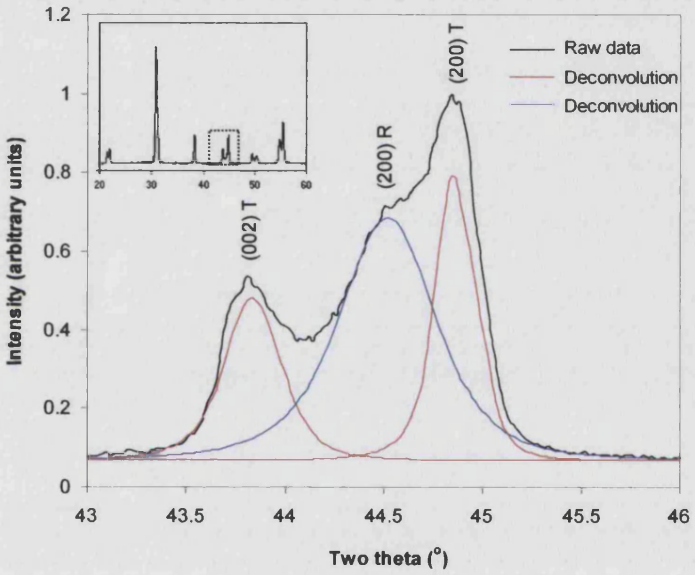

Figure 6.4: An example of the de-convolution process used to extract the two peaks associated with the tetragonal phase (T) and the single peak associated with the rhombohedral phase (R). (shown for the VSSP fibres). The insert, top left, shows the full spectral response from two theta = 20° to 60° and indicates the location of the high resolution scan.

Integrated intensities were calculated for each de-convoluted reflection using the diffractometer software. The amount of rhombohedral phase, P_R, was then calculated from the integrated intensities of the Cu-$K_{\alpha 1}$ reflections using the following equation:[56]

$$P_R = \frac{I_{R(200)}}{I_{R(200)} + I_{T(200)} + I_{T(002)}} \quad (6.5)$$

Where $I_{R(200)}$ = integrated intensity of the (200) reflection of the rhombohedral phase

$I_{T(200)}$ = integrated intensity of the (200) reflection of the tetragonal phase

$I_{T(002)}$ = integrated intensity of the (002) reflection of the tetragonal phase

6.3 Results

6.3.1 Fibre microstructure

Figure 6.5 presents SEM images from the fibre surfaces and fractured ends in a comparative format. The scale of each image is the same, making it possible to compare grain sizes, fracture modes, grain shapes and porosity.

All fibres display an equiaxed grain structure, and the surface and interior of individual fibre types display similar grain size. However, grain size differs considerably between fibre types. The extruded, Alceru-250 and VPP fibres have a similar grain size, which is the smallest of the fibre types examined. The Alceru-125 fibres have a slightly larger grain size, while the VSSP fibres have a larger grain size still. The exaggerated growth of some grains in both Alceru fibres (also seen later in the grain size analysis images) is evidence of preferential grain growth, a process driven by the reduction in grain boundary energy. At this stage it is only possible to make these qualitative descriptions. Shortly the quantitative linear intercept grain size results will be presented.

Comparing the fibre ends allows fracture modes to be established. All fibres exhibit predominantly inter-granular fracture, except for the Alceru-125 fibres, which exhibit a significant degree of trans-granular fracture. A glassy phase is present in those fibres displaying inter-granular fracture modes, and is clearly identifiable in the VPP and VSSP fibre surface micrographs because of preferential migration to this low energy interface. The lack of a glassy phase in the Alceru-125 fibres results in strong grain boundaries, and is though to be responsible for the associated trans-granular fracture.

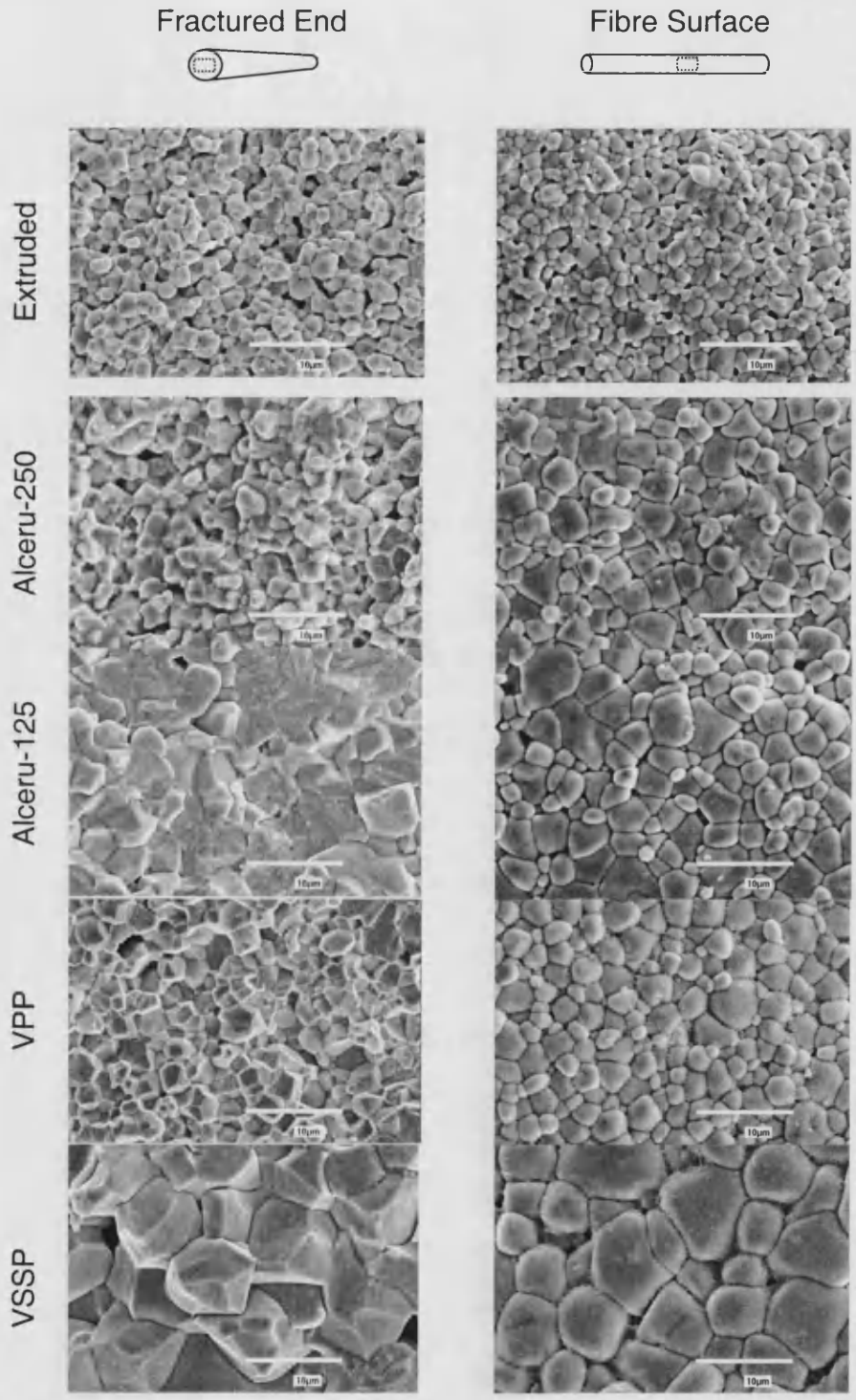

Figure 6.5: Representative SEM images of fractured ends and outer surfaces of the five PZT fibre types. The scale bar in all images is 10 μm.

The micrographs also allow qualitative observations of porosity levels to be made. The extruded fibres display homogeneously distributed porosity, noticeable in both the fractured end and fibre surface micrographs. The porosity, which is small compared to the grain size and evenly distributed, may be a result of excessive use of binders and plasticisers, poor de-agglomeration of the mix or insufficient sintering aid. The remaining fibres all show evidence of being fully sintered low porosity materials, and where any porosity present it is small in comparison to the grain size. This is also apparent in the images used to calculate grain size, presented in the following section.

6.3.2 Grain size

Figure 6.6 contains SEM images of the polished and etched ends of the fibres. These images are representative of those used to measure grain sizes using the linear intercept method. The grains appear randomly distributed in size, with exception of the Alceru-250 and Alceru-125 material that displays bimodal characteristics. The grains in the extruded fibres are difficult to identify because of excessive porosity.

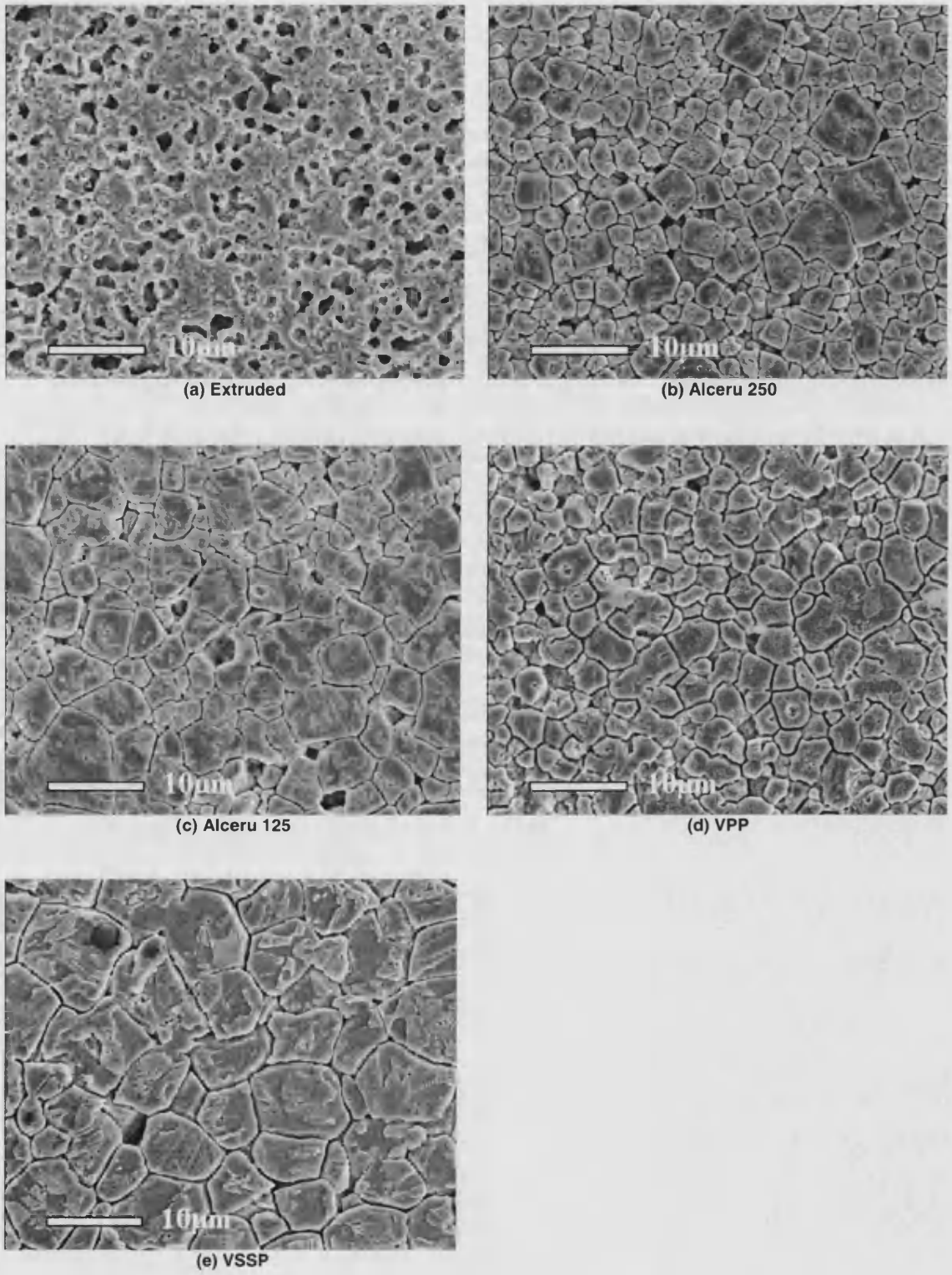

Figure 6.6: Representative SEM micrographs of the polished and etched ends of the five fibre types. These images are typical of those used to measure grain size using the mean linear intercept method.

Linear intercept measurements were tabulated in a spreadsheet program, allowing average grain sizes to be calculated for each material. It was found that distinction of grains for the extruded material was difficult because of the excessive porosity. This limited the linear intercept measurement to two images, compared to five for the other fibre types. However, this still represented a measurement of over 200 individual grains. Mean grain size and standard deviation were calculated for the different fibres and the results are presented in Table 6.1. Measurement error was considered negligible in comparison to the inherent variability of the data. Since the linear intercept method measure a mean grain size, the standard deviation values refer to the variation of the grain size between measurements, not of the grains themselves.

Table 6.1: Mean grain size and standard deviation of the fibre types, calculated by the linear intercept method.

Fibre Type	Grain size (μm) ± 1 S.D
Extruded	1.9 ±0.1
Alceru-250	2.0 ±0.3
Alceru-125	2.9 ±0.5
VPP	2.5 ±0.4
VSSP	**5.9 ±0.8**

Measured grain sizes reveal a wide spread of sizes between the fibre types. The extruded and Alceru-250 fibres possess the smallest grain size, of about 2 μm. The Alceru-125 and VPP fibres have slightly larger grain sizes, of 2.5 - 3 μm, while the VSSP fibres display the largest grain size, approaching 6 μm. Since the grains present in the VSSP material are significantly larger and more constant in size, it is probable that the stock material was formed from coarser grained powder, which may explain the poor morphological control observed in later analysis. However, it is difficult to confidently draw links between the observed grain sizes and the manufacturing process, since little information is available on the powders and binders, proportions of starting materials, and sintering regimes used commercially. However it may be possible to link the measured grain size to the observed level of piezoelectric activity. It is known from research that a large grain size is associated with a large domain size.[86] In turn, a large domain size has been linked to a large piezoelectric activity, measured by d_{33}.[55] Although

it is expected that the larger grain fibres will exhibit large piezoelectric activity it is likely that other factors, particularly composition, are also important, masking the expected trends. This will be reported at the end of this chapter, when the physical and chemical properties are correlated with the electro-mechanical properties measured in Chapters 3 and 5.

6.3.3 Fibre morphology

Fibre geometry was observed to deviate from an ideal circular geometry, with irregularities in cross-section, variation in fibre diameter and deviation from the specified diameter. The irregularity in cross section, measured by the elongation form factor, is expressed as a percentage in Table 6.2.

Table 6.2: Fibre cross-section elongation shape factor. Mean values from 100 fibres, displayed as percentages with ± one standard deviation to illustrate variability.

Fibre Type	Elongation (Percent), ± 1 SD
Extruded	97 ± 1%
Alceru-250	97 ± 1%
Alceru-125	93 ± 5%
VPP	**98 ± 1%**
VSSP	94 ± 3%

Both the Alceru-125 and VSSP fibres exhibited the lowest elongation of 93% and 94% respectively. The other fibres possess elongation form factors of 97% to 98%.

The low elongation of the Alceru-125 fibres can be attributed to the flattened edge often observed, a feature shown in Figure 6.7(a). This is probably a result of the green fibres slumping under their own mass either during storage before sintering, or during sintering. Since this feature was not observed with the coarser Alceru-250 fibres it can be inferred that a lower viscosity precursor was utilised for successful preparation of the finer filaments. Storage and handling of green fibres has been highlighted as problematic and a solution must be sought before successful scaling up of production.[24]

Cross-sectional variation was typical in the VSSP fibres, and is shown in Figure 6.7(b). The variation may result from inadequacies in the spinning technology that has been adapted from the textile industry. The variation, which is reflected in the high elongation factor of this fibre, was not present in the other materials.

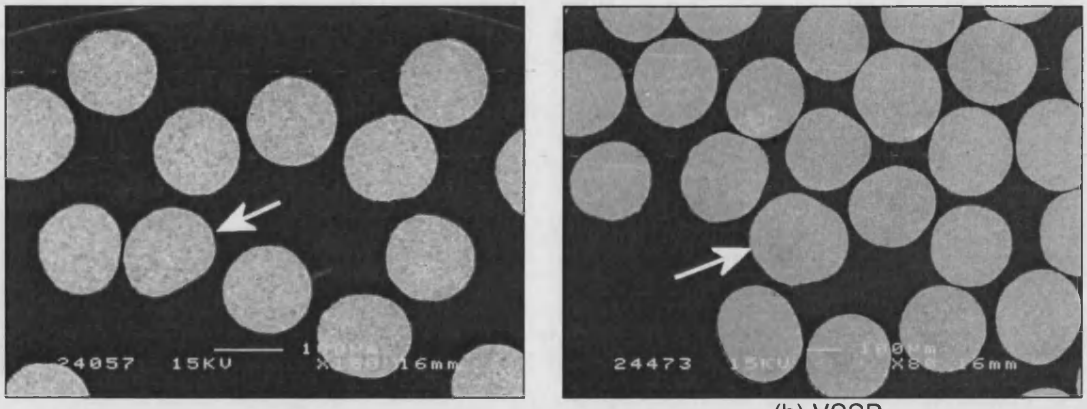

(a) Alceru-125 (b) VSSP

Figure 6.7: Secondary electron images of PZT fibres showing different processing features. (a) Alceru-125 fibres displayed flattened surfaces, probably resulting from the green body slumping under its own mass. (b) VSSP fibres typically had large cross section variability, not apparent in the fibres produced by other methods. Note: images are not to same magnification.

Results of the area equivalent, or feret diameter are presented in Table 6.3. This parameter is a suitable means of assessing the fibre diameter since elongation form factors reveal fibre cross sections very closely approximate a circle. The statistical variations of the fibre diameter are also presented in Table 6.3.

Table 6.3: Fibre area equivalent diameter (mean values from 100 fibres). Variability is statistically compared using standard deviation (S. D) and coefficient of variation (C. V).

Fibre Type	Diameter Information			Statistical Variation	
	Specified Diameter (μm)	Mean Feret Diameter (μm)	Difference (%)	S. D. (μm)	C. V.
Extruded	130	134	+3.1	3	2.4 %
Alceru-250	250	263	+5.2	6	2.4 %
Alceru-125	125	131	+4.8	3	2.1 %
VPP	**240**	**233**	**-2.9**	**4**	**1.7 %**
VSSP	230	251	+9.1	13	5.1 %

Error in the measured area was considered small because high-resolution digital imaging provided micrographs with good definition (30-40,000 pixels per fibre area). Because the 'rough' fibre edges constituted only 1 - 2% of the fibre cross-section, the feret diameter was less sensitive to threshold effects compared to other methods of measuring the diameter.

Table 6.3. shows that, in general, the fibres had a greater diameter than specified. This indicates that shrinkage was less than anticipated by the manufacturers (although it is not known if fibre diameters are calculated prior to manufacture, or measured once manufactured). For this reason, a more useful result for determining the manufacturing control tolerance is the statistical variation of the fibres' diameter. The distribution of diameters was found to be approximately normal for all fibre types, and standard deviation values were calculated. Variation in fibre diameter was assessed by calculating the coefficient of variation, CV. This is a useful descriptive parameter for comparing data with different mean values and is given by:

$$CV = \frac{SD}{Mean} \tag{6.6}$$

For incorporation into AFCs it is desirable that fibres have a circular cross section, and that variation of geometry is minimal. Irregular shaped fibres, and fibres with large diameter distributions, will alter the distance between the fibre layer and electrodes, resulting in uneven electric field and reduced performance. Further, a small variation in diameter suggests a high degree of control in the manufacturing process.

Fibres produced by the VPP method displayed the lowest CV of 1.7% showing that diameter control is near optimum for this process. All fibres, apart from VSSP, have CV values between 2.1% to 2.4%. The VSSP fibres display a comparatively large CV of 5.1%, suggesting inadequate control in the manufacturing process. This issue has previously been identified when images were presented to account for the low elongation form factor (Figure 6.7(b)).

Using the elongation form factor and CV values as measures of circularity and diameter distribution it is suggested that fibres produced by VPP display the most favourable geometric characteristics for AFC manufacture.

6.3.4 Porosity and density

Measured fibre lengths and masses were tabulated in a spreadsheet program. The apparent density for each fibre was determined using the length and mass, together with the mean feret

diameter calculated in Section 6.3.3. Mean fibre densities for each fibre type are given in Table 6.4. The percentage of theoretical density was also calculated, taking the x-ray density of PZT to be 7.75 g cm^{-3}.[99]

Table 6.4: Bulk density for the 5 fibre types. Mean values are calculated for 100 unique fibres.

Fibre Type	Mean density (g cm^{-3})	Percentage of theoretical density
Extruded	6.50	84%
Alceru 250	7.42	96%
Alceru 125	7.15	92%
VPP	**7.70**	**99%**
VSSP	7.49	97%

All fibres except the extruded type have densities over 90%. Fibres formed by the VPP process have the highest density, approaching the theoretical x-ray density for PZT. This is most likely a result of the highly loaded green mix and the high shear mixing process this undergoes, which removes agglomerates prior to fibre forming. The relatively low density of the extruded fibres, which was clearly visible on the SEM micrographs, is speculated to be a result of insufficient PZT loading in the green mix, or poor de-agglomeration. During fibre handling it became apparent that the extruded fibres were more fragile than the other fibres. It is suggested that this is a direct result of the high porosity levels, and highlights that although not necessarily a requirement for high piezoelectric activity, a high density is important for imparting strength and robustness to the fibres. A strong fibre has obvious advantages in AFC manufacturing and operation.

6.3.5 Phase analysis and composition

The XRD traces for the five fibre types are presented in Figure 6.8. All reflections can be accounted for using the PZT reference spectrum. This confirms the absence of any non-piezoelectric pyrochlore phase in the fibres.

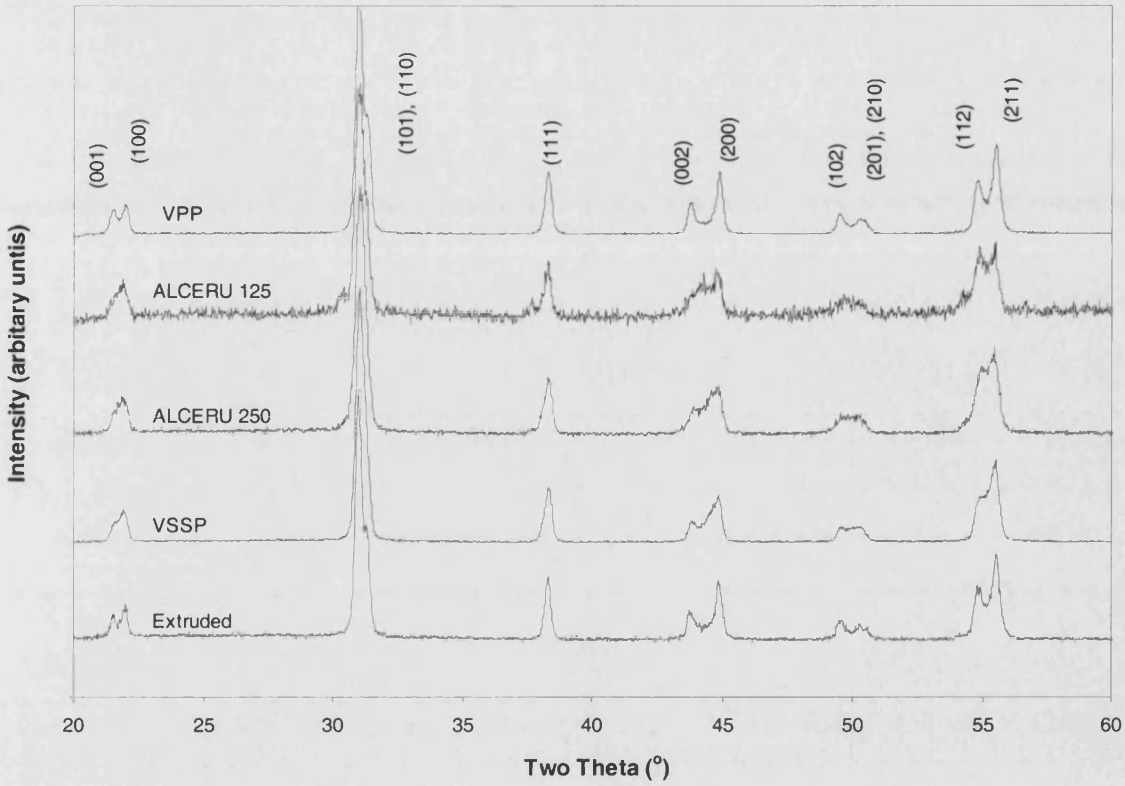

Figure 6.8: XRD profiles for the five fibres, all exhibiting fully developed perovskite structures.

Much study of the pyrochlore phase is related to sol-gel derived thin and thick films.[100-103] Pyrochlore, $Pb(Zr,Ti)_2O_{6+x}$, produces a strong reflection from the (222) plane at an approximate two theta value of 29° and typically transforms to PZT above 550°C to 600°C in sol gel films.[101,102] Since the firing temperature of fibres is estimated to reach at least 900°C it is not surprising that all fibres have a fully developed perovskite structure.

Having confirmed that the fibres are composed of the piezoelectric perovskite phase, it is possible to calculate the relative proportions of the Zr-rich rhombohedral phase and the Ti-rich tetragonal phase. This is achieved using the high-resolution scan performed in the two-theta range 43° to 46° as described in Section 6.2.4. Results are presented in Table 6.5.

Table 6.5: Summary of the phase composition of the fibre types.

Fibre Type	Percentage Rhombohedral Phase
Extruded	34.8
Alceru 250	51.6
Alceru 125	50.5
VPP	27.9
VSSP	53.2

The results in Table 6.5 show all fibres posses a mixture of rhombohedral and tetragonal phases, thus their compositions lie close to the morphotropic phase boundary. Since both Alceru fibres have an almost identical final composition, it can be inferred that they were formed from similar, or perhaps the same stock solution. As with the Alceru fibres, the VSSP fibres have an approximately even tetragonal-rhombohedral phase composition. The extruded fibres, with a high percentage of tetragonal phase PZT, are towards the Ti-rich side of the MPB. The VPP fibres, containing only 28% rhombohedral phase, are closer still to the Ti-rich end of the composition.

Research[13] has shown that the compositions richer in the tetragonal phase exhibit greater piezoelectric activity, as quantified by coupling factors and d_{33} coefficients. Therefore, it would be expected that the extruded and VPP fibres should display the best piezoelectric activity, while both Alceru fibres, and the VSSP fibres should display similar, but reduced activity.

The phase distribution, together with the other parameters measured in this chapter, will be used in the following section, to discuss structure-property links between the fibres.

6.4 Structure-Property Relationships

The large number of variables makes it difficult to draw firm links between the structure (grain size, grain morphology, composition and density) and piezoelectric properties. However, it is possible to draw broad conclusions, which is the aim of this section. It was shown in Chapter 3 that considerable differences exist in the piezoelectric properties of the five fibre types tested. A

general fibre piezoelectric ranking can be made based on the induced strain piezoelectric coefficient, d_{33}. This ranking, together with a summary of the composition, grain size and density is presented in Table 6.6.

Table 6.6: Fibre ranking based on the fibres' measured d_{33}. Also presented is composition, grain size and density information for drawing structure-property links.

Rank	Fibre Type	d_{33} (pCN^{-1})	% Rhombohedral Phase	Grain size (μm)	% Theoretical density
1	VPP	425	27.9	2.5	99%
2	VSSP	355	53.2	5.9	97%
3	Alceru-125	340	50.5	2.9	92%
4	Extruded	315	34.8	1.9	84%
5	Alceru-250	295	51.6	2.0	96%

If one compares the two Alceru fibres it is apparent that they differ greatly in their piezoelectric activity, quantified by their d_{33}. Their compositions are effectively identical, and their densities are high, above 90%. It is therefore possible to associate the reduction in piezoelectric activity with the grain size, which is 2.9 μm for the 125 μm diameter fibres but only 2.0 μm for the 250 μm diameter fibres.

Based on this result it can be postulated that the reduced activity of the extruded fibres is also due to the small grain size (1.9 μm). The 20 pC N^{-1} increase in d_{33} compared to the Alceru-250 fibres is thought to be associated with the composition of the extruded fibres being closer to the tetragonal phase field, which develops greater electro-mechanical coupling.

Since the VSSP fibres have a similar composition to the Alceru fibres, and are adequately dense, it is postulated that the reason for their higher piezoelectric performance is associated with their large grain size of 5.9 μm compared to 2.0 – 2.9 μm for the Alceru fibres.

The combination of favourable factors (a composition close to the tetragonal phase, a large grain size and a high density) associated with the VPP fibres is thought to be responsible for the large piezoelectric activity measured in these fibres.

6.5 AFC Fibre Choice

Chapters 2 through 5 have focused on developing finite element and analytical models, methods for sample preparation and assessing limitations of measurement techniques. This knowledge has allowed electrical, mechanical and piezoelectric property data to be collated for five fibre types. By combining these material property results with work presented in this chapter, it is possible to make an informed selection of the most suitable fibre type to incorporate into the AFC devices to be manufactured. Although it would be possible to incorporate any one of the five fibres characterised, there are certain characteristics that make some more suitable than others.

The low piezoelectric activity of the extruded and Alceru-250 fibres makes them a poor choice. The VSSP fibres, although possessing good piezoelectric performance, suffer from a large diameter variation, and poor consistency in roundness. This would be expected to introduce difficulties in the manufacturing process, and thus they will not be selected. The Alceru-125 fibres have a lower piezoelectric activity than the VSSP and VPP fibres, which is the primary reason for not selecting this fibre type. Their small diameter would also be expected to introduce unnecessary difficulties into the AFC manufacturing process.

Due to the high piezoelectric activity, suitable and constant diameter together with good roundness, the VPP fibres have been selected as the most suitable for AFC manufacture.

6.6 Chapter Summary

This chapter has presented the experimental techniques used, and the results obtained, relating to the physical and chemical analysis of the fibres. The diameter and roundness of the fibres was measured, with Alceru and VSSP fibres exhibiting poor morphological consistency compared with the other fibre types. Grain size, measured by the linear intercept method, was shown to be very different between the fibre types. Density measurements revealed that all except the extruded fibres possess adequate densities, estimated to produce a diminishingly small reduction in piezoelectric activity. Composition and phase analysis revealed the fibres to be comprised entirely of the piezoelectric perovskite phase, although different proportions of tetragonal and rhombohedral phases were measured. The large difference in the piezoelectric activity of the fibres, measured in previous chapters, has been successfully attributed to the combination of grain size, density and compositional differences measured in this chapter. The chapter concluded by selecting the VPP fibres for incorporation into an AFC device.

With the fibre choice made, it is now possible to investigate the other critical aspect of manufacturing an optimised AFC device; the interdigitated electrode. Design and manufacture of this AFC component is the focus of the following chapter.

CHAPTER 7

INTERDIGITATED ELECTRODES

7.1 Introduction

The interdigitated electrode (IDE) design, shown in Figure 1.1 in Chapter 1, is used to direct the electric field into in-plane directions, and excite the fibres' d_{33} response for actuation and sensing purposes. It consists of alternating polarity electrode fingers, attached to one of two side rails to which the driving voltage is applied. This pattern is mirrored on the underside of the composite. The IDE is an important component of the AFC, influencing the transfer of electric field to the active fibres and therefore influencing the device performance. Current research into the effects of IDE geometry on the resulting piezoelectric strain is limited,[16,17,57] and has not fully investigated the underlying reasons why a particular electrode design produces a large piezoelectric response. Because of this, there is a lack of clear design rules, making it difficult to manufacture optimised electrode designs.

Optimisation of the electrode design requires an understanding of the influence of electrode geometry on the transfer of electric field to in-plane directions. Since there are three main geometric variables affecting this process (electrode finger width, electrode separation and substrate thickness), to perform a thorough experimental analysis, involving the manufacture of a large number of IDE devices, would be time consuming. Furthermore, no fundamental understanding of the influence of electrode design on the electric field distribution within the AFC would be obtained. Finite element analysis is suited to such a problem because of the ease with which geometric parameters can be varied. Further, a solved model can be interrogated to provide information on the state of the electric field distribution induced by the various electrode geometries.

The first section in this chapter covers optimisation of the IDE using finite element analysis. Manufacture of the optimised electrode design forms the second section, in which a detailed description of the production process is presented, and issues associated with the manufacturing stages are discussed.

7.2 Optimising Interdigitated Electrode Designs using FE analysis

The finite element analysis method, used to investigate the effects of electrode geometry, is introduced in this section. The actuation performance of a piezoelectric substrate with interdigitated electrodes is influenced by three main parameters:

(i) Electrode width (w)

(ii) Electrode spacing (s)

(iii) Substrate thickness (t)

These three parameters are defined in the 2-D representation of an IDE structure presented in Figure 7.1.

The finite element software ANSYS was used to model an IDE in direct contact with a piezoelectric substrate. For all models a two-dimensional analysis was performed in the x-y plane, simplifying the model and reducing computational time. This analysis is possible since the IDE configuration can be considered infinitely long in the z, or finger length direction. However, two-dimensional modelling is incapable of representing the fibre geometry of the piezoelectric substrate. Therefore, the substrate is modelled as a bulk piezoelectric. Although the AFC response will differ from the modelled response because of this choice, using a bulk substrate simplifies the analysis. This two-dimensional analysis can be considered the first stage in modelling, after which the model can be extended to investigate the more complex situation of incorporating a fibre geometry into the model.

7.2.1 Model construction

A schematic 2-D representation of an IDE on a bulk substrate is shown in Figure 7.1(a), which illustrates the non-uniform electric field lines that are known to result from this electrode geometry. The key parameters associated with interdigitated electrode geometry are; electrode finger width (w), electrode finger spacing (s), and substrate thickness (t). These are labelled in the figure. The modelled representative volume element (RVE) is highlighted in Figure 7.1(a) by a broken black line. An enlarged RVE is shown in Figure 7.1(b) with an example mesh, and is labelled with appropriate dimensions. In this figure the surfaces are numbered 1 to 4 to aid in defining boundary conditions.

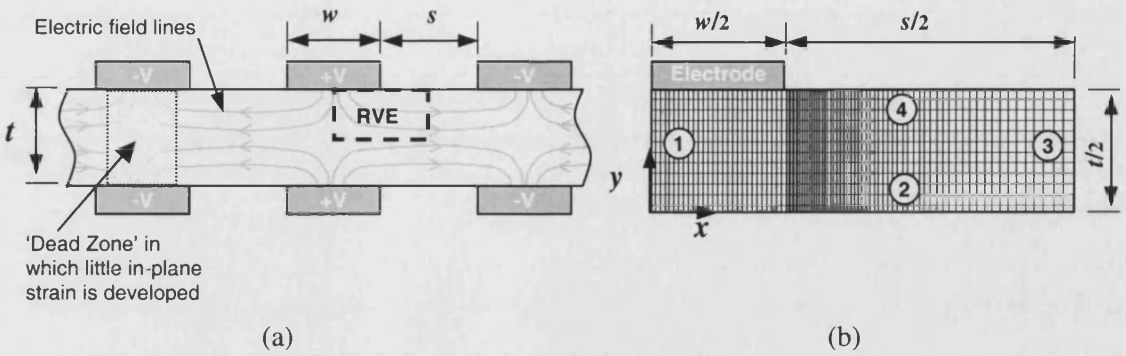

Figure 7.1: (a) Schematic of a 2-D interdigitated electrode showing the electric field lines, geometry notation, and representative volume element (RVE). (b) The enlarged RVE illustrating an example finite element mesh.

The model was constructed in the *x-y* plane, a necessity for 2-D modelling. The substrate was modelled as PZT-5A and meshed with 2-D coupled-field elements with piezoelectric capability (PLANE13: 4-node quadrilateral). The element was set to plane stress conditions, implying that the model extends indefinitely in the *z*-direction (into the page). This will of course not be true for the entire electrode structure, but will represent the conditions experienced by the majority of the device, away from the electrode finger ends, and electrode side rails to which all fingers are connected. The fine element mesh size at the electrode edge was used to capture the localised effects known to exist in this region. The presence of the electrode in Figure 7.1(b) was captured by the imposed electrical boundary conditions at this location on the surface. Appropriate mechanical and electrical boundary conditions are detailed in Table 7.1.

Table 7.1: Boundary conditions of displacement (U), electrical potential (V), and electrical displacement (D) applied to the RVE.

Surface Number	Mechanical Conditions	Electrical Conditions
1	Symmetry (U_x= 0)	D_x = 0
2	Symmetry (U_y= 0)	D_y = 0
3	U_x coupled	V = 0V
4	Free	V = +V/2 on electrode, D_y = 0 elsewere

Previous research[57] has shown that the electric field direction within the substrate is non-uniform and will follow the field lines depicted in Figure 7.1(a). Since poling IDE devices is performed *in-situ*, using the IDEs, the direction of poling will follow these field lines. As a result the material properties will constantly change with respect to the model axis, especially close to the electrode regions. It is not possible to model this variation in material property directionality in ANSYS and simplifications must be made. Therefore, the substrate was assumed to be uniformly poled in the x-direction. This simplification should prove adequate for large electrode separations, in which the majority of the device's response is attributed to the region between the electrodes, where the material is uniformly poled. However, for small electrode separations, differences between the modelled and actual response could exist.

Model dimensions were varied to investigate the effect of electrode finger width, electrode finger separation, and substrate thickness. The figure of merit used to assess the electrode geometry effects was the strain (S) developed in the x-direction per unit applied voltage. To gain an insight into electric field distribution within the substrate, vector plots of electric field were used. Additionally, plots of electric field strength in the x-direction at the substrate centre axis ($y = 0$ in Figure 7.1(b)) were used.

The results of the finite element analysis are presented and discussed below.

7.2.2 Finite element results

Electrode width effects

It is known from previous research that dead zones exist under the electrode fingers, where the field is weak and out of plane. Finite element analysis was performed to investigate the expected degradation in the strain performance as the electrode finger width increases, resulting from dead zone effects. A model was constructed in which the electrode width was varied, while the substrate thickness and applied voltage were held constant at 200 μm and 500 V respectively. Results showing the effect of electrode width (w) on the actuation performance of an electroded substrate are presented in Figure 7.2. The results are presented for three electrode separations.

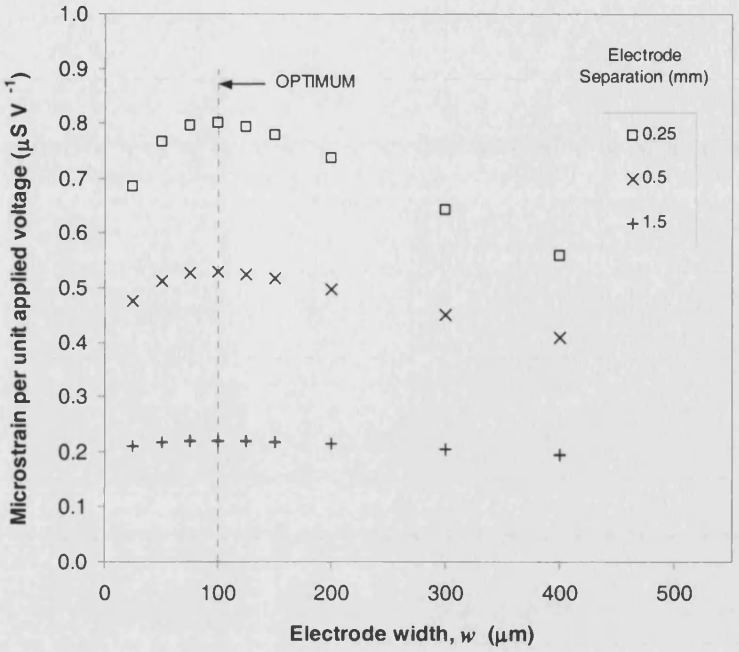

Figure 7.2: Finite element results for electrode width analysis showing the effect of electrode width on the strain response of an interdigital electroded PZT substrate (t = 200 μm) for three electrode separations.

Figure 7.2 shows that as the electrode separation is reduced, the strain per unit applied voltage increases. This can be explained by the higher induced electric field between the electrodes for a fixed voltage as the electrode fingers approach closer, and does not necessarily infer that small electrode separations increase performance. This point will be highlighted later, when the electrode separation results are discussed. More importantly for the present analysis, Figure 7.2 shows that an optimum electrode width exists, at which the strain per unit applied voltage is at a maximum. This width is independent of electrode separation and substrate thickness (data not shown in the figure). The optimum occurs at an electrode width equal to half the substrate thickness (w/t = 0.5), and the strain per unit voltage is increasingly sensitive to the electrode width at small separations.

To understand why this optimum exists it is necessary to examine how the electric field vector in the substrate varies as the electrode width is altered. To simplify the visualisation of this information a path has been specified, located at the centre line of the substrate, as depicted in Figure 7.3. The electric field in the x-direction has been mapped onto this path using the tools available in ANSYS.

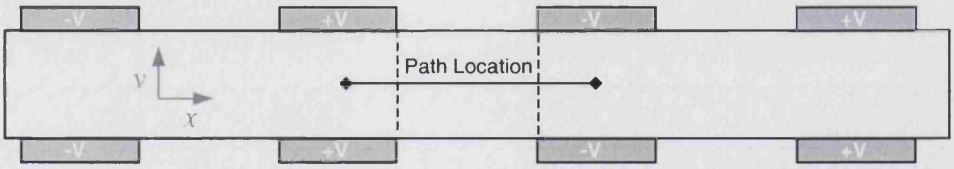

Figure 7.3: Location of the path generated to simplify visualisation of the electric field distribution. Broken lines depict the location of the electrode edge on the path.

Plots of electric field in the *x*-direction on the path illustrated in Figure 7.3, the substrate centre axis, are presented in Figure 7.4. This figure contains electric field plots for the optimum *w/t* ratio of 0.5 (w = 100 μm), and for ratios larger and smaller than the optimum.

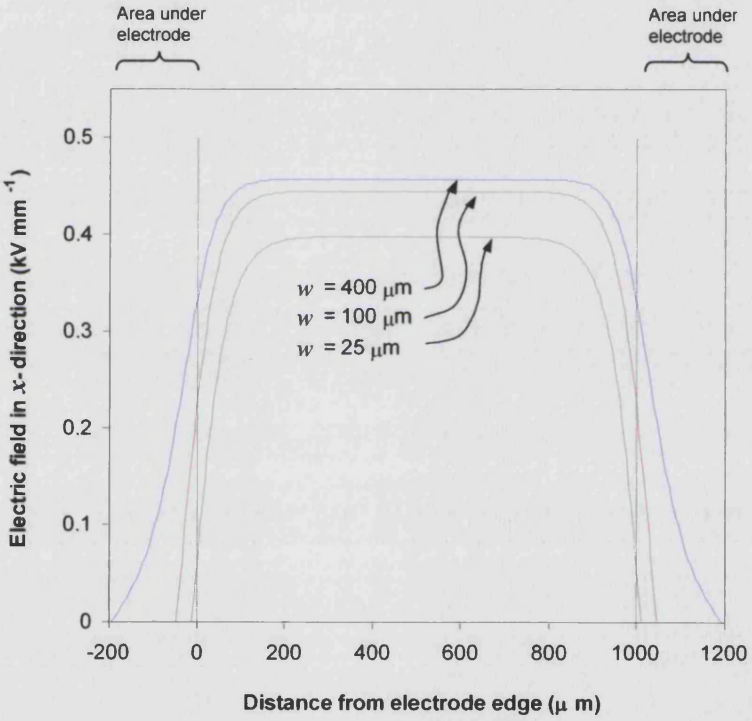

Figure 7.4: Path plots of electric field in *x*-direction at the substrate centre axis (y = 0) for three electrode widths (t = 200 μm, s = 1mm, V = 0.5kV). The broken line is location of the electrode edges.

For wide electrodes (w = 400 μm, w/t = 2) the electric field strength in the *x*–direction between the electrodes is high, but a significant proportion of 'dead area' exists under the electrode, where the field in the *x*-direction is low. For thin electrodes (w = 25 μm, w/t = 0.125) the proportion of dead area is reduced, but this is at the expense of lowering the electric field strength between the electrodes. This implies there is an optimum electrode width between these two extremes, at which

maximum actuation is achieved. The optimum *w/t* ratio, a balance between the proportion of dead area under the electrode and the strength of electric field between the electrodes, occurs at a *w/t* ratio of 0.5 (w = 100 μm), as revealed by the analysis presented in Figure 7.2.

An alternative method of displaying the results of this analysis is in the form of a vector plot. The advantage of this representation over the path plot method is that it becomes possible to visualise both the magnitude and direction of the electric field within the entire substrate. This reveals important information not available from the path plot method presented previously. Located in Figure 7.5 are vector plots of the electric field within the modelled RVE for the three electrode widths presented in Figure 7.4. The direction of the electric field is denoted by the arrow direction, while the colour of the arrow indicates the field strength. The electrode location is indicated by the grey region, on the top surface of each of the substrates.

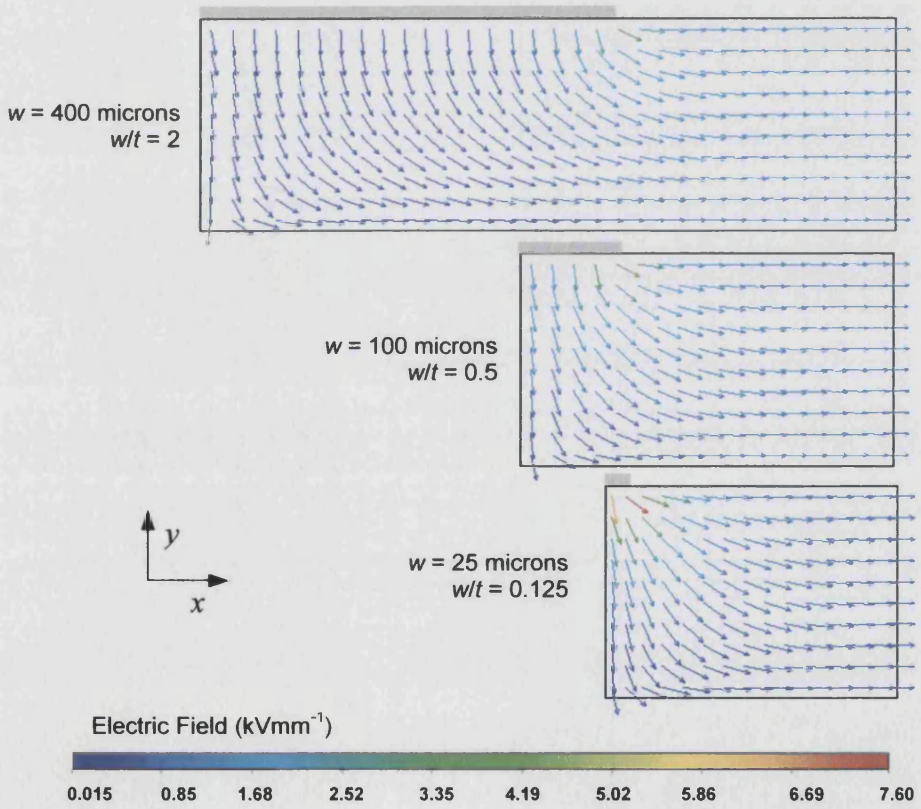

Figure 7.5. Vector plots of electric field distribution within the modelled RVE of an IDE structure with varying electrode widths. Voltage = 0.5 kV, PZT thickness = 200 μm, electrode separation = 1.0 mm. The electrode locations are indicated by the light grey region, on the surface of each substrate.

For large electrode widths, there is a significant dead zone below the electrodes, where the field is perpendicular to the actuation direction (x). For thin electrodes, a relatively weak field is observed between the electrode fingers. In addition to confirming the results of the path plot analysis, the vector plots presented in Figure 7.5 show that a field concentration exists at the electrode edge. The magnitude of the field strength in this location increases as the w/t ratio is reduced, while the direction remains largely unaffected. Modelling and actual device studies,[17,57] show that the non-uniform fields present at electrode edges can cause cracking of the piezoelectric substrate resulting in device deterioration. This is a consequence of the large and non-uniform mechanical stresses induced via the piezoelectric effect. Although induced stresses are not quantified in this study, it is an important effect that could lead to device failure. These effects should therefore be considered in future modelling, which could also investigate functionally graded fibres, and the influence of polymer layers between the electrode and the piezoelectric fibre. These polymer layers could act as a buffer zone for the field and stress concentration effects, although this would be at the expense of reduced strain.

With the optimum electrode width determined, and the underlying reason understood, it is now possible to investigate the effect of substrate thickness on the strain output of the device.

Substrate thickness effects

While investigating the effects of varying the substrate thickness the electrode width is also varied, keeping the w/t ratio at the optimum value of 0.5. Throughout the analysis the electrode spacing s is held constant at 1.0 mm.

Figure 7.6 presents the results of device strain as the substrate thickness varies from 800 to 25 μm.

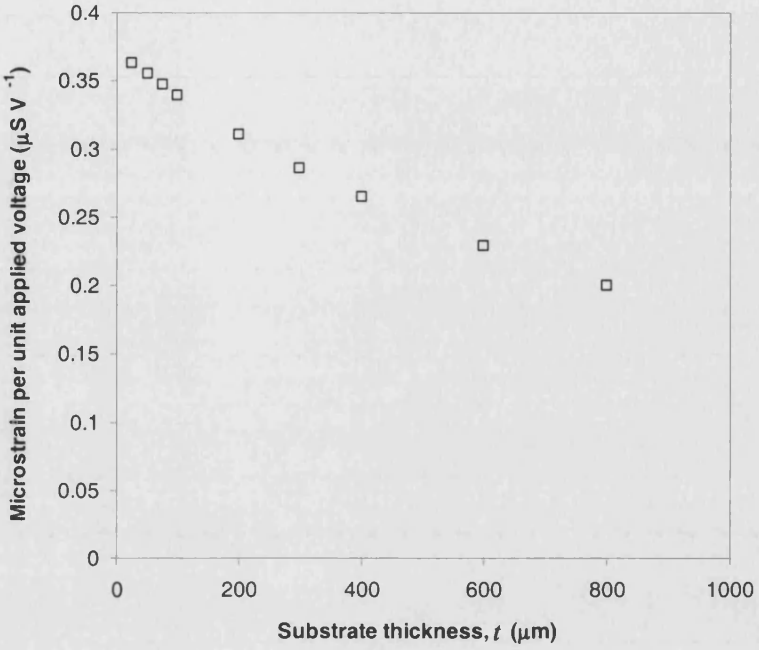

Figure 7.6: Finite element results for substrate thickness analysis, showing its effect on the strain response of an interdigital electroded substrate (w/t = 0.5, s = 1.0 mm).

Figure 7.6 shows that for a fixed voltage, electrode spacing, and optimum w/t ratio of 0.5, the strain per unit applied voltage increases as the PZT thickness is reduced. The reasons for this strain increase become clear if the path plot method is used to analyse the electric field distribution within the substrate.

The results of the path plot analysis are presented in Figure 7.7. In this figure the electric field in the x-direction at the substrate centre axis (Figure 7.3) is plotted for three substrate thicknesses.

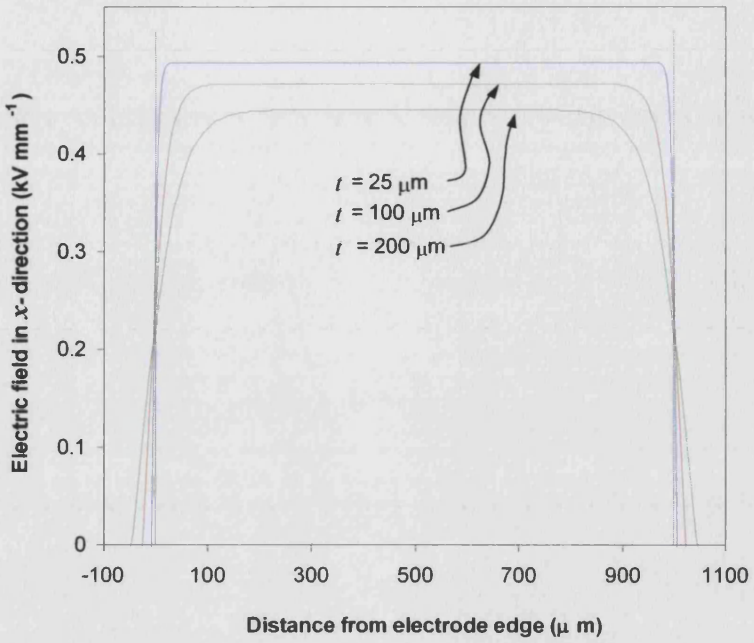

Figure 7.7: Path plots of electric field in x-direction at the substrate centre axis (y = 0) for three substrate thicknesses (w/t = 0.5, s = 1.0 mm, V = 0.5 kV). The broken line is location of the electrode edges

Examination of the path plot results reveal two effects which can explain the trends seen in Figure 7.6. Firstly, as the substrate thickness is reduced, the electric field between the electrodes becomes larger. In addition, the electric field becomes directed into the in-plane direction over a shorter distance, reducing the proportion of 'dead area.' Both these effects are due to opposing electrodes on each side of the ceramic substrate approaching closer as the substrate thickness is reduced, thus exerting a stronger influence on one another.

To quantify the benefits of reducing the substrate thickness, approximately a 17% increase in the strain per unit voltage can be expected when the substrate is reduced from 200 μm to 25 μm. It is likely that a similar trend, and thus similar performance benefits will be observed if the substrate consisted of fibres. This analysis therefore provides evidence of a further benefit resulting from the ability to reduce the diameter of PZT fibres.

The results obtained have shown that thin substrates, and electrodes widths conforming to the optimum w/t ratio of 0.5, provide increased actuation performance. The final parameter for optimisation is the electrode finger spacing, which is now examined.

Electrode spacing effects

It has previously been shown that dead zones exist below the electrode fingers, with the field being weak and out of plane. Between the electrode fingers the field is in the desired in-plane direction, and uniform. With large electrode separations the majority of the field is aligned in the desired direction and the proportion of dead zones is low. This results in little degradation of actuation performance. However, because of the large electrode spacing the voltage required to induce a sufficient field to operate the device is high. In contrast, small electrode separations reduce the operational voltage, but increase the proportion of dead area, degrading the actuation performance. Because of these competing factors a compromise must be made between the desired actuation strain level and the operational voltage. To investigate this issue, a model was constructed with a substrate thickness of 200 μm and electrode width of 100 μm ($w/t = 0.5$). The electrode separation was varied from 0.01 to 100 mm and the strain developed by an electrode potential difference of 500 V was recorded. The figure of merit used to compare the results obtained was the strain per unit applied voltage.

By simply plotting the results of actuation strain per unit applied voltage as a function of electrode separation little insight into the effects of electrode separation is obtained. To gain more from the results it is desirable to quantify how much strain degradation arises from the dead zones. To achieve this, one can compare the FE results to an ideal actuator, in which there are no dead zones (all electric field vectors aligned in the in-plane direction). A schematic of the electric field distribution in a true 'IDE actuator', and the desired 'ideal actuator' are presented in Figure 7.8.

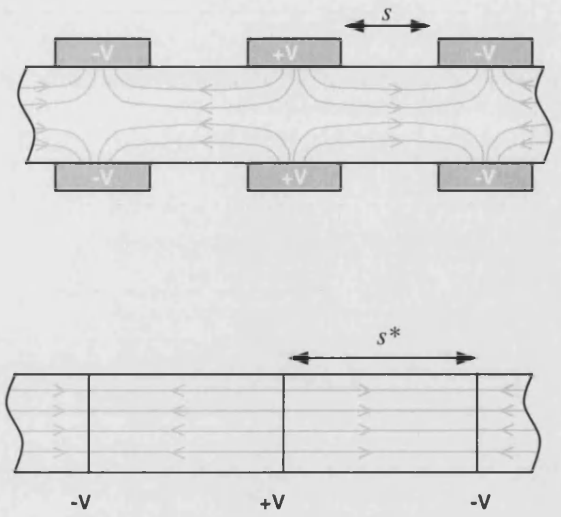

IDE Actuator
Strain per unit applied voltage determined from finite element modelling.

Ideal Actuator
Strain per unit applied voltage determined from electromechanical relationships.

Figure 7.8: Schematic representations of the electric field vector for the interdigitaded geometry electrode, and an ideal case with no dead zones.

The strain for the IDE geometry, S_{IDE}, must be determined from the solved finite element model because of the complex field distribution. For the ideal case the strain, S_{Ideal}, can be calculated from equations describing the electromechanical response. For the ideal case the strain per unit voltage as a function of electrode separation, s^*, will obey the relationship given in Equation (7.1).

$$\frac{S_{Ideal}}{V} = \frac{d_{33}}{s^*} \tag{7.1}$$

Figure 7.9 shows the strain response of the substrate as a function of electrode separation for both the IDE electrode (finite element results) and the ideal response (calculated results).

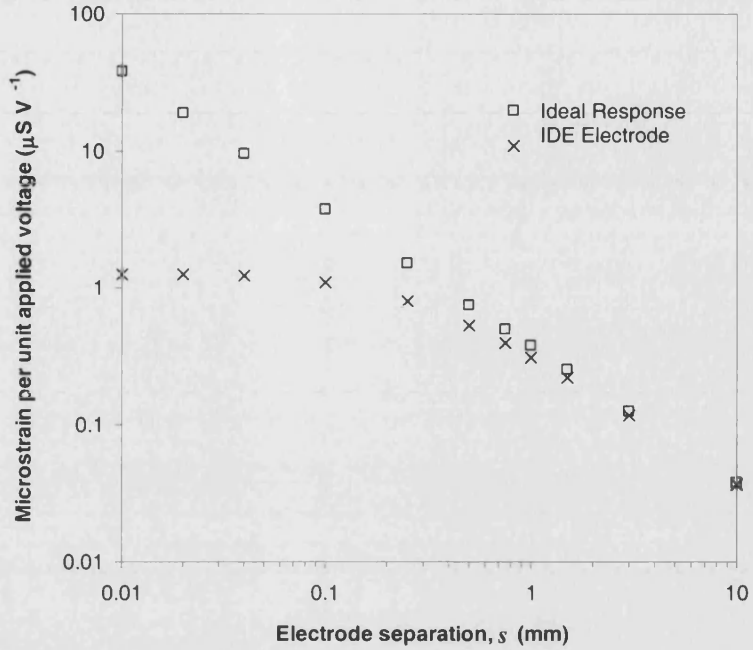

Figure 7.9: Results of the electrode separation analysis showing the IDE and ideal strain response as a function of electrode separation

This data shows that the ideal response is a linear relationship between the strain and the electrode separation. However, the IDE electrode results show that as the electrode spacing is reduced the strain deviates from the 'ideal response' trend. This degradation in strain compared to the ideal case is due to the non-uniform fields present near the electrodes. The magnitude of this effect can be quantified by calculating S_{IDE} / S_{ideal}.

Figure 7.10 plots S_{IDE} / S_{ideal} as a function of electrode separation for three PZT thicknesses. In all cases the electrode width was set so that $w/t = 0.5$.

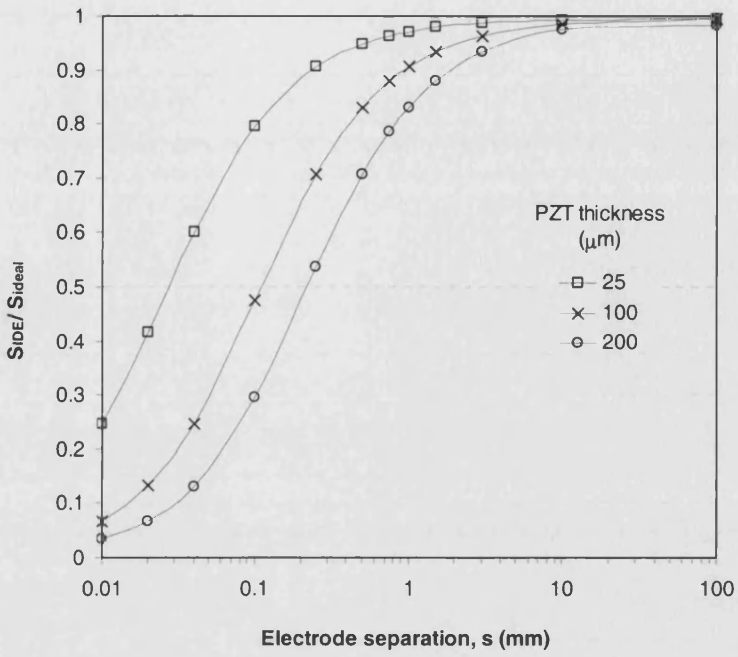

Figure 7.10: The strain response of an IDE substrate compared to that of the idealised strain response for three substrate thicknesses.

Figure 7.10 reveals that at large electrode separations the strain response is close to the ideal case, with $S_{IDE}/S_{ideal} \approx 1$. As the electrode separation is reduced the dead zones begin to dominate, and the IDE strain begins to diminish compared to the ideal response. A primary reason for using an IDE is to take advantage of the d_{33} response, which is approximately twice as large as the d_{31} response. Therefore, once the IDE actuation strain is lower than 50% the ideal case ($S_{IDE}/S_{ideal} <$ 0.5) this benefit is lost. From Figure 7.10 it is apparent that for thinner PZT substrates the electrode separation can be reduced significantly while still maintaining a high percentage of ideal response.

The graph presented in Figure 7.10 can be used as a design guide for IDEs. For example, to obtain at least 80% of the d_{33} response electrode separations must satisfy $s/t > 4$. Using this guideline, substrates with a thickness of 200 μm require electrode separations greater than 0.8 mm. This separation reduces to 0.1 mm for a substrate thickness of 25 μm. This is significant since a reduced electrode separation allows driving voltages, which are typically very high, to be reduced. A clear benefit from using thin substrates (small diameter fibres in AFCs) now becomes apparent. Thus fibre manufacturing techniques have to be capable of producing small diameter fibres of high quality.

7.3 Electrode Manufacture

Based on the finite element modelling, used to understand the fundamentals of the electrode geometry, it now becomes possible to design and manufacture an efficient IDE for use in subsequent AFC manufacture. Many techniques are available for manufacturing electrode structures, and have been discussed in the literature review in Chapter 1. They derive from two main processing routes; photolithography or screen-printing. The requirements below will help to make a decision of how best to choose between these two routes:

(i) *Resolution*: Electrode finger widths need to be 120 μm for the VPP fibres 240 μm in diameter. This is to maintain the optimum *w/t* ratio of 0.5.

(ii) *Design changes*: The IDE design may need to be changed to allow manufacture of different geometry electrodes for use with different fibres, or for a specific application.

(iii) *Cost*: The cost should be kept low because of the available budget. An in-house process is desirable since this would limit the cost to the raw materials (silver, copper substrate material etc.).

Based on the above requirements a photolithography technique was selected as the most appropriate method of electrode manufacture. Although both photolithography and screen-printing are suited to IDE manufacture, the lithography process can be conducted in-house at Bath with proven methods. Design changes are relatively simple, requiring only a new mask to be designed and made.

For photolithography, a thin non-conducting film is required to be clad with copper, which will then be etched to leave the IDE geometry. The film used to make flexible circuit boards is one such material. Its availability in a range of copper and supporting substrate thicknesses makes it an ideal choice for an electrode material. Since the main requirement of the AFC is to actuate, any non-piezoelectric materials incorporated into the design will reduce the effectiveness by clamping the motion of the fibres. With this in mind it is desirable for the electrode assembly to be as thin as possible. The specifications of the chosen electrode material, which has a thickness of 50 μm, are depicted in Figure 7.11.

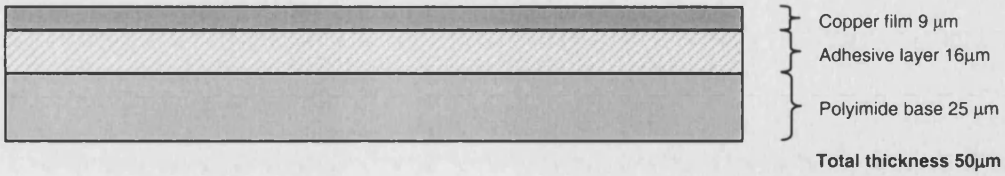

Figure 7.11: Schematic representation of the copper clad polyimide film selected for electrode manufacture.

The following section briefly describes each of the manufacturing stages required to transform this flexible copper clad polyimide film into an interdigitated electrode. Following this, key stages of the process are discussed in more detail.

7.3.1 Manufacturing process

Photolithography, or optical lithography, using UV radiation is the process of transferring geometric shapes from a mask to the surface of a substrate material, in this case the copper clad film. Once this pattern has been transferred a simple etching process is used, removing the exposed copper to leave the IDE geometry. The steps involved are described in the following paragraphs.

Electrode mask design and manufacture

Prior to performing photolithography a suitable electrode geometry must be designed. This is described in more detail in Section 7.3.2, and uses the design guidelines presented in the first part of this chapter. The electrode design was printed 10× oversized onto high quality white paper using a black and white laser printer set to high resolution. Regions required to be copper (i.e. the electrode tracks) were white, while regions desired to be copper-free were black. A photograph was then taken of the electrode design with a camera that was positioned such that a 10× reduction of the mask is formed on the photograph negative. The negative, in which the electrode pattern is now black, is the finished mask of correct dimensions. Once developed, optical microscopy was used to check the quality and dimensions of the tracks. The negative was then fixed to a glass plate ready for insertion into the mask aligner.

Electrode film preparation

A rectangular section, 25 × 50 mm in size, was cut from the roll of copper clad polyimide film. Grease and other surface contaminants were removed from the copper surface using acetone. The copper microstructure has a preferred orientation resulting from the rolling operations used in its production. The electrode finger direction was aligned with the rolling direction, the grain's long axis. It is postulated that this alignment will increase the straightness of the electrode finger edges during etching. In preparation for photo resist spinning a glass slide, with the same dimensions as the electrode, was coated with a thin layer of photo resist. The clean film was positioned onto the glass slide with copper face uppermost. The polyimide film and glass slide assembly was placed in an oven at 90 °C for 1 hour to dry the photo resist, which acted to fix the electrode in place. The film, now held rigidly onto the glass slide, was now suitable for photo resist application using a spinning process.

Photo resist spinning

After removing the polyimide film and glass slide assembly from the oven, surface contaminants, such as dust, were removed from the copper surface using a compressed air jet. This was found to be an essential stage, since a smooth and contaminant free surface is critical for uniform photo resist coverage using the spinning process. For this reason care was also taken not to crease or fold the polyimide film when initially cutting it from the roll. The assembly was then positioned on the vacuum chuck in the photo resist spinning apparatus (Headway Research, Inc. PWM32 Spinner). A 'positive' photo resist (Shipley Microposit S1813) was applied to the copper surface using a syringe fitted with a 0.45 μm filter to remove any contaminants from the resist solution. Spinning at 4000 rpm for 30 seconds resulted in a thin and uniform layer of photo resist coating the copper surface. The assembly was then baked in an oven at 90°C for 45 minutes to remove the solvents from the resist coating. The coated electrode film was then positioned into the mask aligner (Karl Suss, MJB3 Mask Aligner) in preparation for UV exposure.

UV exposure

A contact printing technique was used to transfer the electrode pattern from the mask onto the electrode. The mask was brought into direct physical contact with the electrode using the mask aligner, allowing high-resolution features to be imaged. Once contact has been made, the photo resist was exposed to high intensity UV radiation for 3.5 seconds through the mask. UV radiation was prevented from reaching the entire electrode surface because of the pattern on the mask.

Photo resist development

After exposure the electrode assembly was removed from the mask aligner and developed (Shipley Microposit 151 developer solution) for 30 to 40 seconds. During this process regions that were exposed to UV radiation were removed from the copper surface since they were now soluble in the developer solution. The only resist remaining on the copper surface was in the desired electrode pattern. Once the electrode pattern had been fully developed, the assembly was rinsed with distilled water and dried using compressed air. This prevented any further development of the resist.

Copper etching and quality control

Removal of the exposed copper was achieved by placing the electrode assembly into an etch tank containing ferric chloride ($FeCl_3$) solution. Bubbles formed at the base of the tank induce agitation of the $FeCl_3$ solution. This results in faster and more uniform removal of copper. Etching for 6 minutes at room temperature was sufficient to remove all exposed copper. On removal from the etch tank the electrode was rinsed with distilled water, and the electrode dried with hot air. The remaining photo resist, covering regions with retained copper, was removed with acetone. The resulting electrode pattern was observed under a microscope to assess the quality of the finished product. If the electrode quality was suitable it was peeled from the glass slide using acetone as a solvent to weaken the photo resist 'glue'.

The sections above have briefly discussed the electrode manufacture stages. A few of the key stages (mask design and manufacture, electrode etching, and electrode assessment) are discussed in more detail in the following section.

7.3.2 Key manufacturing stages

Mask design and manufacture

The electrode design should take into consideration electrode spacing, electrode width and overall dimensions. The electrode finger width is set to 120 μm giving a *w/t* ratio of 0.5 for the VPP fibre selected for AFC manufacture (240 μm in diameter). This is the optimised value obtained from the FE modelling (Figure 7.2). The electrode finger spacing was chosen to be 1.0 mm as the graph in Figure 7.10 shows that this attains over 85% of the ideal actuation response while maintaining the ability to pole and actuate with reasonable voltages. The overall dimensions of the electrode are restricted by the manufacturing process chosen since the maximum area that can be exposed in the mask aligner is a 5 cm diameter circle. The distance between the electrode finger ends to the side rail is set to be 1.5× the electrode finger spacing. This maximises the active area while reducing the risk of breakdown to the side rails. As an additional measure to reduce the possibility of breakdown, both the initiation and termination of the electrode fingers have been rounded to reduce field concentrations. Two electrodes were designed, for the top and bottom of the AFC. These are simply mirror images of each other.

The design of the bottom electrode is shown in the scale drawing in Figure 7.12. This image was generated using CorelDRAW 9. The electrode consists of 15 electrode fingers, 120 μm in width with a spacing of 1 mm. The fingers are connected to the two side rails, which are in turn connected to large pads. Wires can be soldered to these pads for the purpose of supplying the driving voltage. The active area of this electrode is approximately 237 mm^2. The active area has been designed to be square to allow manufacture of multi-ply AFCs.

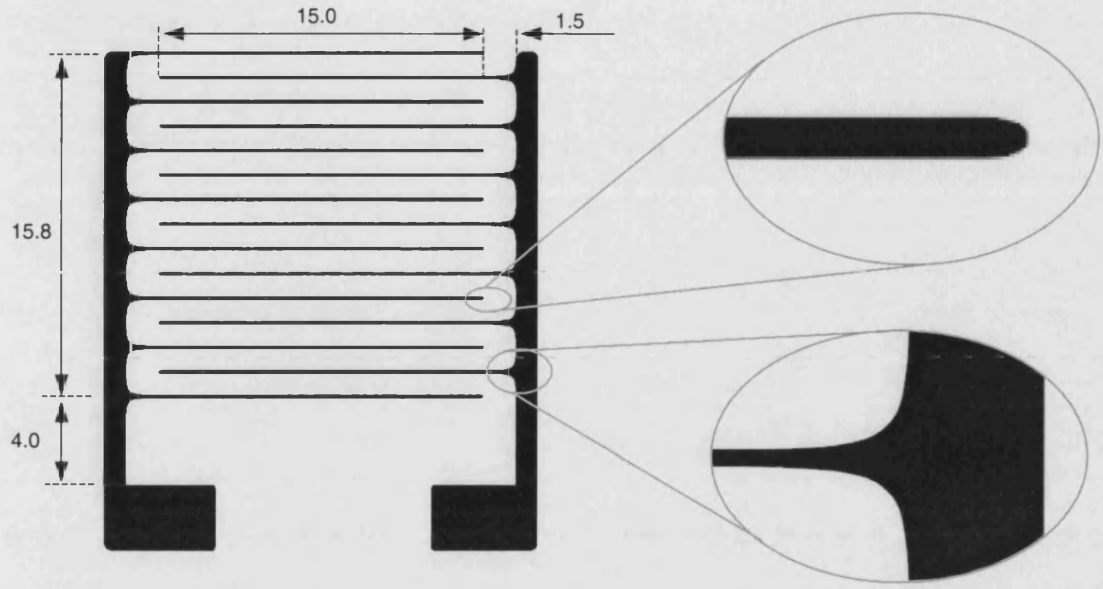

Figure 7.12: A scale drawing of the bottom electrode design. The enlarged sections show the detail of the initiation and termination of the electrode fingers. Dimensions are in mm.

Initially, the mask was created from the computer image file by printing onto clear acetate using a black and white laser printer (HP LaserJet 4.0). However, the electrode masks generated using this method were of low quality, and suffered from poor dimensional reproduction, a result of the limits of the printer capabilities. Improved mask quality was obtained by printing the mask 10× oversized onto standard A4 size paper, and photo reducing the image onto a 35 mm film. High and low magnification images of masks generated from both of these processes are presented in Figure 7.13.

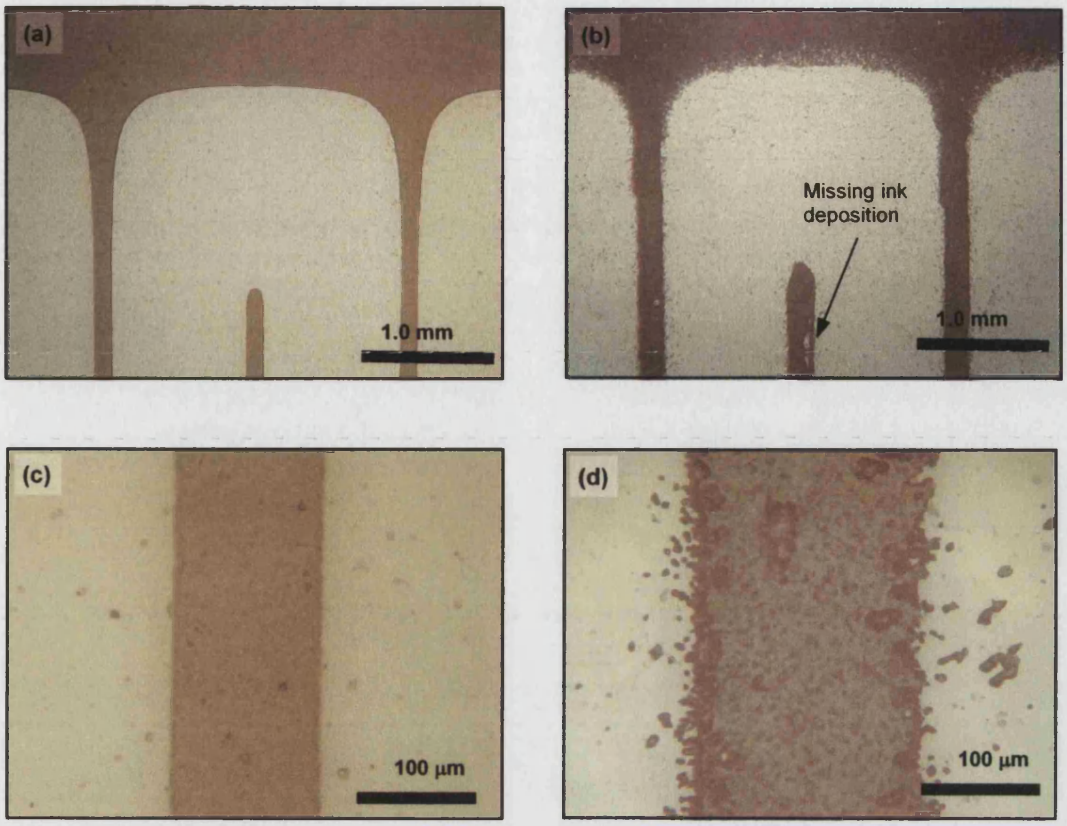

Figure 7.13: Comparison of the overall quality of electrode masks produced by (a) photo reduction and (b) direct printing. Images (c) and (d) show a single electrode finger on the mask formed by photo reduction and direct printing respectively.

Comparing Figure 7.13(a) and (b) it is clear that the quality of the ink deposition in the direct printing is poor, with ink failing to be deposited in some regions, as indicated in Figure 7.13(b). This could potentially result in breakages in the electrode fingers, or worse, in the electrode side rails. The poor edge quality of the direct printed mask is also apparent, with edges exhibiting a 'hazy' appearance. This effect can be seen more clearly in the image of an individual electrode finger, Figure 7.13(d), where ink is deposited in undesired regions. A further problem with the direct printing method is that the electrode finger widths are much wider than desired, while the mask made using photo reduction, Figure 7.13(c), displays the correct electrode finger width of 125 µm. Based on quality, photo reduction was selected as the mask manufacturing route. However, this choice limits the electrode dimensions to the size of the negative. In this case a 35 mm black and white film was used.

After exposing and developing this pattern onto the resist coated copper film it is necessary to etch the exposed copper. Issues arising from this stage are now discussed.

Etching

Factors such as temperature, time and agitation all affect the rate at which the copper is etched, and will also influence the dimensions of the resulting electrode pattern. Figure 7.14 contains optical micrographs of the same section of the electrode after different development times. The images show the copper being removed, and the electrode pattern developing with time.

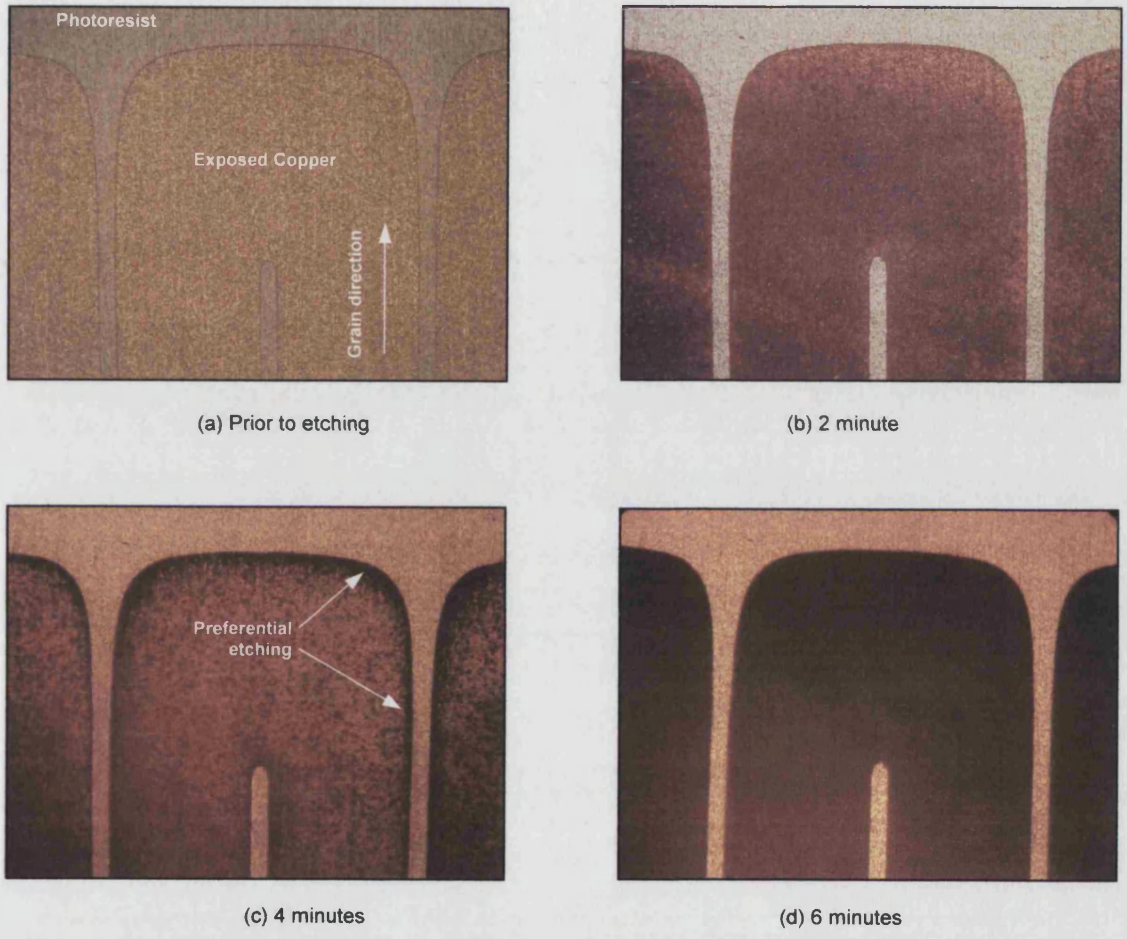

Figure 7.14: Optical images of the stages in electrode etching after various etching times. The electrode finger spacing is 1.0 mm.

Figure 7.14(a) shows how the exposed copper surface and the surface coated by the photo resist are clearly distinguishable prior to etching. In this micrograph the rolling direction of the copper, and hence the grain elongation direction, is aligned with the electrode finger direction, as indicated. Figure 7.14(b) shows that after two minute of etching the copper surface has been attacked by the etch solution, but small areas of the initial copper surface are still present in numerous regions. These regions appear as bright spots in the micrograph and are thought to be associated with the

photograph negative mask not being completely transparent to UV over the entire area. After four minutes of etching (Figure 7.14(c)) some of the regions of exposed copper have been completely removed, leaving the dark streaks of the underlying adhesive visible. It is also clear that preferential etching is occurring at the boundaries between the photo resist and bare copper. The darker colour in these regions, which is the underlying adhesive substrate, provide evidence of this. Large area coverage of the copper still exists. Figure 7.14(d) reveals that after six minutes of etching, copper in exposed regions has been completely removed, while regions covered with photo resist remain un-etched. The electrode pattern has been formed.

The preferential etching at the photo resist edges seen in Figure 7.14(c) leads to 'undercutting'. This is where the etch solution penetrates beneath the photo resist, resulting in thinning of the electrode fingers. The magnitude of this effect can be significant, and is revealed in Figure 7.15, which shows high magnification photos of an electrode finger tip after being exposed to the etch solution for different periods of time.

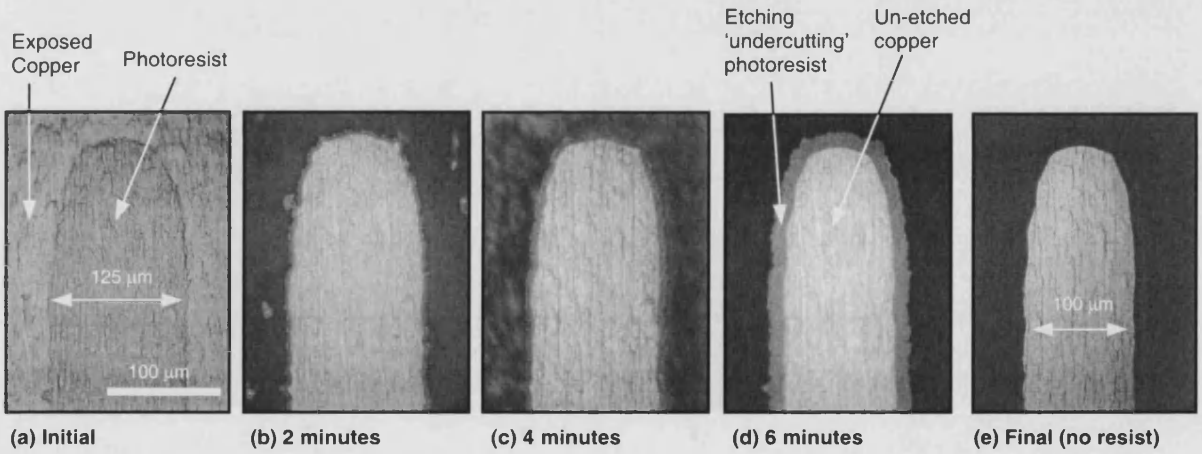

Figure 7.15: Stages in electrode etching showing the undercut of the electrode fingers after various etching times.

Figure 7.15(a), the 'initial' micrograph, shows the photo resist forming an electrode finger tip. The width of this electrode finger is the desired width of 125 µm. After two minutes of etching (Figure 7.15(b)) the exposed copper regions have begun to be attacked by the etch solution but small regions of copper outside the electrode finger region remain untouched by the etch solution. This is because of incomplete removal of the photo-resist in these regions. However, Figure 7.15(c) shows that after four minutes these regions have been fully etched because the etch solution

undercuts the photo-resist. After six minutes, the etching time required to remove all of the exposed copper, the photo resist can clearly be seen extending over the copper finger. It is clear from Figure 7.15(d) that the photo-resist remains intact while the undercut process is occurring, allowing the degree of undercutting to be readily visualised. Figure 7.15(e), the 'final' micrograph, was taken after removing the photo-resist using acetone. Comparing the 'initial' micrograph to the 'final' micrograph the degree of electrode finger thinning becomes apparent. The electrode width has reduced from 125 to 100 μm, a significant reduction.

Since optimum actuation is known to occur for an electrode width to substrate thickness ratio (*w/t*) of 0.5 (Figure 7.2) thinning of the electrode finger from the desired dimension will reduce the potential actuation performance of an AFC device. Undercutting is expected to result in final track widths of approximately 100 μm (*w/t* = 0.4). Figure 7.2 shows that for an electrode spacing of 1.0 mm the potential optimum strain level is not significantly reduced at this *w/t* ratio. This suggests the undercutting will not significantly reduce the AFC performance. Furthermore, a small degree of undercut may well be beneficial since it smoothes out small irregularities present in the developed photo resist, thus preventing sharp notches on electrode fingers, and small spots of copper between electrode fingers, both of which could act preferentially as electrical breakdown nucleation sites.

Electrode assessment (quality control)

After the electrode etching stage has been completed it is important to assess the electrode quality. Features such as excessively large or small electrode track widths, breakages in the tracks and side rails, and poor copper removal could significantly reduce the AFC performance. The electrodes are observed under a low power binocular microscope and any undesirable features noted. Generally the electrode quality was very high, with many passing this quality check. One of the most common reasons for an electrode to fail this stage was the presence of copper between electrode regions. Since the copper is attached to the polyimide film by an adhesive layer, small areas were easily removed using a fine needle. Breakages in side rails and electrode fingers were a rare occurrence, and electrode widths were consistently above 100 μm.

Typical images of various parts of the electrode are presented in Figure 7.16(a) to (d).

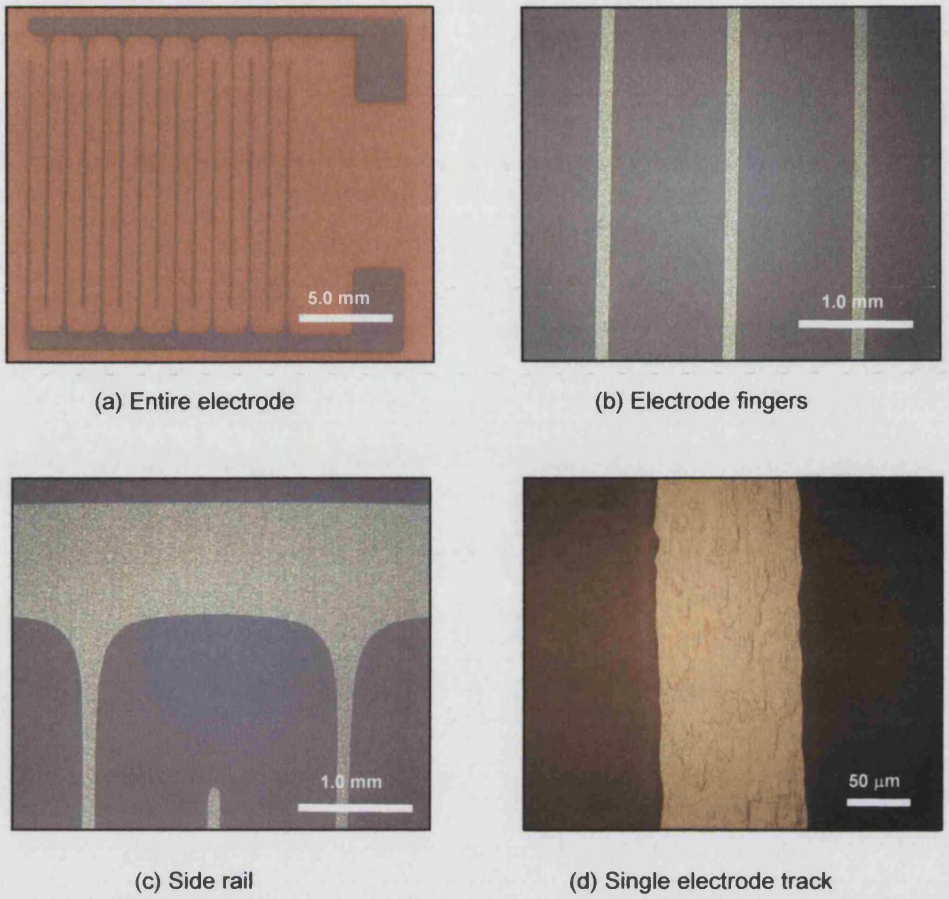

Figure 7.16: Typical images of the finished electrode pattern. All images show the successful removal of copper from undesired regions, while retained copper forms the electrode pattern.

These images clearly demonstrate the high quality of electrodes manufactured. Figure 7.16(a) shows that large areas are capable of being manufactured. Figure 7.16(b) reveals the electrode fingers are parallel, with no retained copper between the tracks. Figure 7.16(c) shows that the initiation and termination of the electrode fingers has been reproduced accurately from the mask. Finally, Figure 7.16(d) shows the electrode fingers are very well defined, and of an appropriate width. In summary, excellent reproduction of the photo negative mask is achieved using the processes described in this chapter.

7.4 Chapter Summary

The first section of this chapter, which covered finite element modelling of the interdigitated electrode structure, has given an insight into how the strain response of a bulk PZT substrate is affected by electrode width, substrate thickness and electrode finger separation. The optimum strain was found to occur at an electrode width to substrate thickness (*w/t*) ratio of 0.5. Reducing the substrate thickness was shown to increase the strain output of the device by reducing 'dead areas' and increasing the field level between the electrode fingers. Finally, it was shown that 80% of the theoretical maximum strain can be achieved with an electrode separation to substrate thickness (*s/t*) ratio greater than 4. This is important since it implies that in order to operate at lower voltages (smaller electrode spacings) substrates must be reduced in thickness. As a result of these findings it becomes clear that low voltage AFC operation requires fibre manufacturing techniques capable of producing fibres with reduced diameters in order to reduce substrate thickness.

The second section of this chapter has given a detailed description of the electrode manufacturing process. The important issue of 'undercutting' has been discussed, and when compared with the results of the finite element study it was concluded that the electrode finger thinning should not significantly reduce the strain output. The successful manufacture of the IDE pattern on a substrate allows the AFC device to be manufactured. This forms the focus of the following chapter.

CHAPTER 8

AFC MANUFACTURE AND TESTING

8.1 Introduction

Previous chapters have covered aspects relating to the components of the active fibre composite; namely the fibres and electrode. In this chapter discussion is concerned with the assembly of these components to manufacture the AFC. Results of the previous chapters are used to design a device which will exhibit optimised performance. This is based on using the most appropriate fibre type, and combining this with the most appropriate electrode design.

This chapter is divided into two distinct sections. The first part of this chapter presents a detailed description of the process used to manufacture the composites. Since few manufacturing principles have been reported in the literature, the initial stages of composite manufacture was a 'trial and error' approach. Because of this a section on 'lessons learnt' during the refinement of the manufacturing process is included. The second section of this chapter presents the experimental characterisation of the devices. The techniques used to characterise the devices are explained, and the testing performed is described. The measured performance of the devices are then compared to predicted actuation levels. These predictions are based on the effects of the electrode structure and fibre volume fraction investigated in earlier chapters. Finally, a summary of the chapter is given.

8.2 AFC Manufacture

8.2.1 Fibre, matrix and electrode selection

As stated at the end of Chapter 6, piezoelectric fibres 240 μm in diameter and of PZT-5A composition, manufactured using the VPP method, were selected for AFC manufacture. These fibres have been shown to display the material properties required for incorporation into AFC actuators. In summary, they exhibit the largest piezoelectric activity at both low and high fields, they have a suitable diameter making individual fibre handling easier, and are readily available.

A low viscosity epoxy resin, Struers Specifix-40, the same as used in the manufacture of 1-3 composites (Chapter 3) was selected as the matrix material. Previous testing on the 1-3 composites has proven that this epoxy is compatible with the piezoelectric fibres. Further, the mechanical and

electrical properties of this material are known. The four features that determined its selection for the 1-3 composite manufacture are relevant requirements for AFC manufacturing. Firstly, the low viscosity of the resin prior to curing allows good infiltration into the small regions between fibres during manufacture. Secondly, any air becoming trapped during mixing or fibre infiltration is readily removed. Thirdly, the epoxy adheres well to the PZT fibres (although the level of adhesion has not been quantitatively determined). The final useful feature exhibited by this resin is optical transparency. This allows manufactured composites to be assessed for fibre misorientations, fibre fracture and trapped voids, all of which could affect the composite performance.

Electrode configuration has been discussed in Chapter 7, which provides details of the electrode geometry and the reasoning behind the geometry selection. In summary, the electrodes are manufactured by etching a copper clad polyimide film, which has the electrode geometry deposited in resist using photolithography processes. The electrodes have a finger width of 120 μm, and a spacing of 1.0 mm. The active area is a square region approximately 15 × 15 mm in size.

8.2.2 Key manufacturing components

In addition to the fibres, matrix, and pair of electrodes (top and bottom), the major components for AFC manufacture are a base plate, a top plate and a shim. These are shown in Figure 8.1.

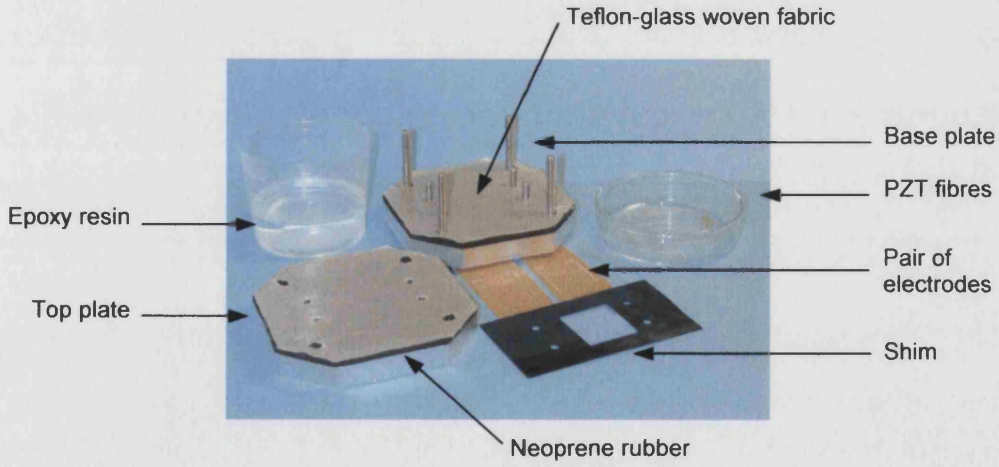

Figure 8.1: Essential components for the manufacture of the active fibre composite.

Essentially, the components of the AFC (fibres matrix and electrodes) are laid up on the base plate. The shim, a polyester sheet 190.5 μm thick, is used in this process to help align and retain the fibres and retain the epoxy matrix. The top plate is then positioned to form a sandwich, which is kept under a compressive load until the matrix has cured. Once cured the composite can be removed and is ready for quality inspection, poling and testing.

The base plate and top plate are made from aluminium, coated with a Neoprene rubber sheet 2.0 mm thick. This is the black layer that can be seen in Figure 8.1. The rubber coating on the base and top plates helps to smooth out any surface irregularities on the aluminium surfaces, and will also conform to the fibres if they are not all exactly the same diameter, helping to evenly distribute the load applied during manufacture. To prevent adhesion of the epoxy to the rubber surface, it is coated with a non-porous Teflon-glass woven fabric. The base plate contains two types of locator pins. The long locator pins align and secure the top plate, keeping the assembly together while the compressive load is applied. The shorter locator pins are used for aligning and fixing the electrodes and shim to the base plate during AFC lay-up and curing. The top plate has holes to insert these pins, ensuring the top plate is secured in position for the entire cure cycle.

8.2.3 Detailed manufacturing stages

Component preparation

Prior to composite lay up the fibres, electrodes, epoxy, shim, and top and base plates need to be prepared. This is discussed below.

Shim

The shim, 75 mm long and 43 mm wide, is cut from a 190.5 μm thick polyester sheet. The central section of the shim, 20 mm long and 22 mm wide, is removed by cutting with a scalpel. This forms the cavity that will retain the fibres and matrix during AFC manufacture.

Electrodes

During AFC manufacture the electrodes need to be precisely aligned. Further, they must keep this alignment while pressure is applied to the mould during the cure stages. Misalignment of the electrode fingers will cause degradation in the AFC performance since the electric field distribution

within the composite will be affected. The degree to which the electrode fingers on the top and bottom electrode are shifted relative to each other will determine the magnitude of the performance degradation. This could potentially lead to a severely reduced actuation performance. To achieve precise electrode alignment, alignment holes are drilled in the four corners of the top and bottom electrode pair. During this procedure the alignment holes in the shim are also created. The stages of this process are shown in Figure 8.2(a) to (e).

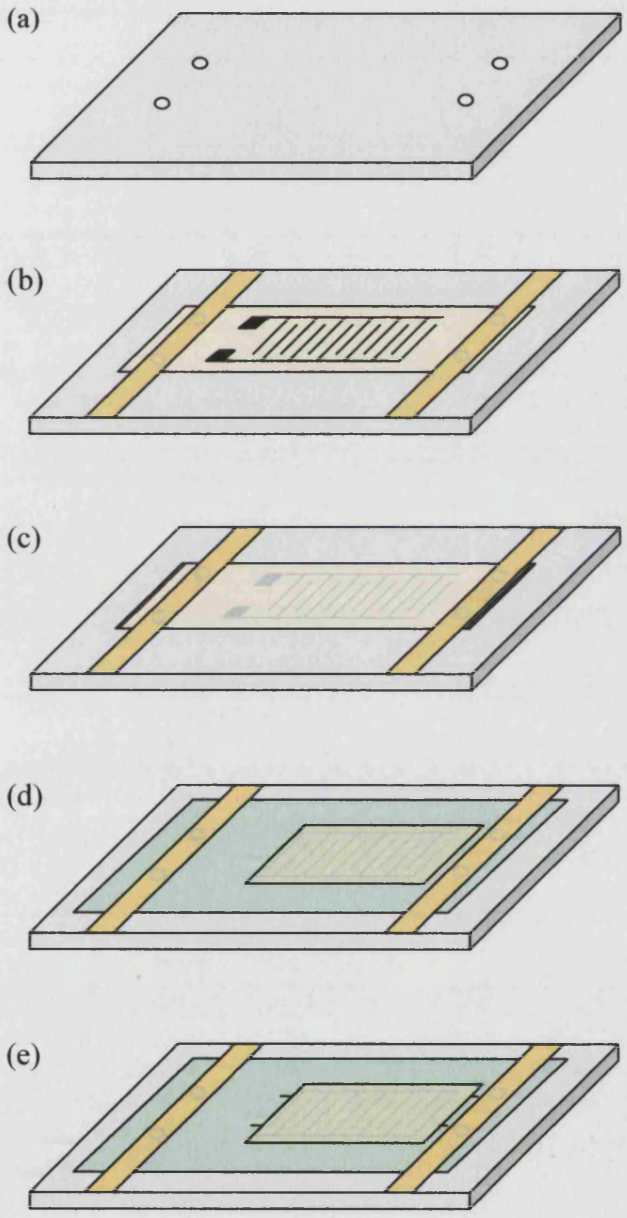

Prepare alignment plate

The surface of the alignment plate used for creating alignment holes in the electrodes and shim is cleaned with acetone.

Secure bottom electrode

The bottom electrode is secured to the alignment plate with adhesive tape.

Position and secure top electrode

The top electrode is aligned with the bottom electrode and secured to the alignment plate with adhesive tape.

Position and secure shim

The shim is positioned to leave the electrodes' active area exposed and secured to the alignment plate with adhesive tape.

Mark retaining slot positions

The location of the electrode finger ends is marked on the shim using a scalpel. The marks will be used at a later stage to indicate the position of the slots cut for the retaining fibres.

Figure 8.2: Stages in the preparation of the alignment holes in the electrodes and shim.

An aluminium plate with holes positioned identically to the top plate is used to produce the alignment holes (Figure 8.2(a)). The bottom electrode is secured in position on this plate, copper electrode face uppermost, using adhesive tape, Figure 8.2(b). It is important that the adhesive tape covers the region of the electrode where the alignment holes are to be formed since it helps prevent tearing of the electrode when the holes are created during drilling, and during subsequent handling. Once secured in position, a few drops of distilled water are placed onto the electrode face. When the top electrode is placed over the bottom electrode so that both copper faces are in contact, the water forms a film between them. This enables the position of the electrode tracks on both electrodes to be seen, and also acts to secure the top electrode in position once it has been aligned. Once the electrode fingers have been aligned adhesive tape is used to firmly secure the top electrode and provide a robust region to create the alignment holes (Figure 8.2(c)). Finally the shim is positioned. The central open section of the shim is aligned over the electrodes so as to keep the active area exposed. The shim is fixed in position with tape as shown in Figure 8.2(d). At this stage a straight edge is used to mark the location of the electrode finger ends on the shim. The shim is scored using a scalpel to create a permanent mark indicating the position of the slots that will be cut into the shim on removal from the alignment plate, to hold the retaining fibres in position.

The alignment holes are now ready to be drilled. The alignment plate, with two electrodes and shim, is placed electrode side down onto a section of wood so that the holes in the alignment plate become visible. These holes are used as a guide for a ⅛″ drill bit which is used to drill through the electrodes and shim. The wooden backing prevents breakout of the drill bit, and ensures a good quality hole edge is formed, free from burrs and tears. Once the four holes have been drilled the electrodes and shim are removed from the alignment plate. The adhesive tape is removed from the shim but left on the electrodes. This increases the durability of the alignment holes in the electrodes, which is useful during the later stages of AFC lay-up.

Final preparation of the electrodes involves cleaning with compressed air to remove dust from the surfaces. The pads of the electrodes are covered with adhesive tape to keep them free from epoxy during manufacture. Once the AFC is cured, removal of the tape reveals a fresh and clean copper surface suitable for electrical connections.

Fibres

Preparation of the fibres involves obtaining 48 straight fibres, 20 mm in length. Two extra fibres are required for the retaining fibres. These are longer, approximately 25 mm. All the fibres are placed into a glass beaker and covered with acetone. The beaker is then placed into an ultrasonic bath for 10 minutes to remove grease and other surface contaminants from the fibres, which could lead to breakdown at undesirable low voltages. After 10 minutes in the ultrasonic bath the acetone

is drained from the beaker, which is then placed into an oven at 120 °C for 10 minutes to dry the fibres. While the fibres are drying the epoxy resin matrix is prepared.

Epoxy Matrix

The epoxy resin and hardener are measured in the recommended quantities, placed into a plastic beaker and stirred until fully mixed. The mixed epoxy is then placed under vacuum until all air trapped during the mixing stage has been expelled. Once removed from the vacuum the matrix preparation is completed.

With all components prepared it is now possible to lay-up the AFC.

AFC lay-up

The base and top plate of the mould (shown in Figure 8.1) are cleaned, ensuring flat smooth mould surfaces. The fibres are removed from the oven, transferred into a shallow glass dish, and the epoxy resin poured over them. The AFC manufacturing stages are depicted in Photographs 1 through 6, which are presented in Figure 8.3 below, with detailed descriptions of each stage.

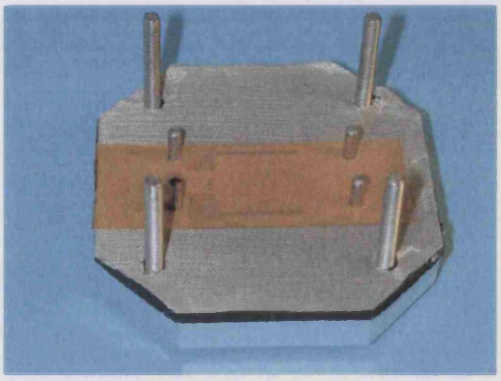

Photograph 1

The base of the bottom electrode is lightly coated in Spray Mount, an aerosol propelled fixing adhesive. The bottom electrode is placed onto the base plate. This adhesive, in addition to the alignment holes, helps to fix the bottom electrode to the base plate.

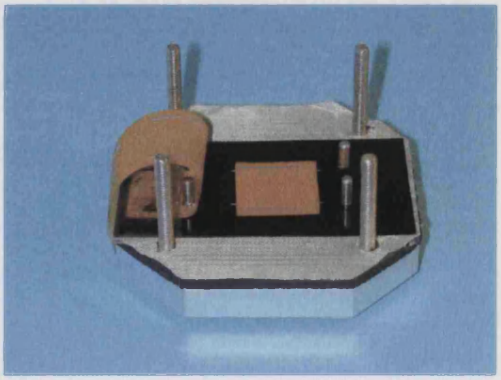

Photograph 2

The shim, the base of which is also coated in Spray Mount, is positioned over electrode on locator pins to leave exposed IDE pattern. The top electrode is then positioned on two of the four alignment pins and secured at one end with adhesive tape.

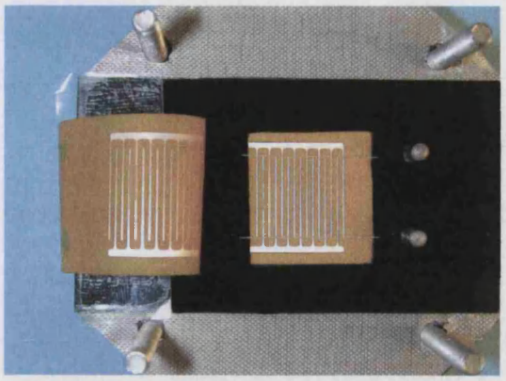

Photograph 3

The two retaining fibres are removed from the epoxy and placed into the slots cut into the shim. These retaining fibres hold the remaining fibres in position on the active area of the electrode. Constraining fibres only to the active portion of the device reduces the clamping from inactive fibres.

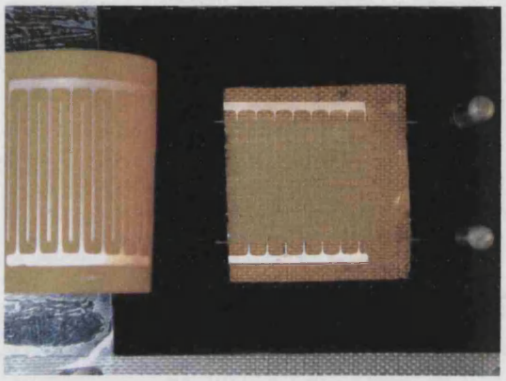

Photograph 4

The fibres are removed from the epoxy and positioned between the retaining fibres. This process reduces void formation compared to filling the mould with dry fibres, and then filling with epoxy. Once all fibres had been transferred to the mould extra epoxy was applied outside the retaining fibres. Obvious entrapped air was removed from the matrix, and the fibres were distributed evenly using tweezers.

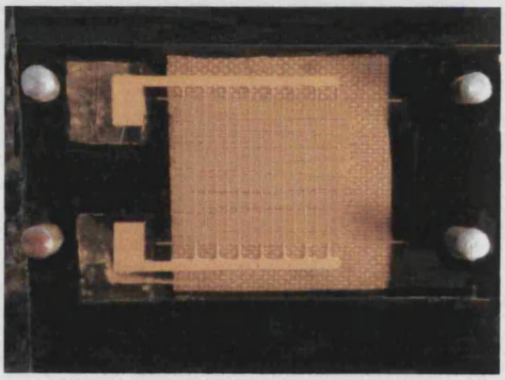

Photograph 5

The top electrode was rolled onto end alignment pins. During this stage. The rolling process helped expel any air to the end of the composite ensuring no air was trapped under the top electrode. Once the top electrode was positioned any fibre overlaps, or poor fibre alignment and spacing that had occurred in the process, was corrected by manipulating the fibres through the top electrode.

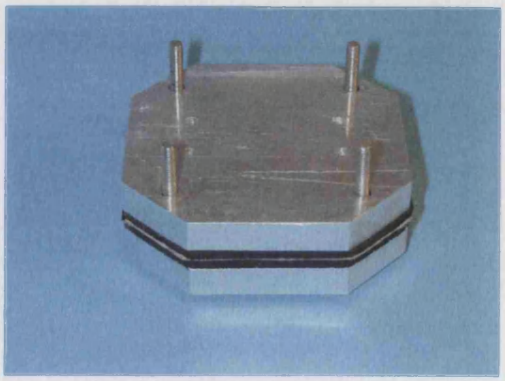

Photograph 6

Once fibre alignment was adequate the composite the top plate was positioned onto the base plate. Free weights were placed on top of the mould to compress the composite. This ensured close contact with the fibres and the electrode tracks.

Figure 8.3: Photographs (1 through 6) of the AFC manufacturing stages with accompanying commentary.

The assembly is left for 24 hours to cure at room temperature. The composite assembly is then removed from the mould and placed in an oven at 40 °C for 12 hours to post cure. Once removed from the oven the composite is trimmed to remove excess electrode and shim material. A finished composite is shown in Figure 8.4.

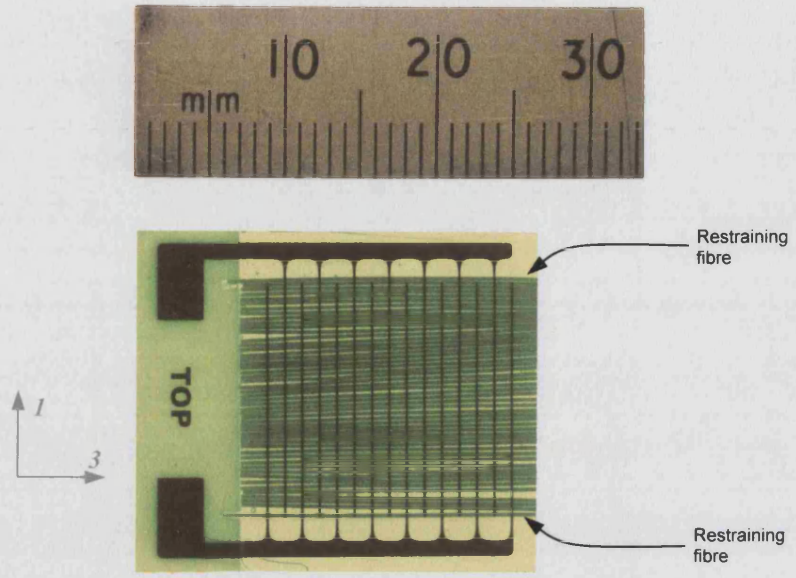

Figure 8.4: Photograph of a finished AFC without the wires attached to electrode pads.

The composite comprises evenly distributed and well aligned fibres. The alignment groves cut into the shim are visible at the base of the AFC, near the electrode bonding pads. These have clearly performed the function of holding the fibres within the active region of the composite during the cure cycle.

8.2.4 Lessons learnt from early composite manufacturing

The manufacturing stages presented in the previous section were not used for all the composites manufactured. During early composite manufacture some key lessons were learnt, enabling the process to be refined to the level presented in the previous section. The key lessons learnt were:

- **Mould coating:** It is important that the coating used for the mould is flat so that equal pressure is exerted on the composite surface during curing. Black Neoprene rubber sheet

was selected for this reason. Initially a cast rubber sheet was used, the poor surface flatness of this resulted in poor quality composites, with large thicknesses.

- **Shim design:** Initially it was thought that a fully enclosed shim, such as that presented in Figure 8.1, would constrain matrix flow from the composite, resulting in thick cross section devices. In reality, this was not the case. In early manufacture, one end of the shim was open to create a channel for excess matrix to flow out of the composite. The problem with this design is that the matrix was forced to flow in the direction of the channel. Fibres became mobile under the matrix flow and migrated out of the composite and into the channel.

- **Fibre quality:** During device manufacture it was noted that bent or wavy fibres greatly increased the potential of fibre overlaps. This often resulted in fibre breakage in the overlap location and poor fibre alignment. Straightness is an important quality for the fibres if device manufacture is to be successful.

- **Degassing:** It is important to de-gas the matrix. It was also considered important to remove any air trapped on the surface of the fibres once they were added to the degassed matrix. However, placing the fibres under a vacuum once they were coated in the matrix was disastrous. The air trapped in the fibres was forced out of the fibres and into the matrix, where it became very difficult to remove with the applied vacuum. Composites manufactured with this technique contained excessive amounts of porosity. Because of this composites were manufactured without degassing the fibres.

- **Electrode substrate strengthening:** In early electrode preparation the adhesive tape, used to fix the electrodes in position while the alignment holes were drilled, was removed once the holes had been formed. However, this increased the risk of tearing the holes when positioning the electrode on the alignment pins. Keeping the tape on the electrodes for the entire manufacturing process reduced this risk considerably.

- **Curing pressure:** Using free weights, or a constant pressure press is important for successful device manufacture. Initially screws were used on each corner of the mould to apply the desired load. However, relaxation of the mould coating reduces the initial applied load, increasing the composite thickness and the occurrence of voids. Adding sufficient weight to reduce fibre-electrode separation, but insufficient to avoid fibre fracture, is also important. Although the fibre fracture limit was not reached, the application of 20 kg of weight was considered adequate, based on the reported applied pressure in other research.[50] Early composites were cured under either 10 kg or 15 kg of free weights, which was seen to detrimentally affect their performance (this is discussed later in the results section).

8.2.5 Quality assessment

Once removed from the mould and trimmed the AFC undergoes a quality assessment process. Composites were examined under a microscope for evidence of any defects that could influence the device performance. Two such defects are voids and fibre damage, both of which can lead to electrical field concentrations and an increased risk of electrical breakdown during poling and operation. Images of fibre breakage and voids are shown in the micrographs presented in Figure 8.5. Instances of voids and fibre damage were noted in the records kept for each composite.

Poor fibre alignment, poor electrode alignment and uneven fibre spacing were other potential manufacturing defects. However, it was not common for these problems to arise.

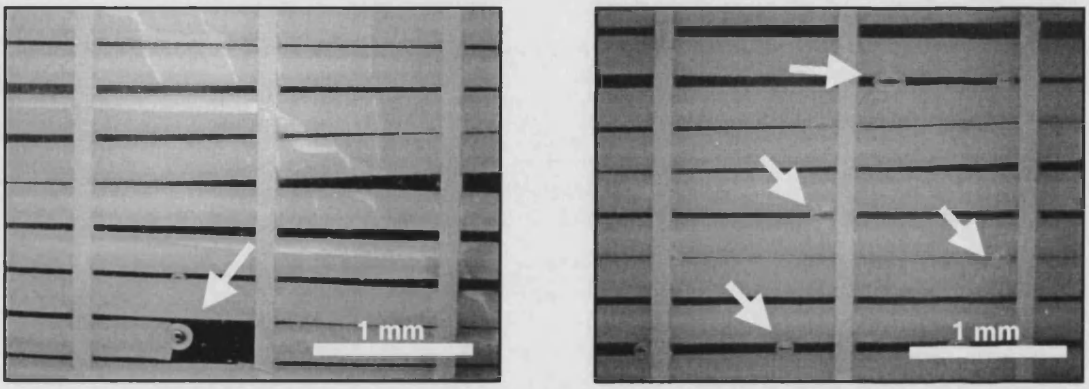

(a) Fibre breakage (b) Air voids in matrix

Figure 8.5: Dark field images showing defects in an AFC resulting from manufacturing.

Fibre breakage has been associated with a lack of uniformity in the loading of the composite during curing. This highlights the need to apply uniform pressure to the composite. Once the weights were positioned more carefully, and in 5 kg increments, no instances of fibre fracture were found.

Trapped voids result from one of three mechanisms; (i) failure to remove trapped air from the epoxy prior to curing, (ii) air becoming trapped during the positioning of the top electrode, (iii) air migrating into the composite once the load was applied. Removal of the air from the epoxy prior to curing, and careful positioning of the top electrode reduced the void content, but instances of voids still occurred. The only explanation was air entering the composite once under pressure. In early composite fabrication the rubber coating on the top plate and base plate was a polymer foam. Additionally, the pressure was applied to the composites by tightening screws on each of the four top plate alignment pins. It is thought that once the initial pressure was applied to the plates using the screws a stress relaxation process took place in the foam. In this processes the foam relaxed, in doing so reducing the pressure on the composite. This reduced pressure was accompanied by

ingress of atmospheric air, forming the voids present in the early samples. Once the foam was replaced by a stiffer rubber, and the pressure was kept constant by using free weights instead of screws, the problems of air voids was significantly reduced.

To achieve optimum strain performance from the AFC device it is important that the applied pressure is high enough to minimise the epoxy resin layer between the fibres and electrode fingers. This layer will act as a capacitor in series with the fibre and, because of the low matrix dielectric constant, will severely reduce the field transferred to the fibre. In an attempt to investigate this, a composite was sectioned along the electrode finger direction and polished to enable this epoxy layer to be investigated. An image of an electrode finger in contact with the fibres is presented in Figure 8.6. The image shows minimal separation exists, suggesting that the applied load is adequate. Also present in this image are blackened regions in the fibre at the fibre-electrode interface. This is thought to be evidence of electrical damage since prior to sectioning this composite had been poled and tested to voltage levels high enough to cause electrical breakdown.

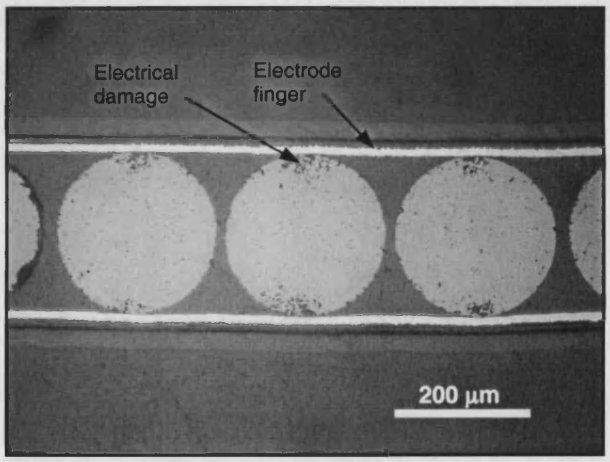

Figure 8.6: Cross section of a manufactured AFC showing minimal fibre-electrode separation. .

Once the composites had been assessed for quality, the tape covering the electrode pads was removed, and they were cleaned with acetone. Wires were soldered to the electrode pads to enable the AFC to be poled and operated.

8.2.6 Poling AFC devices

Breakdown

It is difficult to specify poling conditions that would ensure fully poled PZT fibres. Ideally poling conditions applied to the 1-3 composites should be used (2.25 kV mm^{-1}, 100 °C) since this is known to result in full poling of the PZT-5A fibres. At minimum the poling voltage applied to the AFC devices needs to be 2.25 kV since this could be translated into 2.25 kV mm^{-1} with the IDE electrode separation of 1.0 mm. Because of the unknown field in the fibres resulting from the epoxy layer and electrode configuration, it is desirable to increase this voltage. However, care must be taken not to increase the voltage to such a level that electrical breakdown between the electrode fingers occurs.

To establish the voltage limits of the devices four AFCs were tested with increasing sinusoidal field levels until breakdown occurred. Typically, composites were seen to break down when the voltage exceeded 4.5 kV at room temperature. Since only four composites were tested it is not possible to be statistically accurate about the breakdown voltage, but the experiment acts as a guide from which to set safe voltage limits. Once breakdown had occurred the voltage that could be applied to the composite on subsequent attempts was reduced since a low resistance pathway had been formed along the breakdown path. Effectively, once breakdown has occurred the composite becomes redundant. Although such damage can be drilled out and filled with fresh epoxy, this is not a simple process and is liable to cause further damage in the device.

A typical example of electrical breakdown is shown in the micrograph presented in Figure 8.7(a). The damage in this example spans two electrode finger spacings. Evidence of non-catastrophic breakdown can be seen underneath electrode fingers above the site of the major breakdown, indicated with arrows. This is thought to result from the high electric field concentrations known to exist in these regions, shown in the finite element modelling (Figure 7.5).

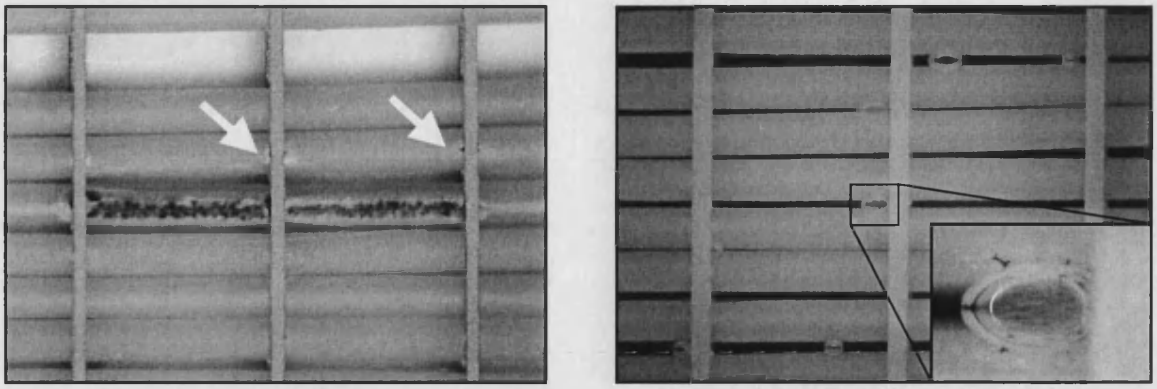

(a) Breakdown at fibres (b) Breakdown at trapped voids.

Figure 8.7: Dark field images showing dielectric breakdown in an AFC device.

Voids can also act as initiation sites for electrical breakdown. Evidence of this is shown in Figure 8.7(b). It is important to note that the preferred site for electrical breakdown is along the top of the fibre, at the fibre-electrode interface, such as the areas indicated in Figure 8.7(a). It is thought that adsorbed moisture, trapped air, and the interface all act to reduce the breakdown field along this pathway. The surface of the fibre therefore becomes a preferential breakdown site. Breakdown was never observed along any other pathway, for example from the electrode finger end to the side rail. The typical breakdown voltage of 4.5 kV mm^{-1} obtained from this study enabled poling voltages to be set.

Poling Conditions

Poling of early composites was performed at 100 °C, with a voltage level of 3.5 - 4.0 kV. Even though this voltage level was 0.5 to 1.0 kV below the breakdown voltage, breakdown often occurred. Subsequent poling attempts then become very ineffective because the voltage had to be reduced. In addition, there is also high risk of breakdown during operation. For the samples that experienced breakdown the poling temperature was lowered to 60 °C, and the voltage was reduced. It is thought that high temperatures severely reduce breakdown voltage. The reduced adhesion between the fibre and matrix as the polymer softens is thought to contribute to the lower breakdown voltage. As a result of these factors, the poling temperature was lowered to 60 °C, and the voltage to 3.5 kV. No devices poled under this lower temperature condition experienced breakdown.

8.3 Experimental Characterisation

Before the AFCs are used in any application, or incorporated into more complex devices, it is important that the response of each AFC is characterised. Device performance indicators are the low field d_{33} and d_{31}, and high field characteristics such as saturation strain. A key device parameter is the coercive field; this ultimately determines the operational voltage cycle since polarisation reversal must be avoided. The coercive field can be used to set the upper and lower bounds of operational voltage, allowing devices to be driven to their maximum potential. All these characteristics (d_{33}, d_{31}, saturation strain and coercive field) require the strain to be monitored as a function of applied voltage. The characterisation method is now introduced

8.3.1 AFC characterisation method

Composites were cleaned with acetone in preparation for bonding strain gauges to their surfaces. The gauges selected were FCB-6·350-11 from Tokyo Sokki Kenkyujo Ltd. These have a gauge length of 6.0 mm, a gauge width of 2.0 mm and a resistance of 350 Ω. They are termed a '0/90 bi-axial gauge' since they comprise two gauges orientated at 90° to one another. The gauge spans six electrode fingers if measuring strain in the 3-direction and approximately two electrode fingers if measuring strain in the 1-direction. The strain gauge output will therefore be an averaged response from these regions. Two gauges were bonded to each sample, on the top and the bottom surfaces of the composite, each measuring strain in the 1 and 3 direction (the 3 direction is the direction of poling; the fibre direction). Measuring the 1 and 3 direction response allows the composite's d_{33} and d_{31} to be measured, and simultaneous measurements on both surfaces allowed any bending in the composite to be quantified. Once the strain gauges were in place, the composite was ready for testing using the experimental set-up shown in Figure 8.8.

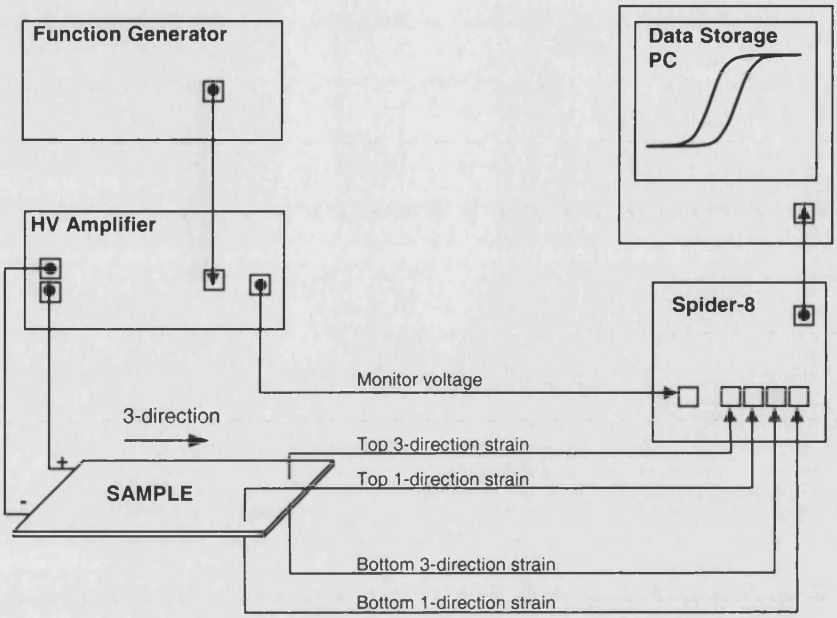

Figure 8.8: A schematic of the experimental set-up used to measure the strain response of the AFCs.

The experimental set-up consists of:

- *Function generator* - used to generate the voltage waveform to be applied to the devices.
- *High voltage amplifier* - used to amplify the voltage waveform.
- *Sample* – the AFC device to which the amplified voltage signal is applied.
- *Spider-8* - a transducer data-logging device capable of monitoring the signals of the strain gauge transducers and the voltage monitor output of the amplifier.
- *Computer* – used to control the Spider-8 and log the data using 'Catman' data acquisition software.

The voltage applied to the samples was sinusoidal at a frequency of 1 Hz. The voltage was increased from 0.1 kVpp (±50 V) up to an upper limit. The upper limit was set to equal the poling voltage since it was known that breakdown was unlikely at this level. For most samples this was 7.0 kVpp (±3.5 kV). However, for samples that suffered breakdown during the poling stage the voltage limit was set to a lower level. Ten cycles at each voltage level were applied to the samples to allow an average of the results to be taken. The voltage levels were chosen to allow examination of both the low and high field responses of the devices. The results obtained are now presented and discussed.

8.3.2 Results and discussion

Experimental results

The composite strain as a function of applied voltage is shown in Figure 8.9(a). The AFC for which these results were taken (AFC07) was considered well manufactured and contained few voids. The slope of each of these strain – voltage curves was measured using least-squared fitting. By taking the electrode separation to be 1.0 mm, the voltage can be used to calculate a field level, and used to determine a pseudo d_{33}. The value of d_{33} for each field level found using this technique is plotted in Figure 8.9(b).

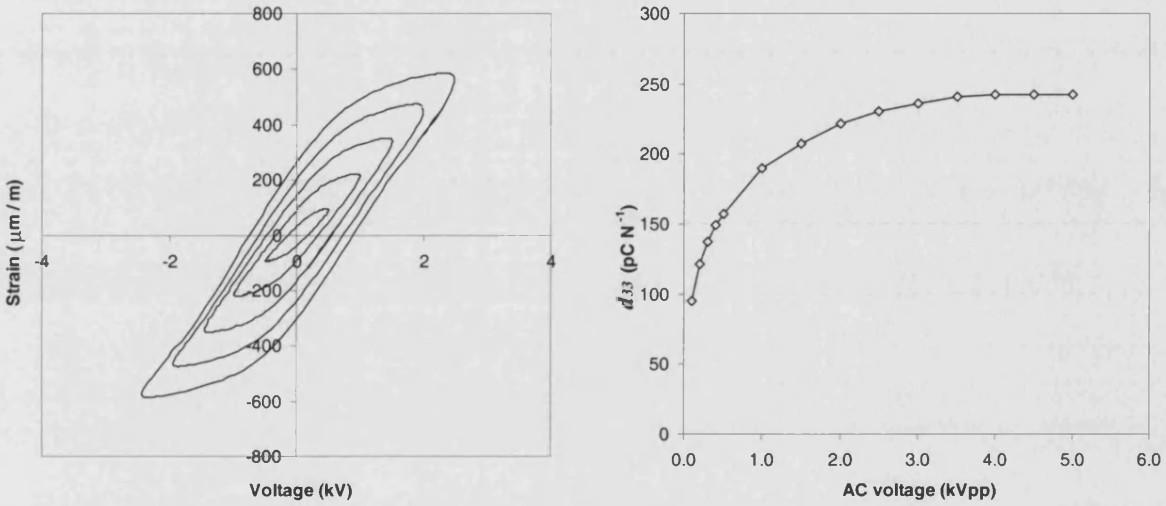

Figure 8.9: (a) An example of an AFC 3-direction strain response with increasing cyclic field. Device d_{33} is plotted against field level in (b). The results presented are from sample AFC07.

Examination of Figure 8.9(a) reveals important and interesting information about the device. The device exhibits the strain-field characteristics expected from a poled piezoelectric. However, an interesting feature of the response is that the coercive field of the device is not reached, evidenced by the lack of a full butterfly loop being developed. Testing in Chapter 5 established the coercive field of the fibres to be 1.38 kV mm^{-1}. Based on the assumption that the full field applied to the composite is experienced by the fibres, a butterfly loop could be expected to occur at voltage levels of approximately 1.38 kV. The results show that even at 2.5 kV there is no evidence of a butterfly loop beginning to form, suggesting that a proportion of the field is not being experienced by the fibres. This is reflected in the low values of d_{33} seen in Figure 8.9(b).

The d_{31} response of the same device is presented in Figure 8.10. Figure 8.10(a) shows the device exhibits a similar trend to the d_{33} response. The exceptions are that the strain developed is opposite in sign and approximately half the magnitude. This is expected based on the d_{31}/d_{33} ratio of the fibres, which is known to be approximately 0.5.

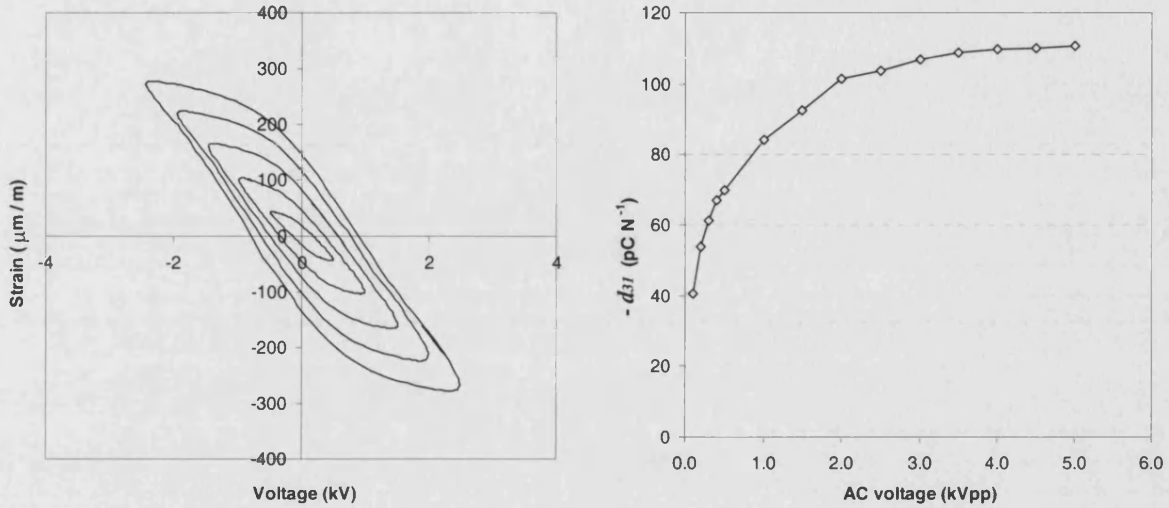

(a) (b)

Figure 8.10: (a) An example of an AFC 1-direction strain response with increasing cyclic field. Device d_{31} is plotted against field level in (b). The results presented are from sample AFC07.

The strains in the 1 and the 3 direction measured on the top of the devices were typically within 10 % of the corresponding strains on the bottom of the device. This suggests that the devices respond in a uniform manner.

All the devices tested displayed responses similar to that presented in Figure 8.9 and Figure 8.10, but the strain magnitude, and therefore the d_{33} and d_{31} coefficients, varied significantly between devices. To visualise the spread in the device performance a graph plotting the device d_{33} versus the testing voltage for each of the ten devices tested is presented in Figure 8.11.

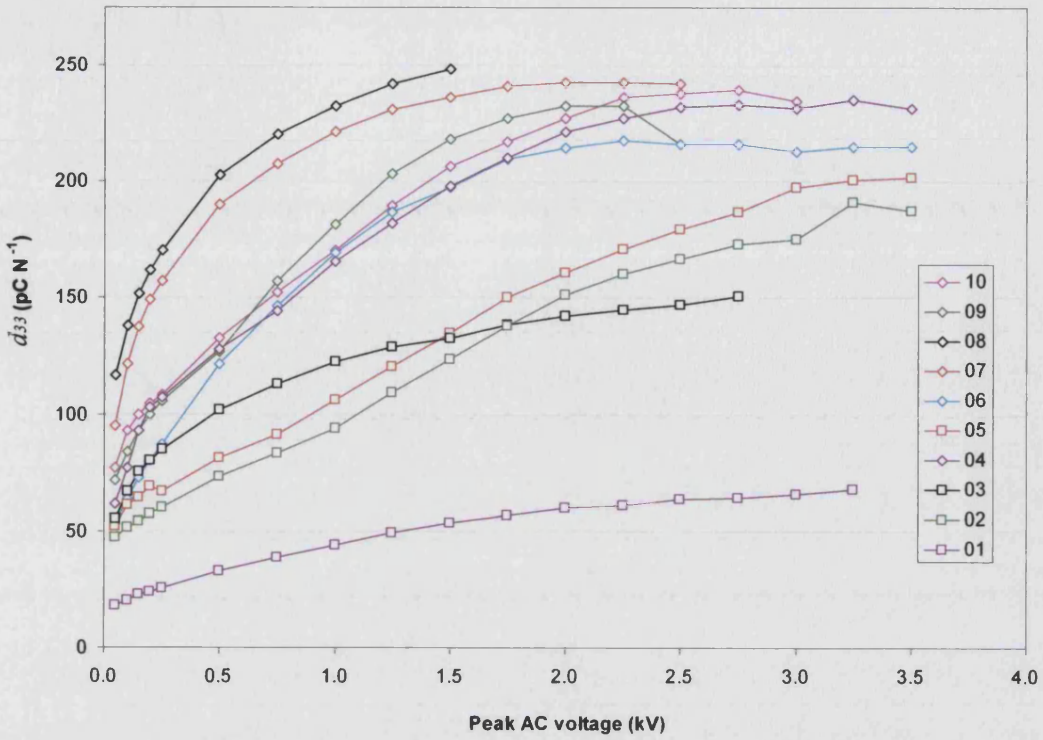

Figure 8.11: A summary graph for the 10 AFC samples manufactured plotting the d_{33} value versus field level.

In general, devices made early on in the programme (low sample numbers) exhibit poor strain performance. A device performing particularly poorly was sample number AFC01. This composite was manufactured using an uneven mould coating, which produced a device with non-uniform thickness. This is evidence of a variation in the fibre-electrode separation. Devices exhibiting the highest strain performance were sample numbers AFC07 and AFC08. These devices were cured under higher loads than the earlier composites, suggesting these composites have a reduced fibre-electrode separation.

It is clear from Figure 8.11 that the d_{33} of the devices does not match the value of the fibres' d_{33}, measured in Chapter 3 at 425 pC N^{-1}. This is to be expected because of the various mechanical and electrical factors acting to reduce the strain developed in the AFC. These factors are now discussed and used to explain why the magnitude of the device responses measured experimentally is low compared to the free fibre values.

Comparison of AFC strain with predicted strain levels

Mechanical effects

The matrix and electrode substrate material will act to clamp the strain of the fibres because they are non-piezoelectric passive elements of the system. Since the majority of the copper on the electrode substrate is etched away, and the remainder is only connected in the 1-direction, the thin copper electrode is assumed to have a negligible clamping effect. The soft adhesive layer bonding the copper to the film is of very low stiffness and is therefore neglected. The only part of the electrode assumed to be contributing to the clamping is the polyimide carrier layer itself, which is 25 μm thick. Since the carrier film is a polymer having a Young's modulus of 2.8 GPa, a value comparable to the epoxy matrix, it can be assumed to be a part of the matrix. The fibre volume fraction in a composite is simply the fibre cross sectional area, A_{fibre}, divided by the total composite cross sectional area, A_{total}:

$$\frac{A_{fibre}}{A_{total}} = \frac{n\pi r^2}{2w_a(r+t)} \tag{8.1}$$

where: n = number of fibres

r = average fibre radius

w_a = width of the active area

t = substrate thickness

These symbols are defined in Figure 8.12, which depicts a cross section of an AFC.

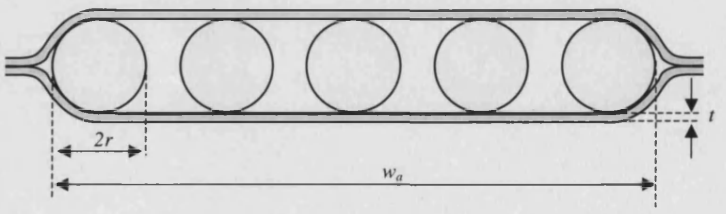

Figure 8.12: Schematic cross-section depiction of an AFC composite with 5 fibres (n = 5) of diameter 2r. The composite width is w_a, and the electrode substrate thickness is t.

Equation (8.1) is valid if it is assumed that the fibres and electrode are in direct contact, since the composite thickness is the sum of the fibre diameter and the electrode substrate thickness.

A typically composite will contain 50 fibres, with a mean fibre diameter of 233 μm, distributed across the active width of the composites, which is 15.0 mm. As previously mentioned, the polyimide electrode substrate thickness is 25 μm. Using these values in Equation (8.1) results in a fibre volume fraction of 0.50, or 50%, for each AFC manufactured. Results from Chapter 2, plotting d_{33} versus fibre volume fraction in a 1-3 composite (Figure 2.5(a)), indicate that a composite comprising 50% fibres will develop 95% of the free fibre strain, or 95% of the fibres' d_{33}.

Clamping can therefore only account for a small percentage of the strain reduction seen in the AFCs. A further reduction can be attributed to the IDE electrode configuration, which is now discussed.

Electrical effects

Results from the finite element analysis presented in Chapter 7 show that a bulk PZT substrate develops 80% of the ideal (bulk d_{33}) response with the electrode configuration used for AFC manufacture. Although the optimum electrode dimensions were calculated from the finite element analysis presented in Chapter 7, it should be emphasised that the substrate was bulk PZT, not a fibre-matrix construction as the case in AFC devices. It is therefore difficult to quantify the exact reduction in performance resulting from using the IDE electrode structure on the AFCs manufactured in this chapter. It is therefore assumed that the strain reduction in an AFC substrate is the same as for a bulk substrate. This value is 80% as previously mentioned.

Comparison and explanation of AFC strain response

Combining the mechanical and electrical reduction factors results in a device that, under ideal conditions, will develop approximately 75% of the free fibre d_{33}. Thus we expect to achieve an optimised d_{33} of no more than 318 pC N^{-1} (75% of 425 pC N^{-1}). In reality, values lower than this are being achieved, as seen in Figure 8.11. At best a low field d_{33} of 120 pC N^{-1} has been measured for device AFC08 (measured at ±50 V). This represents a 62% reduction from the expected value.

This additional reduction could result from the unknown interaction of the electrode with the fibre-matrix substrate, as previously discussed. However, it is thought that a large proportion can be attributed to the separation of the fibre and electrode by a thin epoxy layer. The epoxy layer will act as a capacitor in series with the fibre and, because of the low matrix dielectric constant, will

severely reduce the field transferred to the fibre. For maximum electric field transfer it is desirable to make this layer as thin as possible. The thickness of this layer is expected to reduce with increasing pressure applied during the curing cycle, accounting for the large variation in strain values observed between the devices.

In practice it is difficult to quantify the size of the epoxy layer thought to be responsible for the reduction in performance. Simply preparing a cross section of the composite, such as that presented in Figure 8.6, only provides a very localised examination. Furthermore, it is a destructive technique, which is far from ideal. Measuring the composite thickness using a micrometer is possible, but the degree of accuracy required is similar to the micrometer resolution making this technique prone to large errors. However, it is possible to quantify the thickness of this layer indirectly by measuring the total capacitance of the AFC devices. It is expected that because each AFC has the same geometry, contains the same proportion of fibre and matrix, and uses identical electrode configurations, the major contributor to differences in device capacitance would be the thickness of the epoxy layer separating the electrodes from the fibres. A large fibre-electrode separation (thick epoxy layer) will result in a low dielectric constant because a high proportion of voltage is dropped over the polymer. Thus the device capacitance gives an indication of the epoxy layer thickness. Figure 8.13 presents a graph of device d_{33} versus the device capacitance measured prior to poling. This allows the effect of the epoxy layer thickness on the device performance to be established.

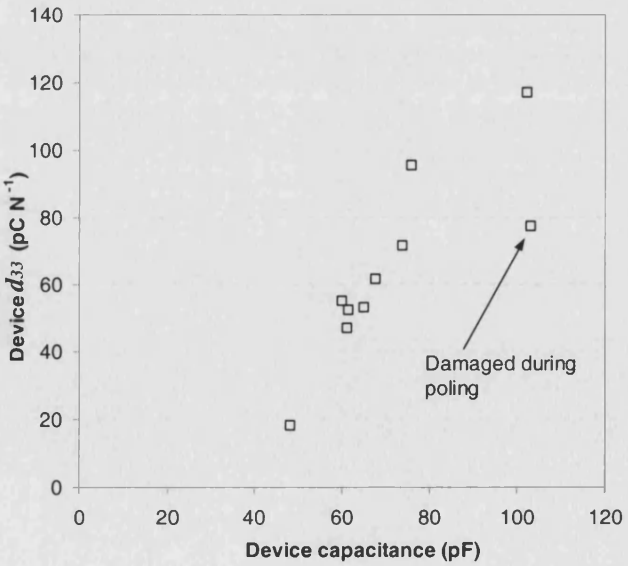

Figure 8.13: A graph comparing the AFC device d_{33} with the measure device capacitance, which is an indirect measure of the fibre-electrode separation.

The results in Figure 8.13 show that as the device capacitance increases (the electrodes approach closer to the fibres), there is an associated increase in the device d_{33}. This trend is approximately linear with the exception of one anomalous result, which is attributed to a device that suffered excessive electrical breakdown damage during the poling stage.

Because of the differences in fibre-electrode separation the fibre in the AFC devices will experience different fields for identical voltages, thus the poling of the devices is not comparable. Even in the best performing composites the poling voltage does not exceed the coercive voltage of the device because of the voltage limits imposed by the risk of breakdown. This indicates that the fibres in all the AFCs are incompletely poled. The low degree of poling in the AFCs is a large contributor to their reduced performance because any electrical field reaching the fibres will not be efficiently transformed into mechanical motion. In addition, during operation it will be the AFCs with a large fibre-electrode separation that will suffer from the largest field degradation affecting the fibres, which already suffer from a low degree of poling. This field reduction during operation, combined with the poor poling in such composites, will severely reduce the strain developed. This is considered to be the explanation of the magnitude of, and variation in, the strain results presented for the AFCs manufactured in this chapter. There is every possibility that with an increased cure pressure, the strain response of the devices will approach expected values.

A note on application specific properties

Even the devices manufactured and discussed in this chapter, which develop lower strains than predicted, offer many advantageous properties making them suitable for applications. The fact that the strain has not been optimised does not subtract from these beneficial properties.

The first benefit AFCs have over the traditional actuators is their high anisotropy. This attribute brings advantages to devices manufactured from AFCs by enabling de-coupling of the stresses developed in the 1 and the 3 directions. This enables bending to be induced in a multi-ply AFC in one direction while inducing minimum bending in the orthogonal direction.

The degree to which the bending moments become decoupled depends on the ratio of the stiffness in the two directions. The compliance of the AFC devices in the 3 and 1 directions ($\bar{s}_3^E$, $\bar{s}_1^E$) can be estimated using the iso-strain and iso-stress assumptions of continuous fibre reinforced composites respectively:

$$\bar{s}_3^E = \frac{s_{33}^E s_{11}}{v_f s_{11} + (1 - v_f) s_{33}^E} \tag{8.2}$$

$$\bar{s}_1^E = (1 - v_f) s_{11} + v_f s_{11}^E \tag{8.3}$$

The only unknown term in these equations that has not been experimentally determined from previous testing is the s_{11}^E coefficient of the fibres. However, it is possible to estimate this value by assuming the s_{11}^E / s_{33}^E ratio is identical in the fibre and bulk PZT-5A. Using this assumption together with the measured fibre and matrix properties, the value of Young's modulus for the composite in the 3 and 1 direction can be estimated as 28.7 GPa and 5.4 GPa respectively. When compared to values of 53.2 GPa and 61.0 GPa for bulk PZT in the 3 and 1 direction, it is clear that the AFC offers significantly higher anisotropy. This advantage is examined briefly in the 'Future Work' section of Chapter 9, where finite element analysis results of multi-ply lay-ups are presented and compared to those obtained with bulk PZT sheets.

The robust nature of the composite construction and ability to conform to more irregular surface profiles are also advantageous properties, but these have not been examined in this thesis.

8.4 Chapter Summary

This chapter has covered aspects relating to the manufacture and testing of active fibre composites. The manufacturing stages were discussed in detail since there is very little literature regarding the manufacturing of these devices. Devices were cured under increasing pressures to reduce the fibre-electrode separation, while reducing the instances of fibre fracture. Poling of the devices was performed at voltages below the breakdown voltage level, which was found to be in the range 4.0-4.5 kV. Initially, composites were poled at 100 °C and at 3.5 kV. Since electrical breakdown occasionally occurred under these circumstances the poling temperature was reduced to 60 °C for later samples. In total, ten devices were manufactured. Testing the strain response of the AFCs was achieved with strain gauges positioned on the top and bottom surfaces of each device. Strains in directions parallel and perpendicular to the fibre direction were recorded for voltage levels increasing from ±50 V to ±3500 V. Although each device developed a measurable strain, the

magnitude was lower than expected. Since no device developed a full 'butterfly loop' (associated with domain reorientation) it was concluded that a large proportion of the field was being lost due to the fibres being separated from the electrode by a thin layer of the matrix material; a low dielectric epoxy resin. A graph of device d_{33} versus device capacitance (an indirect measure of the fibre-electrode separation) revealed a strong correlation, with an increase in capacitance resulting in a larger d_{33}, as expected. Based on these results it is thought that simply applying a larger pressure during the cure cycle will reduce the separation and increase the performance of the AFC to expected levels. Another solution includes using non-circular cross sectional fibres, eg square cross section fibres, which would increase the fibre-electrode contact.

CHAPTER 9

THESIS SUMMARY AND FUTURE WORK

9.1 Thesis Summary

This thesis has examined some of the key aspects affecting the performance of the active fibre composite in an attempt to optimise its design. Chapter 1 provided a review of the literature, summarising fundamental principles within the field of piezoelectricity in relation to the field of 'smart materials'. The current state of the research field regarding the AFC was then reviewed, highlighting areas in which further research was needed to advance the understanding of this device. They include a need to evaluate fibre properties at both low and high electrical fields, and relating the fibre properties to physical and chemical properties. A second area identified was to improve the understanding of the influence of the interdigitated electrode design on the device performance. The findings presented in this thesis relating to these areas are now briefly summarised.

9.1.1 Low field properties of piezoelectric fibres

Piezoelectric fibres have been available to researchers for only a limited time and this, combined with their small diameters, has meant techniques for measuring their mechanical and piezoelectric properties had not been fully developed or tested. Chapter 2 introduced analytical and finite element models, and used these to demonstrate that it is possible to calculate the properties of fibres from measurements made on 1-3 geometry composites. The accuracy of the analytical models, initially developed for the optimisation of 1-3 composites for hydrophones and ultrasonic transducer applications, was investigated using the finite element technique. This work gave a thorough understanding of the interactions occurring in 1-3 composites, and how these affect the composite's piezoelectric, mechanical and electrical properties.

Chapter 3 compared analytical model predictions with results obtained from experimental testing. Since there had been no comprehensive experimental studies in the literature this was an important stage in the research. Commercially available fibres were incorporated into 1-3 composites with volume fractions spanning the entire range from 0.02 to 0.72. These were manufactured using a

variety of techniques to obtain a random fibre distribution. Standard characterisation techniques were used to measure the variation in d_{33}, d_{31}, coupling factor, dielectric constant and stiffness with fibre volume fraction. The trends in these properties were found to fit the analytical model predictions with accuracy at high volume fractions, providing confidence that fibre properties could be determined using the composite results in combination with the analytical models. Large errors observed when calculating fibre properties from composites with low volume fractions placed a lower volume fraction limit of 0.2 on the technique.

The technique was then used to extract properties from a range of commercially available fibres manufactured using different production methods. The methods compared were extrusion, viscous suspension spinning process (VSSP), Alceru and viscous plastic processing (VPP). This provided, for the first time, comparative material property data for the range of commercially available fibres allowing fibres, and the fibre production techniques, to be compared. A large variation in properties between the fibre types was seen. Interestingly, even fibres produced using the same process, but with different diameters (Alceru-125 and Alceru-250), displayed markedly different properties. Reasons for these differences were discussed later in Chapter 6.

9.1.2 High field properties of piezoelectric fibres

Chapters 4 and 5 dealt with the high field response of the fibres. In Chapter 4 models were developed to predict the strain and polarisation response of fibres from measurements made on 1-3 composites. These models used the assumptions and principles of the low field models presented in Chapter 2. The effects of deviation from the model assumptions were investigated and shown to have important implications under some circumstances. Errors associated with the polarisation response of the 1-3 composite are dominated by the non-linear nature of the piezoelectric d_{33} coefficient. The composite strain response was less influenced by non-linear material properties, but rather strongly influenced by deviation from the iso-strain assumption. This was examined using FE modelling, which showed that the extension and contraction of the active fibres from the surrounding passive matrix causes the measured composite strain to be lower than predicted. Since errors in both the strain and polarisation response of 1-3 composites were shown to be lower at high volume fractions, it was concluded that to increase the accuracy of calculated fibre responses, high volume fraction composites are required.

Chapter 5 compared experimentally measured high field strain and polarisation response of 1-3 composites to predictions made using the models developed in Chapter 4. For both the strain and the polarisation response it was found that composites with low fibre volume fractions deviated as

expected from the analytical model predictions. It was concluded that the volume faction of composite should be above 0.6 to avoid introducing errors inherent in the technique.

With the range of validity of the model confirmed, high field strain and polarisation responses from the full range of commercially available fibres tested in Chapter 3 were determined. The responses differed markedly between the fibre types, and trends agreed with those seen previously in the low field results of Chapter 3.

9.1.3 Physical and chemical fibre properties

Chapter 6 dealt with the characterisation of the physical and chemical properties of the full range of fibres tested in earlier chapters. The grain and fibre morphology was quantified using scanning electron microscopy. Grain sizes varied considerably; from 1.9 μm for the extruded fibres to 5.9 μm for the VSSP fibres. The fibres were all found to be approximately circular in cross section, although the Alceru fibres displayed a large variation in the calculated fibre diameter. Density measurements revealed that all fibres were adequately dense, except perhaps for the extruded fibres which had densities of 84% of the theoretical maximum. Fibre chemistry was characterised using x-ray diffraction, which showed that all fibres were composed entirely of the piezoelectric perovskite phase, and displayed no evidence of the non-piezoelectric pyrochlore phase. The ratio of tetragonal to rhombohedral perovskite phases varied between the fibre types, but all had compositions close to the MPB.

Information gained from the physical and chemical analysis was used to explain the differences observed in the piezoelectric properties of the fibres. In general it was found that a large grain size, high density and excess of tetragonal phase was associated with a large piezoelectric activity.

Having completed studies on the performance of the fibres at low and high electrical fields, and the physical and chemical analysis, fibres produced by the VPP process were selected as being the most suitable choice for incorporating into AFC devices.

9.1.4 Interdigitated electrode optimisation and manufacture

The goal of Chapter 7 was to understand the effect of the electrode design on the strain performance of AFC devices. Due to the complex geometry and number of variables in the IDE design, finite element analysis was selected as the most appropriate method to conduct this study. To simplify the model and reduce computational time, the IDE was modelled in two-dimensional space. Vector plots of the electric field within the substrate allowed the electric field transfer into

in-plane directions to be visualised, while path plots were used to gain a fundamental understanding of the factors influencing the field level within the substrate.

Varying the electrode width, w, substrate thickness, t, and electrode finger separation, s, revealed important information regarding the design of the IDE. It was found that the optimum electrode finger width was equal to half the substrate thickness. A reduction in substrate thickness therefore allows the electrode width, and the accompanying 'dead-zone' volume, to be reduced. The modelling also revealed that at large separation the influence of dead zones is small, while at low separations a high density of dead zones reduces the actuation compared to an ideal case. The reduction in strain was quantified by comparing the strain developed with the IDE to an ideal case in which all the electric field components are aligned with the desired actuation direction. It was shown that to maintain at least 80% of the ideal d_{33} response the electrode separation must satisfy $s/t > 4$.

A lithographic process was then used to manufacture the optimised IDE design in preparation for AFC manufacture. After developing the photoresist on the surface of the copper clad polyimide film in the desired geometry, the entire electrode was placed into $FeCl_3$ solution to etch the exposed copper. Although undercutting was found to occur, the associated reduction in the electrode finger width did not significantly degrade the device performance. This was supported by the results of the finite element study.

9.1.5 AFC manufacture and characterisation

AFC manufacture was discussed in Chapter 8. Fibres manufactured using the VPP technique were selected to construct the AFC device based on the results presented in Chapters 3, 5 and 6, which covered the low field properties, high field properties and physical and chemical properties respectively. The electrode design was based on the optimisation study presented in Chapter 7. Manufacturing the AFC device was very much by trial and error, and many early attempts resulted in failure for various reasons. Eventually a robust method of manufacture was developed, which was used for the majority of the AFC devices tested in this thesis. Ten AFC devices were successfully manufactured.

Devices were characterised by measuring their voltage-strain characteristics. The strain response, monitored with biaxial strain gauges, varied greatly from sample to sample. The expected device strain was predicted to be 75% of the free fibre strain response. This prediction was based on the reductions known to result from mechanical clamping of the fibres and electrical field degradation

from the IDE. In general, early samples (which were cured under a lower pressure compared to later devices) exhibited poor strain performance. Even the later devices did not develop the predicted level of strain. The poor strain performance, and large strain variation between the devices, was successfully associated with the variation in fibre-electrode separation. This was measured indirectly by the device capacitance. It was therefore concluded that simply increasing the pressure during the cure cycle of device manufacture should result in increased actuation performance. It is expected that this simple correction will result in AFC devices with optimised strain performance.

9.2 Future work

There are many avenues of future work that could be followed. Perhaps the most urgent is the necessity to reduce fibre-electrode separation to increase the strain response of the composites to the expected level, and to quantify the relationship between fibre-electrode contact and device strain. Once the AFC device has been optimised the 'component technology' (fibre production techniques and electrode technology) must continue to mature. In parallel, investigations into the practical uses of such a device can be made, thereby 'advancing the AFC concept'.

9.2.1 Fibre and electrode technology

There is a need to manufacture fibres with smaller diameters, since this is fundamental to lowering the driving voltage. Fibres with reduced diameter will form less of the total volume in an AFC and the force that can be generated will reduce. It is therefore likely that AFCs with more than a single layer of fibres will be required, raising issues associated with the electrodes and transfer of electric field. It can be expected that if the dielectric constant of the matrix remains low compared to the fibres then the field reaching the majority of the fibres will be severely reduced.

The recent advances in manufacturing metal core fibres[104] may solve this problem. Using the metal core as an electrode, and an outer coating as the other electrode, the full field will be experienced by the fibres and the driving voltage will be lowered considerably. However, fibres operating in this mode generate strains in the fibre direction via the d_{31} strain of the fibre. The d_{33} strain is directed in the fibre's radial direction.

Recent developments in textured and single crystal fibres[105] are expected to enhance AFC performance. If this technology is combined with metal core fibre technology adequate actuation strains could be generated without relying on the d_{33} response.

Further performance increases can be expected by manufacturing rectangular cross-section fibres, which still impart high anisotropy to devices, but benefit from higher packing densities. The transfer of electric field to such fibres needs to be investigated; it is speculated that because more of the fibre's surface is closer to the electrode fingers, the field reaching the fibres will be larger.

The structural nature of the AFC is very important, but to date under researched. Knowledge of the tensile and bend strengths of the active fibres is key to structural integrity. The fibres' interfacial chemistry and interaction with the matrix will be important, especially as fibre diameters become smaller. Surface coatings, such as silane coupling agents, could be used to promote adhesion with the matrix. Reinforcing the AFC device by incorporation of glass fibres (typically 3.5 to 24 μm diameter) could prove beneficial, although this will be at the expense of a lower actuation strain because of clamping, as discussed earlier.

As fibres begin to reduce in diameter there will be a need to reduce the electrode finger width. A possible technique is to weave continuous conducting wire around active fibres. This is particularly appealing for thin fibres, allowing multiple fibre thickness plies to be manufactured with the electrodes approaching close to every fibre. The woven pre-preg will provide simplified manufacturing in the lay-up stages, giving uniformly distributed and aligned fibres with electrodes in position.

9.2.2 Advancing the AFC concept

Laminated structures

An important stage in investigating practical applications of AFCs is characterisation of the performance of multi-ply AFC laminates. Laminated devices are expected to display interesting and useful behaviour allowing new and novel applications to be realised where bulk PZT devices fail to offer suitable responses. Finite element modelling should allow this characterisation to be performed rapidly. For example, Figure 9.1 depicts a 0/90 AFC laminate in which the top and bottom ply are controlled independently.

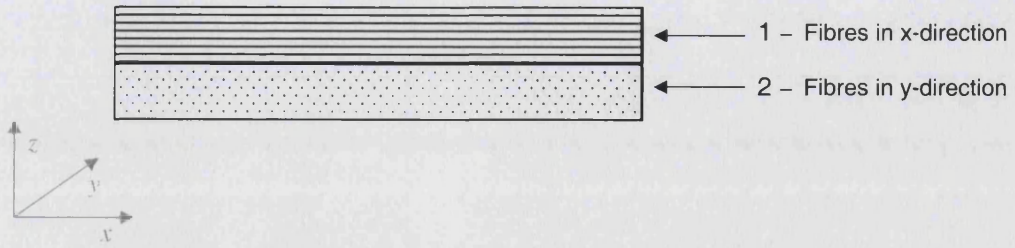

Figure 9.1: A 2D illustration of the 0/90 2-ply AFC laminate.

One potential mode of operation is extension of a single ply in the fibre direction while the other remains inactive. The images presented in Figure 9.2 are of a solved ANSYS model in which the top ply has been extended by 10 μm in the x direction. The response of the AFC laminate, presented in Figure 9.2(a), is compared to that of a laminate in which the two plies are bulk PZT-5A poled in the x and y direction as appropriate.

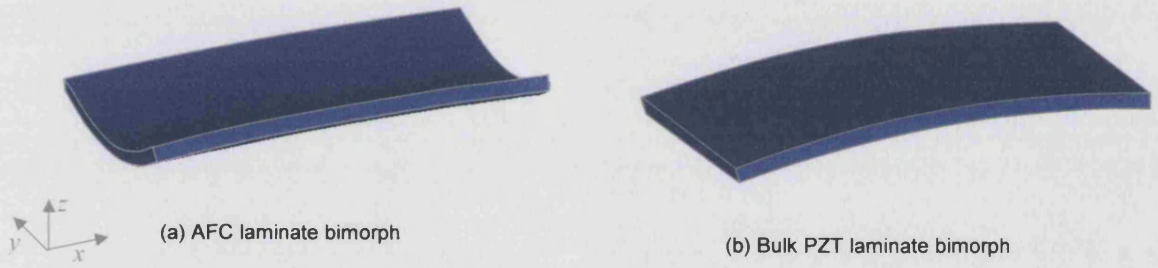

Figure 9.2: Comparison of surface profiles developed when the top ply is active in (a) a 0/90 2-ply AFC laminate compared to (b) a bulk PZT laminate. Displacements magnified by 100 times.

The profile developed for the bulk PZT laminated composite, Figure 9.2(b), displays the expected bimorph bender profile. However, the profile developed for the AFC laminated composite differs considerably. The major bending moment is about the x-axis, while very little bending is generated about the y-axis. It is also clear from these profiles that a greater bending moment is developed by the AFC laminate compared to the bulk PZT laminate due to its anisotropic stiffness.

A more complicated AFC laminate device can be conceived which comprises four plies in a 0/90/0/90 configuration. A depiction of this lay-up is presented in Figure 9.3.

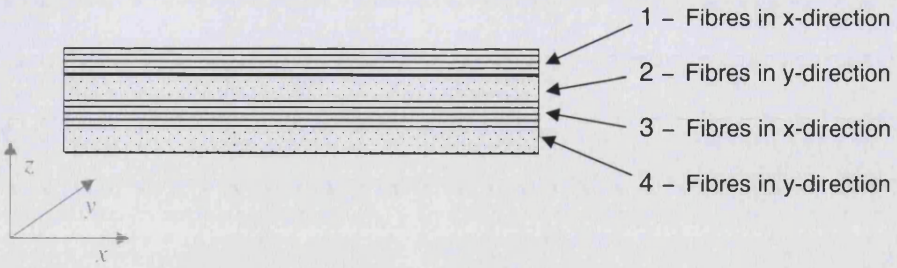

Figure 9.3: A 2D illustration of the 0/90/0/90 4-ply AFC laminate.

Solved models of this laminate are presented in Figure 9.4 and Figure 9.5. Again, the response of an identical model in which each ply is bulk PZT-5A poled in the *x* or *y* direction as appropriate is presented for comparison. Figure 9.4 shows the response if ply 1 and 3 are activated to generate a bending moment about the *y*-axis, using the principles of operation of a bimorph, while plies 2 and 4 remain inactive.

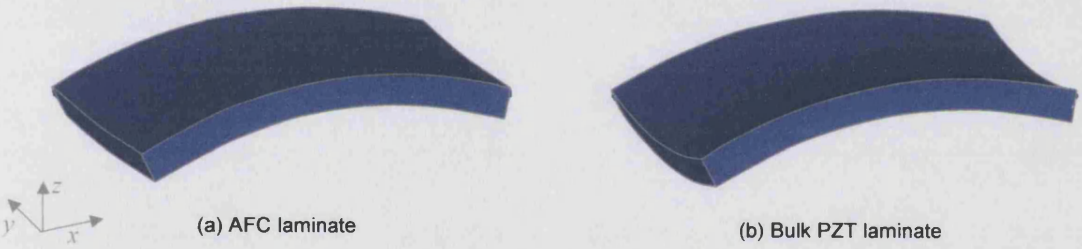

Figure 9.4: Comparison of surface profiles developed when plies 1 & 3 are active in (a) a 0/90/0/90 4-ply AFC laminate compared to (b) a bulk PZT laminate. Displacements magnified by 30 times.

Both the AFC and bulk PZT profiles look very similar in the *x* direction, generating a similar radius of curvature. However, when attention is focused in the *y* direction it is clear that the 'saddle' effect seen in the bulk laminate is reduced in the AFC laminate design. The ability to decouple the *x* and *y* bending moments is an inherent advantage of the high anisotropy present in each AFC ply.

The effect is also noticeable in Figure 9.5, which shows the profiles developed when plies 2 and 4 are activated to generate a bending moment about the *x*-axis, while plies 1 and 3 remain inactive.

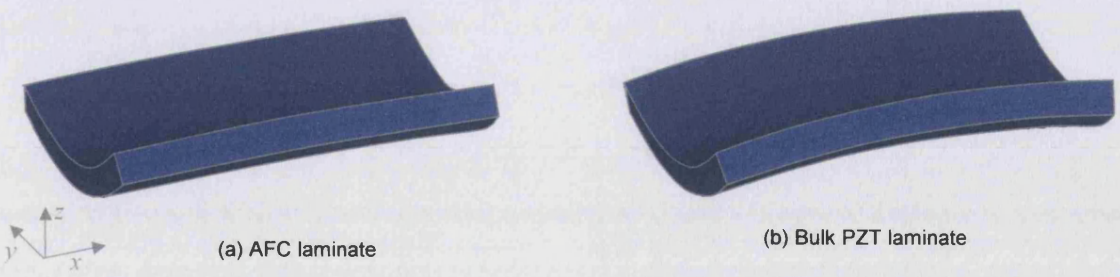

Figure 9.5: Comparison of surface profiles developed in a 0/90/0/90 laminate when plies 2 & 4 are active in (a) a 4-ply AFC compared to (b) a bulk PZT laminate. Displacements magnified by 30 times.

In this figure both laminates develop similar bending in the *y* direction, while the AFC laminate develops considerably less bending in the *x* direction.

By extending this type of FE characterisation further, the benefits offered by the high anisotropy and high flexibility of AFC devices are sure to open novel applications areas.

Segmented AFCs

Exciting actuation possibilities exist if the electrode geometry can be re-designing to allow individual segments of the AFC device to be independently actuated. AFC sheets could be actuated to induce travelling waves, much like the mode of operation of the peristaltic pump model presented in the literature review in Chapter 1. Such a device could be used to generate caterpillar type motion. If operating as a sensor, a segmented device would allow resolution of impact location in addition to the magnitude of impact.

Novel geometry fibre composites

Large dome type actuation may be possible by arranging the fibres radially in a circular geometry AFC (much like the spokes on a bicycle wheel), and actuating the fibres along their length. If two plies are operated back-to-back this type of motion could be used to pump liquids. It is also possible that an array of such devices could be used to generate sound, such as in flat panel speakers. Small deformable mirrors could also be an interesting application for this mode of actuation.

The research presented in this thesis, and the future work which will help advance it, is expected to enable the Active Fibre Composite to emerge as a viable actuation or sensing option for the smart structure engineer. This will open new and exciting application areas where current actuators would not be suitable.

APPENDICES

A1. Modelling piezoelectric materials using ANSYS

The following report was written as a user guide for modelling piezoelectric using ANSYS. It is included since it contains useful information regarding the material properties, and modelling in both 2-D and 3-D.

USING ANSYS TO MODEL PIEZOELECTRIC MATERIALS

(COVERING: MATERIAL PROPERTIES IN 3-D, MATERIAL PROPERTIES IN 2-D, AND ELEMENT TYPES)

LUKE NELSON

UNIVERSITY OF BATH

25/4/03

1.0 MATERIAL PROPERTIES IN 3-D

Introduction

ANSYS uses the following form of the linear piezoelectric constitutive relation to solve piezoelectric problems:

$$\begin{Bmatrix} T \\ D \end{Bmatrix} = \begin{bmatrix} c^E & -e_t \\ e & \varepsilon^S \end{bmatrix} \begin{Bmatrix} S \\ E \end{Bmatrix}$$

where T is the stress, D is the electrical displacement, S is the strain and E is the electric field. These are related through the material properties: stiffness under constant field c^E, the induced stress piezoelectric constant e, and the constant strain dielectric constant ε^S. The subscript t denotes a matrix transpose.

ANSYS requires the user to input the c^E and e matrix and the dielectric constants, ε^S. This section describes the format in which the ANSYS program requires this information to be input, which is slightly different from the conventional matrix representation of the constants. Firstly the mechanical properties are dealt with from a fundamental level, such that the ANSYS user has a better understanding of the required ANSYS format. Then the piezoelectric properties are explained. Finally the dielectric constant is explained.

Mechanical Properties

Stress

The state of stress σ at a point in a body can be represented by a tensor containing 9 stress components as below:

$$\sigma_{ij} = \begin{bmatrix} \sigma_{11} & \sigma_{12} & \sigma_{13} \\ \sigma_{21} & \sigma_{22} & \sigma_{23} \\ \sigma_{31} & \sigma_{32} & \sigma_{33} \end{bmatrix}$$

In this notation the first subscript denotes the normal to the plane on which the stress acts, and the second denotes the direction. This is expressed in **Error! Reference source not found.**. If the body is in equilibrium (not rotating) then the following conditions are true:

$$\sigma_{21} = \sigma_{12}, \qquad \sigma_{23} = \sigma_{32}, \qquad \sigma_{13} = \sigma_{31}$$

reducing the nine stress components to six.

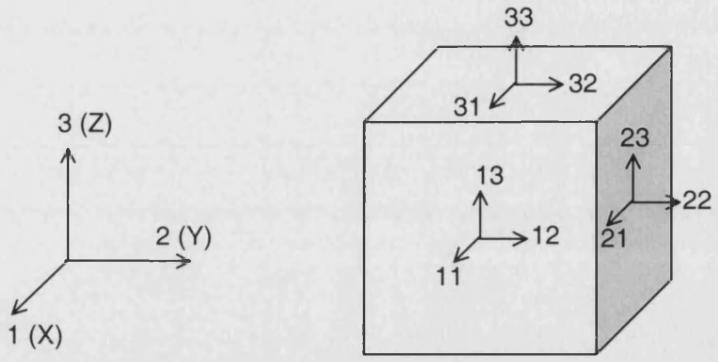

Figure 1. Coordinate system for resolution of stress components. (Bracketed letters denote the ANSYS coordinate notation)

Thus the state of stress at a point in a body at equilibrium can be defined by a stress tensor with six independent components:

$$\sigma_{ij} = \begin{bmatrix} \sigma_{11} & \sigma_{12} & \sigma_{13} \\ \sigma_{12} & \sigma_{22} & \sigma_{23} \\ \sigma_{13} & \sigma_{23} & \sigma_{33} \end{bmatrix}$$

which is commonly reduced to:

$$\sigma_{ij} = \begin{bmatrix} \sigma_1 & \sigma_6 & \sigma_5 \\ \sigma_6 & \sigma_2 & \sigma_4 \\ \sigma_5 & \sigma_4 & \sigma_3 \end{bmatrix}$$

where the diagonal components are normal stresses and the off-diagonal components are shear stresses.

Strain

Consider a body that has been deformed from its original position. The displacement of any point, P_1, in the body can be resolved into its components u, v, and w parallel to the x, y, and z axis, so that if the coordinates of the point in the undisplaced position were (x, y, z) they become $(x + u, y + v, z + w)$. The 9 tensor components of strain are defined by the symmetric strain tensor:

$$\varepsilon_{ij} = \begin{bmatrix} \dfrac{\partial u}{\partial x} & \dfrac{1}{2}\left(\dfrac{\partial v}{\partial x} + \dfrac{\partial u}{\partial y}\right) & \dfrac{1}{2}\left(\dfrac{\partial w}{\partial x} + \dfrac{\partial u}{\partial z}\right) \\ \dfrac{1}{2}\left(\dfrac{\partial v}{\partial x} + \dfrac{\partial u}{\partial y}\right) & \dfrac{\partial v}{\partial y} & \dfrac{1}{2}\left(\dfrac{\partial v}{\partial z} + \dfrac{\partial w}{\partial y}\right) \\ \dfrac{1}{2}\left(\dfrac{\partial w}{\partial x} + \dfrac{\partial u}{\partial z}\right) & \dfrac{1}{2}\left(\dfrac{\partial v}{\partial z} + \dfrac{\partial w}{\partial y}\right) & \dfrac{\partial w}{\partial z} \end{bmatrix}$$

which can be represented as:

$$\varepsilon_{ij} = \begin{bmatrix} \varepsilon_{11} & \varepsilon_{12} & \varepsilon_{13} \\ \varepsilon_{12} & \varepsilon_{22} & \varepsilon_{23} \\ \varepsilon_{13} & \varepsilon_{23} & \varepsilon_{33} \end{bmatrix}$$

which is commonly reduced to:

$$\varepsilon_{ij} = \begin{bmatrix} \varepsilon_1 & \varepsilon_6 & \varepsilon_5 \\ \varepsilon_6 & \varepsilon_2 & \varepsilon_4 \\ \varepsilon_5 & \varepsilon_4 & \varepsilon_3 \end{bmatrix}$$

In this notation the diagonal components correspond to tensile strains parallel to the axis and the off diagonals represent shear strains.

Stress-Strain Relationships

The second rank stress and strain tensors are related by the fourth rank stiffness *c* and compliance *s* tensors:

$$[\sigma] = [c][\varepsilon], \qquad [\varepsilon] = [s][\sigma]$$

The theoretical 9×9 = 81 stiffness and 81 compliance components reduces to 36 (6×6) due to the reduction in the stress and strain tensors.

$$\begin{bmatrix} \sigma_1 \\ \sigma_2 \\ \sigma_3 \\ \sigma_4 \\ \sigma_5 \\ \sigma_6 \end{bmatrix} = \begin{bmatrix} c_{11} & c_{12} & c_{13} & c_{14} & c_{15} & c_{16} \\ c_{21} & c_{22} & c_{23} & c_{24} & c_{25} & c_{26} \\ c_{31} & c_{32} & c_{33} & c_{34} & c_{35} & c_{36} \\ c_{41} & c_{42} & c_{43} & c_{44} & c_{45} & c_{46} \\ c_{51} & c_{52} & c_{53} & c_{54} & c_{55} & c_{56} \\ c_{61} & c_{62} & c_{63} & c_{64} & c_{65} & c_{66} \end{bmatrix} \begin{bmatrix} \varepsilon_1 \\ \varepsilon_2 \\ \varepsilon_3 \\ \varepsilon_4 \\ \varepsilon_5 \\ \varepsilon_6 \end{bmatrix}$$

The 36 components can be reduced to 21 since strain energy considerations show that:

$$c_{ij} = c_{ji}$$

Thus the stiffness tensor matrix becomes symmetric. Below is the stiffness matrix for a fully anisotropic material showing the 21 independent stiffness components that are needed to describe it fully.

$$[c_{ij}] = \begin{bmatrix} c_{11} & c_{12} & c_{13} & c_{14} & c_{15} & c_{16} \\ c_{12} & c_{22} & c_{23} & c_{24} & c_{25} & c_{26} \\ c_{13} & c_{23} & c_{33} & c_{34} & c_{35} & c_{36} \\ c_{14} & c_{24} & c_{34} & c_{44} & c_{45} & c_{46} \\ c_{15} & c_{25} & c_{35} & c_{45} & c_{55} & c_{56} \\ c_{16} & c_{26} & c_{36} & c_{46} & c_{56} & c_{66} \end{bmatrix}$$

The light grey letters represent the ANSYS (i.e. X, Y, Z) notation of the matrix of tensors if the stress and strain had not been represented in a reduced notation. Note that in the stress and strain reduction procedure the following conversions were made:

11 = 1
22 = 2
33 = 3
23 = 4
13 = 5
12 = 6

The matrix notation of c_{ij} already described is in the order XX, YY, ZZ, YZ, XZ, XY. However, ANSYS requires the order as XX, YY, ZZ, XY, YZ, XZ. Thus the matrix of tensors for input into ANSYS is:

$$[c_{ij}] = \begin{bmatrix} c_{11} & c_{12} & c_{13} & c_{16} & c_{14} & c_{15} \\ c_{12} & c_{22} & c_{23} & c_{26} & c_{24} & c_{25} \\ c_{13} & c_{23} & c_{33} & c_{36} & c_{34} & c_{35} \\ c_{16} & c_{26} & c_{36} & c_{66} & c_{46} & c_{56} \\ c_{14} & c_{24} & c_{34} & c_{46} & c_{44} & c_{45} \\ c_{15} & c_{25} & c_{35} & c_{56} & c_{45} & c_{55} \end{bmatrix}$$

These constants can be input into an active anisotropic elastic data table using the TBDATA command. Note that ANSYS requires the constant field compliances (c^E) to be input (see constitutive equation).

Symmetry

In practical cases most materials exhibit some level of symmetry allowing the 21 components to be reduced still further.

Orthotropic:
For an orthotropic material, with three orthogonal planes of symmetry, there can exist no interactions between normal stresses and shear strains, or between normal strains and shear stresses i.e. a volume element in the form of a rectangular parallelepiped with sides parallel to the planes of symmetry, after deformation under the action of normal stresses σ_1, σ_2 and σ_3 remains a rectangular parallelepiped. Thus the stiffness tensor reduces to:

$$[c_{ij}] = \begin{bmatrix} c_{11} & c_{12} & c_{13} & 0 & 0 & 0 \\ c_{12} & c_{22} & c_{23} & 0 & 0 & 0 \\ c_{13} & c_{23} & c_{33} & 0 & 0 & 0 \\ 0 & 0 & 0 & c_{44} & 0 & 0 \\ 0 & 0 & 0 & 0 & c_{55} & 0 \\ 0 & 0 & 0 & 0 & 0 & c_{66} \end{bmatrix}$$

Transversely isotropic:
Poled piezoelectric materials are transversely isotropic about the Z or 3 axis, which results in a further reduction in tensor components since:

$$c_{23} = c_{13}, \qquad c_{55} = c_{44}, \qquad c_{22} = c_{11}$$

Which results in:

$$[c_{ij}] = \begin{bmatrix} c_{11} & c_{12} & c_{13} & 0 & 0 & 0 \\ c_{12} & c_{11} & c_{13} & 0 & 0 & 0 \\ c_{13} & c_{13} & c_{33} & 0 & 0 & 0 \\ 0 & 0 & 0 & c_{44} & 0 & 0 \\ 0 & 0 & 0 & 0 & c_{44} & 0 \\ 0 & 0 & 0 & 0 & 0 & c_{66} \end{bmatrix}$$

Which, when translated into the ANSYS format becomes:

$$[c_{ij}] = \begin{bmatrix} c_{11} & c_{12} & c_{13} & 0 & 0 & 0 \\ c_{12} & c_{11} & c_{13} & 0 & 0 & 0 \\ c_{13} & c_{13} & c_{33} & 0 & 0 & 0 \\ 0 & 0 & 0 & c_{66} & 0 & 0 \\ 0 & 0 & 0 & 0 & c_{44} & 0 \\ 0 & 0 & 0 & 0 & 0 & c_{44} \end{bmatrix}$$

Piezoelectric Properties

Piezoelectric induced stress constants, e_{ij}:

A piezoelectric ceramic has only one type of piezoelectric matrix regardless of the symmetry of the constituent crystals. Once poled the ceramic has cylindrical symmetry about the polar axis. Shear stresses in a plane perpendicular to the polar axis (3) do not excite a piezoelectric response. Therefore the *e* matrix becomes:

$$e_{ij} = \begin{bmatrix} 0 & 0 & 0 & 0 & e_{15} & 0 \\ 0 & 0 & 0 & e_{15} & 0 & 0 \\ e_{31} & e_{31} & e_{33} & 0 & 0 & 0 \end{bmatrix}$$

Where the first subscript is the electrical direction (field or dielectric displacement), a vector quantity that can have subscripts 1, 2, or 3. The second subscript is the mechanical direction, a second order tensor quantity that can have subscripts 1 to 6 (see reduced stress notation for an explanation of the subscripts). The light grey letters represent the ANSYS (i.e. X, Y, Z) notation of the matrix. ANSYS requires the *e* coefficient matrix to be input

in transpose form in the order XX, YY, ZZ, XY, YZ, XZ. Thus the 3-D matrix for input into ANSYS is:

$$e_{ij} = \begin{bmatrix} 0 & 0 & e_{13} \\ 0 & 0 & e_{13} \\ 0 & 0 & e_{33} \\ 0 & 0 & 0 \\ 0 & e_{15} & 0 \\ e_{15} & 0 & 0 \end{bmatrix}$$

The constants can be input into an active piezoelectric data table using the TBDATA command.

Dielectric Constant

The dielectric is a second order tensor quantity that relates dielectric displacement to electric field. For input into ANSYS the constant strain dielectric constants (ε^S) are required (see constitutive relation). Only two dielectric constants are required to describe the system completely since symmetry relations give $\varepsilon_{22} = \varepsilon_{11}$:

$$\varepsilon_{ij} = \begin{bmatrix} \varepsilon_{11} & 0 & 0 \\ 0 & \varepsilon_{11} & 0 \\ 0 & 0 & \varepsilon_{33} \end{bmatrix}$$

In reduced notation these constants are given only one subscript, and become ε_1, and ε_3. These constants can be input by using the MP,PERX, MP,PERY and MP,PERZ commands.

Relationships Between Material Constants

Another commonly used form of constitutive equation to describe the behaviour of piezoelectric materials is:

$$\begin{Bmatrix} D \\ S \end{Bmatrix} = \begin{bmatrix} \varepsilon^T & d \\ d_t & s^E \end{bmatrix} \begin{Bmatrix} E \\ T \end{Bmatrix}$$

In this form D, S, E and T are related through the material properties: compliance under constant field s^E, the induced strain piezoelectric constant d, and the constant stress dielectric constant ε^T. To convert these material constants into the ANSYS required c^E, e and ε^S the following relationships can be used (Bent, 1997) (also see Moulson and Herbert, 1990):

$$c^E = (s^E)^{-1} \qquad e = dc^E \qquad \varepsilon^S = \varepsilon^T - dc^E d_t$$

2.0 MATERIAL PROPERTIES IN 2-D

Introduction

2D models can be used for
1) Thin, planar structures (plane strain)
2) 'Infinitely long' structures (plane stress)
3) Axisymmetric solid structures

Properties for piezoelectric materials are usually given such that the Z or 3-direction is the direction of poling. However a 2-D ANSYS model must be constructed in the X-Y plane. This requires the user to transform the 3-D stiffness, piezoelectric and dielectric matrix into the required 2-D matrix with the direction of poling in either the X or Y direction.

This section explains how the material properties should be input into ANSYS for a valid 2D solution.

2-D Mechanical Properties

For a 2-D models, a 4×4 matrix of stiffness constants is expected, relating the terms ordered XX, YY, ZZ, XY.

Poled in the Y-axis:

The axis of symmetry must be transformed such that the direction of poling is in the 2 or Y direction. This requires the 3D stiffness matrix notation to be rearranged. Using the light grey ANSYS notation, the Y's are replaced by Z's and the Z's by Y's. The required 2D tensor components can now be taken directly from the relabelled 3D tensor matrix and input into the 2D tensor matrix in the appropriate positions. Thus the 2-D stiffness matrix in ANSYS format becomes:

$$[c_{ij}] = \begin{bmatrix} c_{11} & c_{13} & c_{12} & 0 \\ c_{13} & c_{33} & c_{13} & 0 \\ c_{12} & c_{13} & c_{11} & 0 \\ 0 & 0 & 0 & c_{44} \end{bmatrix}$$

Poled in the X-axis:

The axis of symmetry must be transformed such that the direction of poling is in the 1 or X direction. This requires the 3D stiffness matrix notation to be rearranged. Using the light grey ANSYS notation, the X's are replaced by Z's and the Z's by X's. The required 2D tensor components can now be taken directly from the relabelled 3D tensor matrix and input into the 2D tensor matrix in the appropriate positions. Thus the 2-D stiffness matrix in ANSYS format becomes:

$$[c_{ij}] = \begin{bmatrix} c_{33} & c_{13} & c_{13} & 0 \\ c_{13} & c_{11} & c_{12} & 0 \\ c_{13} & c_{12} & c_{11} & 0 \\ 0 & 0 & 0 & c_{44} \end{bmatrix}$$

This data is input into the full 6×6 matrix that is used for 3D problems.
Note that that XZ = ZX, YZ = ZY and XY = YX.

2-D Piezoelectric Properties

Only a 2×4 *e* coefficient matrix is required relating the terms ordered XX, YY, ZZ, XY to X, Y

Poled in the Y-axis:
The poling axis becomes the Y or 2-axis. This requires the 3D *e* matrix notation to be rearranged. The Y's are replaced by Z's and the Z's by Y's. The required 2D components can now be taken directly from the relabelled 3D matrix and input into the 2D matrix in the appropriate positions. Thus the 2-D stiffness matrix in ANSYS format becomes:

$$e_{ij} = \begin{bmatrix} 0 & e_{13} \\ 0 & e_{33} \\ 0 & e_{13} \\ e_{15} & 0 \end{bmatrix}$$

Poled in the X-axis:
The poling axis becomes the X or 1-axis. This requires the 3D *e* matrix notation to be rearranged. The X's are replaced by Z's and the Z's by X's. The required 2D components can now be taken directly from the relabelled 3D matrix and input into the 2D matrix in the appropriate positions. Thus the 2-D stiffness matrix in ANSYS format becomes:

$$e_{ij} = \begin{bmatrix} e_{33} & 0 \\ e_{13} & 0 \\ e_{13} & 0 \\ 0 & e_{15} \end{bmatrix}$$

2-D Dielectric Properties

This simply requires transforming the 3-D properties into the correct positions:

Poled in Y: $\varepsilon_{xx} = \varepsilon_{11}$, $\varepsilon_{yy} = \varepsilon_{33}$, $\varepsilon_{zz} = \varepsilon_{11}$

Poled in X: $\varepsilon_{xx} = \varepsilon_{33}$, $\varepsilon_{yy} = \varepsilon_{11}$, $\varepsilon_{zz} = \varepsilon_{11}$

Note on Axisymmetry

Any structure that displays geometric symmetry about a centre axis (such as a shell or solid of revolution) is an axisymmetric structure. Examples would include straight pipes, cones, circular plates, domes, and so forth.

Models of axisymmetric 3-D structures may be represented in equivalent 2-D form in ANSYS. This not only reduces computation time but also increases the accuracy of results.

The model must be constructed with 2D axisymmetric elements. For piezoelectrics the appropriate element is PLANE13 with KEYOPT (3) set to 1. The model must be constructed such that the axis of symmetry is in coincidence with the global Cartesian Y-axis. As with other 2-D models the axisymmetric model must be constructed in the X-Y plane

Note on Arbitrary Poling Directions

By transformation of the material properties matrices it is possible to change the poling direction of a 3-D and 2-D model to lie at any angle from the chosen poling direction. It is not the intention of this guide to cover this in detail since many texts are available which describe this process.

3.0. ELEMENTS TYPES

Introduction

ANSYS has three element types that support the piezoelectric effect. These are SOLID5, SOLID98 and PLANE13. These element types are now introduced.

Element Types

SOLID5	Scalar Brick	8 Node	Hexahedral (6 faces)	3D
SOLID98	Scalar Tet.	10 Node	Tetrahedral (4 faces)	3D
PLANE13	Vector Quad.	4 Node	Quadrilateral (4 sides)	2D

Further information about the element types, situations in which they should be used and options for each element type (KEYOPT) can be found in the element reference library in the ANSYS program.

4.0 REFERENCES

ANSYS Modelling and Meshing Guide, 000862, 2nd Edition (Release 5.4), Sept. 1997

A. Bent, Active Fiber Composites for Structural Actuation, *PhD Thesis*, Massachusetts Institute of Technology (AMSL), pp. 203-204, **1997.**

A. J. Moulson and J. M. Herbert, 'Electroceramics: Materials, properties and applications', Chapman and Hall, 1990, pp.314-316.

A2. Material properties for finite element modelling

Unless otherwise specified, the material property values for PZT-5A used for the finite element modelling are those given in Table A2.1.

Table A2.1: Material property data for PZT-5A.[99]

Material Property	Value
e_{33}	15.8 Cm^{-1}
e_{31}	-5.2 Cm^{-1}
e_{15}	12.3 Cm^{-1}
$\varepsilon_{33}^{S}/\varepsilon_0$	830
$\varepsilon_{11}^{S}/\varepsilon_0$	916
c_{11}^{E}	12.0×10^{10} Pa
c_{12}^{E}	7.52×10^{10} Pa
c_{13}^{E}	7.51×10^{10} Pa
c_{33}^{E}	11.1×10^{10} Pa
c_{44}^{E}	2.10×10^{10} Pa

Material properties for any general polymer and for Struers Specifix-40 are stated in relevant chapters.

A3. Finite element modelling test cases

An important stage in finite element modelling is to ensure that modelling of a simple geometry yields the expected results. This confirms that the modelling procedure, including applied boundary conditions and material properties, are correct. A simple model of a piezoelectric fibre was developed and solved to ensure confidence can be placed in the more complex modelling presented in this thesis.

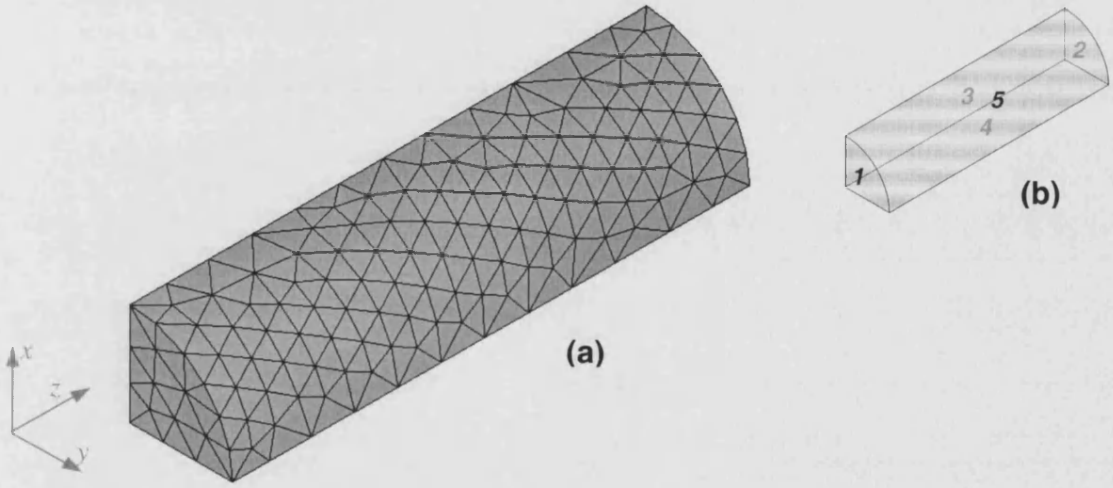

Figure A3.1: (a) Meshed model of a fibre with coordinate axis defined. Defined in (b) are the face numbers for reference to boundary condition and load application sites.

A 1/8th model of a fibre was constructed as pictured in Figure A2.1. The fibre had a radius of 100 μm and a length of 1.0 mm. It was meshed with SOLID98 elements with material properties of PZT-5A poled in the $+z$ direction. Symmetry was applied on faces 1, 3 and 4. The nodes on faces 1 and 2 had their voltage degree of freedom coupled to represent equipotential electroded surfaces.

The material properties require by ANSYS to described the coupling between stress (T), strain (S), electrical displacement (D) and electric field (E), are the stiffness matrix under constant field c^E, the induced stress piezoelectric e matrix, and the constant strain dielectric ε^S matrix. The constitutive relationship between these parameters is given below.

$$\begin{Bmatrix} T \\ D \end{Bmatrix} = \begin{bmatrix} c^E & -e_t \\ e & \varepsilon^S \end{bmatrix} \begin{Bmatrix} S \\ E \end{Bmatrix} \tag{A3.1}$$

This equation describes completely the electro-mechanical coupling present in piezoelectric materials. However, measurements made on piezoelectrics typically yield a complimentary set of material properties. These are the compliance under constant electric field s^E, the induced strain piezoelectric coefficient d, and the constant stress dielectric constant ε^T. The constitutive relationship between these parameters is given below.

$$\begin{Bmatrix} D \\ S \end{Bmatrix} = \begin{bmatrix} \varepsilon^T & d \\ d_t & s^E \end{bmatrix} \begin{Bmatrix} E \\ T \end{Bmatrix} \tag{A3.2}$$

A complete set of experimentally determined material constants were obtained from a manufacturer.[99] The test case (verification) involved supplying ANSYS with the required material parameters (c^E, e, ε^S). Load cases were applied to the model, and the response analysed, to measure the complementary material constants (s^E, d and ε^T). Comparing the finite element results with the manufacturer's measured properties ensures confidence in the modelling procedure.

The mechanical and electrical load cases applied to the modelled fibre, and the material properties determined for each load case are given in Table A3.1.

Table A3.1: FEM load cases to determine the complimentary material properties

Case	Mechanical Loading	Electrical Loading	Properties Obtained		
1	Face 2: Free Face 5: Free	Face 1: V = 0 Face 2: Apply Voltage	d_{33}	d_{31}	ε_{33}^T
2	Face 2: Apply Force Face 5: Free	Face 1: V = 0 Face 2: V = 0	d_{33}	s_{33}^E	s_{13}^E

Modelling results are compared to manufacturer's experimental results in Table A3.2.

Table A3.2: A comparison of FE and manufacturer's key material property values.

Material Property	Manufactures Value	FE Analysis Value	Deviation of FE from Manufactures Values (%)
d_{33} ($x10^{-12}$ CN^{-1})	374	372	0.5
d_{31} ($x10^{-12}$ CN^{-1})	-171	-170	0.6
$\varepsilon_{33}^{T}/\varepsilon_0$	1700	1694	0.4
s_{33}^{E} ($x10^{-12}$ Pa^{-1})	18.8	18.8	0
s_{13}^{E} ($x10^{-12}$ Pa^{-1})	-7.2	-7.2	0

Material properties predicted by ANSYS are close to manufacturer's values, in some cases the results are identical. The deviation in the results arises from the fact that manufacturer's values are experimentally determined, while the FE results are arrived at from manipulation of the input material properties. The point to note from this exercise is that confidence can be placed in the FE modelling procedure.

A4. Example ANSYS macros

Macros were written to perform the FE modelling presented in this thesis. A macro consists of lines of ANSYS commands written in a basic text editor (Windows Notepad). The file is saved in the directory specified as the ANSYS working directory for the current project and executed by typing *use, filename.txt at the ANSYS command input line. A representative selection of the macros used in Chapter 2, Chapter 4 and Chapter 7 (the three chapters in which FE modelling was performed) now follow.

Example from Chapter 2: Macro to measure the d_{33} of a 1-3 composite.

```
FINISH
/CLEAR,START
/PREP7
ET,1,SOLID98,3
/PAGE,1000000,,1000000

*ASK,V,Fibre Volume fraction,0.5
*ASK,A,Fibre Aspect Ratio,10
*ASK,Y,Polymer Modulus (GPa),1

CYL4,0,0,100e-6,0,0,90,((200E-6)/A)/2
BLOCK,0,(SQRT((3.141593*(100E-
        6)*(100E-6))/V))
        /2,0,(SQRT((3.141593*(100E-
        6)*(100E-6))/V))
        /2,0,((200E-6)/A)/2

VSBV,2,1
CYL4,0,0,100e-6,0,0,90,((200E-6)/A)/2
VGLUE,ALL


MAT,1

MP,PERX,1,916
MP,PERY,1,916
MP,PERZ,1,830

TB,PIEZ,1
TBDATA,3,-5.2
TBDATA,6,-5.2
TBDATA,9,15.8
TBDATA,14,12.3
TBDATA,16,12.3
```

```
TB,ANEL,1,,,0
TBDATA,1,12.0e10,7.52e10,7.51e10
TBDATA,7,12.0e10,7.51e10
TBDATA,12,11.1e10
TBDATA,16,2.3e10
TBDATA,19,2.1e10

TBDATA,21,2.1e10MAT,2
MP,EX,2,Y*1000000000
MP,NUXY,2,0.38
MP,PERX,2,5

VSEL,S,VOLU,,1
VATT,1,,,0
VSEL,S,VOLU,,2,
VATT,2,,,0

VSEL,ALL

SMRT,1
VMESH,ALL

ASEL,S,AREA,,2
ASEL,A,AREA,,16
NSLA,S,1
CP,1,VOLT,ALL
D,ALL,VOLT,0

ASEL,S,AREA,,1
ASEL,A,AREA,,10
NSLA,S,1
CP,2,VOLT,ALL
D,ALL,VOLT,0
```

```
ASEL,S,AREA,,5
ASEL,A,AREA,,6
ASEL,A,AREA,,7
ASEL,A,AREA,,8
ASEL,A,AREA,,1
ASEL,A,AREA,,10
DA,ALL,SYMM

ASEL,S,AREA,,2
ASEL,A,AREA,,16
NSLA,S,1
CP,3,UZ,ALL

ASEL,S,AREA,,11
NSLA,S,1
CP,4,UX,ALL

ASEL,S,AREA,,9
NSLA,S,1
CP,5,UY,ALL

ASEL,S,AREA,,2
ASEL,A,AREA,,16
SFA,ALL,,PRES,1

ALLSEL,ALL

CNVTOL,F,,,,1E-6
CNVTOL,AMPS,,,,1E-6
CNVTOL,VOLTS,,,,1E-6

/SOLU

SOLVE
```

Example from Chapter 4: Macro to investigate the effect of deviation from the iso-strain assumption in a 1-3 composite.

```
FINISH
/CLEAR,START
/PREP7
ET,1,SOLID98,3
/PAGE,1000000,,1000000

*ASK,V,Fibre Volume fraction,0.7
*ASK,A,Fibre Aspect Ratio,0.05
*ASK,Y,Polymer Modulus (GPa),2.8

CYL4,0,0,125e-6,0,0,90,((250E-6)/A)/2
BLOCK,0,(SQRT((3.141593*(125E-
        6)*(125E-6))/V))
        /2,0,(SQRT((3.141593*(125E-
        6)*(125E-6))/V))
        /2,0,((250E-6)/A)/2

VSBV,2,1
CYL4,0,0,125e-6,0,0,90,((250E-6)/A)/2
VGLUE,ALL

MAT,1
MP,PERX,1,916
MP,PERY,1,916
MP,PERZ,1,830

TB,PIEZ,1
TBDATA,3,-5.2
TBDATA,6,-5.2
TBDATA,9,15.8
TBDATA,14,12.3
TBDATA,16,12.3

TB,ANEL,1,,,0
TBDATA,1,12.0e10,7.52e10,7.51e10
TBDATA,7,12.0e10,7.51e10
TBDATA,12,11.1e10
TBDATA,16,2.3e10
TBDATA,19,2.1e10
TBDATA,21,2.1e10

MAT,2
MP,EX,2,Y*1000000000
MP,NUXY,2,0.38
MP,PERX,2,5

VSEL,S,VOLU,,1
VATT,1,,,0

VSEL,S,VOLU,,2,
VATT,2,,,0

VSEL,ALL
SMRT,1
VMESH,ALL

ASEL,S,AREA,,2
ASEL,A,AREA,,16
AREFINE,ALL,,,1,1,CLEAN
ALLSEL,ALL

ASEL,S,AREA,,2
ASEL,A,AREA,,16
NSLA,S,1
CP,1,VOLT,ALL
D,ALL,VOLT,-1000

ASEL,S,AREA,,1
ASEL,A,AREA,,10
NSLA,S,1
CP,2,VOLT,ALL
D,ALL,VOLT,0

ASEL,S,AREA,,5
ASEL,A,AREA,,6
ASEL,A,AREA,,7
ASEL,A,AREA,,8
ASEL,A,AREA,,1
ASEL,A,AREA,,10
DA,ALL,SYMM

ASEL,S,AREA,,11
NSLA,S,1
CP,4,UX,ALL

ASEL,S,AREA,,9
NSLA,S,1
CP,5,UY,ALL

ALLSEL,ALL

CNVTOL,F,,,,1E-6
CNVTOL,AMPS,,,,1E-6
CNVTOL,VOLTS,,,,1E-6

/SOLU

SOLVE
```

Example from Chapter 7: Macro to investigate the effect of electrode parameters on the strain response of an IDE.

```
FINISH
/CLEAR,START
/PREP7
/PAGE,10000,,10000,

multipro,'start',

*CSET,1,3,T,'thickness (microns)',200
*CSET,4,6,S,'E-to-E electrode spacing
(mm)',1
*CSET,7,9,W,'Electrode Width
(microns)',100
*CSET,10,12,V,'Voltage on Electrode
(kV)',0.5
*CSET,13,15,P,'thickness of polymer
layer (microns)',1
*CSET,16,18,D,'polymer relative
dielectric cnst',5

Multipro,'END',

ET,1,PLANE13,7,,2,0,0

MP,PERX,1,830
MP,PERY,1,916
MP,PERZ,1,916

TB,PIEZ,1
TBDATA,1,15.8
TBDATA,4,-5.2
TBDATA,7,-5.2
TBDATA,11,12.3

TB,ANEL,1,,,0
TBDATA,1,11.1e10,7.51e10,7.51e10
TBDATA,7,12.0e10,7.52e10
TBDATA,12,12.0e10
TBDATA,16,2.1e10

RECTNG,0,(S/2000),0,(T/2000000)

RECTNG,0,-(W/2000000),0,(T/2000000)

AGLUE,1,2

!ESIZE,(1/1000000)
LESIZE,3,,,100,0.05,,,0
LESIZE,1,,,100,20,,,0
LSEL,S,LINE,,2,8,2
!LESIZE,ALL,,,20,,,,0
LESIZE,ALL,,,50,,,,0
LSEL,S,LINE,,9,10,1
LESIZE,ALL,,,50,,,,0

ALLSEL,ALL
MSHAPE,0,2D
MSHKEY,1
AMESH,ALL

NSEL,S,LOC,Y,(T/2000000)
NSEL,U,LOC,X,0,(S/2000)
CP,1,VOLT,ALL
D,ALL,VOLT,(V*500)

NSEL,S,LOC,X,(S/2000)
CP,2,VOLT,ALL
D,ALL,VOLT,0

NSEL,S,LOC,X,-(W/2000000)
CP,3,UX,ALL
LSEL,S,LINE,,1,2,1
LSEL,A,LINE,,9
DL,ALL,,SYMM
NSEL,S,LOC,X,(S/2000)
D,ALL,UX,0

ALLSEL,ALL
CNVTOL,F,,,,1E-6
CNVTOL,AMPS,,,,1E-6
CNVTOL,VOLTS,,,,1E-6

/SOLU
solve
```

A5. Summary of AFC devices manufactured

Table A5.1 contains information regarding the AFC devices manufactured and tested in Chapter 8 of this thesis.

Table A5.1: Summary of the AFC devices manufactured.

AFC Number	Date Manuf.	No. Fibres	Applied Load	Poling Conditions	General Comments	Capacitance Prior to Poling (pF)
AFC_DENT01	8/22/2003	56	10 kg	3.5 kV, 100°C	Yellow casting rubber mould coating (not perfectly smooth), channel in 254mm shim causing matrix flow, poor fibre alignment and overlap.	48.1
AFC_DENT02	8/29/2003	56	10 kg	3.5 kV, 100°C	Neoprene rubber mould coating, no channel in 190.5 mm shim. This mould coating and shim type are used in all subsequent AFC runs.	61.2
AFC_DENT03	9/2/2003	53	10 kg	3.0 kV, 100°C	Not great electrode registration, Poling at 3.5 kV caused breakdown, which was drilled out.	60.0
AFC_DENT04	9/3/2003	50	10 kg	4.0 kV, 100°C	Good fibre and electrode alignment, a slight bunching of the fibres towards the LHS if viewing from the top.	67.7
AFC_DENT05	9/9/2003	50	10 kg	3.5 kV, 100°C	Good fibre and electrode alignment.	61.6
AFC_DENT06	9/11/2003	50	10 kg	3.5 kV, 100°C	Good fibre and electrode alignment.	65.0
AFC_DENT07	9/16/2003	50	10 kg	3.3 kV, 100°C	Poling at 3.5 kV caused breakdown, reduced to 3.3 kV for remainder. Good electrode alignment, fibres are slightly bowed, evidence of large amounts of porosity.	76.0
AFC_DENT08	10/20/2003	50	20 kg	2.0 kV, 100°C	Sample removed form mould too early so electrode not fixed in place. Replaced, but voids created caused breakdown at 3.5 kV. Damage drilled and filled, but still occasional breakdown at the 2.0 kV selected for remainder of poling.	102.4
AFC_DENT09	10/22/2003	50	20 kg	3.0 kV, 60°C	Initially poled at 4.0 kV but extensive breakdown at end of sample caused amp to switch to current control. Cut end of sample with scalpel and re-poled 60°C at lower voltage.	103.2
AFC_DENT10	10/29/2003	50	20 kg	3.5 kV, 60°C	Void at sample edge filled with epoxy using a syringe. Lower poling temp. selected because it was thought that high temperatures could weaken the interface between the fibre and electrode, increasing potential of breakdown. Unexpectedly low Cp considering the pressure applied.	74.0

REFERENCES

[1] A. BENT: 'Active fibre composite material systems for structural control applications,' in 'Smart Structures and Materials 1999: Industrial and Commercial Applications of Smart Structures Technologies', 1999, *Proc. of SPIE*, **3674**, 166-177.

[2] M. SCHULZ, M. SUNDARESAN, A. GHOSHAL, P. PAI: 'Active fiber composites for structural health monitoring', in 'Smart Structure and Materials 2000: Active materials: Behaviour and Mechanics', 2000, *Proc. of SPIE*, **3992**, 13-24.

[3] N. HAGOOD, A. BENT: 'Composites for structural control', US Pat. No. 6,048,622, 2000.

[4] SMART MATERIAL CORP.: http://www.smart-material.com, 2003.

[5] ADVANCED CERAMETRICS INC.: http://www.advancedcerametrics.com, 2003, P.O. Box 128, 245 North Main Street, Lambertville, N.J.

[6] S. PARK, W. HACKENBERGER: 'High performance single crystal piezoelectrics: applications and issues', *Current Opinion in Solid State & Materials Science*, 2002, **6** (1), 11-18.

[7] W. SPILLMAN JR., J. SIRKIS, P. GARDINER: 'Smart materials and structures: what are they?', *Smart Mater. Struct.*, 1996, **5**, 247-254.

[8] INTELLIMAT: 'The "definition" of intelligent materials', *http://intellimat.com*, 2001.

[9] J. HODGKINSON: 'What are smart materials anyway?', *Materials World*, Aug. 1993, 449-451.

[10] E. CRAWLEY, A. BENT, D. WARKENTIN, N. HAGOOD: 'Recent progress in intelligent material systems', *Materiaux & Techniques*, 1994, **12**, 31-37.

[11] R. LIND, N. JOHNSON, C. DOUMANIDIS: 'Active deformable sheets: prototype implementation, modelling and control', in 'Smart Structures and Materials 2000: Smart Structures and Integrated Systems', 2000, *Proc. of SPIE*, **3985**, 572-582.

[12] G. HAERTLING: *J. Am. Ceram. Soc.*, 1999, **82** (4), 797-818.

[13] B. JAFFE, W. COOK JR., H. JAFFE: 'Piezoelectric Ceramics', 1971, New York, Academic Press.

[14] N. HAGOOD, A. BENT: 'Development of piezoelectric fiber composites for structural actuation', in 'Proc. 34th AIAA Structures, Structural Dynamics, and Materials Conference', La Jolla, CA, AIAA Paper No. 93-1717, 1993, 3625-3638.

[15] A. BENT, N. HAGOOD, J. RODGERS: 'Anisotropic actuation with piezoelectric fiber composites', *J. Intell. Mater. Syst. Struct.*, 1995, **6** (3), 338-349.

[16] N. HAGOOD, R. KINDEL, K. GHANDI, P. GAUDENZI: 'Improving transverse actuation of piezoceramics using interdigitated surface electrodes', in 'Smart Structures and Materials 1993: Smart Structures and Intelligent Systems', 1993, *Proc. of SPIE*, **1917**, 341-353.

[17] C. BOWEN, A. BOWLES, S. DRAKE, N. JOHNSON, S. MAHON: 'Fabrication and finite element modelling of interdigitated electrodes', *Ferroelectrics*, 1999, **228**, 257-969.

[18] H. HANSELKA: 'Overview of the German industrial research project ADAPTRONIC', in 'Smart Structures and Materials 2000: Industrial and Commercial Applications of Smart Structures Technologies', 2000, *Proc. of SPIE*, **3991**, 2-10.

[19] A. BENT, N. HAGOOD: 'Piezoelectric fiber composites with interdigitated electrodes', *J. Intell. Mater. Syst. Struct.*, 1997, **8** (11), 903-919.

[20] R. NEWHAM, D. SKINNER, L. CROSS: 'Connectivity and piezoelectric-pyroelectric composites,' *Mat. Res. Bull*, 1978, **13**, 525-536.

[21] R. MEYER JR., T. SHROUT, S. YOSHIKAWA: 'Development of ultra-fine scale piezoelectric fibers for use in high frequency 1-3 transducers', in Proc. '10th IEEE Int. Symp. on Applications of Ferroelectrics (ISAF)', 1996, New Jersey, 547-550.

[22] V. JANAS, A. SAFARI: 'Overview of fine-scale piezoelectric ceramic/polymer processing', *J. Am. Ceram. Soc.*, 1995, **78** (11), 2945-2955.

[23] D. SPORN, W. WATZKA, A. SCHÖNECKER, K. PANNKOKE: 'Smart structures by integration of piezoelectric PZT fibers – present state and future applications', in '9th CIMTEC World Forum on New Materials', Symposium VIII – Smart Material Systems, 1999, P. Vincenzini (Ed.), 279-286.

[24] H. STROCK, M. PASCUCCI, M. PARISH, A. BENT, T. SHROUT: 'Active PZT fibres, a commercial production process', in 'Smart Structures and Materials 1999: Smart Materials Technologies', 1999, *Proc. of SPIE*, **3675**, 22-31.

[25] D. WALLER, A. SAFARI, R. CARD, M. O'TOOLE: 'Lead zirconate titanate fiber/polymer composites prepared by a replication process', *J. Am. Ceram. Soc.*, 1990, **73**, (11), 3503-3506.

[26] M. TING, V. JANAS, A. SAFARI: 'Relic processing of fine-scale, large-area piezoelectric ceramic fiber/polymer composites', *J. Am. Ceram. Soc.*, 1996, **79**, 1689-1692.

[27] W. BECKERT, W. KREHER, W. BRAUW, M. ANTE: 'Effective properties of composites utilising fibres with a piezoelectric coating,' *J. Europ. Ceram. Soc*, 2001, **21**, 1455-1258.

[28] A. BENT, A. PIZZOCHERO: 'Recent advances in active fiber composites for structural control', in 'Smart Structures and Materials 2000: Industrial and Commercial Applications of Smart Structures Technologies', 2000, *Proc. of SPIE*, **3991**, 244-254.

[29] N. MCN. ALFORD, J. BIRCHALL, K. KENDALL: 'High strength ceramics through colloidal control to remove defects', *Nature*, 1987, **300**, 51-53.

[30] D. PEARCE, G. DOLMAN, C. MEGGS, T. BUTTON: 'Viscous processed versus conventional piezoelectric ceramics: experimental comparisons using real world devices', in *'Ferroelectrics 2000 UK'*, 2000, N. Alford & E. Yeatman (Eds.), London: IOM Communications, 145-152.

[31] B. SU, D. PEARCE, T. BUTTON: 'Plastic forming routes to net shape ferroelectric ceramics, thick films and devices', in '*Ferroelectrics 2000 UK*', 2000, N. Alford & E. Yeatman (Eds.), London: IOM Communications. 153-160.

[32] B. SU, Private communication, 2002.

[33] R. CASS: 'Fabrication of continuous ceramic fiber by the viscous suspension spinning process', *J. Am. Ceram. Soc. Bull.*, 1991, **70** (3), 424-429.

[34] R. CASS, J. FRENCH: 'Developing innovative ceramic fibres', *J. Am. Ceram. Soc. Bull.*, 1998, **76** (5), 61-65.

[35] A. SAFARI, V. JANAS, B. JADIDIAN, J. FRENCH, G. WEITZ, J. LUKE. R. CASS: 'Incorporation of piezoelectric Pb(Zr,Ti)O3 fibers into ceramic/polymer composites', in 'Smart Structures and Materials 1996: Industrial and Commercial Applications of Smart Structures Technologies', 1996, *Proc. of SPIE*, **2721**, 240-250.

[36] J. FRENCH, G. WEITZ, J. LUKE, R. CASS, B. JADIDIAN, P. BHARGAVA, A. SAFARI: 'Production of continuous piezoelectric ceramic fibers for smart materials and active control devices', in 'Smart Structures and Materials 1997: Industrial and Commercial Applications of Smart Structures Technologies', 1997, *Proc. of SPIE*, **3044**, 406-412.

[37] S. ZIKELI: 'Lyocell fibres with health-promoting effect through incorporation of seaweed', *Chemical Fibres International*, 2001, **51**, 272-276.

[38] R. MEYER JR., T. SHROUT, S. YOSHIKAWA: 'Lead zirconate titanate fibres derived from alkoxide-based sol-gel technology', *J. Am. Ceram. Soc.*, 1998, **81** (4), 861-868.

[39] S. YOSHIKAWA, U. SELVARAJ, K. BROOKS, S. KURTZ: 'Piezoelectric PZT tubes and fibers for passive vibrational damping', in Proc. '8th IEEE Int. Symp. on Applications of Ferroelectrics (ISAF)', 1992, 269-272.

[40] S. YOSHIKAWA, U. SELVARAJ, P. MOSES, J. WITHAM, R. MEYER, T. SHROUT: 'Pb(Zr,Ti)O3 [PZT] fibers – Fabrication and measurement methods', *J. Intell. Mater. Syst. Struct.*, 1995, **6** (2), 152-158.

[41] A. SCHÖNECKER, D. SPORN, W. WATZKA, L. SEFFNER, K. PANNKOKE, P. WIERACH: 'High-performance piezoelectric thin fibers and sheets as functional components for smart materials', in 'Smart Structures and Materials 2000: Industrial and Commercial Applications of Smart Structures Technologies', 2000, *Proc. of SPIE*, **3991**, 11-16.

[42] G. YI, Z. WU, M. SAYER: 'Preparation of Pb(Zr,Ti)O3 thin films by sol-gel processing – electrical, optical and electro-optic properties', *J. Appl. Phys.*, 1988, **64** (5), 2717-2724.

[43] Q. ZHOU, H. CHAN, C. CHOY: 'Nanocrystalline powder and fibres of lead zirconate titanate prepared by the sol-gel process', *Journal of Materials Processing and Technology*, 1997, **63**, 281-285.

[44] L. NELSON, C. BOWEN: 'Determination of the piezoelectric properties of fine-scale PZT fibres', *Key Engineering Materials*, 2002, **206** (2), 1509-1512.

[45] R. STEINHAUSEN, T. HAUKE, W. SEIFERT, H. BEIGE, W. WATZKA, S. SEIFERT, D. SPORN, S. STARK, A. SCHONECKER: 'Finescaled piezoelectric 1-3 composites: properties and modelling', *J. Euroean Ceram. Soc.*, 1999, **19**, 1289-1293.

[46] S. GEBHARDT, A. SCHONECKER, R. STEINHAUSEN, T. HAUKE, S. WOLFGANG, H. BEIGE: 'Fine-scale 1-3 composites fabricated by the soft mold process: preparation and modelling', *Ferroelectrics*, 2000, **241**, 67-73.

[47] W. SMITH, B. AULD: 'Modelling 1-3 composite piezoelectrics: thickness mode oscillations', *IEEE Trans. Ultrason. Ferroelec. Freq. Contr.*, 1991, **38** (1), 40-47.

[48] H. CHAN, J. UNSWORTH: 'Simple model for piezoelectric/polymer 1-3 composites used in ultrasonic transducer applications', *IEEE Trans. Ultrason. Ferroelec. Freq. Contr.*, 1989, **36**, 434-441.

[49] C-W NAN, L. LIU, D. GUO, L. LI: 'Calculation of the effective properties of 1-3 type piezoelectric composites with various rod/fibre orientations', *J. Phys. D: Appl. Phys.*, 2000, **33**, 2977-2984.

[50] A. BENT: 'Active fiber composites for structural actuation', 1997, *PhD Thesis*, Massachusetts Institute of Technology (AMSL).

[51] R. STEINHAUSEN, T. HAUKE, W. SEIFERET, H. BEIGE, U. LANGE, D. SPORN, G. GEBHARDT, A, SCHONECKER: 'A new method for the determination of elastic properties of thin piezoelectric PZT fibers', *Ferroelectrics*, 2002, **268**, 53-58.

[52] H. IWANAGA, T. IWASAKI, K. REIZEN, T. MATSUNAMI, M. ICHIHARA, S. TAKEUCHI: 'Method for tensile experiments with ceramic fibres having a diameter of a few micrometers', *J. Am. Ceram. Soc.*, 1992, **75** (5), 1297-1299.

[53] B. KING, J. HALLORAN: 'Polycrystalline yttrium aluminium garnet fibers from colloidal sols', *J. Am. Ceram. Soc.*, 1995, **78** (8), 2141-2148.

[54] P. BYSTRICKY: 'Ceramic piezoelectric fibers: correlating single fiber properties with active fiber composite performance', in 'Smart Structures and Materials 2000: Smart Structures and Integrated Systems', 2000, *Proc. of SPIE*, **3985**, 552-559.

[55] W. HACKENBERGER, M-J. PAN, V. VEDULA, P. PERTSCH, W-W. CAO, C. RANDALL, T. SHROUT: 'Effect of grain size on actuator properties of piezoelectric ceramics', in 'Smart Structures and Materials 1998: Smart Materials Technologies', 1998, *Proc. SPIE*, **3324**, 28-36.

[56] R. STEINHAUSEN, T. HAUKE, H. BEIGE, W. WATZKA, U. LANGE, D. SPORN, S. GEBHARDT, A. SCHNOECKER: 'Properties of fine scale piezoelectric PZT fibres with different Zr content', *J. European Ceram. Soc.*, 2001, **21**, 1459-1462.

[57] D. WARKENTIN: 'Modeling and electrode optimisation for torsional IDE piezoceramics', in 'Smart Structures and Materials 2000: Smart Structures and Integrated Systems', 2000, *Proc. of SPIE*, **3985**, 840-854.

[58] T. GESANG, H. KNÄBEL, U. MAURIESCHAT, A. HARTWIG, A. BATTERMAN, J. PERL, H. JOACHIMI: 'The use of adhesives in manufacturing adaptronic Microsystems for fight weight structures', in 'Smart Structures and Materials 2000: Industrial and Commercial Applications of Smart Structures Technologies', 2000, *Proc. of SPIE*, **3991**, 37-42.

[59] D. SPORN, W. WATZKA, K. PANNKOKE, A. SCHÖNECKER: 'Smart Structures by Integrated Piezoelectric Thin Fibres (I): Preparation, Properties and Integration of Fibres in the System Pb(Zr,Ti)O3', *Ferroelectrics*, 1999, **224**, 1-6.

[60] B. JANOS, N. HAGOOD: 'Magnetic particle doping for anisotropic matrix materials in Active Fiber Composites', in 'Smart Structures and Materials 1999: Smart Materials Technologies', 1999, *Proc. of SPIE*, **3675**, 10-21.

[61] J. RODGERS, A. BENT, N. HAGOOD: 'Characterization of interdigitated electrode piezoelectric fiber composites under high electrical and mechanical loading', in 'Smart Structures and Materials 1996: Smart Structures and Integrated Systems', 1996, *Proc. of SPIE*, **2717**, 642-659.

[62] N. HAGOOD, A. PIZZOCHERO: 'Residual stiffness and actuation properties of piezoelectric composites: theory and experiment', *J. Intell. Mater. Syst. Struct.*, 1997, **8** (9), 724-737.

[63] W. WILKIE, R. BRYANT, J. HIGH, R. FOX, R. HELLBAUM, A. JALINK JR., B. LITTLE, P. MIRICK: 'Low-cost piezocomposite actuator for structural control applications', in 'Smart Structures and Materials 2000: Industrial and Commercial Applications of Smart Structures Technologies', 2000, *Proc. of SPIE*, **3991**, 323-334.

[64] S-W. ZHOU, C. ROGERS: 'Heat generation, temperature, and thermal stress of structurally integrated piezo-actuators', *J. Intell. Mater. Syst. Struct.*, 1995, **6**, 372-379.

[65] A. SCHÖNECKER, U. KEITEL, W. KREHER, D. SPORN, W. WATZKA, K. PANNKOKE: 'Smart structures by integrated piezoelectric thin fibres (II): Properties of composites and their physical description', *Ferroelectrics*, 1999, **224**, 7-12.

[66] G. YANG, S-F. LIU, W. REN, B. MUKHEREJEE: 'Uniaxial stress dependence of the piezoelectric properties of lead zirconate titanate ceramics', in 'Smart Structures and Materials 2000: Active Materials: Behaviour and Mechanics', 2000, *Proc. of SPIE*, **3992**, 103-113.

[67] M. ALGUERO, B. CHENG, F. GUIU, M. REECE, M. POOLE, N. ALFORD: 'Degradation of the d33 piezoelectric coefficient for PZT ceramics under static and cyclic compressive loading', *J. European Ceram. Soc.*, 2001, **21**, 1437-1440.

[68] C-Y. LIN, N. HAGOOD: 'Compression depolarization of PZT piezoelectric materials under high electromechanical driving levels', in 'Smart Structures and Materials 2000: Active Materials: Behaviour and Mechanics', 2000, *Proc. of SPIE*, **3992**, 114-125.

[69] D. MORRIS, N. HAGOOD, A. PIZZOCHERO: 'An experimental investigation on the effect of environmental stress on Active Fiber Composite actuators', in 'Smart Structures and Materials 1999: Industrial and Commercial Applications of Smart Structures Technologies', 1999, *Proc. of SPIE*, **3674**, 296-305.

[70] A. PIZZOCHERO: 'Residual actuation and stiffness properties of piezoelectric composites: theory and experiment', 1998, *S.M. Thesis*, Massachusetts Institute of Technology (AMSL).

[71] M. SESTER, C. POIZAT: 'Simulation techniques for piezoelectric composite materials and their application to smart structures', in 'Smart Structures and Materials 2000: Smart Structures and Integrated Systems', 2000, *Proc. of SPIE*, **3985**, 750-778.

[72] D. HALL: 'Nonlinearity in piezoelectric ceramics', *J. Mater. Sci.*, 2001, **36**, 4575-4601.

[73] J. DURR, U. HEROLD-SCHMIDT, H. ZAGLAUER, F. ARENDTS: 'Integration of piezoceramic actucators in fibre-reinforced structures for aerospace applications', in 'Smart Structures and Materials 1998: Industrial and Commercial Applications of Smart Structures Technologies', 1998, *Proc. of SPIE*, **3326**, 81-92.

[74] R. PARACIES, M. RUGE: 'In Situ fabrication of active fibre feinforced structures with integrated piezoelectric actuators', *Smart Mater. Struct.*, 2000, **9**, 220-225.

[75] R. MOSES, C. WIESEMAN, A. BENT, A. PIZZOCHERO: 'Evaluation of new actuators in a buffet load environment', in 'Smart Structures and Materials 2001: Industrial and Commercial Applications of Smart Structures Technologies', 2001, *Proc. SPIE*, **4332**, 10-21.

[76] W. SMITH: 'Modelling 1-3 composite piezoelectrics: Hydrostatic response', *IEEE Trans. Ultrason., Ferroelec., Freq. Contr.*, 1993, **40** (1), 41-49.

[77] BS EN 50324-2:2002: 'Piezoelectric properties of ceramic materials and components - Part 2: Methods of measurement – Low power'.

[78] BS EN ISO 527-1:1996: 'Plastics- Determination of the tensile properties'.

[79] L. MASCIA: 'Thermoplastics: Materials engineering', Applied Science Publishers Ltd., London, 1982, p. 143.

[80] http://www.matweb.com, 2004.

[81] A. SCHÄUFELE, K. HÄRDTL: 'Ferroelastic properties of lead zirconate titanate ceramics', *J. Am. Ceram. Soc.*, 1996, **79** (10), 2637-2640.

[82] T. HAUKE, R. STEINHAUSEN, W. SEIRFERT, H. BEIGE: 'Modelling poling behaviour of ferroelectric 1-3 composites', *J. Appl. Phys.*, 2001, **89** (9), 5040-5047.

[83] D. DAMJANOVIC, M. DEMARTIN: 'The Rayleigh law in piezoelectric ceramics', *J. Phys. D: Appl. Phys.*, 1996, **29** (7), 2057-2060.

[84] M. STEWART, M. CAIN, D. HALL: 'Ferroelectric hysteresis measurement and analysis', Report CMMT (A) 152, *National Physical Laboratory*, Teddington, May 1999.

[85] J. RODGERS, A. BENT, N. HAGOOD: 'High load characterization of interdigitated electrode fibre composites', *Proceedings of the 1996 North American Conference on Smart Structures and Materials*, San Diego, CA, February 1996.

[86] W. CAO, C. RANDALL: 'Grain size and domain size relations in bulk ceramic ferroelectric materials', *J. Phys. Chem. Solids*, 1996, **57**, 1499-1505.

[87] E. RONCARI, C. GALASSI, F. CRACIUN, C. CAPIANA, A. PIANCASTELLI: 'A microstructural study of porous piezoelectric ceramics', *J. Europ. Ceram. Soc.*, 2001, **21**, 409-417.

[88] X. KORNMANN, C. HUBER, H. ELSENER: 'Piezoelectric ceramic fibers for active fiber composites: a comparative study', in 'Smart structures and materials 2003: Smart structures and integrated systems', 2003, *Proc. of SPIE,* **5056**, 330-337.

[89] L. CELL, A. CABALLERO, M. VILLEGAS, J. FRUTOS, J. FERNANDEZ: 'Effect of grain growth control on PZT properties', *Ferroelectrics*, 2002, **270**, 105-110.

[90] C. RANDALL, K. NAMCHUL, J. KUCERA, W. CAO, T. SHROUT: 'Intrinsic and extrinsic size effects in fine-grained morphotropic-phase-boundary lead zirconate titanate ceramics', *J. Am. Ceram. Soc.*, 1998, **81**, 677-688.

[91] F. ERNST, O. KIENSLE, M. RUHLE: 'Structure and composition of grain boundaries in ceramics', *J. Europ. Ceram. Soc.*, 1999, **19**, 665-673.

[92] G. ARLT: 'Review: Twinning in ferroelectric and ferroelastic ceramics: stress relief', *J. Mater. Sci.*, 1990, **25**, 2655-2666.

[93] E. DIMITRIU, C. BUNESCU, A. IUGA, R. RAMER: 'Influence of microstructure on physical properties of PT porous ceramics', *Ferroelectrics*, 2002, **270**, 45-50.

[94] A. DENT, 'Microstructure and properties of PZT fibres', 2003, *Final year research project*, Department of Engineering an Applied Science, University of Bath.

[95] D. BRANDON, W. KAPLAN, (1999): 'Microstructural characterisation of materials', Chichester: John Wiley & Sons. pp. 20-22.

[96] BS EN 623-3:2001: 'Advanced technical ceramics- monolithic ceramics- general and textural properties- part 3: Determination of grain size and size distribution (characterised by the linear intercept method)'.

[97] POWDER DIFFRACTION FILE PDF-2: Database sets 1 – 45, International Centre for Diffraction Data (ICDD).

[98] S. MISHRA, D. PANDEY, A. SINGH: 'Effect of phase coexistence at morpotropic phase boundary on the properties of Pb(Zr*x*Ti1-*x*)O3 ceramics', *Appl. Phys. Lett.*, 1996, **69** (12), 1707-1709.

[99] MORGAN TECHNICAL PUBLICATION TP-226: 'Properties of piezoelectric ceramics'.

[100] C. KWOK, S. DESU: 'Pyrochlore to perovskite phase transformation in sol-gel derived lead-zirconate-titanate thin films', *Appl. Phys. Lett.*, 1992, **60** (12), 1430-1432.

[101] K. YAO, L. ZHANG, X. YAO, W. ZHU, 'Controlled crystalisation in lead zirconate titanate glass-ceramics prepared by the sol-gel process', *J. Am. Ceram. Soc.*, 1998, **81** (6), 1571-1576.

[102] H. LEE, W. LEE, Y. KIM, C. WHANG: 'The seeding effects on the phase transformation of sol gel derived PZT powder', *Bull. Korean Chem. Soc.*, 2002, **23** (8), 1078-1084.

[103] X. PU, W. LOU, A. DING, H. TIAN, P. QUI: 'One-step firing process in synthesis of sol-gel derived PZT thick films', *Phys. Stat. Sol. (a)*, 2000, **182**, R10.

[104] J. QUI, J. TANI, N. YAMADA, H. TAKAHASHI: 'Fabrication of piezoelectric fibres with metal core', in 'Smart Structures and Materials 2003: Active Materials: Behaviour and Mechanics', 2003, *Proc. SPIE*, **5053**, 475-483.

[105] R. GENTILMAN, K. MCNEAL, G. SCHMIDT, A. PIZZOCHERO, G. ROSSETTI (JR.): ' Enhanced-performance active fiber composites', in 'Smart Structures and Materials 2003: Industrial and Commercial Applications of Smart Structures Technology', 2003, *Proc. SPIE*, **5054**, 350-359.